

The Study and Shielding of Electromagnetic Radiation from SuperKEKB Electron and
Positron Beam Interactions

by

Alexandre Beaulieu
BEng, Université de Sherbrooke, 2009
MAsc, Université de Sherbrooke, 2011
MSc, University of Victoria, 2013

A Dissertation submitted in partial fulfilment of the
requirements for the degree of

DOCTOR OF PHILOSOPHY

in the Department of Physics and Astronomy

© Alexandre Beaulieu, 2019
University of Victoria

All rights reserved. This dissertation may not be reproduced in whole or in part, by
photocopy or other means, without the permission of the author.

Supervisory Committee

The Study and Shielding of Electromagnetic Radiation from SuperKEKB Electron and Positron Beam Interactions

by

Alexandre Beaulieu
BEng, Université de Sherbrooke, 2009
MAsc, Université de Sherbrooke, 2011
MSc, University of Victoria, 2013

Supervisory Committee

Dr. J. M. Roney, Supervisor
(Department of Physics and Astronomy)

Dr. M. Pospelov, Department Member
(Department of Physics and Astronomy)

Dr. C. Bradley, Outside Member
(Department of Mechanical Engineering)

Abstract

This project contributes to the research and development studies towards successful commissioning of the SuperKEKB electron-positron collider. This accelerator and storage rings complex aims at delivering the high-luminosity collisions of beams of electrons and positrons needed for the Belle II experiment. Such beams produce parasitic radiation — called “machine-induced backgrounds”, or simply “beam backgrounds” — that have detrimental effects on the experimental apparatus performance and durability. The Beast II effort is dedicated to measuring the beam backgrounds, and aims at testing the predictive power of the background models that were used in various phases of the Belle II design. A second objective is to ensure that the environment is safe for the detector prior to installing it around the beam lines.

A major component of beam backgrounds consists of electromagnetic radiation. This study focusses on measuring this radiation at the location of the Belle II electromagnetic calorimeter. The measurements were achieved by placing scintillator crystals at positions representative of the Belle II calorimeter crystals that are the closest to the beam lines, and comparing the data with predictions for different operating parameters of the accelerator.

Different phenomena related to machine backgrounds were observed: vacuum scrubbing, the electron-cloud effect, injection-related noise, beam-gas scattering and Touschek losses. Studies on the positron ring showed average background levels 13.5 ± 3.5 times larger than simulation, whereas that ratio reached $\mathcal{O}(10^2 - 10^3)$ for the electron ring. In the latter, the large uncertainty on the pressure measurements and the gas constituents limit the predictive power of the measurements. Radiation shields were also designed, fabricated, delivered and installed in the detector to protect the electromagnetic calorimeter from radiation coming from the beam lines.

Contents

Supervisory Committee	ii
Abstract	iii
Contents	iv
List of Figures	viii
List of Tables	xiii
Acknowledgements	xv
Dedication	xvi
Personal contributions to Belle II	xvii
1 Introduction	1
1.1 The Belle II experiment	1
1.1.1 The Physics program	2
1.1.2 The accelerator: SuperKEKB	5
1.1.3 The detector: Belle II	8
1.2 Beam-induced background and measurement	12
1.2.1 Overview	12
1.2.2 Beast II, the accelerator commissioning detector	13
1.3 The research question	13
1.4 Goals of the project	13
1.4.1 General goal	13
1.4.2 Specific goals	15
1.5 Dissertation outline	15
2 Source of accelerator-induced background at Belle II and their mitigation	17
2.1 The beams circulating at SuperKEKB	17
2.1.1 Electron production	17
2.1.2 Positron production	18
2.1.3 Storage and beam structure	18
2.1.4 Beam conditions during commissioning	18
2.2 Main background sources at Belle II	18
2.2.1 Touschek radiation	20
2.2.2 Beam-gas interactions	21
2.2.3 Injection particle losses	22

2.2.4	Electron cloud effect	24
2.2.5	Beam-dust events	24
2.3	Background mitigation measures present at Belle II	25
2.3.1	Vacuum chamber design	25
2.3.2	Collimators	27
2.3.3	ECL shields	27
3	Design and construction of ECL radiation shields	30
3.1	Project definition: context, requirements, and deliverables	31
3.1.1	The end users	31
3.1.2	Performance goals	32
3.1.3	Design constraints	33
3.1.4	Deliverables	36
3.2	Conceptual design	38
3.2.1	Methodology	38
3.2.2	Concepts studied	41
3.2.3	Results	43
3.2.4	Discussion and recommendations	46
3.3	Technical design	49
3.3.1	General design of the shields	49
3.3.2	Structural analyses	50
3.3.3	Final detailed designs	52
3.3.4	Commissioning	53
4	Experimental methodology for measuring single-beam-induced electromagnetic radiation	56
4.1	Background studies in the first phase of beam commissioning	56
4.1.1	Influence of pressure	57
4.1.2	Influence of beam size	58
4.1.3	Influence of injection efficiency	61
4.2	Analysis of residual gas constituents	62
4.2.1	Gas model	62
4.2.2	Calculation of the proportion of each gas	63
4.2.3	Calculation of an effective Z for this gas mixture	63
4.2.4	Propagation of uncertainties	63
4.3	Detectors and technology overview	64
4.3.1	CsI(Tl), CsI(pure) and LYSO crystal scintillators	64
4.3.2	Photo-detectors	66
4.3.3	Mechanical integration	68
4.3.4	Signal chain and data acquisition	71
4.4	Calibration	72
4.4.1	Dedicated campaign	72

4.4.2	Time-dependence of the gain	74
4.5	Comparisons between data and simulation	75
4.5.1	Heuristic description of background measurements	75
4.5.2	Re-weighting procedure for simulated data	77
4.5.3	Hypotheses related with the vacuum chamber pressure and gas constituents	78
4.5.4	The data-to-simulation ratio	79
4.5.5	Statistical uncertainty	79
4.5.6	Systematic uncertainties	79
4.6	Beam-gas interactions and beam conditions evolution in Phase 1	84
4.6.1	Vacuum scrubbing	84
4.6.2	Analysis of transient “beam-dust” events	87
5	Results and simulation	89
5.1	Specific results from the CsI(Tl), CsI(pure) and LYSO system	89
5.1.1	Calibration and time-dependence of the gain	89
5.1.2	Energy spectra for different conditions	91
5.2	Beam-gas interactions and beam conditions evolution in Phase 1	110
5.2.1	Effect of gas mixture on beam backgrounds	110
5.2.2	Time series of pressures, background and effective atomic number in pressure bump experiments	112
5.2.3	Uncertainty on Z_e	113
5.2.4	Vacuum scrubbing and dynamic pressure	115
5.2.5	Transient “beam-dust” events	118
5.3	Quantitative comparison of data and simulation	125
5.4	Extrapolation to commissioning phases 2 and 3	131
5.4.1	Phase 2 of commissioning: $\mathcal{L} = 5.4 \times 10^{33} \text{ cm}^{-2}\text{s}^{-1}$	133
5.4.2	Early physics operation: $\mathcal{L} = 5 \times 10^{34} \text{ cm}^{-2}\text{s}^{-1}$	134
5.4.3	Full design luminosity: $\mathcal{L} = 8 \times 10^{35} \text{ cm}^{-2}\text{s}^{-1}$	136
6	Concluding remarks	141
6.1	Aims	141
6.2	Findings	142
6.2.1	Energy distributions	142
6.2.2	Evolution of beam conditions in Phase 1	142
6.2.3	Agreement between data and simulation	143
6.3	Implications	144
6.3.1	For Belle II	144
6.3.2	For future e^+e^- colliders	144
6.4	Recommendations	145
6.4.1	Background measurement methodologies	145
6.4.2	Background models	146

6.4.3	Background management	147
6.5	Final remarks	149

Appendices

A	Detailed calibration results	A-1
A.1	Initial calibration campaign	A-2
A.2	Gain degradation as a function of beam dose	A-6
B	Mechanical Drawings	B-1
B.1	Belle-II Top View 41.5-R14	B-2
B.2	ECL Endcap Shields Envelopes ECL-SHLDS-000	B-3
C	Results of the ECL shields conceptual design studies	C-1
C.1	Without shields	C-2
C.2	Concepts 0	C-4
C.3	Concepts A_1	C-6
C.4	Concepts A_2	C-8
C.5	Concepts B_1	C-10
C.6	Concepts B_2	C-12
C.7	Concepts C_1	C-14
C.8	Concepts C_2	C-16
D	Detail of the ECL shields technical design	D-1
D.1	General design of the shields	D-1
	D.1.1 System of reference	D-1
	D.1.2 Applied loads and design safety factor	D-2
D.2	Design of the backward shield	D-9
	D.2.1 Shell	D-9
	D.2.2 Electromagnetic radiation shield	D-11
	D.2.3 Neutron shield	D-12
	D.2.4 Mounting points for transport and installation	D-15
	D.2.5 Attachments to end-cap	D-18
D.3	Design of the forward shield	D-23
	D.3.1 Shell	D-23
	D.3.2 Electromagnetic Radiation Shield	D-27
	D.3.3 Neutron Shield	D-28
	D.3.4 Mounting points for transport and installation	D-30
	D.3.5 Attachments to end-cap	D-36
D.4	Summary of structural analyses	D-40
D.5	Fabrication and commissioning	D-42
	D.5.1 Vendor	D-42
	D.5.2 Modifications from design drawings	D-42

List of Figures

1.1	Belle II projected luminosity Profile	3
1.2	Schematic representation of SuperKEKB	6
1.3	Technical drawing of the SuperKEKB storage rings	7
1.4	Schematic of the Belle II detector	8
1.5	Schematic side-view of TOP counter and internal reflecting Cherenkov photons	10
2.1	Plot of $D(\xi)$	21
2.2	Background processes from beam-gas scattering	22
2.3	Trigger time distributions for LER injection	23
2.4	Photograph of the antechamber design of the SuperKEKB vacuum chamber	26
2.5	Photograph of the permanent magnets around the LER	27
2.6	Cut-away view of a horizontal collimator system	28
2.7	Top view of the Belle-II detector showing the location of the ECL shields	29
3.1	Photograph of the forward ECL shield in the first Belle detector.	31
3.2	Organisational Chart of the Belle-II Collaboration	32
3.3	Envelopes available for the ECL end-cap shields represented as cross-sectional views of axisymmetric volumes.	34
3.4	The photon mass attenuation length (or mean free path) $\lambda = 1/(\mu/\rho)$	38
3.5	Hot spot in the forward end-cap from the HER radiative Bhabha sample	41
3.6	Effect of varying the lead thickness on the radiation level safety factor	45
3.7	Effect of varying the relative thickness of the neutron absorber on the neutron flux safety factor	46
3.8	1 MeV equivalent neutron flux in the second innermost row of forward crystals for different boron concentrations in the HDPE layer.	47
3.9	Conceptual representation of the ECL end-cap shields, with the main dimensions in mm	48
3.10	Configuration of the shields: example for the backward shield	50
3.11	Complete design of the backward shield	52
3.12	Complete design of the forward shield	53
3.13	Photographs of the ECL shields at various stages during the manufacturing process.	54

3.14	Photographs of the shields taken during the installation tests at KEK.	55
4.1	Schematic representation of the pressure bump studies run plan	57
4.2	Photograph of the PMT and base assembly from the ZEUS experiment.	66
4.3	Specifications of the Hamamatsu R580 photomultiplier tube.	67
4.4	Distribution of the voltage supplied to each electrode of the PMT by the ZEUS base	67
4.5	One calorimeter unit in Beast II	68
4.6	Integration of the calorimeters in Beast II	69
4.7	Disposition, naming scheme and coordinate system of the crystal calorime- ter units	69
4.8	Signal chain based on the use of the CAEN DPP-PSD firmware	71
4.9	Photograph of a crystal dark box with a calibration source	73
4.10	Example of the charge distribution of cosmic ray muon signals in CsI(Tl) used for calibrations	74
4.11	Relative calibration uncertainty of the crystal calorimeter units.	82
4.12	Three examples of DAQ livetime distributions.	83
4.13	Example of P-I curves on a full day	86
5.1	Relative gain curves for the three different crystal types.	91
5.2	Simulated pile-up effects in CsI(Tl) and LYSO crystals under different as- sumptions for the background rates.	93
5.3	Representative spectra from an early HER run	95
5.4	Representative spectra from an early LER run	96
5.5	Representative spectra from a Beast II nominal HER run	97
5.6	Representative spectra from a Beast II nominal LER run	99
5.7	Representative spectra from a Touschek-diminished LER run	101
5.8	Representative spectra from a Touschek-enhanced LER run	102
5.9	Representative spectra from a Touschek-diminished HER run	103
5.10	Representative spectra from a Touschek-enhanced HER run	104
5.11	Representative spectra from a beam-gas enhanced LER run	105
5.12	Representative spectra from a beam-gas enhanced HER run	106
5.13	Example spectra for typical injection conditions.	108
5.14	Gas contents off-line panel.	111
5.15	Time series of a pressure bump experiment and results	112
5.16	Confidence intervals around the Z_e^2 time series	113
5.17	Example probability distribution of Z_e^2	114
5.18	Confidence intervals around Z_e^2 as a function of Z_e^2	114
5.19	Base pressure measured as a function of date	115
5.20	Comparison of two methods used to estimate the dynamic pressure	116
5.21	Measured Touschek-subtracted HER beam-induced background as a func- tion of delivered current.	117

5.22	Measured Touschek-subtracted LER beam-induced background as a function of delivered current.	118
5.23	Example of beam-dust events and peak identification	119
5.24	Comparison of the time structure of beam-dust events between SuperKEKB and Beast II data	120
5.25	Scatter-plot of the beam-dust events 48-hour rate of from the SuperKEKB and Beast II lists.	120
5.26	Cross-correlation between the beam-dust events from SuperKEKB and Beast II datasets.	121
5.27	Example of beam dust events and corresponding pressure readings	122
5.28	Probability distributions of the beam-dust events amplitude	124
5.29	Examples of observed and simulated background rates in the Beast II dedicated studies	125
5.30	Data to simulation ratio for the crystals detectors.	126
5.31	Uncertainty budget examples: LYSO crystal in position F2.	130
5.32	Mapping of the angular index θ_{ID} in the ECL.	133
5.33	Total radiation dose projections for Phase 2 assuming the optimistic data/simulation scaling.	134
5.34	Total radiation dose projections for Phase 2 assuming the pessimistic data/simulation scaling.	134
5.35	Total radiation dose projections for early Phase 3 conditions assuming the optimistic data/simulation scaling.	135
5.36	Total radiation dose projections for early Phase 3 conditions assuming the pessimistic data/simulation scaling.	136
5.37	Total radiation dose projections for nominal Phase 3 conditions assuming the optimistic data/simulation scaling.	137
5.38	Total radiation dose projections for nominal Phase 3 conditions assuming the pessimistic data/simulation scaling.	138
5.39	Relative light yield projection for nominal Phase 3 conditions assuming the optimistic data/simulation scaling.	139
5.40	Relative light yield projection for nominal Phase 3 conditions assuming the pessimistic data/simulation scaling.	139
A.1	Calibration curves for the six CsI(Tl) channels	A-2
A.2	Measured energy resolution for the six CsI(Tl) channels.	A-3
A.3	Calibration curves for the six CsI(pure) channels	A-4
A.4	Calibration curves for the six LYSO channels	A-5
A.5	Relative gain curves for the six CsI(Tl) channels	A-6
A.6	Relative gain curves for the six CsI(pure) channels	A-7
A.7	Relative gain curves for the six LYSO channels	A-8
C.1	Material scan without shields	C-2
C.2	Map of the does (in log scale) deposited in the ECL without shields	C-2

C.3	Radiation dose as a function for crystal row index without shields	C-3
C.4	Neutron flux as a function for crystal row index without shields	C-3
C.5	Material scan of concepts 0	C-4
C.6	Map of the dose (in log scale) deposited in the ECL with concepts 0	C-4
C.7	Radiation dose as a function for crystal row index for concepts 0	C-5
C.8	Neutron flux as a function for crystal row index for concepts 0	C-5
C.9	Material scan of concepts A_1	C-6
C.10	Map of the dose (in log scale) deposited in the ECL with concepts A_1	C-6
C.11	Radiation dose as a function for crystal row index for concepts A_1	C-7
C.12	Neutron flux as a function for crystal row index for concepts A_1	C-7
C.13	Material scan of concepts A_2	C-8
C.14	Map of the dose (in log scale) deposited in the ECL with concepts A_2	C-8
C.15	Radiation dose as a function for crystal row index for concepts A_2	C-9
C.16	Neutron flux as a function for crystal row index for concepts A_2	C-9
C.17	Material scan of concepts B_1	C-10
C.18	Map of the dose (in log scale) deposited in the ECL with concepts B_1	C-10
C.19	Radiation dose as a function for crystal row index for concepts B_1	C-11
C.20	Neutron flux as a function for crystal row index for concepts B_1	C-11
C.21	Material scan of concepts B_2	C-12
C.22	Map of the dose (in log scale) deposited in the ECL with concepts B_2	C-12
C.23	Radiation dose as a function for crystal row index for concepts B_2	C-13
C.24	Neutron flux as a function for crystal row index for concepts B_2	C-13
C.25	Material scan of concepts C_1	C-14
C.26	Map of the dose (in log scale) deposited in the ECL with concepts C_1	C-14
C.27	Radiation dose as a function for crystal row index for concepts C_1	C-15
C.28	Neutron flux as a function for crystal row index for concepts C_1	C-15
C.29	Material scan of concepts C_2	C-16
C.30	Map of the dose (in log scale) deposited in the ECL with concepts C_2	C-16
C.31	Radiation dose as a function for crystal row index for concepts C_2	C-17
C.32	Neutron flux as a function for crystal row index for concepts C_2	C-17
D.1	System of reference for the load cases	D-2
D.2	Load and support scenarios	D-4
D.3	Example of meshed model	D-8
D.4	Geometry of the shells of the backward shield	D-10
D.5	Method of connecting the two backward shield halves together	D-10
D.6	Geometry of the backward electromagnetic radiation shield	D-11
D.7	Layout of the backward neutron radiation shield system	D-13
D.8	Geometry of a backward neutron absorber sub-assembly	D-13
D.9	Exploded view showing the assembly method of the backward neutron absorber	D-14
D.10	Details of the backward neutron absorber cover	D-15

D.11 Components of the backward shield during crane operation	D-16
D.12 Layout of the mounting points to fix the backward jig adapter	D-17
D.13 Geometry of a mounting point for the backward jig adapter	D-17
D.14 Mounting points for backward lifting support	D-18
D.15 Equivalent stress distribution of the backward shield during loading case 5	D-19
D.16 Equivalent stress distribution of the backward shield during loading case 8	D-20
D.17 Geometry of the attachments to backward ECL end-cap	D-21
D.18 Equivalent stress distribution in the backward shield during loading case #13.	D-23
D.19 Details of the equivalent stress distribution in the backward shield end-cap attachment during loading case #13.	D-24
D.20 Convergence study for the equivalent stress on the backward ECL attach- ment plate in loading case #13	D-25
D.21 Geometry of the shell of the forward shield	D-26
D.22 Method of connecting the two forward shield halves together	D-26
D.23 Geometry of the forward electromagnetic radiation shield	D-27
D.24 Geometry of a forward neutron absorber sub-assembly	D-28
D.25 Section view showing the assembly method of the forward neutron absorber	D-29
D.26 Components of the forward shield during crane operation	D-30
D.27 Layout of the mounting points to fix the forward jig adapter	D-32
D.28 Geometry of a mounting point for the forward jig adapter	D-32
D.29 Mounting points for lifting supports	D-33
D.30 Equivalent stress distribution of the forward shield during loading case 8	D-35
D.31 Geometry of the attachments to forward ECL end-cap	D-36
D.32 Equivalent stress distribution in the forward shield during loading case #13.	D-38
D.33 Details of the equivalent stress distribution in the forward shield end-cap attachment during loading case #13.	D-39
D.34 Convergence study for the equivalent stress on the forward ECL attachment plate in loading case #13	D-39
D.35 Example picture of the forward shield bushing welds (as built)	D-43
D.36 As-built geometry of the loaded weld beads on the forward shield bushings	D-44
D.37 Failure plane in a fillet weld	D-44
D.38 As-built backward end-cap attachment plate.	D-47

List of Tables

1.1	Comparison of the two Beast II phases	14
2.1	Beam conditions during commissioning.	19
3.1	Limits for the radiation levels in the ECL.	33
3.2	Masses of the Belle shields	35
3.3	Preliminary costing of the project	37
3.4	Design matrix of the end-cap shields	42
3.5	Comparison of the average yearly crystal doses for the different concepts. The uncertainties are not shown: they are driven by the accuracy of simula- tion, which will be measured in the Beast II program.	44
3.6	Comparison of the average yearly neutron fluxes for the different concepts. The uncertainties are not shown: they are driven by the accuracy of simula- tion, which will be measured in the Beast II program.	44
4.1	Run plan for the HER size study.	58
4.2	Run plan for the LER size study.	60
4.3	Properties of several inorganic crystal scintillators.	65
4.4	Position and numbering scheme of the crystals	70
5.1	Crystals system calibration parameters versus crystal channel number from the initial calibration campaign.	90
5.2	Summary of the crystals spectra: average energy and standard deviation above 1 MeV.	109
5.3	Number of vacuum bursts observed by Beast II detectors for each SuperKEKB section	123
5.4	Summary of the HER data/simulation results for the backward channels. . .	127
5.5	Summary of the HER data/simulation results for the forward channels. . .	128
5.6	Summary of the LER data/simulation results for the backward channels. . .	128
5.7	Summary of the LER data/simulation results for the forward channels. . .	129
5.8	Summary of the data/simulation results with the crystals in Phase 1.	131
D.1	Load and support scenarios for both shields	D-3

D.2	Convergence study results for the equivalent stresses on the backward ECL front cover during loading case 5	D-21
D.3	Convergence study results for the equivalent stresses on the backward ECL assembly jig bushing during loading case 8	D-21
D.4	Convergence study results for the equivalent stresses on the backward ECL assembly jig bushing during loading case 8	D-34
D.5	Summary of the results of the Finite Element Analysis for structural resistance	D-41

Acknowledgements

I would like to thank:

My partner, Audrey, for her constant love and indefectible support, even when my involvement in research and constant travel meant difficult compromises. Je t'aime.

My family, for providing me with invaluable role models that pushed me, by both their good words and their good example, to reach my goals and ambitions.

Dr. J. Michael Roney, for his mentoring, much appreciated teaching skills and patience.

The Belle II Collaboration, for the positive feedback on my analysis and for providing one of the best learning environments I could think of. Special mentions to Dr. Peter Lewis who developed high-quality tools essential to my work, and to Dr. Michael Hedges for the moral and social support, as well as the progress we made together towards our respective goals.

My fellow colleagues and office mates (and friends, in some cases 😊), for making the usually lonely life of a graduate student much more pleasurable and gratifying. It's been an honour to work in your company.

NSERC and the University of Victoria, for funding my work with and allowing me to focus on the scientific aspects of the project.

Dedication

À mon père, Romain.

Personal contributions to Belle II

A. Beaulieu's personal contributions to the Belle II experiment are categorized in three different topics: the Belle II detector hardware, the Beast II effort and the Belle II analysis software framework (BASF2).

Contributions to the Belle II detector hardware

The candidate was responsible for the calorimeter radiation shield design and commissioning work described in Chapter 3. He took charge of the project from the beginning, starting with the definition of performance goals and design constraints. He then undertook a beam-background simulation driven conceptual study to select the best layout and materials, followed by a complete technical design with fabrication and assembly drawings. The candidate then collaborated with the University of Victoria purchasing service to select a manufacturer for the devices, and provided assistance during fabrication and design revisions where required. Finally, he helped the final installation in 2017. A. Beaulieu authored three internal notes describing the progress of the work.

Contributions to the Beast II effort

A. Beaulieu contributed to the Beast II effort by providing the hardware integration of the Phase 1 crystals systems, assisted the installation of the Beast II detectors, helped with calibration work and conducted measurements for the geometrical description of the experiment in the simulation framework. The candidate also delivered Phase 1 data analyses, including comparisons with simulation, that are focussed on the crystals systems data and on the evolution of machine conditions during the experiment. He contributed to the development of the residual gas model and the framework to interpret the gas analyzer readings. The Beast II effort forms the core of this Dissertation, and the material has now been published [1], with the exception of the discussion on extrapolation of Phase 1 data to future beam conditions. He also produced 3D drawings of the Belle II area where many Beast II Phase 2 systems were installed.

Contributions to BASF2

A. Beaulieu acted as the librarian of the structure package between September 2015 and May 2017. He was thus in charge of the code quality, participated to the review process for new functionalities and contributed to providing and updating documentation.

Chapter 1

Introduction

1.1 The Belle II experiment

Belle II is an asymmetric e^+e^- collider experiment nominally operating at the $\Upsilon(4S)$ resonance with a centre-of-mass (CM) energy of $\sqrt{s} = 10.58$ GeV. As such, it is optimized to study CP -violation in the B -meson sector, yet the general purpose detector is excellent to probe a broad range of physics including τ and c flavour physics and precision tests of the Standard Model (SM). Because of the high luminosity — an integrated 50 ab^{-1} is expected — and the clean e^+e^- initial state, such a B -Factory provides an ideal environment to conduct these tests and measurements. It also offers an ideal environment to conduct searches for exotic phenomena, otherwise known as Physics beyond the Standard Model (BSM).

Belle II is the successor to the Belle and *BABAR* experiments, which collected respectively 1040 fb^{-1} and 514 fb^{-1} of data [2, 3]. Most of these data were recorded at the $\Upsilon(4S)$ resonance centre-of-mass energy, just above the $B\bar{B}$ threshold, but smaller data sets were also taken at other $\Upsilon(nS)$ ($n = 1, 2, 3, 5$ for Belle, $n = 2, 3$ for *BABAR*). The scientific program of these B -Factories was successful with scientific highlights such as

- the discovery of CP violation in the B system [4, 5], which was necessary for and cited in the awarding of the 2008 Nobel Prize in physics [6, 7, 8];
- the precision measurement of the CKM matrix elements [9]; or

- the observation of new particles (*i.e.* the $X(3872)$ [10]).

However the precision of many measurements was still limited by the statistical power of the data, therefore a high-luminosity B -Factory is prescribed to pursue the quest for the observation of BSM phenomena. The next section provides more detail about the physics program of Belle II, and the hardware developed for this experiment: the SuperKEKB e^+e^- accelerator-collider and the Belle II particle detector.

1.1.1 The Physics program

The Belle II Physics program has been explored in depth by the Belle II Theory Interface Platform (B2TiP). The work consisted of a series of workshops started in 2014, and the results are presented in the Belle II Physics Book, in preparation [11]. The primary goals of the experiment are to search for BSM Physics in the flavour sector, and increase the precision of the Standard Model (SM) parameter measurements. These two are interconnected, since a significant deviation in a SM parameter could be an indication of a new physical phenomenon whose description lies beyond the SM.

The main advantage of the Belle II experiment (with its large sample of e^+e^- collisions) over hadron colliders is that the initial state is a well-defined collision of fundamental particles. A well known initial state with fewer background processes that contaminate the signals is typically what is meant by a *clean* environment. The large number of collision per unit time provides statistical power to the data set, and is referred to as a *high luminosity* environment. The expected luminosity profile is reported in Figure 1.1. The peak instantaneous luminosity is expected to be achieved in the middle of 2022, and data taking will continue until 2025 to reach 50 ab^{-1} corresponding to over 4.1×10^9 delivered $B\bar{B}$ pairs. This clean and high-statistics environment will enable data analysis techniques employing fully reconstructed B meson decays to improve the precision on the CKM matrix elements by a factor of at least two [13], and reduce the limits of any BSM contribution to the CP-violating phases by a factor of five [14].

Moreover, the Belle II experiment is studying collisions from an asymmetric collider. This means that the electron and positron beams are each circulating at a different energy, which is often tuned to provide 10.58 GeV in the centre of mass frame. Electron and positron collisions at this energy produce $\Upsilon(4S)$ mesons, which then decay into $B\bar{B}$ pairs that are

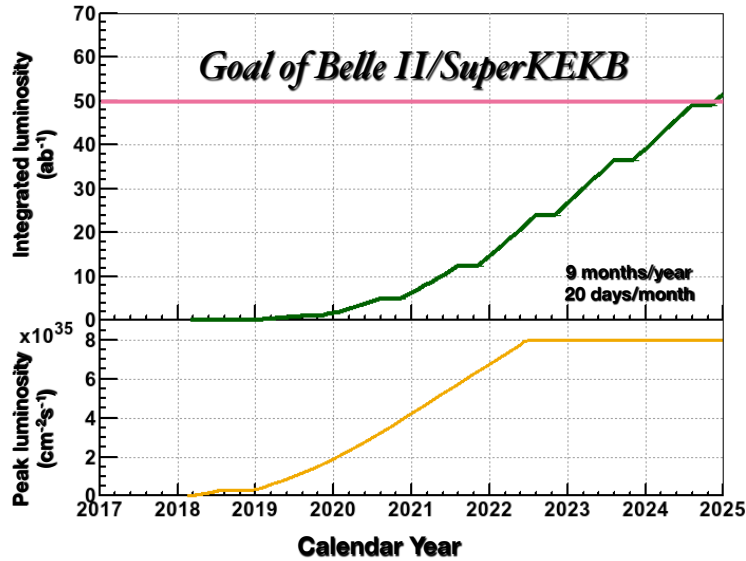


Figure 1.1: Belle II projected luminosity profile as of March 2017. Reproduced from [12].

boosted in the laboratory frame. This allows measurements of the distance between the decay points of each B meson, which are critical for studying time-dependent CP violation [15].

Beyond CKM measurements, the B2TiP report lists four interesting questions to be addressed by the research program [11]. They are reproduced in italics below with few comments on how this will be studied at Belle II.

- *“Are there new CP violating phases in the quark sector?”* CP violation is likely needed to explain the matter-antimatter asymmetry in the universe. It is one of the three “Sakharov conditions” for baryon asymmetry, together with Baryon number violation and interactions out of thermal equilibrium [16]. However, the observed SM sources of CP violation are insufficient to provide the sole explanation of the asymmetry. More knowledge will be gained by studying the difference in decay rates between the B^0 and the \bar{B}^0 in processes involving penguin transitions of $b \rightarrow s$ and $b \rightarrow d$ quarks, such as $B \rightarrow \phi K^0$ and $B \rightarrow \eta' K^0$. Results from *BABAR* and Belle showed less than 3σ deviations from the Standard Model expectations [17, 18, 19]. A larger data sample is required to conclude more decisively on the existence of new, BSM CP violation in the $b \rightarrow s$ and $b \rightarrow d$ transitions.

- *“Does nature have multiple Higgs bosons?”* New charged Higgs bosons, in addition to the SM Higgs, are predicted by many models of new physics. Such charged Higgses could manifest themselves in processes involving heavy flavour transitions, such as $B \rightarrow \tau\nu$ and $B \rightarrow D^{(*)}\tau\nu$. The first process is in fact considered a golden decay mode for the observation of a contribution from a charged Higgs [20]. *BABAR* already observed a discrepancy greater than 3σ in these [21, 22], which was pushed beyond 4σ with the addition of Belle and LHCb data [23], so further study will of this topic is warranted.
- *“Are there sources of lepton flavour violation (LFV) beyond the SM?”* The only lepton flavour violating phenomena observed so far are the neutrino oscillations. Finding evidence for processes such as $\tau \rightarrow \mu\gamma$ in Belle II would provide crucial information to solve the neutrino mass generation problem, for example by discriminating between different Majorana neutrino mass models [24]. Moreover, such direct lepton flavour violation is highly suppressed in the SM with branching fractions on order of 10^{-54} [25]. Unexpectedly large rates for this process — some models predict branching fractions around $10^{-7} - 10^{-10}$ — would be a strong indication of BSM physics [20]. However, latest *B-Factory* results from *BABAR* and Belle showed no evidence of signals for this process [26, 27].

Moreover, the Belle II experiment can leverage the general-purpose detector, the clean environment and the high statistical power of the data set to address questions not directly related to flavour physics. The B2TiP report [11] lists two of these fundamental questions.

- *“Is there a dark sector of particle physics at the same mass scale as ordinary matter?”* Direct searches for dark matter candidates will be conducted using missing energy decays. Belle II has sensitivity to new particles at the MeV to GeV scale such as weakly interacting massive particles. Some models predict a vast hidden sector that would couple to the Standard Model via new gauge symmetries [28]. *B* factories are a good environment to search for such objects [29][30], and the single photon trigger lines of Belle II would provide a path to search for such hidden-sector particles including dark matter candidates and gauge bosons.
- *“What is the nature of the strong force in binding hadrons?”* Exotic quarkonium states were recently observed in *B* factories and hadron colliders such as the LHC. The

Belle II program will contribute to this research topic by scanning the beam energies and exploiting initial-state radiation processes to study a range of collision energies. Moreover, with its near 4π coverage and good particle identification performance, the detector will be able to enable the characterization of these newly discovered quarkonia states and continue the study of QCD in the low-energy regime.

1.1.2 The accelerator: SuperKEKB

The SuperKEKB accelerator represented in Figure 1.2 is a major upgrade to KEKB, and aims to deliver more than 40 times the integrated luminosity of its predecessor. The luminosity is a key factor in determining the performance of an experiment, since the production rate of a particle is the product of the delivered luminosity and its production cross section. It is given by

$$\mathcal{L} = \frac{f n_{e^+} n_{e^-}}{4\pi \sqrt{\epsilon_x \beta_x^* \epsilon_y \beta_y^*}} \mathcal{F} \quad (1.1)$$

where f is the frequency of the bunch crossings, n_{e^+} , n_{e^-} are the number of electrons per bunch, and $\epsilon_{\{x,y\}}$ are the emittances of the bunches in the transverse directions (x and y), and $\beta_{\{x,y\}}^*$ are the transverse amplitude functions β in the interaction region. The asterisk in β^* denotes an evaluation at the vicinity of the interaction point. The extra factor $\mathcal{F} < 1$ is an efficiency term taking into account imperfections such as the non-zero crossing angle [9]. It is interesting to note that the product of bunch crossing frequency and the number of particles per bunches is directly proportional to the beam currents. Moreover, the emittance is the area in phase space of an ellipse containing the particles. The emittance is defined, in each transverse direction i , with respect to the local rms size of the bunch and the β function:

$$\epsilon_i \equiv \frac{\sigma_i^2}{\beta_i}. \quad (1.2)$$

It is the envelope of the motion of the particles. The 40-fold increase in luminosity expected for SuperKEKB will be achieved by acting on all fronts: a factor 2 is gained by increasing the beam currents, and the remaining 20-fold increase is obtained by focussing the beams more tightly in the interaction region (IR).

The main technological improvements required for the upgrade are indicated in Figure 1.2 and consist of new

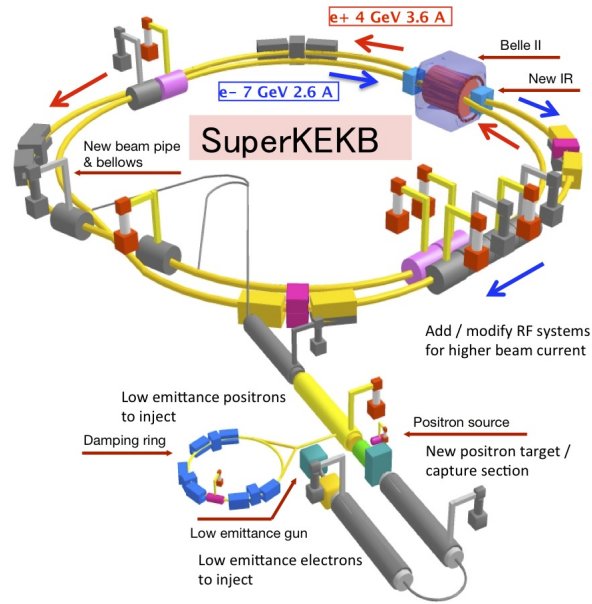


Figure 1.2: Schematic representation of SuperKEKB with labels indicating the main improvements. Reproduced from [31].

- radio-frequency (RF) system to sustain higher currents by increasing power delivered to the beams;
- ceramic-coated positron beam vacuum chamber walls with ante-chambers to reduce electrons-cloud effect (see Section 2.2.4);
- low-emittance electron gun for high-quality electron beam;
- positron source and damping ring for low-emittance positron beam;
- superconducting final-focussing system to reduce beam size to $60 \text{ nm} \times 10 \text{ } \mu\text{m}$;
- crab cavities to rotate bunches before the IR for head-on collisions; and
- smaller boost for improved low-energy ring (LER) lifetime and smaller high-energy ring (HER) emittance¹.

¹The e^+ and e^- energies at SuperKEKB are 4 GeV and 7 GeV respectively, for a boost factor of 0.284, where as the KEKB energies were 3.5 GeV (e^+) and 8.0 GeV (e^-) for a boost of 0.425 [32].

For future reference in this document, a technical drawing of the SuperKEKB storage rings, including the specific names of the beam sections and experimental halls, is reported in Figure 1.3 below.

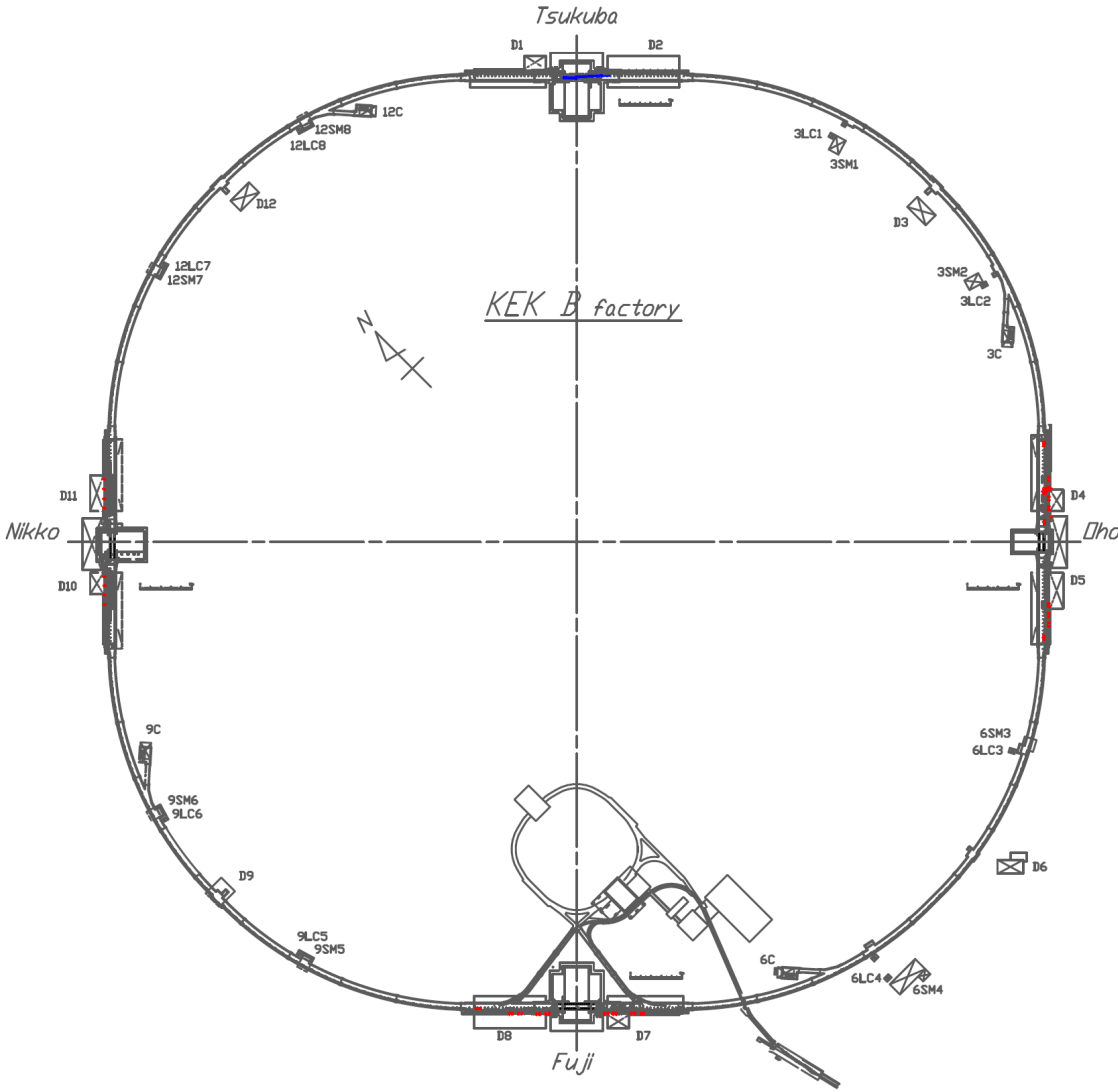


Figure 1.3: Technical drawing of the SuperKEKB storage rings. Belle II is located inside the Tsukuba hall, at the top of this drawing. Reproduced from [33].

1.1.3 The detector: Belle II

The Belle II detector represents a major upgrade of its precursor Belle where only the structural elements, the crystals in the electromagnetic calorimeter, and the 1.5 T superconducting solenoid magnet are conserved. It is represented in Figure 1.4 with the main coordinate system, and each of the numbered sub-detectors are detailed in the paragraphs below [34]. The main coordinate system is centred at the nominal interaction point: y points up, z is collinear with the solenoid axis and points in the electron beam direction, and x completes a right-handed coordinate system by pointing away from the centre in the plane of the storage ring.

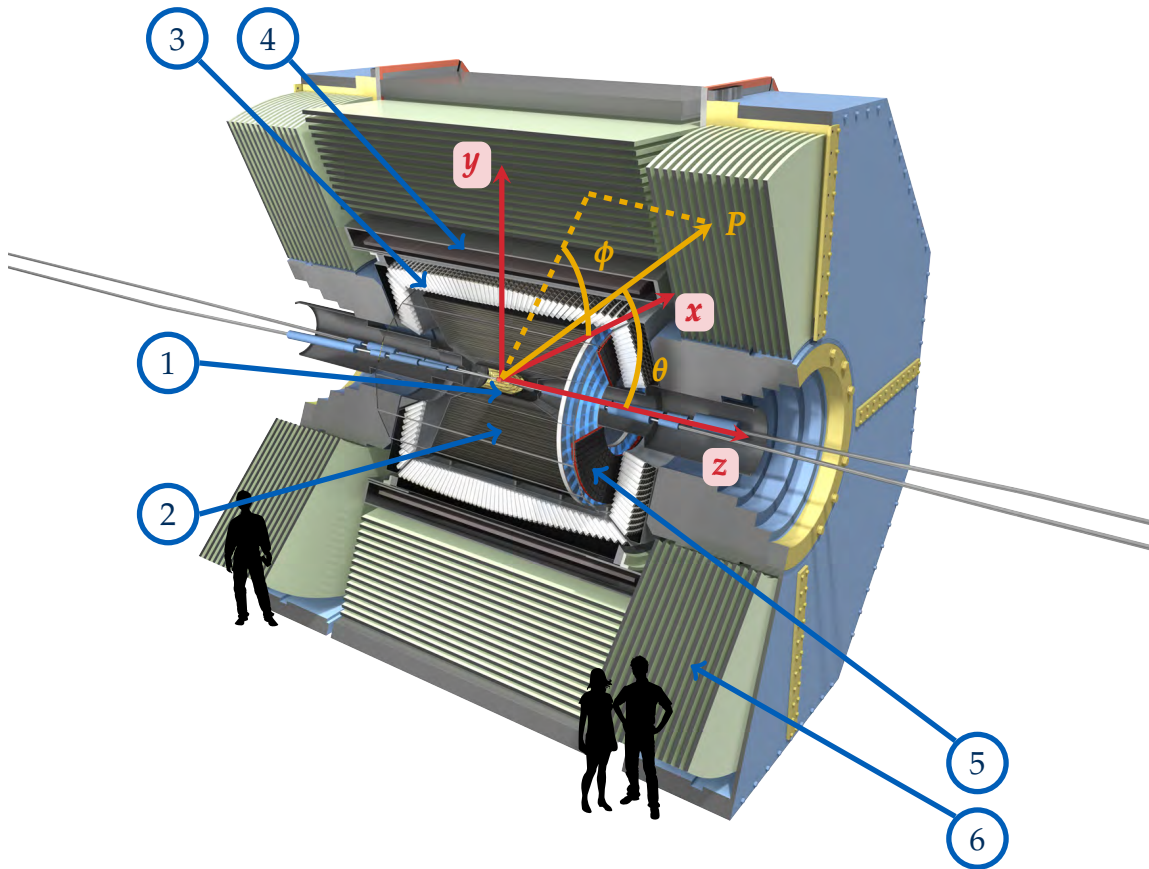


Figure 1.4: Schematic of the Belle II detector and associated coordinate system, 1: Pixel and vertex detector (PXD/SVD). 2: Central drift chamber (CDC). 3: Electromagnetic calorimeter (ECL) 4: Time-of-propagation counter (TOP). 5: Aerogel ring-imaging Cherenkov detector (ARICH). 6: K_L and muon detector (KLM). Reproduced from [12] with modifications (addition of the labels and coordinate system).

Pixel and vertex detector (VXD) The role of the innermost system of the Belle II detector is to measure the decay vertices of the B - and D -mesons, and the τ -leptons and connect them to the tracks reconstructed in the central drift chamber. It is composed of two layers of silicon pixel detector and four layers of double-sided silicon strip detectors. The layers are located at radii between $r = 14$ mm and $r = 140$ mm, with a layout that is hermetic in ϕ , and the polar acceptance ranges from $\theta = 17^\circ$ to $\theta = 150^\circ$. The design performance specification is an impact parameter resolution $\sigma_{z0} \sim 20 \mu\text{m}$.

Central drift chamber (CDC) The drift chamber is used to reconstruct tracks and measure the momentum of charged particles, contribute to particle identification (PID) by measuring energy losses (dE/dx), and provide a trigger signal for charged particles. When a charged particle travels through the gas, it leaves a track of ionized molecules with the liberated electrons drifting towards the positively biased sense wires. At the sense wires, the electrons initiate an avalanche that ultimately produces a measurable signal. There are 14,336 sense wires in the CDC and the location of ionization associated with the signal on each sense wire is determined by measuring the drift times of electrons produced in the ionization. Pre-amplifiers and front-end-digitizer boards are attached directly to these wires to provide the signal conditioning for data extraction, and the fast logic necessary for triggering. There are also 42,240 field wires that shape the electric field within the CDC for a more uniform drift velocity. The Belle II CDC is an entirely new detector that extends to a larger radius from the beam pipe that did the Belle drift chamber. The other improvements for Belle II are faster electronics and a higher cell density, especially at smaller radii. As with the inner detectors, the CDC is hermetic in ϕ , and the polar acceptance ranges from 17° to 150° . The expected transverse momentum resolution is given as a function of the velocity of the particle β , and component of momentum transverse to the solenoidal magnetic field, p_t :

$$\sigma_{p_t}/p_t = \sqrt{(0.2\%p_t)^2 + (0.3\%\beta)^2} \quad (1.3)$$

Time-of-propagation counter (TOP) The time-of-propagation counter is a PID device aiming at better pion/kaon separation using a novel technology. As depicted schematically in Figure 1.5, the TOP consists of rectangular quartz radiators coupled to micro-channel plate photo-multiplier tubes (MCP-PMT). Charged particles travelling through the quartz bars faster than the speed of light in that medium emit a light cone —

Cherenkov radiation — whose opening angle depends on the velocity of the incoming particle. The array of photon detectors to the right of the figure then provides a time-resolved image of the Cherenkov light cones. Because the momentum is measured in the CDC, measuring the velocity constrains the mass of the particle therefore revealing its identity. There are 16 quartz bars forming the TOP, providing azimuthal coverage of approximately 93% and a polar acceptance ranging from 32° to 128° . The K/π separation performance is expected to be 99% kaon selection efficiency at $\leq 0.5\%$ pion misidentification probability.

The novel feature of the Belle II TOP is that it also measures the time of propagation of the photons and enhances the PID by adding time-of-flight information of particles produced in the collisions.

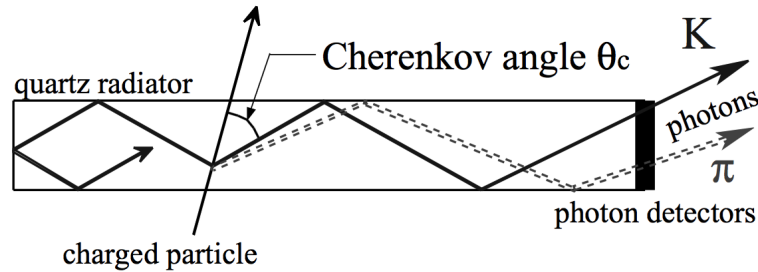


Figure 1.5: Schematic side-view of TOP counter and internal reflecting Cherenkov photons. Reproduced from [34].

Aerogel ring-imaging Cherenkov detector (ARICH) The ARICH is responsible for particle identification in the forward end-cap region. Similar to the TOP counter, the goal is to use Cherenkov radiation to discriminate between pions and kaons. However the technology here is different: the ARICH works by using radiators made of two layers of aerogel — a light silica foam material that can be manufactured to a specific index of refraction — to focus the light onto a plane of position-sensitive photon detector. These detectors, hybrid avalanche photo-diodes (HAPD), are developed specifically for this application in the Belle II experiment. These are hybrids between conventional PMTs and APDs: photo-electrons are generated by a negatively biased photocathode while the readout is accomplished via pixelated avalanche photo-diodes. The K/π separation performance is expected to be 96% kaon selection efficiency at 1% pion misidentification probability.

Electromagnetic calorimeter (ECL) The ECL serves more than one purpose: the main

function is to measure the direction and energy of photons and electrons, but the strength of the signal left by other particles is also used by PID algorithms. The ECL is composed of an array of 8736 thallium-doped caesium iodide — CsI(Tl) — crystals aimed near the interaction point. These crystals are typically 30 cm long trapezoidal prisms. The actual dimensions of the end faces vary between crystals to ensure a close fit, but, as a specific example, crystal #14 of the forward end-cap has a small end measuring $b = 5.4$, $B = 5.8$, $h = 5.6$ and a large end measuring $b = 6.2$, $B = 6.6$, $h = 6.4$ where b is the length of the small base, B , the length of the large base and h , the height of the trapeze. The dimensions of the other crystals vary by less than 30% of those values. These crystals are dense scintillators: the above dimensions correspond to just over 3 Molière radii across by 16 radiation lengths long. Therefore, any incoming photon or electron produces an electromagnetic shower generally contained within the volume of few neighbouring crystals. Individual shower particles can in turn excite atomic electrons which re-emits visible or near-UV light when returning to the ground state. The electromagnetic shower process is what makes this system more sensitive to electrons and photons, however any charged particle will excite some atomic electrons through regular dE/dx so a small signal can be observed. Hadrons (pions, kaons, protons, neutrons) may also interact in the ECL and produce hadronic showers since the nuclear interaction length of CsI(Tl) is 38 cm[9].

K_L and muon detector (KLM) The KLM is the outermost subsystem of the Belle II detector. The design principle is to have steel (iron) plates interleaved with active material. The iron plates both provide a return path for the magnetic flux and act as thick a target material for the charged particles to deposit energy, or, in the case of long-lived kaons K_L or other hadrons, initiate a hadronic showers. It is split into two parts: the barrel, covering polar angles between 45° and 125° , and the end-caps that bring the total acceptance to $[20 - 145]^\circ$. The barrel region remains unchanged from Belle: the 14 iron plates are sandwiched between resistive plate chambers (RPC) that act as the active material. In the end-cap region, however, the performance of the RPCs is degraded due to the large background rate, so faster plastic scintillators coupled to wavelength-shifting fibres and readout by silicon photo-multipliers are used instead.

1.2 Beam-induced background and measurement

1.2.1 Overview

One challenge of commissioning a new collider experiment is to understand the different sources of beam-induced background and keep them under control. The typical contributions to detector backgrounds at e^+e^- collision experiments are the following: [35]

1. Beam-gas interactions
2. Intra-beam interactions
3. Synchrotron radiation
4. "Physics" backgrounds such as Bhabha scattering
5. Interaction with thermal photons
6. Operational particle losses (*e.g.* beam injections losses and electron-cloud effect)

The first three components are independent of luminosity such that they are relevant to the first accelerator commissioning phase as discussed below. There will be no focussing of the beams during that period, so sources that require collisions between the e^+ and e^- beam particles are expected to be negligible. Furthermore, beam losses due to elastic scattering off thermal photons — the infra-red photons coming from black-body radiation of the vacuum chamber walls at room temperature — are only important at high energy e^+e^- colliders such as LEP and LEP2 (where the centre-of-mass energy ranged from 45 GeV to nearly 100 GeV).

Continuous injection is an interesting feature of the SuperKEKB accelerator, although predictions of the related background time structure are notoriously difficult [35]. One has to rely on experimental methods to assess it, such as part of the project being presented.

A more detailed description of the different sources of machine-induced background relevant to the proposed project are reported in Section 2.2.

1.2.2 Beast II, the accelerator commissioning detector

The Beast II project (for Beam Exorcism for a Stable Experiment) aimed at studying the accelerator-induced background before taking so-called “Physics” data. It was separated in two distinct phases as presented in Table 1.1.

The research project that is the subject of this Dissertation pertains only to the first of these phases, Phase 1. In summary, this initial phase provided a first insight into the reliability of background estimates coming from simulation during first operation of the SuperKEKB accelerator. Certain types of background were enhanced due to the higher vacuum chamber pressure, while all luminosity-dependent sources were strongly suppressed because there wasn't any final focussing of the beams. Even though these conditions were far from what is expected during physics data taking, Beast II Phase 1 represented a unique opportunity to measure exclusively the luminosity-independent background sources.

The second phase, Phase 2, involved using the Belle II detector without its vertex detector. The goal was to measure the background in more realistic conditions, and also determine when the radiation levels were safe for the vertex system to be added.

1.3 The research question

The research question is formulated as follows:

What are the quantitative characteristics of the beam-induced background radiation associated with single beams in Phase 1 of SuperKEKB operations under different beam configurations, and how precisely are these modelled in simulations of the accelerator?

1.4 Goals of the project

1.4.1 General goal

The general goal of this project was to measure the machine-induced background near the intended position of the ECL end-cap of the Belle II detector, and to use these measurements to correct predictions from simulations of the accelerator and assess an uncertainty

Table 1.1: Comparison of the two Beast II phases

	Phase 1	Phase 2
Run period	February 2016 – June 2016	March 2018 - June 2018
Beam final focus	No	Yes
Vacuum chamber pressure (in Pa)	10^{-6}	10^{-7}
Detector	Ad-hoc elements sensitive to specific background sources	Belle II without VXD
Concurrent activities	Vacuum scrubbing Test of new LER collimators	Belle II DAQ & Trigger Slow-control integration Final collimator installation Monitoring systems
Critical Goals	Measure x-ray dose along z-axis Test diamond beam-abord system	Ensure VXD can be safely installed and operated Provide BG levels from each detectors to SuperKEKB for collimator optimization Measure dose rates and neutron fluxes from individual BG contributions
Desired Goals	System test of all Phase 2 systems Measure EM BG in end-cap region, check scaling predicted by simulation First measurement of radiation doses and neutron fluxes vs (z, ϕ) Measure time-dependence of BG	Measure time-dependence of BG

Acronyms:

LER: Low-energy ring: positron beam with an energy of 4.0 GeV
 DAQ: Data acquisition
 VXD: Pixel and vertex detector system
 EM: Electromagnetic
 BG: Background

on those predictions. In addition, this work mitigated the impact of the predicted machine-induced background through the provision of a radiation shield for the ECL.

1.4.2 Specific goals

The specific goals of this project were the following:

- Use tools developed by the Belle II Collaboration and SuperKEKB team to simulate operating conditions during Phase 1, and predict impact on observed background in the forward and backward calorimeter regions.
- Design and assemble the measurement apparatus, and integrate with the other Beast II sub-detectors.
- Measure the relationship between the observed background and the pressure in the vacuum chamber, and follow its evolution during commissioning
- Measure the relationship between observed background levels and the size, current and time-structure of bunches that comprise the beam, as described in Chapter 2.
- Measure the time-structure of background during beam injection.
- Combine the information to make predictions about the background level throughout the Belle II lifetime.

1.5 Dissertation outline

This Dissertation is organized as follows.

Chapter 2 provides more information about the context and the physics motivation for the research question which relates to accelerator-induced background and the quality of our understanding of these phenomena.

Chapter 3 details the author's personal contribution to the construction of the Belle II detector: the design, overseeing construction, and the commissioning of a pair of radiation

shields. The purpose of these shield is to protect a region of the calorimeter against electromagnetic and neutron radiation arising from machine background, and their design is based of the same simulation we aim to improve by the current measurement project.

Chapter 4 describes the experimental apparatus and the methodology employed to conduct the background characterization. Chapter 5 presents the experimental results in comparison with the simulation, as well as projections to future operating conditions.

*
**

Chapter 2

Source of accelerator-induced background at Belle II and their mitigation

2.1 The beams circulating at SuperKEKB

This description about accelerator-induced background starts with how beams are produced and stored.

2.1.1 Electron production

Electrons are generated by a photocathode RF gun (or “electron gun”) specifically designed to deliver large charge and low emittance beams to SuperKEKB [36]. The pulsed laser of the RF gun is directed to a photocathode that liberates two 10 nC bunches of electrons. These are accelerated, first by cavities within the gun itself, then by linear accelerator cavities, up to 3.3 GeV. At this point, the electron bunches can then be directed to the positron source 3.5 mm away from the beamline in order to produce positrons for the LER, or they can pass through and be further accelerated up to 7 GeV before being delivered to the HER [37, 38].

2.1.2 Positron production

In the positron mode, 3.3 GeV electron bunches collide with a 14 mm thick ($4 X_0$) tungsten target where they create an electromagnetic cascade, thus generating lower energy positrons and electrons. Positrons are captured in the positron-capture section with a flux concentrator, large aperture accelerating structures, and solenoid focusing coils. Approximately 1 positron is retrieved for 10 incoming electrons [39]. The positrons are then accelerated to 1.1 GeV, directed into the damping ring to reduce the emittance of the bunches, and finally accelerated to 4 GeV before delivery into the storage rings [37, 38].

2.1.3 Storage and beam structure

The storage rings store the beams in two 3 km circumference vacuum chambers. These are in fact squares with rounded corners (four straight section and four arc sections), as is visible in Figure 1.3. The straight sections also contain RF cavities that compensate energy losses.

The beams are structured in trains of bunches. The design values for physics operation are 2503 bunches per train for either species, with an average bunch current of 1.04 mA/bunch for electrons and 1.44 mA/bunch for positrons [34]. As described in Section 1.1.2, the volume of these bunches in phase space determines the emittance. A low emittance is desirable to increase instantaneous luminosity, however a large amount of charge confined to a small volume enhances beam losses via the Touschek effect, as discussed in Section 2.2.1.

2.1.4 Beam conditions during commissioning

Table 2.1 lists the conditions observed in Phases 1 and 2, and those expected in Phase 3.

2.2 Main background sources at Belle II

Three main sources of beam background are expected during the first phase of SuperKEKB commissioning experiment: particles resulting from intra-bunch Touschek losses, interactions between beam particles and residual gas atoms in the beam pipe, and particle losses

Table 2.1: Beam conditions during commissioning. All data are given as LER/HER.

	Phase 1*	Phase 2 [†]	Phase 3 (nominal)
Current [mA]	720/630	340/280	3600/2600
Pressure [nPa]	1000/100	100/100	100/100
Vertical size [μm] [‡]	140/50	0.40/0.50	0.45/0.62

* Operating conditions evolved continuously in Phase 1.

Using typical maximum current data for the Beast II studies of 2018-05-17.

† Operating conditions evolved continuously in Phase 2.

Using typical data for Phase 2.1.4 (2018-06-12).

‡ Vertical beam size measured with the x-ray monitors in Phases 1 and 2.

during injection. Moreover, other operational or transient losses such as those due to the electron-cloud effect and beam-dust collisions are expected. All these background sources will be introduced in more detail below.

Conventionally in accelerator physics, the loss probability is expressed in terms of inverse lifetime of the beam. The net inverse lifetime $1/\tau$ during beam storage is therefore the sum of the inverse lifetimes due to each individual process (beam-material, intra-beam, and beam-gas interactions).

$$\frac{1}{\tau} = \frac{1}{\tau_{\text{b-m}}} + \frac{1}{\tau_{\text{i-b}}} + \frac{1}{\tau_{\text{b-g}}} \quad (2.1)$$

The injection losses are treated separately because they arise from imperfect matching of the injected bunch to the acceptance of the beam, and they do not affect the stored beams.

It is worth noting that a major contribution to Belle II background is radiative Bhabha events in which photons are exchanged between beam electrons and positrons with extra photons radiated off the initial or final state particles. However it requires collisions between the e^+ and e^- beams and therefore its impact was expected to be minimal in Phase 1. The dominant background contributions in Phase 1 were the intra-beam and the beam-gas effect, with their relative importance depending on the operating conditions. The typical lifetimes in this phase were on the order of 500 minutes for the HER and 100 minutes for the LER.

2.2.1 Touschek radiation

The Touschek effect is the scattering of particles of the same species within a beam bunch of those particles. Such scattering induces an interchange between the transverse and longitudinal momentum components of a pair of particles. These off-momentum particles fall out of the stable orbit of the synchrotron and are deflected towards the walls of the vacuum chamber, producing electromagnetic showers.

This effect was first demonstrated in a paper by Bernardini and colleagues [40] in 1963, then described in more details by various authors [41, 42, 43]. It is expected to be the dominant intra-beam interaction contributing to the beam lifetime between injections. The Touschek lifetime $\tau_{\text{Tous.}}$ is:

$$\frac{1}{\tau_{\text{Tous.}}} = \frac{Nr_e^2c}{8\pi\sigma_x\sigma_y\sigma_z} \frac{\lambda^3}{\gamma^2} D(\varepsilon, \sigma_p), \quad (2.2)$$

where N is the number of electrons or positrons in a bunch of volume $\sigma_x\sigma_y\sigma_z$, and r_e is the electron classical radius ($r_e \approx 2.82 \times 10^{-15}$ m). The beam parameters are γ the beam lab-frame energy in units of particle mass (the Lorentz factor for a beam particle), σ_p the root mean squared value of the individual particle momenta, and ε the accelerator limiting acceptance (either RF, momentum or geometric). The parameter λ is the relative acceptance:

$$\lambda^{-1} = \frac{\Delta E}{E} = \frac{\varepsilon}{\gamma m_0 c}. \quad (2.3)$$

The function $D(\varepsilon, \sigma_p)$ is not analytical. However it has a flat maximum at 0.3 around the usual region of interest and it is reported in Figure 2.1.

From Equation 2.2, it is evident that that the rate of Touschek losses is proportional to the square of the bunch current and inversely proportional to the bunch size.

At Belle II, the Touschek effect is simulated in the Strategic Accelerator Design (SAD) framework [44] which propagates the particles until they hit the wall of the vacuum chamber or a collimator. The resulting particle/matter interaction is then modelled with the Belle II implementation of the Geant4 simulation package [45].

In the context of the work, the Touschek lifetime $\tau_{\text{Tous.}}$ is the only lifetime related to intra-beam effects τ_{i-b} in Equation 2.1. Moreover, it is worth noting that the factor $1/\gamma^2$ in the inverse lifetime of Equation 2.2 suggests that, for equal beam sizes, the Touschek background contribution should be smaller in the HER than in the LER.

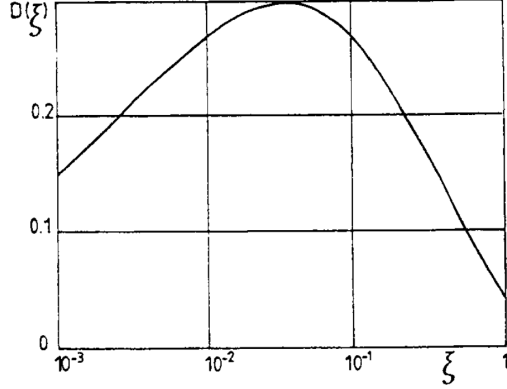


Figure 2.1: Plot of $D(\xi)$ with $\xi = (\epsilon/\gamma\sigma_p)^2$ using the notation of (2.2). Reproduced from [43].

2.2.2 Beam-gas interactions

The interactions of beam particles with residual gas atoms in the vacuum chamber are mainly due to bremsstrahlung and Rutherford scattering. Both processes, represented in Figure 2.2, result in off-momentum beam particles colliding with the wall of the chamber.

The beam-gas losses can be expressed as the sum of the contributions due to all gas species.

$$\frac{1}{\tau_{\text{gas}}} = c \sum_i \sigma_{\text{gas},i} n_i \quad (2.4)$$

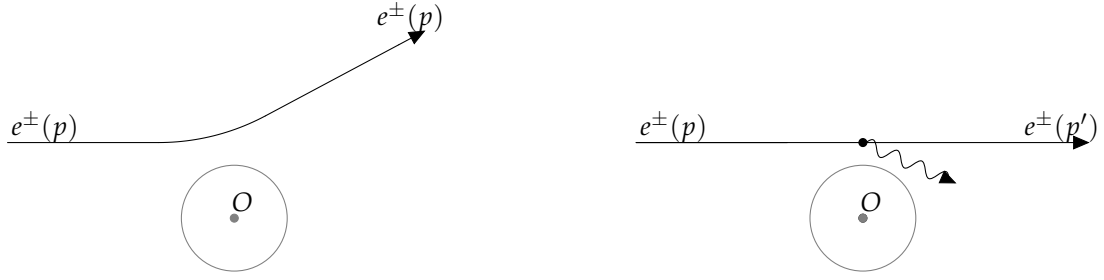
where c is a velocity of the beam particles, $\sigma_{\text{gas},i}$ and n_i are respectively the beam-gas effective interaction cross section and the density of gas species i [46]. Moreover, the effective cross section for a given species with an atomic number Z_i is in turn the sum of the contributions from Rutherford scattering $\sigma_{\text{Ruth.}}(Z_i)$ and bremsstrahlung $\sigma_{\text{brems}}(Z_i)$.

The first case is shown in Figure 2.2a and produces a beam particle with large transverse momentum. The second contribution, represented in Figure 2.2b, produces an off-momentum particle and a photon. The integrated cross sections with approximations suitable for B factories conditions have been calculated to be

$$\sigma_{\text{Ruth.}}(Z_i) \approx \frac{4\pi Z_i^2 \alpha^2}{E^2 \theta_{\text{min}}^2} \quad (2.5)$$

for the Rutherford scattering and

$$\sigma_{\text{brems}}(Z_i) \approx \frac{16\alpha Z_i^2 r_e^2}{3} \cdot \ln\left(\frac{184}{Z_i^{1/3}}\right) \cdot \ln\left(\frac{1}{(\Delta E/E)_{\text{lim}}} - \frac{5}{8}\right) \quad (2.6)$$



(a) Rutherford scattering: change of e^\pm direction (b) Bremsstrahlung: radiation and loss of e momentum

Figure 2.2: Background processes from beam-gas scattering off atom centred at O

for bremsstrahlung near an atomic nucleus [9, 47, 48].

In these equations, α is the fine structure constant ($\alpha \approx 1/137$), E is the energy of the beam particles, θ_{\min} is minimum scattering angle for particle loss (which is related to the geometric acceptance), and r_e is the electron classical radius ($r_e \approx 2.82 \times 10^{-15}$ m), and $(\Delta E/E)_{\lim}$ is the limiting relative energy acceptance of the ring.

It is worth noting that the $\ln\left(\frac{184}{Z_i^{1/3}}\right)$ contribution to the bremsstrahlung cross section in Equation 2.6 varies much slower than the first term in Z_i^2 , such that it can be approximated as a multiplicative constant. Therefore, for fixed beam energies and collimator settings, the beam-gas interaction cross section is only proportional to Z_i^2 , however with different proportionality factors for the HER and LER.

Both the Rutherford and the bremsstrahlung processes contribute to the beam-gas lifetime τ_{b-g} in Equation 2.1. The relative importance of these contributions depends strongly on the operating parameters of the accelerator, as discussed further in Section 4.5.1. In the early phases of commissioning, beam-gas interactions were expected to be the limiting factor to the total beam lifetime.

2.2.3 Injection particle losses

SuperKEKB uses a continuous injection scheme, meaning that the bunches with the lower currents are automatically topped-up during data taking. Injection is a lossy process, and this translates into larger backgrounds when the injected bunch passes by the detectors.

In Belle, the DAQ was vetoed for 4 ms after each injections to avoid recording data that would be flooded with noise hits. However at an injection rate of 50 Hz in Belle II this would correspond to a dead time of 20% [34].

No simulation exist for this background contribution. One of the goals in Beast II is therefore to understand the time structure of the injection-related background in order to apply a more elaborate veto strategy and increase the recorded luminosity. A preliminary study was conducted towards this goal at the end of Belle operation. A special run was recorded with no injection veto, and the collaboration used the signals from the backward end-cap crystals to study the timing characteristics of the injection background. The results of that study are presented in Figure 2.3: the left panel displays a scatter plot of the arrival time of the hits with, on the vertical axis the time within one revolution period (time-in-revolution), and on the horizontal axis, the time elapsed after the injection (time-after-injection). The other two panels show the projected distributions on the Time-after-injection and the time-in-revolution axes.

The key message is that the first $150 \mu\text{s}$ after injection are where most hits occur. After that period, the signals are much quieter except when the injected bunch passes the interaction point at around $3 \mu\text{s}$ in the revolution, and to a much lesser extend at around $3.5 \mu\text{s}$ after that. This is the type of measurement we would like to conduct in Phase 1, and also extend the study by scanning different injection conditions such as timing, number of bunches, or injection efficiency.

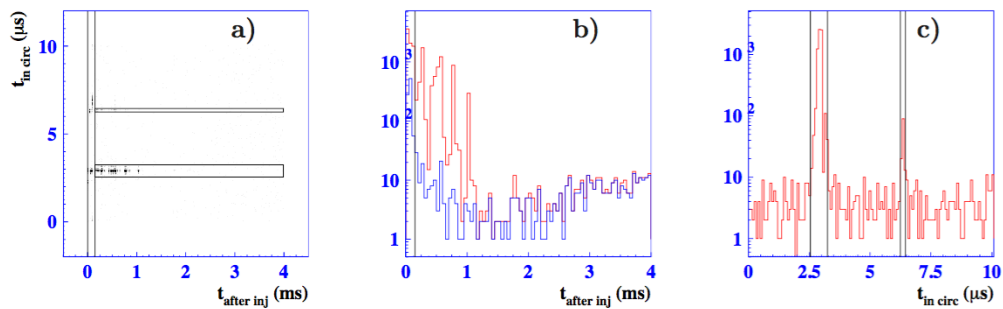


Figure 2.3: Trigger time distributions for LER injection. a) Scatter plot of time within a revolution period vs. time after injection. b) Time-after-injection distribution (red: all events; blue: excluding the two horizontal bands in (a)). c) Time-in-revolution distribution for $t_{\text{after inj.}} < 150 \mu\text{s}$. Reproduced from [34].

2.2.4 Electron cloud effect

The electron cloud effect is typically a consequence of synchrotron radiation photons hitting the material of the vacuum chamber of the beam pipe and ejecting electrons via the photo-electric effect. These primary photo-electrons are then accelerated by successive bunch crossings and often collide with the chamber material with a broad energy spectrum, generating more secondary electron emissions. Such amplification processes are often what determines the strength of the electron cloud effect, and factors of ten in gain can be reached. The electron cloud effect occurs predominantly in positively-charged beams since these attract the electrons. Other factors include beam currents, energy and bunch spacing, as well as vacuum chamber geometry, pressure, and the electronic properties of the surface material. Because of the many parameters involved, a numerical model is usually required for any quantitative prediction of this effect, however in modern positron or proton beams the average density of electrons can reach 10^{10} m^{-3} to 10^{12} m^{-3} [49].

2.2.5 Beam-dust events¹

During commissioning of the accelerator, one concern was the observation of localized pressure bursts and accompanying background spikes. The prevalent hypothesis for these observations are collisions between the beam electrons and positrons, and small particles such as dust coming off the vacuum chamber material [50, 51, 52, 53]. These events will therefore be referred to as “beam-dust” events in this dissertation.

Such beam-dust events are important during commissioning and running of an accelerator, since the corresponding increase in observed background often results in beam aborts and loss of operation time. The SuperKEKB group monitors these events by measuring pressure peaks around the beam pipe. The questions addressed in the present dissertation are

- What is the time structure of these beam-dust events during Phase 1 of SuperKEKB, and does it change as vacuum scrubbing progresses?
- Do the pressure bursts measured by SuperKEKB correspond to background peaks seen in the Beast II detectors?

¹Written by the author of this dissertation, this subsection is also included textually in [1].

- Could the radiation resulting from these events be damaging to the detectors?

2.3 Background mitigation measures present at Belle II

Accelerator-induced background is almost exclusively the result of “lost” off-momentum particles hitting interaction region (IR) material and generating showers of debris. Such backgrounds can reduce the lifetime of detector components through radiation damage and also introduce spurious noise in the detectors that interfere with the extraction of genuine physics signals from particles produced in the collisions. Three important measures to mitigate these processes are: vacuum chamber design features (which include low operating pressures, the antechamber geometry, surface treatment and permanent magnets that help to control the electron-cloud effect), collimators upstream of the interaction region (IR), and shielding near the IR with dense material [54].

2.3.1 Vacuum chamber design

Vacuum levels

The design value for cavity pressure is 10^{-7} Pa and the residual gas is mainly composed of H_2 and CO. However since the cross sections for beam-gas interactions increase with A and Z , the partial pressure of dihydrogen is a negligible parameter when modelling beam-gas backgrounds. The vacuum chambers of the LER are instrumented with mass spectrometers so the dependence on the gas species can be verified experimentally. The pressure in the cavity is expected to be comparable in SuperKEKB to what is was in KEKB: around 10^{-7} Pa.

The relevant quantity to monitor the quality of the vacuum is the so-called “dynamic” pressure: we model the total pressure as the sum of the base pressure P_{base} and a dynamic term that is proportional to beam current [50]:

$$P = P_{\text{base}} + \frac{dP}{dI} I. \quad (2.7)$$

During commissioning, the second contribution, which is expected to track the gas desorption rate from the walls of the vacuum chamber, is vastly dominating.

Geometry

The vacuum chamber uses an antechamber designed to limit the effect of the electron cloud effect, visible in Figure 2.4. This feature is a countermeasure for the electron cloud effect: the synchrotron photons hit the chamber material in a special region further away from the circulating beams thus suppressing the amplification of the electron cloud as well as its interaction with the bunches [55].



Figure 2.4: Photograph of the antechamber design of the SuperKEKB vacuum chamber. Reproduced from [33].

Surface treatment

The inner surfaces of the LER vacuum chambers are coated with titanium nitride (TiN) to reduce the electron cloud effect. Recall that the LER contains the positron beam and is therefore subjected to a large electron-cloud effect. TiN ceramic is often used for that purpose because of its low secondary electron yield [56]. The 200 nm TiN layer provides a 100-fold reduction of the near-beam electron cloud density at nominal beam currents [55].

Permanent magnets

Another electron cloud effect countermeasure is the placement of permanent magnets around the uncoated aluminum bellows and some straight sections of the LER. An example of such magnet implementation is depicted in Figure 2.5. By providing an axial field of

approximately 100 G, the cloud electrons are directed away from the beam particles. This concept was envisioned as a fall-back solution implemented during commissioning, when it became evident that the other countermeasures were not effective enough [50].

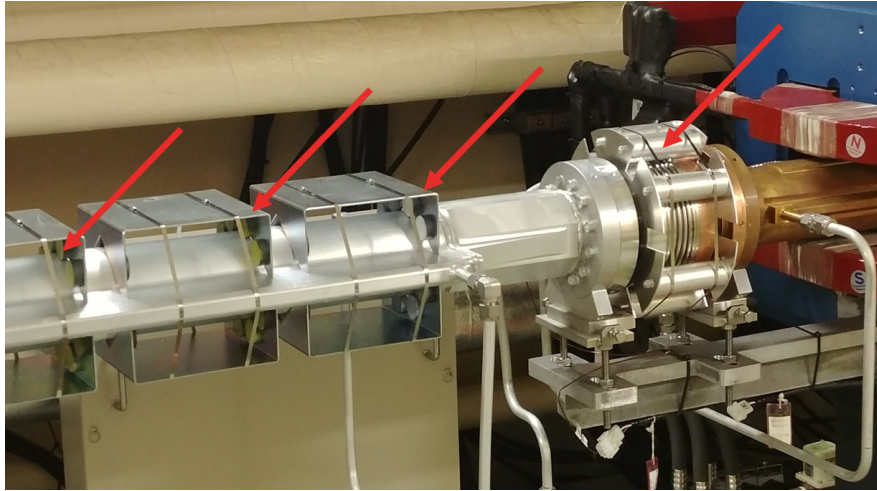


Figure 2.5: Photograph of the permanent magnets around the LER. The arrows point to the magnet arrays around an aluminum bellow (the rightmost arrow) and a straight drift section (the three leftmost arrows).

2.3.2 Collimators

The collimators, as their name imply, provide horizontal collimation to stop off-momentum beam particles before they can reach the interaction region. They have a movable aperture, as shown in Figure 2.6 and are adjusted to block the tails of the lateral spatial distribution of the off-momentum beam particles.

In Phase 1, there were two new collimators on the LER, at 1200 m upstream of the interaction region, and 16 collimators from KEKB at positions ranging from approximately 70 m to 1000 m upstream of the interaction region [1, 57].

2.3.3 ECL shields

The ECL end-caps are located in a region of high background radiation, so the crystals and photo-detectors must be well protected to be able to survive for the duration of the

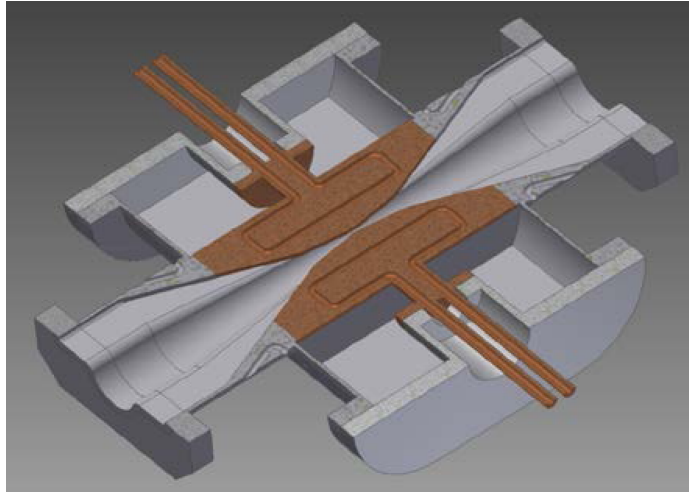


Figure 2.6: Cut-away view of a horizontal collimator system. The brown components are moveable and allow adjustment of the collimator width. Reproduced from [58] without modification.

experiment. As a service task to the Collaboration, new ECL shields are designed, built and commissioned by the University of Victoria. These elements are located between the ECL end-caps and the cryostat of the final focussing system, as indicated in Figure 2.7.

They are composed of a stainless steel shell that is filled with lead to absorb electromagnetic radiation. Moreover, a layer of boron-loaded polyethylene is inserted between the steel part and the beam line to moderate and capture neutrons. The technical design of these shields is documented Belle II internal note BELLE2-NOTE-TE-2016-002, and the key points are reproduced here in Chapter 3.

*

**

Chapter 3

Design and construction of ECL radiation shields

In the forward and backward regions of the Belle II detector’s electromagnetic calorimeter (ECL), a high level of radiation is undergone by the crystals and the avalanche photodiodes (APD)¹. To reduce the level of beam-induced background in the forward and backward end-caps — the “lids” on either side of the barrel of the ECL — heavy metal shields were placed between these end-caps and the final focusing system (QCS). In Belle, such shields were made of a wedge of lead cast in a stainless steel shell. To give a better idea of these devices, the shield in place in the forward region of the Belle detector is depicted in Figure 3.1. Engineering drawings of the forward and backward shields are reported in the “Belle Forward ECL End-cap Shield KB-01785” and the “Belle Backward ECL End-cap Shield KB-01786” drawings, available within the KEK network.

The Belle shields have been discarded, so a new design study must be conducted accounting for the 20-fold increase in luminosity. Early simulation studies indicated that, without such shields, both the crystal radiation dose and the neutron flux in the photodiodes were expected to lie above tolerance [61]². The new shield designs will need to bring those levels as low as possible, yet respect the mass and volume constraints.

The purpose of this chapter is to document the design work related to these radiation

¹An APD is a special category of photodiodes designed to be operated with large reverse bias voltages (on the order of 100 V) such that a charged particle travelling through them triggers an avalanche ionisation process that amplifies the signal. Thus, APDs generally provide a larger gain than regular photodiodes.

²Later simulation with different QCS shielding showed this is not always the case.

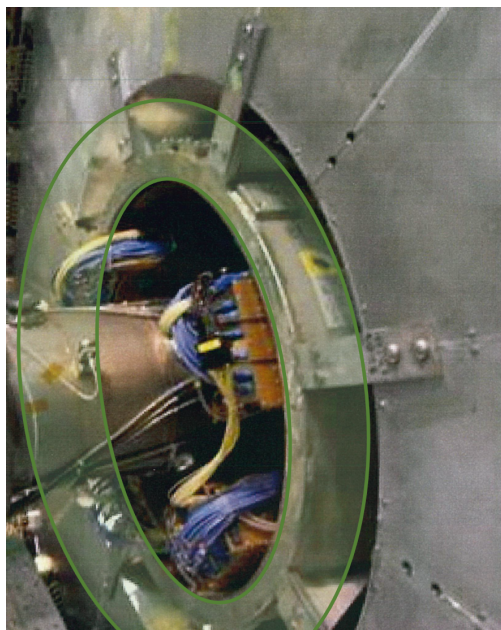


Figure 3.1: Photograph of the forward ECL shield in the first Belle detector. The shield is in the area highlighted by the green ellipses. Reproduced from [60] with modifications.

shields. It is built from Belle II technical notes: the Project Definition Report (PDR) [62] presenting the more general context and the scope of the project; the Conceptual Design Report (CDR) [63] which describes the studies leading to material selection and the nominal dimensions; and, finally, the Technical Design Report (TDR) [64] presenting the detailed design of each shield and the results of the mechanical resistance studies. This chapter is also organized along these three main components of the design work, with an added section about updates on fabrication and commissioning.

3.1 Project definition: context, requirements, and deliverables

3.1.1 The end users

Broadly defined, the customer is the Belle II Collaboration, with a management structure for its over 700 members depicted in the organization chart of Figure 3.2. More specifically, the performance criteria are determined by the ECL group, led by Dr. Alexander Kuzmin

Belle II Organisation

1-July-2017

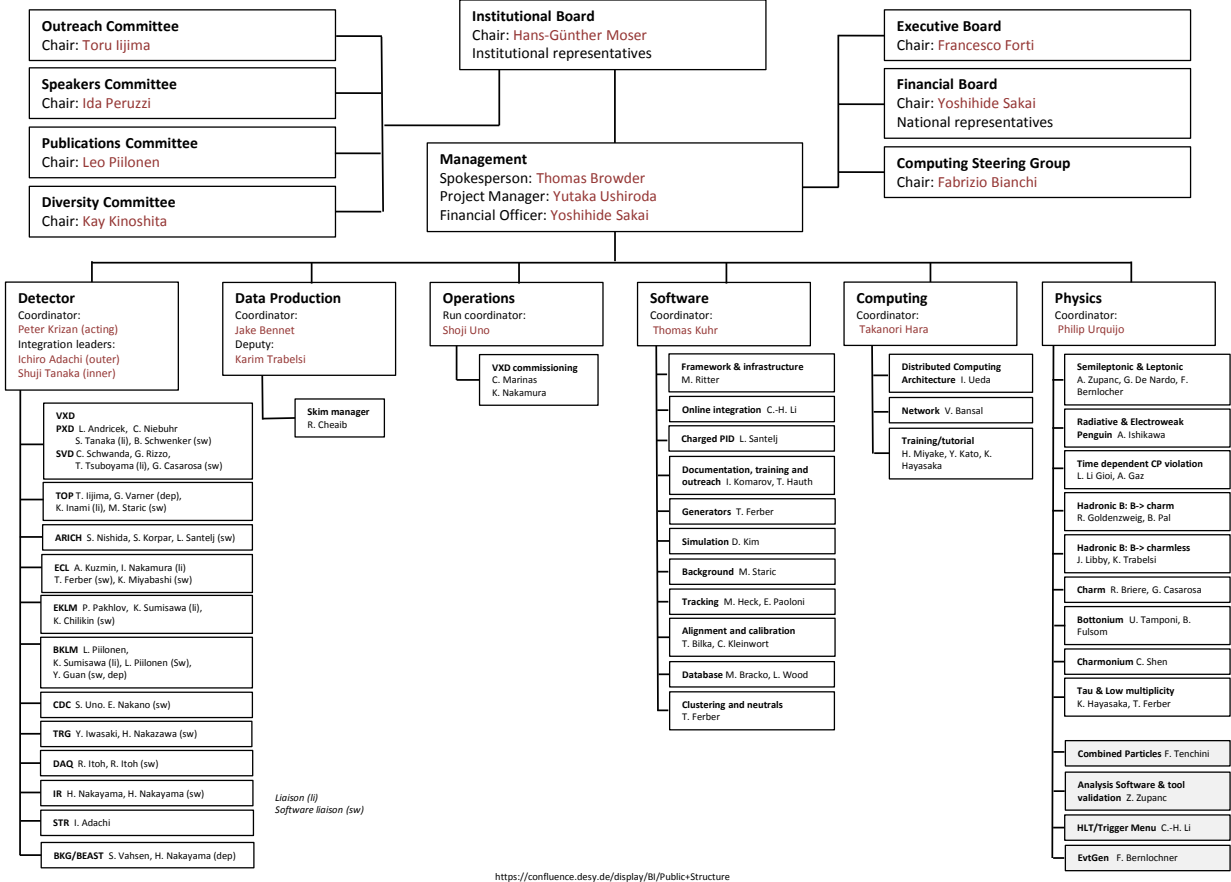


Figure 3.2: Organisational Chart of the Belle-II Collaboration as of July 1st, 2017. Reproduced from [65].

and for which Dr. Isamu Nakamura ensures liaison at KEK. Dr. Ichiro Adachi is in charge of the integration of all outer detector components, and the final detailed drawings will be delivered to Dr. Hiroruki Nakayama, who is the first point of contact at KEK for this project.

3.1.2 Performance goals

The primary purpose of the shields is to protect the thalium-doped caesium iodide [CsI(Tl)] crystals and the diodes of the ECL end-caps against radiation coming from SuperKEKB’s final focussing system (QCS). The radiation limits for these components, which will be

used as key performance indicators (KPI) for the shields, are listed in Table 3.1.

Table 3.1: Limits for the radiation levels in the ECL, according to [61]. The numbers in **bold** correspond to the critical figures of merit used to evaluate the performance of the shields. Results are given per *nominal* operating year: $1 \text{ yr} = 10^7 \text{ s}$.

CsI(Tl) Crystals		Photo-diodes	
Radiation dose (Gy yr ⁻¹)	Neutron Flux ($\times 10^9 \text{ yr}^{-1} \text{cm}^{-2}$)	Radiation dose (Gy yr ⁻¹)	Neutron Flux ($\times 10^9 \text{ yr}^{-1} \text{cm}^{-2}$)
10	1000	70	100

Preliminary simulation studies [61] showed that the crystal radiation dose and the diode neutron flux, highlighted in bold in Table 3.1, were the two critical figures of merit (or KPI) used to evaluate radiation damage in the ECL end-caps, therefore we will base our design decisions on these two variables.

More specifically, the average doses in the second rows of crystals starting from the beam line will be used. Belle II uses a numbering scheme where the row denoted $\theta_{ID} = 0$ is the innermost row of the forward end-cap, and the last row, denoted $\theta_{ID} = 69$, is the innermost row of the backward end-cap. Therefore the design goal is to minimize the radiation dose and the neutron flux in rows 1 and 68 by implementing radiation shields respectively below the forward end-cap and the backward end-cap. The radiation levels expected with the selected concept must be lower than the limits reported in Table 3.1.

Moreover, other detector components of Belle II, such as the ARICH in the forward direction, will also benefit from these shields. The design studies will however be focussed on performance with respect to ECL protection.

3.1.3 Design constraints

The three constraints that the shields have to meet is that they must fit in the available volume between the beam line and the other sub-detectors, the mass should not exceed the mass of the Belle shields, and they must allow removal of the end-caps for the inner detector maintenance.

Available volume

The most recent Belle-II detector assembly drawing is reported in Figure 2.7. However, this drawing does not include critical elements such as the silicon pixel and vertex detector service space (SVD/VXD docks) and the ARICH shield. The relevant information was gathered from the appropriate sub-detector groups, and is synthesized in the ECL-SHLDS-000 drawing reported here in Appendix B.2. The shields must be contained in the envelopes shown in Figure 3.3.

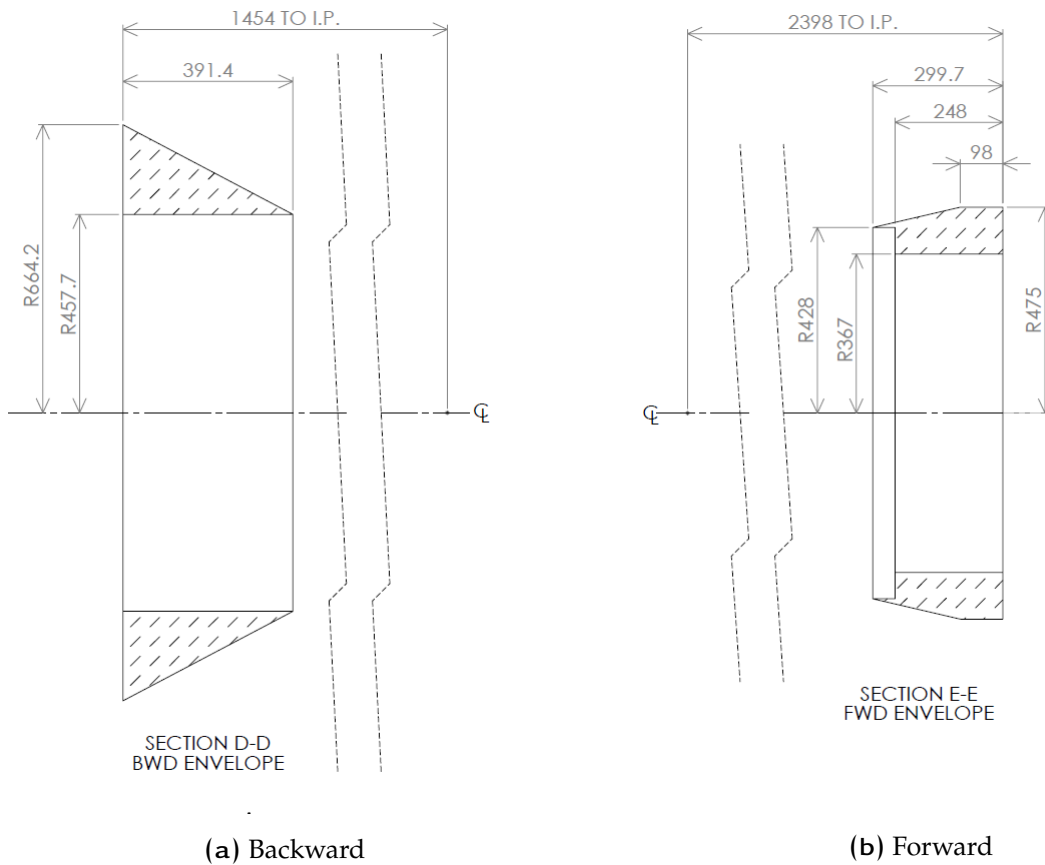


Figure 3.3: Envelopes available for the ECL end-cap shields represented as cross-sectional views of axisymmetric volumes. The hatched areas are the “keep-in” zones. All dimension units are in mm.

Attachment points and mass budget

In order to err on the safe side, we use as a constraint that the shields must not be more massive than the ones present in Belle. The reason for that is that all supporting structure remains unchanged, and the engineering resources are not sufficient to conduct a new detailed mechanical resistance study of the overall detector. For the same reason, the attachment points for the Belle shields must be re-used in the updated concepts.

Since the original Belle shields were discarded, their masses were assessed by modelling them in SolidWorks[66] according to the existing fabrication drawings. The results are reported in Table 3.2. The masses of the elements were calculated according to a lead density of $\rho_{\text{Pb}} = 11,000 \text{ kg/m}^3$ and type-304 stainless steel density of $\rho_{\text{SS304}} = 8,000 \text{ kg/m}^3$, which are the default values defined in the software.

Table 3.2: Masses of the Belle shields according to the 3D models. Pb mass is the mass of the lead shielding element alone. Net mass includes contribution from the stainless steel casing. Total mass includes all hardware and the attachment members to the ECL end-caps.

	Pb mass (kg)	Net mass (kg)	Total mass (kg)
Forward	298	369	382
Backward	521	613	636

Inner detector maintenance

The shields must not interfere with the end-caps extraction work. They should also allow installation and removal with the final focussing system being either on line or retracted. In order to allow end-cap extraction, the shields attach to the same ECL extractor device used with Belle, and use the existing threaded holes on the end-cap. This ensures the methodology developed for Belle end-cap shield extraction work can be employed as is in Belle II. The shields are also split along the vertical plane, as in Belle, to make sure they can be installed with any configuration of the final focussing system.

3.1.4 Deliverables

Items delivered as part of the Canadian contribution to the ECL shields

The Canadian group is responsible for the following components:

- one backward shield assembly composed of two half-rings,
- one forward shield assembly composed of two half-rings,
- all brackets and fasteners needed to complete each assembly, and
- all brackets and fasteners needed to attach the assemblies to the ECL end-caps.

Other required items outside the scope of the shield design project

Other parts are needed to successfully install the shields on the ECL end-caps. These parts are either already at KEK from the Belle experiment, or will be purchased by KEK prior to installation.

- Installation jigs to hold the shield in the vertical orientation and move them in the axial direction towards the end-caps. The assembly is represented in drawings KC-05036 and KC-05037, available within the KEK network.
- Forward and backward installation attachment to fix the shield to the above-mentioned jig during installation. These are represented by drawings KB-05030 and KB-05028, available within the KEK network.

Overall schedule and revisions

The original end date of the project was scheduled to be December 1st, 2016 since the shields were to be installed on the Belle-II detector in April 2017 or May 2017. Unfortunately, commissioning of Belle II suffered delays so the installation of the shields were re-scheduled to September and October, 2017.

The design and fabrication work of the shield themselves was also delayed. Delivery at KEK was originally scheduled in December 2016, at the latest. Instead, the actual delivery date was May 14th, 2017. Since this is well ahead of the installation date, the delays in design and fabrication of the shields will not have any impact on the experiment.

Preliminary cost estimates

Budgetary prices were requested in December 2014 with a preliminary concept of the backward shield in order to set the order of magnitude of the cost of the diverse components. The neutron shield design was not ready at the time of these budgetary quote requests. Table 3.3 contains the gathered information. There is a large variation between estimates, likely resulting from the fact this the project was considered “exotic” by some vendors. To distil this down to one budgetary price, we used the estimate from the company that is the most experienced in radiation shielding, MarShield, and added 25% contingency for the uncertainties on the project in this preliminary phase. Our early cost estimate for the complete project was \$45,000.

Table 3.3: Preliminary costing of the project. Prices (in CAD) are for a single shield, and were obtained between January 2015 and June 2015.

Supplier	Price per shield			
	Steel assembly	Lead casting	Neutron shield	Shipping
Ramsay Group Ltd [†]	29,950	-	-	-
Altech Machining	14,000	-	-	-
MarShield	9,250	3,100	-	1,800
Ultraray	-	8,000	-	-
Our estimate [‡]	-	-	3,000	-

[†]: This company is not in business anymore

[‡]: Our estimate is based on raw material prices and \$100/hr shop rate

3.2 Conceptual design

3.2.1 Methodology

Selection of materials

The choice of materials is based on a study of the existing systems used at other experiments to shield against electromagnetic (γ) and neutron (n) radiation.

For γ radiation shielding, the desirable materials have a short electromagnetic attenuation length λ . This λ is the mean free path of a photon in a given material, and is a function of the photon energy. Figure 3.4 reports this length as a function of energy for different elemental materials [9]. It is important to note that the values are given in units of g/cm^2 , such that a length in cm is obtained by dividing by the material's density. From this plot, we see that heavy metals are usually good candidates to shield against γ in a wide energy range.

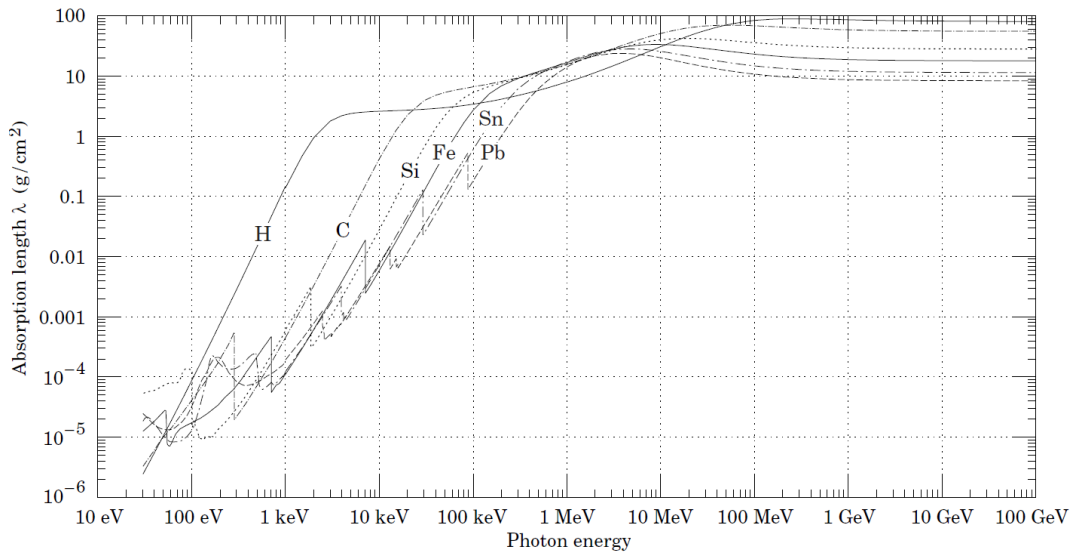


Figure 3.4: The photon mass attenuation length (or mean free path) $\lambda = 1/(\mu/\rho)$. Reproduced figure with permission from [9]. Copyright (2012) by the American Physical Society.

For shielding against neutrons, the usual approach is “first moderate, then capture” [9], therefore a layered geometry is often used, which includes an element to slow neutron

down to thermal energies, an element with high neutron absorption cross section, and finally a layer of dense material to block photon emitted by the neutron capture reactions.

Below is a list of commonly used materials for neutron shielding in high-energy physics (HEP) experiments.

- Low-cost materials
 - Water [67]
 - Concrete [68]
- Hydrocarbons
 - Paraffin [69]
 - Polyethylene [70, 71]
- Metals
 - Iron (and steel) [70, 71, 72]
 - Aluminum [72]
 - Copper [73]
 - Lead [69, 70, 71]
- Other high neutron-absorption cross section elements
 - Boron [69, 70, 71, 72, 74]
 - Lithium [69, 72]

Because the volume, mass and price budgets are all similar to the Belle shields, we focused our selection to similar materials: lead cast into stainless steel casings, but with extra components made of neutron-flux mitigating material. The latter is most efficiently a hydrogen-rich compound and may be loaded with elements having a high neutron absorption cross-section such as boron or lithium.

While the nature of the electromagnetic shielding material is already defined, the exact formulation of the neutron absorption element will be determined in the design optimization

phase. For the conceptual studies, a likely candidate, high-density polyethylene (HDPE), is considered. Moreover, it is relevant at this stage to study the impact of using boron-loaded HDPE — which is commercially available for neutron absorption applications — compared to regular HDPE. The theoretical benefits are an improved neutron capture cross section and a lower-energy emitted photon which is more easily absorbed afterwards. The material cost is on the order of 2 to 3 times higher than conventional polyethylene.³

Performance simulations

The performance simulations use the 11th campaign of machine-induced background samples published by the accelerator group. These files include events arising from beam-gas scattering interaction, radiative Bhabha, and Touschek scattering in both the high-energy ring (HER) and the low-energy ring (LER).

After the detector interaction is simulated with the `FullSim` module in the Belle II Analysis Software Framework (BASF2), data are analyzed with a modified version of `ec1BgModule` to retrieve the radiation dose in the crystals and the neutron flux in the diodes. Both quantities are expressed as the yearly irradiation using 10^7 s/yr. The radiation dose D_i in rad in the i -th ECL crystal is calculated by:

$$D_i = \frac{E_{\text{dep}}^i}{m_i} \cdot \left(1.6 \times 10^{-10} \text{ Gy kg / GeV}\right), \quad (3.1)$$

where E_{dep}^i is the energy in GeV deposited in the crystal by all the `SimHits` particles⁴, and m_i the crystal mass in kg.

The neutron flux is determined for 1 MeV equivalent neutrons, using the energy-dependent weights w_n [75, 76]. The neutron flux Φ_n^i in the diode of the i -th channel is given by

$$\Phi_n^i = \frac{w_n^i}{A} \quad (3.2)$$

where w_n^i is the sum of the weighted neutron hits⁵ reaching the i -th channel, $A = 4 \text{ cm}^2$ is the area of the diodes.

³An estimate obtained by comparing items [8619K117](#) and [96150A720](#) from the supplier McMaster-Carr (Elmhurst IL, U.S.A.)

⁴A `SimHits` denotes a simulated hit in BASF2

⁵The `BeamBackHits` array in BASF2

The performances are simulated for pairs of backward and forward concepts, and the results in either region is assumed to be independent of the configuration in the other.

One final note is that some events have been discarded from the beam background files in this analysis. Indeed, in one event, a primary beam electron hits one of the ECL crystals and deposits a large amount of energy. This event appears 12 times in the 100-ns HER radiative Bhabha sample, resulting in a single cell in the forward end-cap that receives a very large dose, as seen in Figure 3.5. By requiring the number of ECLSimHits in the event to be less than 3000, we make sure we don't consider that event in the shield performance simulations, without rejecting any other events. The phenomenon is an error in the background sample file, and the beam background group typically rejects such events.

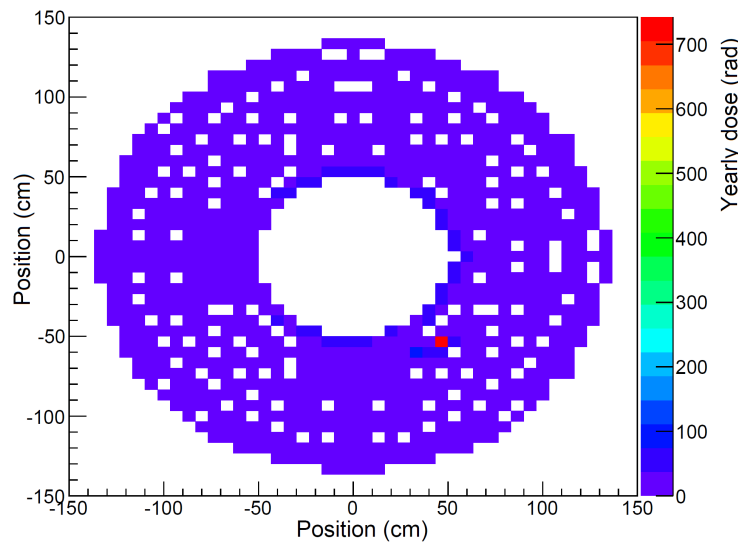


Figure 3.5: Hot spot in the forward end-cap from the HER radiative Bhabha sample

3.2.2 Concepts studied

Layout

With the restrictive choice of materials explained above, the conceptual design study consists of determining the best layout of lead and polyethylene to achieve the best figures of merit (crystal radiation dose and neutron flux in the diodes).

The solutions are classified in three different families, and the design matrix is shown in Table 3.4. The study also includes so-called concept “0”: the same components as in Belle.

To get the dimensions of the simulated shields, we adjusted the various thicknesses in order to match the mass of the lead in Belle shields — that is the mass of concept “0” — to within 10%. For concept B₂ however, we wanted to see what performance we can expect with a very massive shield in order to determine if it is appropriate to re-address the design mass constraint. The mass of BWD-B₂ is 1315 kg, while that of FWD-B₂ is 789 kg.

A better tuning of the mass is conducted during the detailed design phase, since all steel supporting elements will have a significant contribution.

Table 3.4: Design matrix of the end-cap shields. Materials:  HDPE  Lead. The thicknesses are not to scale.

Code	Layouts [est. mass]			
	Backward		Forward	
0		[555 kg]		[315 kg]
A ₁		[528 kg]		[333 kg]
A ₂		[531 kg]		[318 kg]
B ₁		[536 kg]		[316 kg]
B ₂ [†]		[1315 kg]		[789 kg]
C ₁		[558 kg]		[311 kg]
C ₂		[553 kg]		[324 kg]

[†]: The mass is much higher than concept 0

Effect of changing the lead thickness

The effect of changing the lead thickness was assessed by running simulations with shield geometries that include more lead than the default value (set to respect the mass constraint). In all cases, the thickness of the polyethylene layer was adjusted to fill the available volume. The aim of this study is twofold. First, it is to check whether or not there is some

benefit to be gained by adding more material, at the expense of making the shields heavier thus adding more lead on the end-cap supporting structures. Second, we would like to know what is the benefit of increasing the thickness of the polyethylene layer to improve neutron shielding, at the expense of having less lead to block electromagnetic radiation. The compromise comes from the limit on the total thickness that these shields can have.

The first figure of merit employed to compare the different design versions is the safety factor on the electromagnetic radiation dose, SF_D , which is nothing but the ratio between the dose calculated from background simulations D_{EM}^{sim} and the upper limit D_{EM}^{max} from Table 3.1:

$$SF_D = \frac{D_{EM}^{sim}}{D_{EM}^{max}}. \quad (3.3)$$

The second figure of merit to consider for performance comparisons is the safety factor on the neutron flux,

$$SF_n = \frac{\Phi_n^{sim}}{\Phi_n^{max}}, \quad (3.4)$$

where Φ_n^{sim} the simulated 1 MeV equivalent neutron flux for the given geometry and Φ_n^{max} is the upper limit from Table 3.1.

Effect of boron-enriched polyethylene

As with the lead thickness, the effect adding boron to the polyethylene to increase neutron capture cross section was studied using the best layout from the simulation results. The percentages of boron (by weight) chosen for conducting this study are 1%, 3% and 5%, readily available on the market, and 10%, 15%, as well as 20%, 25%, 30% to check for a change of behaviour at higher concentrations. The figure of merit for performance comparisons is the 1 MeV equivalent neutron flux as defined in Equation 3.2, averaged over the second ring of crystals ($\theta_{ID} = 1$).

3.2.3 Results

Shield geometries

The results are plotted for all tested geometries in Appendix C. They are summarized in Table 3.5, for the radiation dose, and Table 3.6, for the 1 MeV equivalent neutron flux,

below. The figures of merit used for concept selection are in the columns labelled averages for $\theta_{ID}=1$ and $\theta_{ID}=68$. The averages over four rows are also reported for reference. The last column shows the figure of merit for the first row of ARICH aerogel and photo-detector cells.

Table 3.5: Comparison of the average yearly crystal doses for the different concepts. The uncertainties are not shown: they are driven by the accuracy of simulation, which will be measured in the Beast II program.

Concept	Radiation dose (Gy/yr)				
	ECL θ_{ID}				ARICH
	1	1-4	68	64-68	row 1
No Shield	1.59	0.85	2.02	1.46	3.46
FWDA0+BWDA0	1.33	0.73	1.77	1.38	3.46
FWDA1+BWDA1	1.28	0.68	1.75	1.36	3.30
FWDA2+BWDA2	1.34	0.74	1.77	1.38	3.46
FWDB1+BWDB1	1.40	0.73	1.79	1.37	3.36
FWDB2+BWDB2	1.30	0.71	1.76	1.37	3.40
FWDC1+BWDC1	1.34	0.70	1.78	1.37	3.30
FWDC2+BWDC2	1.38	0.73	1.81	1.38	3.38

Table 3.6: Comparison of the average yearly neutron fluxes for the different concepts. The uncertainties are not shown: they are driven by the accuracy of simulation, which will be measured in the Beast II program.

Concept	1 MeV equivalent n flux ($10^9 \text{ cm}^{-2}\text{yr}^{-1}$)				
	ECL θ_{ID}				ARICH
	1	1-4	68	64-68	row 1
No Shield	47.3	32.1	20.1	13.0	47.9
FWDA0+BWDA0	42.5	29.0	15.5	10.9	48.2
FWDA1+BWDA1	19.5	14.7	8.6	6.5	35.6
FWDA2+BWDA2	42.1	28.4	15.6	10.8	47.6
FWDB1+BWDB1	20.5	15.4	8.6	6.5	39.9
FWDB2+BWDB2	40.9	26.8	14.8	9.6	47.5
FWDC1+BWDC1	20.2	15.4	9.7	6.8	38.0
FWDC2+BWDC2	21.3	15.8	9.5	7.0	38.4

Since the ARICH is located directly in front of the ECL end-cap (see Figure 1.4), the ARICH sub-detector group asked us to check the impact of our design on their expected dose

and neutron flux. We want to ensure the shields don't have a detrimental effect on the radiation in the ARICH, but also this last column is a potential tie-breaker in case two or more concepts provided otherwise identical performances.

Lead thickness

The results of the lead thickness scan are reported in Figures 3.6 and 3.7. The most striking common result is that the safety factors on the radiation doses and neutron fluxes are well beyond unity for all scenarios considered.

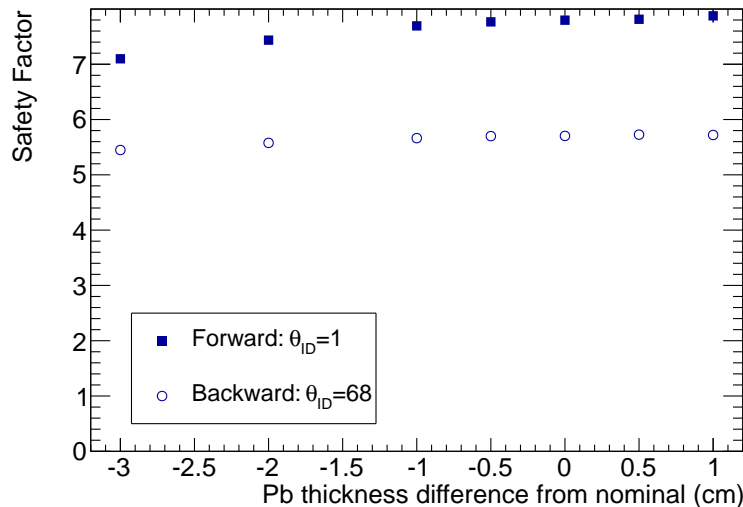


Figure 3.6: Effect of varying the lead thickness on the radiation level safety factor. The safety factor is acceptable dose divided by the predicted dose (higher is better). The nominal thickness value is 40 mm for the backward shield, and 39.5 mm for the forward shield. The error bars are not shown: the driving uncertainty contribution comes from the accuracy of the background simulations.

From Figure 3.6, we see that increasing the lead thickness by one centimetre has only a small impact — approximately 1% — on the shield's efficiency to block electromagnetic radiation from reaching the end-caps. This does not warrant the associated mass increase and corresponding larger stresses in the end-cap structure. On the other hand, making the lead layer thinner by 3 cm reduces the safety factor by around 10%.

Figure 3.7, shows that changes in lead-to-polyethylene thickness ratio also affect the neutron flux. This effect is more notable on the backward side, with around 15% variation, yet the safety factor always remains greater than 10. There is also no appreciable gain in using

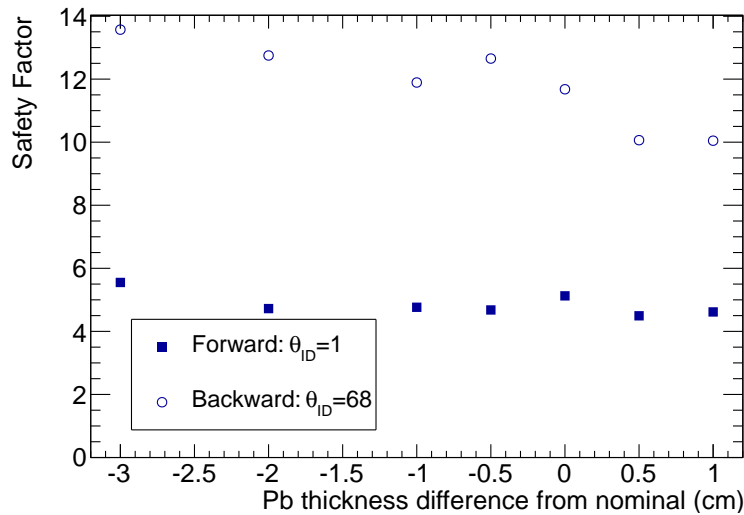


Figure 3.7: Effect of varying the relative thickness of the neutron absorber on the neutron flux safety factor. The safety factor is acceptable dose divided by the predicted dose (higher is better). The total height is set constant such that an increase in Pb thickness corresponds to a decrease in HDPE thickness. The nominal HDPE thickness is 50 mm for the backward shield, and 60.5 mm for the forward shield. The error bars are not shown: the driving uncertainty contribution comes from the accuracy of the background simulations.

a thinner lead layer to leave more volume for the neutron absorber: the $< 10\%$ increase in the neutron flux safety factor with a 3 cm smaller lead layer is comparable to the statistical fluctuation between data points.

Level of boron-enriched polyethylene

Figure 3.8 shows the result of the boron concentration scan in the neutron absorbing layer. There is no statistically significant trend in the data, meaning that the simulation cannot resolve any impact of boron loading on the radiation damage from neutrons.

3.2.4 Discussion and recommendations

Results in Tables 3.5 and 3.6 indicate that concepts “ A_1 ”, in which the shields are composed of a polyethylene neutron-absorbing layer next to the cryostat, surrounded with a second layer of lead, is the best solution for both the backward and the forward shields. In their

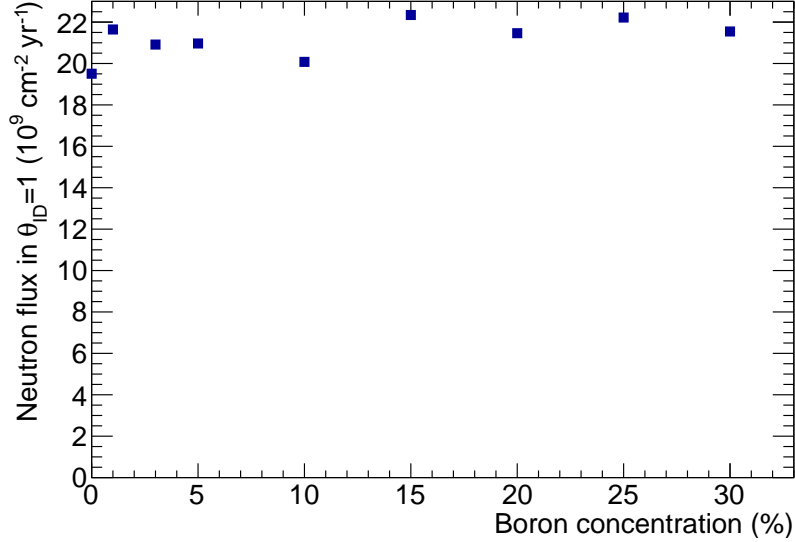


Figure 3.8: 1 MeV equivalent neutron flux in the second innermost row of forward crystals for different boron concentrations in the HDPE layer. The error bars are not shown: the driving uncertainty contribution comes from the accuracy of the background simulations.

default version, the lead and polyethylene layers are adjusted such that the total mass is close to the previous Belle shields.

The results of the thickness scan in Figures 3.6 and 3.7 show that there is no added benefit of violating the Belle mass initial requirement. Reasonable changes in the lead thickness, by a few centimetres upwards or downwards, wouldn't lead to appreciable gains in stopping efficiency for electromagnetic or neutron radiation according to simulation studies. Setting the main dimensions in such a way that the shields fill as much of the available volume as possible, yet having a mass close to that of the Belle shields is the best solution. A conceptual representation of each shield, showing the main dimensions and materials, is shown in Figure 3.9.

Finally, even if the boron concentration is not predicted to have an impact on the 1 MeV equivalent neutron flux, we chose to use a 5% boron content polyethylene (by weight) for the neutron absorbing layer. This brings an added safety for the ARICH readout circuits and the ECL PIN diodes and pre-amps, since low-energy neutrons are damaging the bulk material in silicon circuits [75]. Moreover, boron-loaded polyethylene is readily available from Canadian suppliers and there is no added cost to machine this material over regular

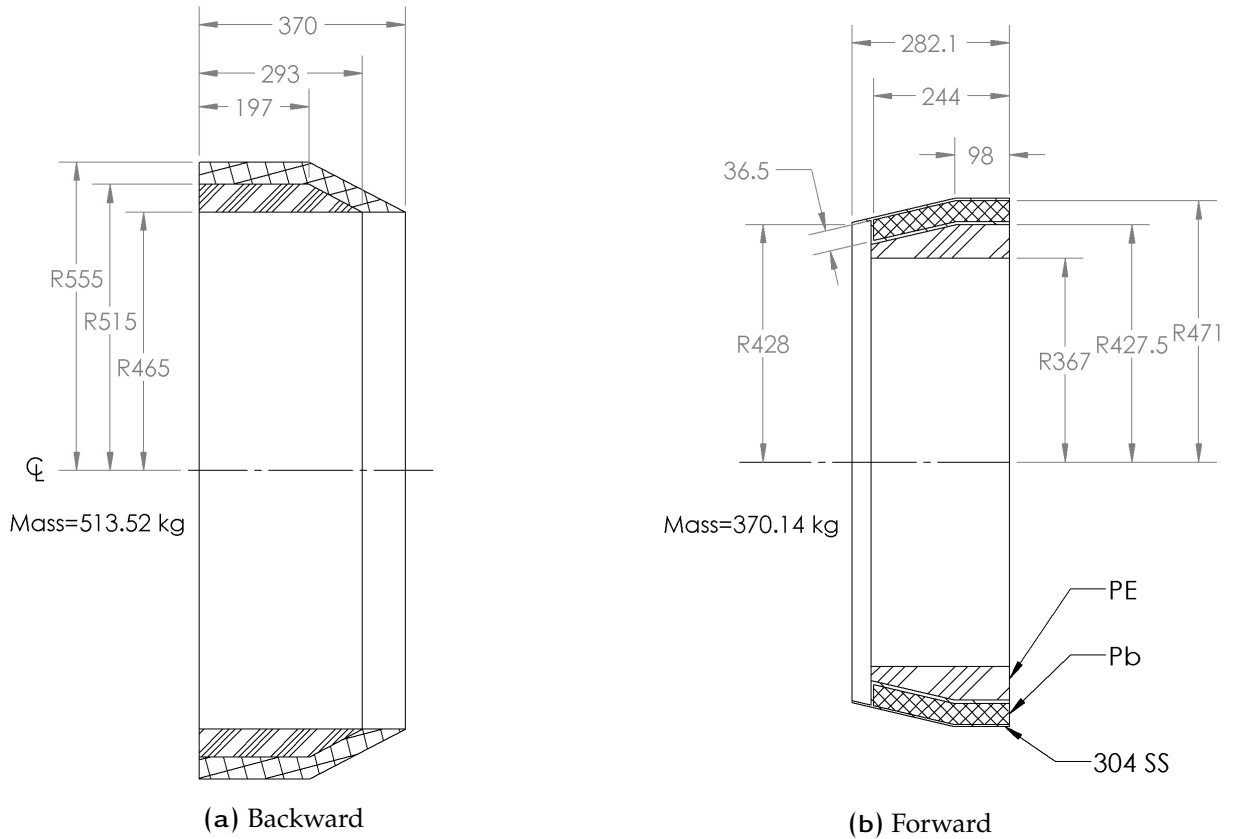


Figure 3.9: Conceptual representation of the ECL end-cap shields, with the main dimensions in mm

HDPE. Lastly, neutron propagation is notoriously difficult to simulate, so we believe it is preferable to add this extra precaution in case simulation underestimates the actual flux reaching the end-caps.

According to all figures-of-merit, these choices will provide a significantly better performance than the Belle shields (concepts "0"). The most dramatic impact is seen in the neutron flux predictions, since the Belle shields did not have neutron absorbing elements. The dimensions in Figure 3.9 are the basis of the detailed technical design that include all stainless steel casing, fasteners and mounting points.

3.3 Technical design

3.3.1 General design of the shields

Sub-systems and naming scheme

The project is part of the electromagnetic calorimeter (ECL) detector, and comprises two products, the forward shield (ECL-100-000) and the backward shield (ECL-200-000). Each shield is broken down into five (5) sub-systems with corresponding assembly numbers:

- the shell: ECL-X00-100,
- the electromagnetic radiation shield: ECL-X00-200,
- the neutron radiation shield: ECL-X00-300,
- the mounting points for transport and installation: ECL-X00-400,
- the attachments to the end-caps: ECL-X00-500,

where $X = 1$ for forward, and $X = 2$ for backward.

Configuration

The configuration, or layout of the different sub-systems in the products was studied in the Conceptual Design Report (CDR)[63] and summarized in section 3.2. The general concepts of the Belle shield were re-used, and each product is made of two symmetrical halves, split along the vertical plane. The enclosures used to contain the electromagnetic radiation shields and attach the two halves together — also referred to as the “shells” — are made of 304 stainless steel. The neutron radiation shield is attached below the electromagnetic radiation shield, *i.e.* at a smaller radius. The mounting points for transport are located at the same coordinates as the Belle shields, and the attachment to the end-caps are the same parts as what was used in Belle, for compatibility reasons. The configuration is represented in Figure 3.10. It is given for the example of the backward shield, but is identical in both assemblies.

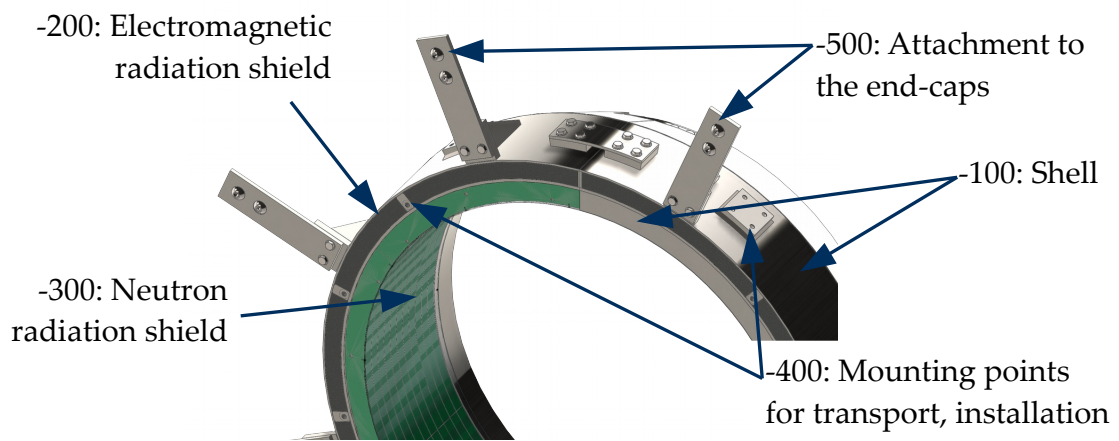


Figure 3.10: Configuration of the shields: example for the backward shield. Covers are removed on the left-hand side to show the neutron absorber.

3.3.2 Structural analyses

Overview of the methodology

The methodology used to conduct the mechanical resistance studies using ANSYS [77] is outlined below.

1. Simplify the model to make the analysis more manageable: use symmetries and remove non-structural features.
2. Define loads and supports for each load scenario. See paragraphs “[Definition of the loads](#)” and “[Description of the supports](#)” in section D.1.2 for the support type and location of each case.
3. Define material properties that are common to all load and support scenarios. See paragraph “[Mechanical properties of selected materials](#)” in section D.1.2 for values entered in the FEA software.
4. Define model mesh: use default “medium” mesh with size controls in the critical areas, leaving the element order to be program-controlled. An example of such meshed model is reported in Figure D.3a.

5. Converge maximum stresses with ANSYS's automatic mesh-refinement convergence methods. An example of refined mesh is reported in Figure D.3b.

Design safety factor

We use the stress safety factor SF_σ of 4 to determine whether or not the product has the required mechanical resistance for the application. This safety factor is defined as

$$SF_\sigma = \frac{\sigma_y}{\sigma_v} \geq 4, \quad (3.5)$$

where σ_y is the elastic limit of the material (also known as yield strength), and σ_v is the von Mises equivalent tensile stress [78].

The maximal displacements d_{\max} were also checked to ensure the shields would not contact surrounding structures during operation or installation. They are expected to be much smaller than the clearances around the product, which are at least 10 mm. The criterion for acceptance was set to be smaller than the 1.5 mm default manufacturing tolerance:

$$d_{\max} \leq 1 \text{ mm}. \quad (3.6)$$

Summary of the results

Complete results are reported in Appendix D. In particular, detailed structural analysis are described in Section D.2, for the backward shield, and D.3, for the forward shield. All results are summarized in Table D.5, and the main points are highlighted below.

The minimal safety factor on the structural elements is 5.9 for the backward shield, and 4.7 for the forward shield. These values are above 4, so we consider that the current design is safe.

The equivalent stresses on the fasteners can be calculated using the von Mises criterion. The safety factors for a standard 316 stainless steel fastener, rated up to 689 MPa (100,000 psi), are always over 30, so no fastener resistance issue is expected.

The maximal displacements are also all below 0.1 mm, so no interference or contact issues are expected under load.

3.3.3 Final detailed designs

Backward shield

The reader should refer to section [D.2](#) for the full technical description of the backward shield design and load simulations. The complete CAD model is shown in [Figure 3.11a](#), and a picture taken during installation at KEK is shown in [Figure 3.11b](#).

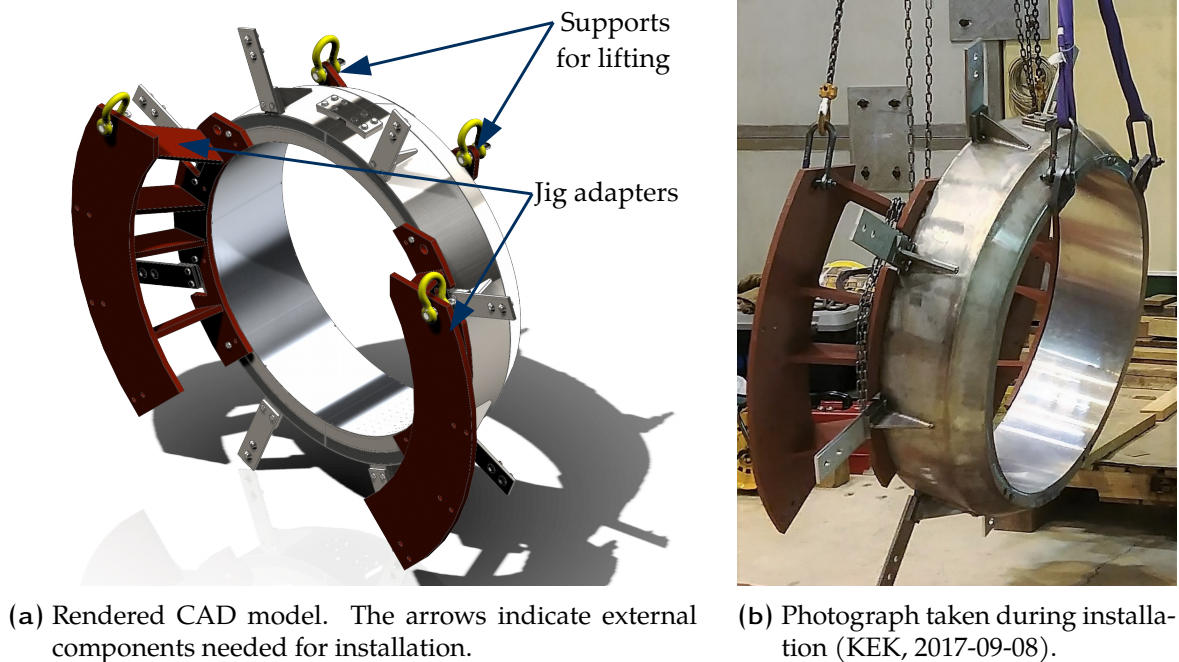


Figure 3.11: Complete design of the backward shield

Forward shield

The general design of the forward shield is similar to that of the backward one, and is documented in section [D.3](#). [Figure 3.12a](#) shows a computer-rendered model of the final design, while [Figure 3.12b](#) shows a picture taken during installation at KEK.

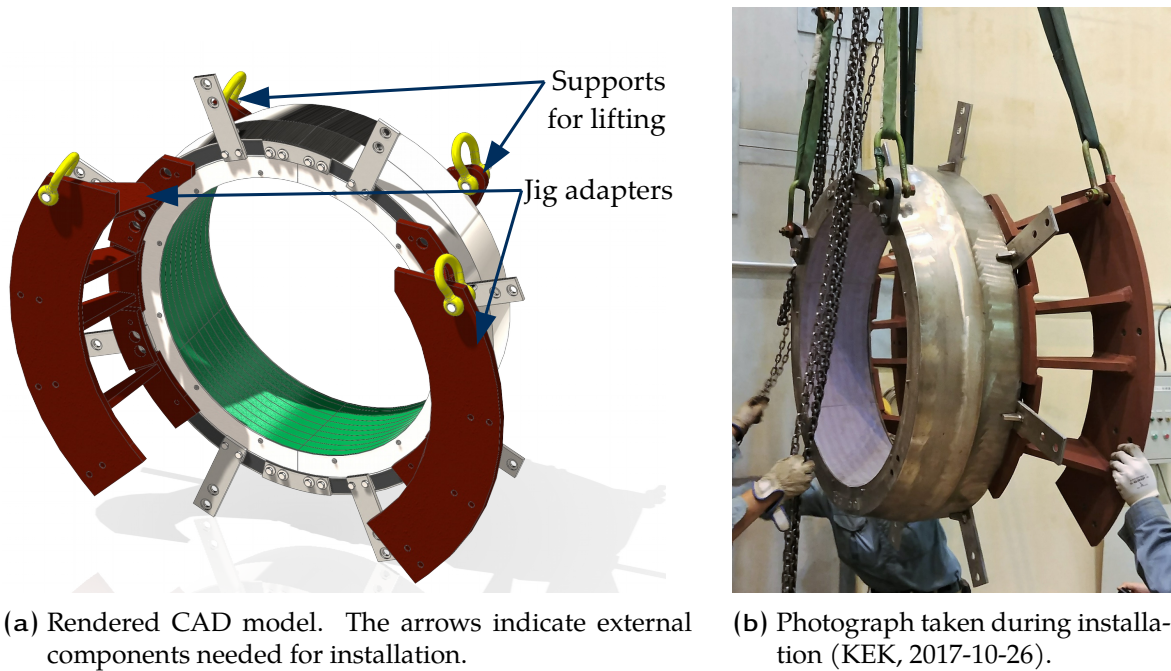


Figure 3.12: Complete design of the forward shield

3.3.4 Commissioning

Manufacturing

The bidding process conducted together with the University of Victoria Purchasing Service. The project was awarded to Turbulent Diffusion Technologies (Port Moody, BC), who managed and sub-contracted the steel cutting, forming and welding work to Brenco Industries (Delta, BC) in agreement with our contract terms. The borated polyethylene parts were fabricated at the Camosun Technology Access Centre (Victoria, BC) from raw material provided by MarShield Custom Radiation Shielding Products (Burlington, ON). The proximity of the manufacturers made possible frequent visits to follow the fabrication process more closely.

Figure 3.13 presents the shields at various stages of the manufacturing process. Modifications to the design during fabrication and studies of their impacts are documented in Section D.5.2.



(a) Backward shield during shell welding.



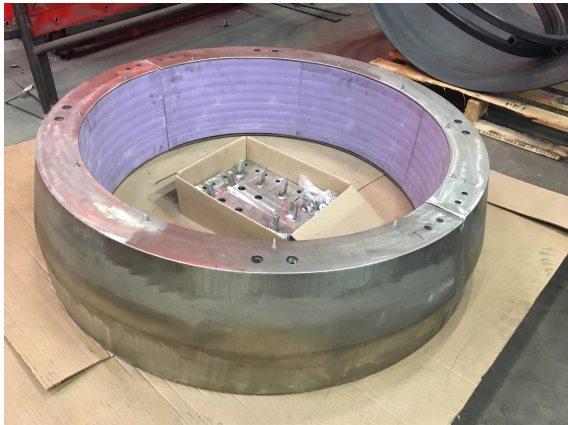
(b) Forward shield's hardware and HDPE parts.



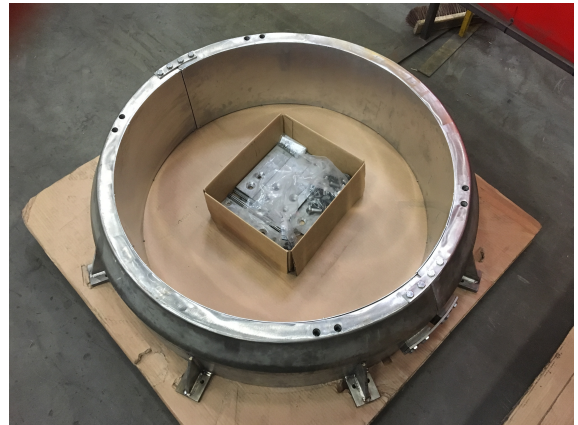
(c) Backward shield after lead casting.



(d) Forward shield braces prior to lead casting.



(e) Backward shield ready for packaging and shipping.

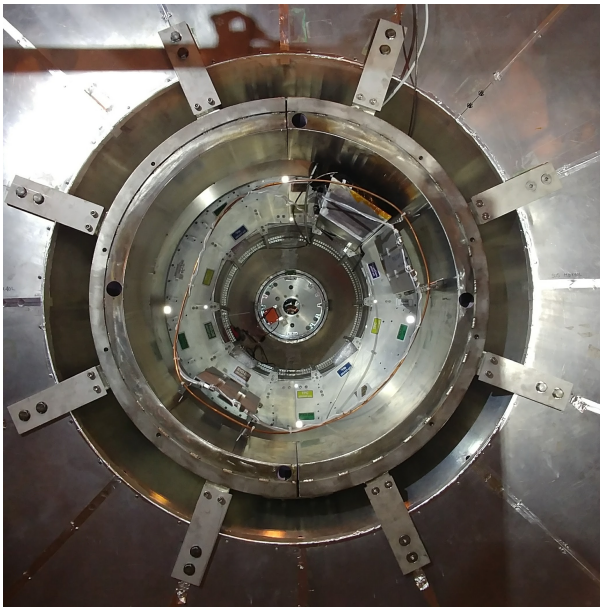


(f) Forward shield ready for packaging and shipping.

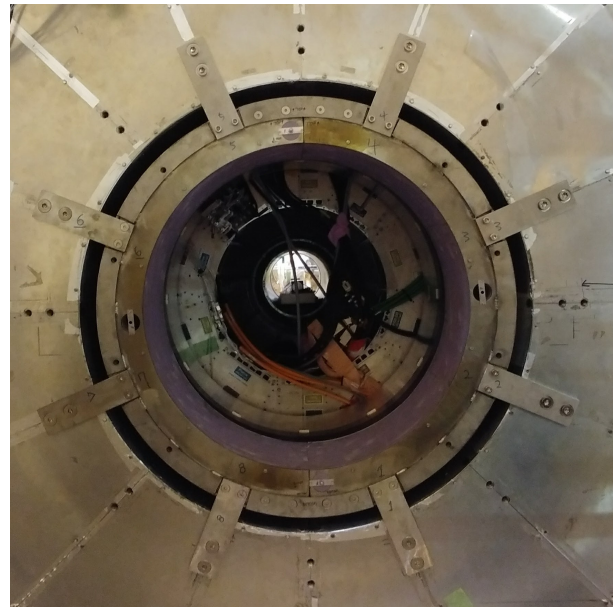
Figure 3.13: Photographs of the ECL shields at various stages during the manufacturing process.

Installation

The shields were shipped by air to KEK, and received on 2017-05-15. After an unsuccessful installation test was conducted in June 2017, attachment plates with a looser fit for the bolt holes connecting to the ECL end-cap were manufactured. Subsequent installation tests were successful: for the backward shield on 2017-09-08, and for the forward shield on 2017-10-26. Figure 3.14 shows photographs of the shields taken during these installation tests at KEK.



(a) The backward shield on 2017-09-08.



(b) The forward shield on 2017-10-26.

Figure 3.14: Photographs of the shields taken during the installation tests at KEK.

*
**

Chapter 4

Experimental methodology for measuring single-beam-induced electromagnetic radiation

4.1 Background studies in the first phase of beam commissioning

Phase 1 of the commissioning of the accelerator was conducted between February and June of 2016. The first months were mostly dedicated to increasing beam current and commissioning the different components of the accelerator and storage rings such as the electron gun and the wigglers, as well as fixing potential problems as they arise. Then there were two weeks dedicated to Beast II studies, where the influence of pressure, beam size and injection conditions were systematically studied. These measurements, described below, were always repeated for a range of beam currents, and separately for HER and LER beams. Before presenting the experiment design for these dedicated studies in more detail, it is useful to allow a short digression on the model that is used to express the recorded data in terms of the sensitivities for different conditions. Such quantities play a key role in the comparisons between data and simulation.

4.1.1 Influence of pressure

Vacuum bump experiments are conducted by heating the non-evaporable getters¹ (NEG) at various locations in the tunnel, far and near the Beast II region to release gas molecules into the vacuum chamber. The target is to heat the NEGs enough to increase the pressure by a factor ~ 100 . We measured the pressure-dependence of the background rates versus the location of the vacuum bump. Moreover, the low-energy ring is equipped with a residual gas analyzer so a more refined analysis is possible by studying the effect of gas composition. The run plan is schematically represented in Figure 4.1.

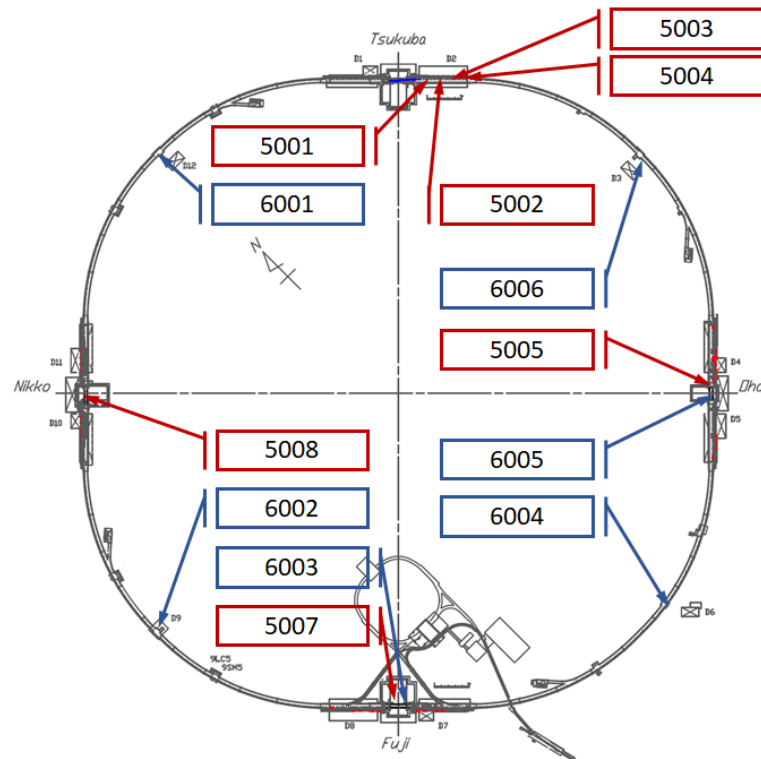


Figure 4.1: Schematic representation of the pressure bump studies run plan. The arrows point to the location where the pressure bump was applied, with the associated run number in each box. The colours indicate which ring was studied: blue, the 6000 series, means the high-energy ring; while red, the 5000 series, means the low-energy ring. Reproduced from [33] with modifications (addition of labels).

¹NEGs are used in conjunction with vacuum pumps to bring the pressures down to the design values of 1×10^{-7} Pa.

4.1.2 Influence of beam size

The size of the beams should have a direct impact on the Touschek lifetime. To quantify the effect, this parameter is scanned for different beam currents, again independently in both beams. For the LER, we have access to a so-called "emittance control knob" (ECK) to control the beam size. For the HER, the approach is instead to use a vertical steering magnet to displace or "bump" the beam by a few millimetres right after injection, which makes it larger all around the cycle. Moreover, varying the number of bunches in the train helps to disentangle the contribution of different bunch currents which should also contribute linearly to the Touschek losses.

The sizes are measured using the x-ray beam profile monitors (BPM) available for both rings. Unfortunately these monitors were not calibrated at the time of taking the measurements so their readings can't be compared directly between both beams. Tables 4.1 and 4.2 present the run parameters for size scans in the HER and in the LER, respectively. When available, the average pressure in the vacuum chamber and the beam lifetime — calculated from the beam current signals — are also added to enable comparisons between the the background conditions and the lifetime.

Table 4.1: Run plan for the HER size study. Column titles: P_e : average pressure; I : beam current; N_b : number of bunches in the train; I_b : bunch current; h_{bump} : vertical bump size; σ_y : vertical size of the bunches (horizontal and longitudinal sizes are kept constant); τ_{beam} : average beam lifetime.

Run No.	P_e [10^{-8} Pa]	I [mA]	N_b	I_b [mA/bunch]	h_{bump} [mm]	σ_y	τ_{beam} [min]
2001.1	3.0	161	1576	0.102	0.00	41	557
2001.2	3.9	318	1576	0.202	0.00	52	403
2001.3	4.9	479	1576	0.304	0.00	65	420
2001.4	6.1	639	1576	0.405	0.00	92	498
2002.1	3.0	120	1182	0.101	0.00	40	588
2002.2	3.5	240	1182	0.203	0.00	48	390
2002.3	4.2	360	1182	0.304	0.00	56	359
2002.4	5.1	480	1182	0.406	0.00	76	412
2003.1	2.6	81	789	0.103	0.00	38	-
2003.2	2.9	160	789	0.203	0.00	42	500
2003.3	3.4	240	789	0.304	0.00	46	425
2003.4	4.0	322	789	0.408	0.00	59	485

Continued on next page...

Table 4.1: Run plan for the HER size study (continued from last page).

Run No.	P_e [10^{-8} Pa]	I [mA]	N_b	I_b [mA/bunch]	h_{bump} [mm]	σ_y	τ_{beam} [min]
2004.1	2.3	41	395	0.103	0.00	12	-
2004.2	2.4	81	395	0.205	0.00	41	-
2004.3	2.6	121	395	0.306	0.00	41	-
2004.4	3.3	159	295	0.537	0.00	50	260
2005.1	2.7	160	1576	0.102	3.00	90	2220
2005.2	3.6	321	1576	0.204	2.50	82	1280
2005.3	4.8	481	1576	0.305	2.50	90	840
2005.4	7.8	639	1576	0.405	2.00	90	702
2006.1	-	161	1576	0.102	3.00	90	-
2006.2	2.6	160	1576	0.102	2.25	75	1860
2006.3	2.6	160	1576	0.102	1.50	51	1650
2006.4	2.6	159	1576	0.101	0.75	46	763
2006.5	2.6	156	1576	0.099	0.00	42	910
2007.0	3.3	160	1576	0.102	3.00	72	2070
2007.1	4.0	320	1576	0.203	3.00	90	1300
2007.2	4.0	320	1576	0.203	2.25	70	1050
2007.3	4.0	320	1576	0.203	1.50	52	750
2007.4	4.0	320	1576	0.203	0.75	52	750
2007.5	4.0	320	1576	0.203	0.00	52	750
2008.1	5.1	480	1576	0.305	3.00	93	950
2008.2	5.0	480	1576	0.305	2.25	73	750
2008.3	5.0	475	1576	0.301	1.50	54	500
2008.4	5.0	470	1576	0.298	0.75	44	360
2008.5	5.0	460	1576	0.292	0.00	53	500
2009.1	6.3	640	1576	0.406	3.00	123	900
2009.2	6.3	635	1576	0.403	2.25	78	660
2009.3	6.3	630	1576	0.400	1.50	57	450
2009.4	6.2	625	1576	0.397	0.75	51	380
2009.5	6.1	620	1576	0.393	0.00	62	520

Table 4.2: Run plan for the LER size study. Column titles: P_e : average pressure; I : beam current; N_b : number of bunches in the train; I_b : beam bunch current; ECK: Emittance control knob; σ_y : vertical size of the bunches (horizontal and longitudinal sizes are kept constant); τ_{beam} : average beam lifetime. Note: missing ECK values in the table were not recorded in the SuperKEKB database. They are assumed to be 0 since the corresponding runs were N_b studies.

Run No.	P_e [10^{-7} Pa]	I [mA]	N_b	I_b [mA/bunch]	ECK setting	σ_y	τ_{beam} [min]
3001.1	1.1	45	395	0.114	-	-	145
3001.2	1.1	90	395	0.228	-	35.0	90
3001.3	1.4	135	395	0.342	-	40.0	66
3001.4	1.6	180	395	0.456	-	48.0	55
3002.1	1.2	90	789	0.114	-	45.0	140
3002.2	1.5	180	789	0.228	-	45.0	85
3002.3	2.0	270	789	0.342	-	50.0	60
3002.4	2.8	360	789	0.456	-	55.0	56
3003.1	1.4	135	1182	0.114	-	50.0	135
3003.2	1.9	270	1182	0.228	-	60.0	80
3003.3	2.9	405	1182	0.343	-	64.0	65
3003.4	5.0	540	1182	0.457	-	78.0	62
3004.1	1.8	180	1576	0.114	-	60.0	130
3004.2	2.4	360	1576	0.228	-	68.0	80
3004.3	4.1	540	1576	0.343	-	70.0	70
3004.4	7.6	720	1576	0.457	-	140.0	80
3006.1	2.0	180	1576	0.114	1.00	80.0	225
3006.2	2.0	180	1576	0.114	0.75	70.0	200
3006.3	1.9	180	1576	0.114	0.50	50.0	170
3006.4	1.8	180	1576	0.114	0.25	40.0	140
3006.5	1.7	180	1576	0.114	0.00	34.0	130
3007.1	2.4	360	1576	0.228	1.00	82.0	145
3007.2	2.4	360	1576	0.228	0.75	66.0	125
3007.3	2.4	361	1576	0.229	0.50	52.0	105
3007.4	2.5	359	1576	0.228	0.25	40.0	85
3007.5	2.5	359	1576	0.228	0.00	35.0	80
3008.1	4.1	532	1576	0.338	1.00	90.0	100
3008.2	4.2	540	1576	0.343	0.75	74.0	95
3008.3	4.4	539	1576	0.342	0.50	65.0	80
3008.4	4.4	540	1576	0.343	0.25	55.0	75
3008.5	4.5	540	1576	0.343	0.00	52.0	70
3009.1	7.8	720	1576	0.457	1.00	155.0	80

Continued on next page...

Table 4.2: Run plan for the LER size study (continued from last page).

Run No.	P_e [10^{-7} Pa]	I [mA]	N_b	I_b [mA/bunch]	ECK setting	σ_y	τ_{beam} [min]
3009.2	8.4	720	1576	0.457	0.75	150.0	80
3009.3	8.6	720	1576	0.457	0.50	145.0	75
3009.4	8.8	720	1576	0.457	0.25	145.0	75
3009.5	8.9	720	1576	0.457	0.00	145.0	75

A dedicated study of the accuracy of the lifetime estimation in the accelerator simulations is reported in [1], where the lifetimes simulated by SAD are compared to those measured by SuperKEKB from the beam current signals. Using these lifetimes as proxies for beam backgrounds, the authors documented the dependence of backgrounds on beam conditions in the same way as done in this Dissertation. They note large variations in the data/simulation ratios throughout Phase 1, with a general excess of beam-gas background in the measurements. This situation is consistent with the results from the other Beast II detectors discussed in the same reference, and those presented in this Dissertation.

4.1.3 Influence of injection efficiency

The injection efficiency is expected to have an impact on the related injection background noise and its time structure. Different means of degrading the efficiency are explored and compared. The available “handles” are

- the number of injected bunches (one or two),
- the phase shift between the injected bunch and the circulating bunches, and
- the strength of the vertical steering magnets.

Detailed studies of these parameters were conducted by other Beast II collaborators and are reported in [1].

4.2 Analysis of residual gas constituents

The gas contents in the vacuum chambers have a large impact on the beam-gas background because their rate depends on Z_i^2 . However, the simplest model of beam-gas interactions assumes that the losses, hence the recorded background rate, are proportional to the product of the average pressure and beam current. The following section describes the methodology used to exploit the information coming from the residual gas analyzers (RGA) at SuperKEKB in order to improve our description of beam-gas interactions. The work was done in collaboration with Dr. Samuel R. de Jong [79] and the discussion below follows that in the published Beast II report [1].

The SuperKEKB accelerator is instrumented with two RGAs: one near the Beast II detector on the positron storage ring, and the other — approximately diametrically opposite in the storage ring — near the positron injection site. These RGAs are in fact mass spectrometers providing the partial pressure for gas fragment mass-to-charge ratios m/z between 1 and 50. In order to compare measurements with the simulations generated assuming a pure gas of atomic number $Z = 7$, we need to extract information of the relative importance of each gas constituent, and calculate an effective Z for this gas, noted Z_e . The analysis method can be broken down in three steps: definition of the gas model, calculation of the proportion of each gas constituent, and calculation of the corresponding Z_e .

4.2.1 Gas model

Because mass spectrometers only give distributions of the m/z for the different gas ion fragments, any further effort to interpret these as gas molecule abundances already involves an act of interpretation [80]. Some early assumption about the nature of the gas are therefore required. Di-hydrogen and air constituents are first added to the list of gases as the default hypothesis: H_2 , H_2O , N_2 , O_2 , CO , CO_2 , Ar . Then, light hydrocarbons are added progressively starting from CH_4 until all peaks in the spectra could be accounted for: CH_4 , C_2H_6 , C_2H_4 , C_3H_4 , C_3H_6 , C_3H_8 .

4.2.2 Calculation of the proportion of each gas

The proportion of each gas species in the residual gas is then found by calculating the optimal proportions to explain the measured spectra in the least-squares sense. The problem is expressed as solving

$$\arg \min_{\mathbf{x}} \|\mathbf{Ax} - \mathbf{y}\|_2, \mathbf{x} \geq 0 \quad (4.1)$$

where \mathbf{y} is a column vector of the observed relative abundances for each m/z peak, \mathbf{A} is a matrix whose columns each correspond to the standard spectrum for a gas model constituents, and \mathbf{x} is a column vector of the relative proportion (in number of molecules) of each gas in the mix. The vector of the optimal proportions of each gas, $\hat{\mathbf{x}}$, is therefore

$$\hat{\mathbf{x}} = (\mathbf{A}^T \mathbf{A})^{-1} \mathbf{A}^T \mathbf{y}. \quad (4.2)$$

4.2.3 Calculation of an effective Z for this gas mixture

The gas proportions \hat{x}_i , together with their molecular formulae, are then used to calculate the number b_j of atoms of element Z_j by simply multiplying each \hat{x}_i by the number of atoms of Z_j in the gas molecules. Assuming that the probability of interaction between a beam electron and an atom Z_j is proportional to Z_j^2 — this follows the typical cross section equations for Coulomb scattering and bremsstrahlung off atomic nuclei — the so-called effective Z , Z_e , is expressed as a weighted average of Z_j^2 .

$$\langle Z^2 \rangle = \frac{\sum_j Z_j^2 b_j}{\sum_j b_j} \quad (4.3)$$

$$Z_e = \sqrt{\langle Z^2 \rangle} \quad (4.4)$$

It is “effective” in the sense that this Z_e is the atomic number of a pure gas that would produce the same level of beam-gas interactions as the gas mix found in the vacuum chamber. This number can then readily be used to scale the simulation that has been generated with a single value of $Z = 7$.

4.2.4 Propagation of uncertainties

The RGA used in Phase 1 was not calibrated for the gases present in the vacuum chamber. As such, the SuperKEKB vacuum group reported that we can reasonably expect a factor

3 on the relative sensitivities for each m/z channels [81]. This uncertainty comes from the variations in relative ionization probabilities of each gas species, and variations in the transmission efficiencies of each fragments [82].

To model these effects, the pressure bump experiment was re-analyzed while generating uniformly-distributed random numbers between 1 and 3, and multiplying or dividing each channel reading by these independent random values. This procedure was conducted 1000 times with different random seeds in order to draw the 68% and 95% confidence intervals (C.I.) around the nominal Z_e value. In other words, we use Monte Carlo methods to propagate and quote an uncertainty for Z_e .

4.3 Detectors and technology overview

This section describes the system for measuring the electromagnetic background in the ECL end-cap region. The justification for the choice of scintillator material is first presented, then the characteristics of the selected photo-detectors and the signal processing chain are described.

4.3.1 CsI(Tl), CsI(pure) and LYSO crystal scintillators

Properties of the most common scintillating crystals are reported in Table 4.3 below. In Beast II Phase 1, we installed pure caesium iodide (CsI), thallium-doped CsI, CsI(Tl), and lutetium-yttrium oxyorthosilicate (LYSO) at the nominal ECL end-cap positions.

While Belle II uses CsI(Tl) for its electromagnetic calorimeter, there were some discussions of replacing a portion of the solid angle with pure CsI in a future detector upgrade to cope with the expected higher rate due to increasing luminosity. The pure CsI crystals, being much faster than the doped ones (see Table 4.3), would be more immune to pile-up noise and hence provide better energy resolution.

LYSO was a candidate for the cancelled SuperB experiment in Italy. Both its light output and time resolution are excellent, but their much higher cost demands a refined cost-benefit analysis prior to using them on a large project. Moreover, dedicated studies have demonstrated that the improvements may not be sufficiently substantial as to justify the

Table 4.3: Properties of several inorganic crystal scintillators. Reproduced table with permission from [9]. Copyright (2012) by the American Physical Society. Notation is defined in Section 6 of the above reference.

Parameter: Units:	ρ g/cm ³	MP °C	X_0^a cm	R_M^a cm	dE/dx^a MeV/cm	λ_I^a cm	τ_{decay} ns	λ_{max} nm	n^b	Relative output ^d	Hygro- scopic?	$d(\text{LY}/dT)^c$ % °C
NaI(Tl)	3.67	651	2.59	4.13	4.8	42.9	245	410	1.85	100	yes	-0.2
BGO	7.13	1050	1.12	2.23	9.0	22.8	300	480	2.15	21	no	-0.9
BaF ₂	4.89	1280	2.03	3.10	6.5	30.7	650 ^s 0.9 ^f	300 ^s 220 ^f	1.50	36 ^s 4.1 ^f	no	-1.9 ^s 0.1 ^f
CsI(Tl)	4.51	621	1.86	3.57	5.6	39.3	1220	550	1.79	165	slight	0.4
CsI(pure)	4.51	621	1.86	3.57	5.6	39.3	30 ^s 6 ^f	420 ^s 310 ^f	1.95	3.6 ^s 1.1 ^f	slight	-1.4
PbWO ₄	8.3	1123	0.89	2.00	10.1	20.7	30 ^s 10 ^f	425 ^s 420 ^f	2.20	0.3 ^s 0.077 ^f	no	-2.5
LSO(Ce)	7.40	2050	1.14	2.07	9.6	20.9	40	402	1.82	85	no	-0.2
LaBr ₃ (Ce)	5.29	788	1.88	2.85	6.9	30.4	20	356	1.9	130	yes	0.2

^a Numerical values calculated using formulae in [9].

^b Refractive index at the wavelength of the emission maximum.

^c Variation of light yield with temperature evaluated at the room temperature.

^d Relative light output measured for samples of 1.5 X_0 cube with a Tyvek paper wrapping and a full end face coupled to a photodetector.

The quantum efficiencies of the photodetector are taken out.

^s Slow component

^f Fast component

replacement of the CsI(Tl) with CsI for Belle II running. Beast II Phase 1, with its expected high rates, provides a good environment for comparing the crystals side-by-side.

4.3.2 Photo-detectors

The light spectrum of the CsI(Tl) peaks at around 550 nm, while the pure CsI produces a “prompt” light component (with a 6 ns time constant) at 310 nm and a “slow” component peaking at 420 nm. Therefore the choice of photo-detector depends on the quantum efficiency integrated over those wavelengths. Other factors include the gain, the dark noise level, the time response characteristics, the size of the photo-cathode and, the price and availability of the devices. As with many high-energy physics applications, the use of photomultiplier tubes is natural in our context because of the large light collection area, high gain, low noise and ease of integration.

We decided to use the Hamamatsu R580 tubes obtained with a custom high-voltage DC-to-DC converter base from the ZEUS experiment [83]. A photograph of an example of these PMT and base assemblies is shown in Figure 4.2, and the specifications data from the manufacturer of the tube are reported in Figure 4.3.

The high-voltage base was custom-built for the ZEUS experiment. As such the specifications are not available. However we measured the voltage distribution at each pin of the base, and the results are reported in Figure 4.4.

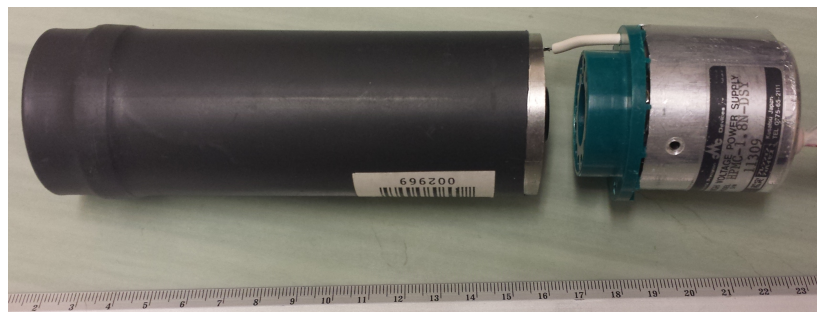
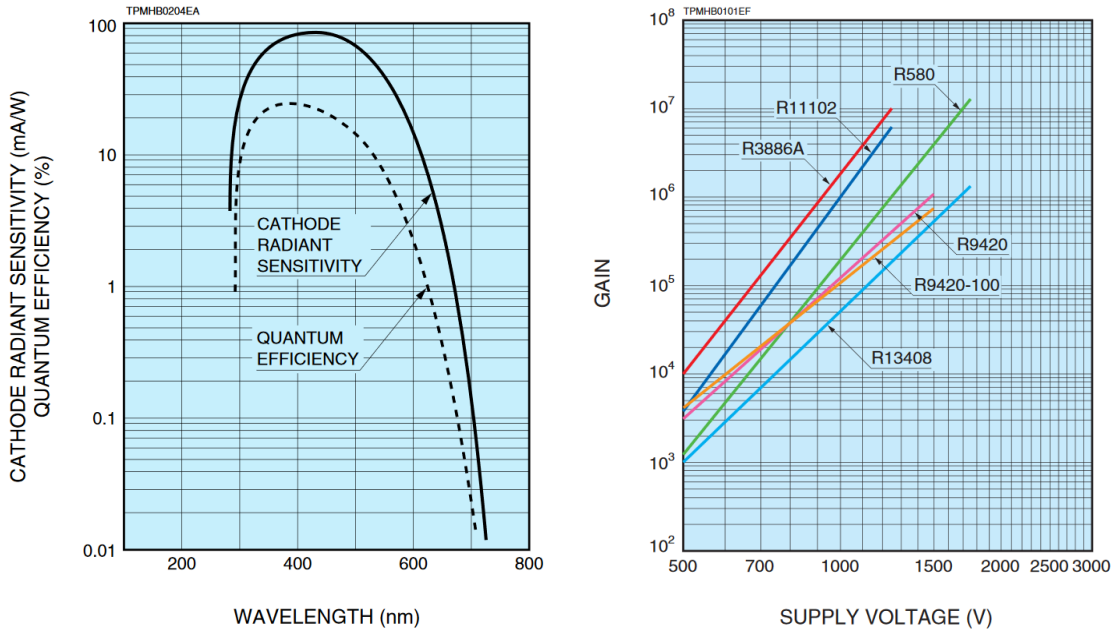


Figure 4.2: Photograph of the PMT and base assembly from the ZEUS experiment.



(a) Quantum efficiency vs. wavelength. Reproduced from [84]. (b) Gain vs. supply voltage. Reproduced from [85].

Figure 4.3: Specifications of the Hamamatsu R580 photomultiplier tube. Courtesy of Hamamatsu Photonics K.K.

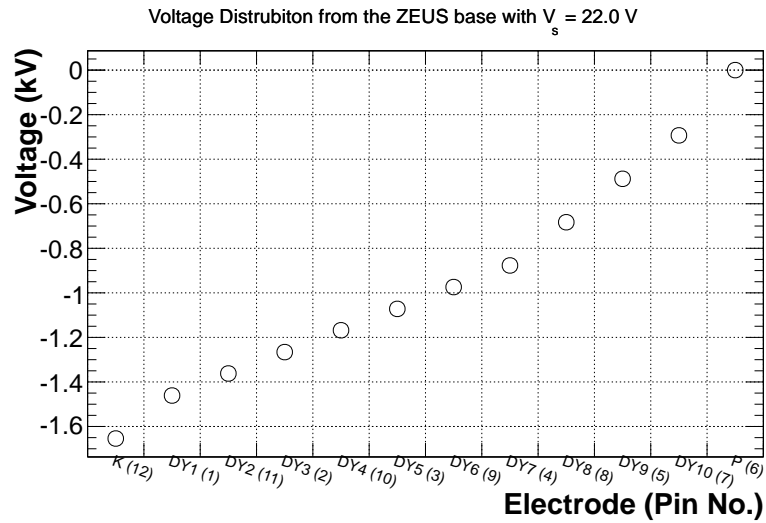


Figure 4.4: Distribution of the voltage supplied to each electrode of the PMT by the ZEUS base

4.3.3 Mechanical integration

The mechanical setup is composed of six dark boxes each containing three scintillators: a pure CsI crystal a CsI(Tl) crystal and a LYSO crystal. A picture of one of such boxes is reported in Figure 4.5. The CsI and LYSO crystals and the related readout chains are a contribution from our colleagues at INFN.



Figure 4.5: One calorimeter unit in Beast II. PMT: photomultiplier tube; T°: temperature sensor; R.H.: relative humidity sensor.

The dark boxes, also referred to as calorimeter “units”, were located at the nominal ECL end-cap position at Belle-II in the Beast II cavern. The integration of the calorimeters in Beast II is depicted in Figure 4.6, while Figure 4.7 shows a simplified view together with the naming scheme for the units and the coordinate system.

For reference, Table 4.4 below lists the positions and index of each channel, together with the serial numbers of the crystals and photo-detectors used for readout.

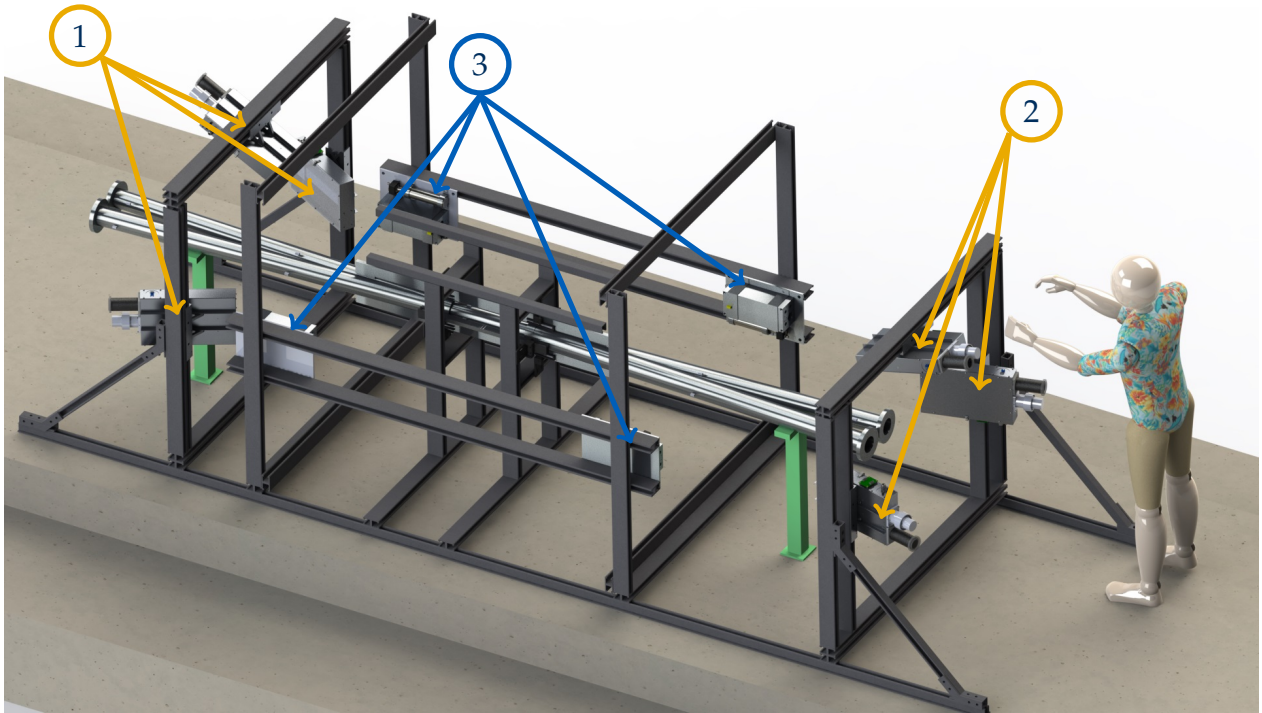


Figure 4.6: Integration of the calorimeters in Beast II. A typical University of Hawaii engineer is added to show the scale. 1. Backward calorimeter units; 2. Forward calorimeter units; 3. Neutron detectors (slow and fast, not part of this project); other subsystems of Beast II have been removed from the picture for clarity.

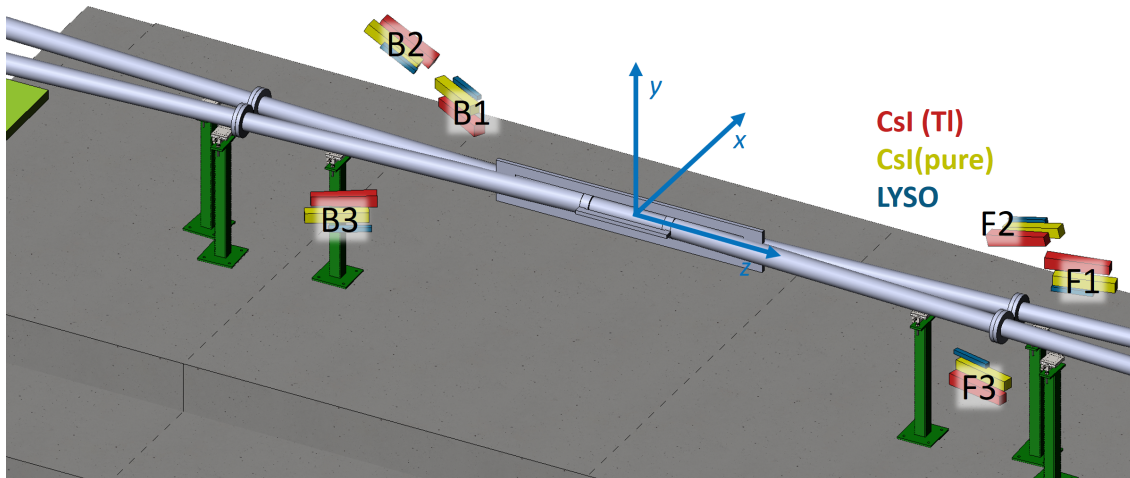


Figure 4.7: Disposition, naming scheme and coordinate system of the crystal calorimeter units. The colour encodes crystal material information, and the unit identifiers are overlaid to the six different locations.

Table 4.4: Position and numbering scheme of the crystals. The positions are given for the centre of mass of each crystals, with respect to the reference frame defined in Figure 4.7. The serial numbers (s/n) of the devices are also reported for reference.

Channel Id.	Material	Unit Id.	Crystal s/n	PMT s/n ^a	Position (cm)		
					r	ϕ	z
0	CsI(Tl)	F1	5637	3394	48.8	8.0	209.8
1	CsI(pure)	F1	15008	36773	49.2	-2.7	213.5
2	LYSO	F1	SG-S10	Ch3	49.9	-10.2	207.0
3	CsI(Tl)	F2	2922	4180	51.7	101.0	208.7
4	CsI(pure)	F2	15005	36768	51.5	90.9	212.4
5	LYSO	F2	SG-S09	Ch1	51.9	83.7	205.9
6	CsI(Tl)	F3	5391	4125	52.4	-171.6	209.7
7	CsI(pure)	F3	14002	40006	52.6	178.5	213.4
8	LYSO	F3	SG-S07	Ch4	53.2	171.4	206.9
9	CsI(Tl)	B1	4105	5762	56.3	-8.6	-118.0
10	CsI(pure)	B1	15007	40007	57.4	0.6	-121.4
11	LYSO	B1	SG-S11	Ch0	56.2	7.3	-115.1
12	CsI(Tl)	B2	3334	2494	59.0	85.6	-118.7
13	CsI(pure)	B2	15006	40301	60.7	94.3	-122.1
14	LYSO	B2	SG-S08	Ch5	59.9	100.6	-115.8
15	CsI(Tl)	B3	5234	2495	59.2	173.7	-119.6
16	CsI(pure)	B3	14001	39327	60.6	-177.5	-123.0
17	LYSO	B3	SG-S12	Ch2	59.6	-171.2	-116.7

^aFor LYSO channels, the identifier is the label number instead of the serial number

4.3.4 Signal chain and data acquisition

The data acquisition (DAQ) setup is achieved by connecting the signals from the PMT's directly to the digitizer board. The latter is connected to a standard PC via Ethernet through the VME controller. The chosen digitizer, the CAEN V1730, allows digital pulse-processing (DPP) such that the hardware calculates the integrated charge and assigns a 2-ns resolution time stamp for every event. This allows for faster speeds by dramatically decreasing data throughput compared to waveform recording. Using this functionality also reduces the number of devices required in the signal chain, which is represented in Figure 4.8. Fast counters are also installed in parallel to be able to normalize the spectra in case the rates are so high that the rest of the system can't handle the data throughput.

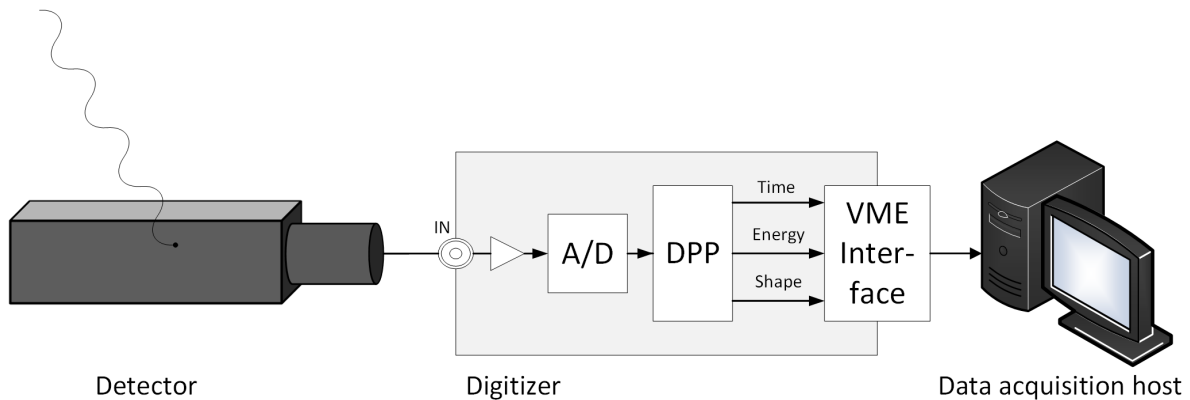


Figure 4.8: Signal chain based on the use of the CAEN DPP-PSD firmware. The signal from the detector is connected directly on the digitizer board, where it is converted to digital (A/D). The Digital Pulse Processing (DPP) algorithms provide the timing, energy and shape information of each pulse. A VME-USB bridge ensures the interface between the digitizer and the data acquisition host.

The acquisition is gated to reduce the data throughput. During nominal running (outside injection periods), an acquisition gate is left open for approximately 1.25 ms at 2 Hz, effectively applying a *nominal*² pre-scale factor of 1:400 to the digitized data.

²The pre-scale factor was measured to be significantly different from this value, as reported in Section 4.5.6.

4.4 Calibration

4.4.1 Dedicated campaign

A calibration campaign was conducted after installation of the experimental apparatus and also during data-taking when the PMT supply voltages are changed. We use two radioactive calibration sources, ^{137}Cs with 273 kBq activity (one photo-peak at 0.662 MeV), and ^{60}Co with 431 kBq activity (two photo-peaks at 1.173 MeV and 1.333 MeV) to obtain a four-point calibration curve where

- $E_1 = 0$ is obtained by acquiring signal at random triggers;
- $E_2 = 0.662$ MeV corresponds to the ^{137}Cs photo-peak;
- $E_3 = 1.253$ MeV corresponds to the average of the two ^{60}Co photo-peaks³;
- $E_4 \approx 30$ MeV (depending on the crystal size and orientation) corresponds to the energy deposited by a minimum-ionizing particle (MIP) coming from a cosmic ray muon passing through the crystal⁴

The energy deposited by a MIP E_{MIP} is given by

$$E_{\text{MIP}} = \frac{\rho t}{\sin\theta_z} \left\langle -\frac{dE}{dx} \right\rangle_{\min} \quad (4.5)$$

where ρ is the material density, t the thickness of the crystal, θ_z the zenith angle of the crystal, and $\langle dE/dx \rangle_{\min}$ is the stopping power at minimum ionization given by the empirical relationship as a function of the atomic number Z [9].

$$\left\langle -\frac{dE}{dx} \right\rangle_{\min} = 2.35 - 0.28\ln(Z) \quad (4.6)$$

The sources are placed outside the dark boxes, separated from the crystals by 1.6 mm of aluminum alloy and approximately 2 cm of air, as seen in Figure 4.9. For the calibration

³The height of the photo-peaks are very similar since, for 100 disintegrations, there are 99.85 photons emitted at 1.173 MeV and 99.9826 photons emitted at 1.333 MeV [86].

⁴The acquisition is self-triggered on the individual signals. We use the most probable value of the deposited energy distributions as the calibration point, and assume for calculations that this energy value corresponds to cosmic-ray particle coming from the zenith.

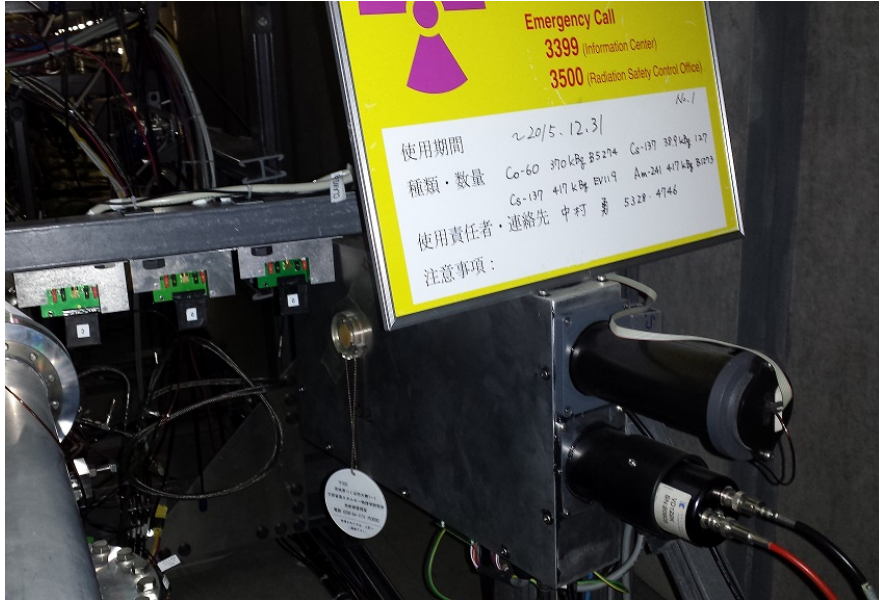


Figure 4.9: Photograph of a crystal dark box with a calibration source

data using test sources, a Gaussian distribution is fitted to each spectrum to obtain the most probable charge q_{MPV} as a function of the deposited energy E_{dep} . For data utilizing minimum ionizing cosmic ray muons, the charge distribution $f_{cosmic}(q)$ is modeled as the sum of a signal part and a background part. The signal is represented as a Landau distribution, peaking at q_{MPV} with a scale parameter η , convoluted with a Gaussian centered at 0 with standard deviation σ . The background contribution is represented by a Gaussian tail with width parameter b_{bkg} :

$$f_{cosmic}(q) = a_{bkg} \cdot \exp\left(-b_{bkg}q^2\right) + A \cdot \text{Landau}(q, q_{MPV}, \eta) * \text{Gaussian}(q, \mu = 0, \sigma). \quad (4.7)$$

In this formulation, parameters a_{bkg} and A represent the relative contributions of the background and signal components, respectively. An example of such a fit is represented in Figure 4.10, and complete results of this calibration campaign are presented in Appendix A.1.

The energy calibration is obtained by a linear regression of the most probable charge as a function of the expected deposited energy:

$$q_{MPV} = c + bE_{dep}. \quad (4.8)$$

Therefore, the equation to calculate the deposited energy corresponding to a total charge

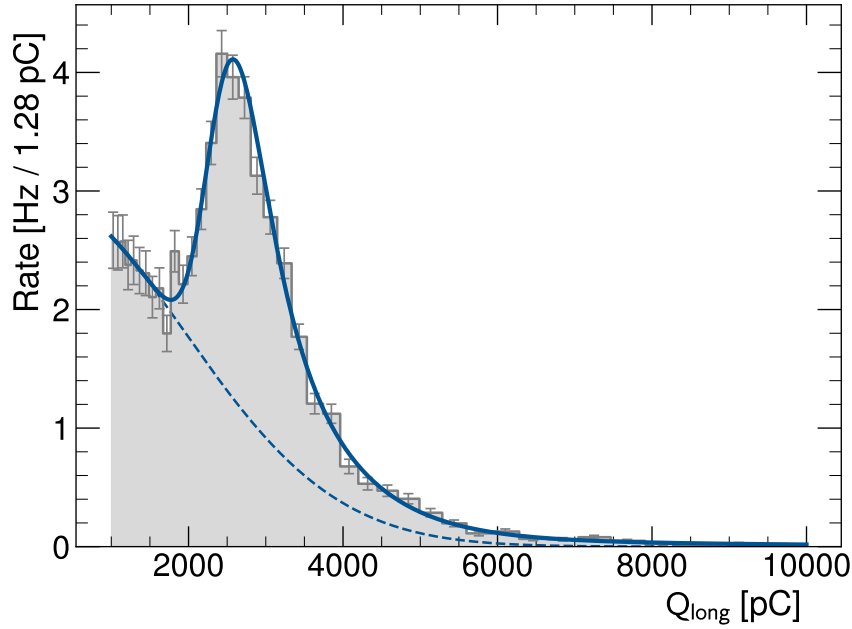


Figure 4.10: Example of the charge distribution of cosmic ray muon signals in CsI(Tl) used for energy calibration. Uncertainties on the bin contents are statistical only. The optimal parameters of Equation 4.7 for this distribution are $a_{bkg} = (2.98 \pm 0.12)$ Hz/pC, $b_{bkg} = (1.31 \times 10^{-6} \pm 2.9 \times 10^{-8})$ pC⁻², $q_{MPV} = (2.62 \times 10^3 \pm 77)$ pC, $\eta = (208 \pm 9)$ pC, $\sigma = (226 \pm 30)$ pC, $A = (2.9 \pm 0.1)$ Hz/pC with a fit $\chi^2/ndf = 21.8/34$. The dashed line represents the contribution of the Gaussian-tail background only. Reproduced from [1].

Q_{long} read out from the digitizers is

$$E [\text{MeV}] = \frac{a \cdot Q_{long} - c}{b} \quad (4.9)$$

where the parameter a comes from the setting of the DSP algorithm in the digitizers, parameters b and c are obtained from a linear fit to the energy points described above.

4.4.2 Time-dependence of the gain

Unfortunately, due to radiation damage, the calibration changed during the Phase 1 operating period. The gain of all channels was degraded, sometimes significantly, by a combination of damage to the crystals themselves — most likely for the CsI(Tl) channels — and to the PMTs.

In order to recover from this, data points recorded when neither beam was circulating are used to measure the position of the MIP peak. On a daily basis, these “beam-off” events are used to populate histograms such as presented in Figure 4.10, and identical parameter estimation is attempted. Successful results, defined based on a list of criteria such as convergence of the algorithm, estimated parameters away from boundaries and adequate signal-to-noise ratio, are then used to measure the shift of the peak’s position as a function of total integrated current, referred here as “beam dose”. It is compared to the value recorded during the initial calibration period. We call the resulting quantity the “relative gain” of the channel.

The relative gain is modeled as a linear function of \log_{10} of the total beam dose, and therefore equation 4.9 is modified to include this term:

$$E(Q_{\text{long}}, I_{\text{int}}) \text{ [MeV]} = \frac{a \cdot Q_{\text{long}} - c}{b} \frac{1}{p_0 + p_1 \log_{10} I_{\text{int}}} \quad (4.10)$$

where I_{int} is the sum of the integrated beam currents in both beams, and p_0, p_1 are the parameters adjusted to data, specific to each channel but constant throughout the experiment.

4.5 Comparisons between data and simulation

4.5.1 Heuristic description of background measurements

As described in Section 2.2, the main sources of background expected in Phase 1 are the Touschek effect, the beam-gas interactions, and the injections losses. The electron-cloud effect is left out of the most simplistic picture since it is suppressed by hardware countermeasures and is not expected to play a major role during normal operation and dedicated background studies. In order to conduct the data-to-simulation comparisons, we need to express the observed background rate in terms of the contributions from the first three underlying processes.

The cross section for both Rutherford scattering and bremsstrahlung is taken to be proportional to Z_i^2 (see Section 2.2.2). Beam-gas scattering is akin to a fixed-target experiment therefore we can define a luminosity as the product of the gas density, the incoming particle flux and a characteristic length such as the storage ring circumference. Then, absorbing

all constants into a single multiplicative factor, we write the beam-gas contribution to the background rate as

$$\mathcal{O}_G = S_G \cdot I P_e Z_e^2, \quad (4.11)$$

where S_G is the beam-gas sensitivity, I is the beam current, P_e is an effective pressure of the vacuum chamber, and Z_e is an effective atomic number for the residual gas in the chamber (see Section 4.2). The S_G parameter is unique to each channel and stable when collimators are fixed, with independent LER and HER values [1].

Equation 2.2 shows that the Touschek lifetime is inversely proportional to the density of particles in a bunch N/σ_y . The loss rate is therefore proportional to the beam particle rate multiplied by the inverse lifetime. Again, absorbing all constants into a single multiplicative factor⁵, we have the Touschek contribution to the observed background rate

$$\mathcal{O}_T = S_T \cdot \frac{I}{N_b} \frac{I}{\sigma_y}, \quad (4.12)$$

where S_T is the Touschek sensitivity, analogue to the beam-gas sensitivity although with different units. Moreover, N_b is the number of bunches in the train so the term $\frac{I}{N_b}$ is the “bunch current” — a measure of the charge in each bunch — which is proportional to N .

Inefficiencies in the continuous injection scheme produce enhanced background during this process. Similarly to the beam-gas and Touschek cases, we also define the injection loss observable

$$\mathcal{O}_{\text{inj}} = S_{\text{inj}} (1 - \epsilon_{\text{inj}}) N_{\text{inj}} \quad (4.13)$$

where ϵ_{inj} is the injection efficiency, N_{inj} is the number of injected particles per bunch and S_{inj} is the injection loss sensitivity.

Each contribution is independent of the other, so the total observable rate is

$$\mathcal{O} = S_G \cdot I P_e Z_e^2 + S_T \cdot \frac{I^2}{\sigma_y} + S_{\text{inj}} \cdot (1 - \epsilon_{\text{inj}}) N_{\text{inj}}. \quad (4.14)$$

The sensitivities S_G , S_T and S_{inj} are unique to each channel and should be stable when collimators and bunch fill patterns are fixed, and have independent LER and HER values. They contain the various geometrical and (fixed) energy parameters, as well as the

⁵Here, both the particle density and the particle flux are proportionally related to the beam current for a given bunch fill pattern.

propagation efficiency of the emitted background particle to the detector cell and the detection efficiency of the full signal chain [1]. In practice, S_{inj} is irrelevant in the dedicated background studies since these are taken outside the injection periods, and the other two parameters are neglected during the injection studies since the injection noise dominates the signals. In equations (4.11) to (4.14), the observable \mathcal{O} can be either the hit rate or dose rate, depending on the sub-detector of interest.

With this functional model in hand, we can discuss how each of these contributions are compared to simulation, and validate our understanding of the driving machine background mechanisms and their scaling.

4.5.2 Re-weighting procedure for simulated data

The simulation is generated with arbitrary beam conditions $I^s, P^s, Z_e^s, \sigma_y^s$ and N_b^s , which are respectively the beam current, the average vacuum chamber pressure, the effective atomic number of the residual gas, the vertical beam size and the number of bunches in the train. The subscripts l, h indicate whether these conditions pertain to the LER or the HER. The simulated output, or observable, is denoted \mathcal{O}_X^s where X can be C for the Coulomb process, B for the Bremsstrahlung process, or T for the Touschek process. As discussed in Section 2.2.2, the beam-gas backgrounds are the sum of the Coulomb and bremsstrahlung contributions such that

$$\mathcal{O}_G^s = \mathcal{O}_C^s + \mathcal{O}_B^s. \quad (4.15)$$

In all the above the superscript s indicates that these are the “*simulated*” conditions and observables, as opposed to superscript d that would indicate experimental, or “*data*” conditions and observables.

In this notation, the simulated background rates re-weighted to experimental conditions are given by

$$\tilde{\mathcal{O}}^s = \mathcal{O}_T^s \left(\frac{(I^d)^2}{\sigma_y^d N_b^d} \right) \left(\frac{\sigma_y^s N_b^s}{(I^s)^2} \right) + \sum_{\text{iD}=1}^{12} \frac{I^d \cdot P^d[\text{iD}] \cdot (Z_e^d)^2}{I^s \cdot P^s \cdot (Z_e^s)^2} (\mathcal{O}_C^s[\text{iD}] + \mathcal{O}_B^s[\text{iD}]), \quad (4.16)$$

where the tilde denotes a re-weighted quantity and the index $[\text{iD}]$ indicates the number of the “D section” of SuperKEKB (see Figure 1.3).

4.5.3 Hypotheses related with the vacuum chamber pressure and gas constituents

One of the difficulties arising from modelling the observed backgrounds with Eq. (4.14) is that the pressure readings from SuperKEKB cold-cathode gauges (CCGs) has a large uncertainty, estimated to be about 50%. On the top of this, we know the gas constituents at only two specific locations in the positron storage ring, namely D02 and D06, and nowhere in the electron storage ring.

Our best knowledge of the actual pressures in the chamber comes from discussions with the SuperKEKB accelerator group, and consists of multiplying the CCG pressure readout by a scale factor [81]

$$\alpha_p = 3.0 \pm 1.5. \quad (4.17)$$

This factor is assumed to be identical between the HER and the LER, since it is thought to arise from calibration and placement of the pressure sensors.

Furthermore, devoid of any information of the contrary, we can only assume that the gas mixture is the same in the HER and in the LER. This particular hypothesis is rather weak because the residual gas constituents are mostly impurities desorbed from the vacuum chamber surfaces. However, the material of the two chambers is different so the contamination due to manufacturing process is expected to be different. Most of the HER sections were also re-used from KEKB, while the effect of 11 years of operation on the surface and contamination conditions has been shown to be significant, even after extended periods of storage [50].

Therefore, we only have a limited knowledge of the actual gas conditions in the vacuum chambers, which are important inputs to the simulation. The high-energy ring results will be the most difficult to interpret for two reasons:

1. there are no data to test any hypothesis on the gas constituents, and
2. the beam-gas background is expected to be a significant, if not the most significant, contribution to the overall background.

The last statement is justified by the dependence of Touschek lifetime on the square of the beam particle energy, as expressed in Eq (2.2). A larger beam energy translates into a

longer Touschek lifetime (and hence less Touschek background).

4.5.4 The data-to-simulation ratio

The comparisons between data and simulation are conducted using the simulated observables re-weighted as shown in Equation (4.16), however using $\alpha_P P^d[\text{iD}]$ instead of $P^d[\text{iD}]$ to account for our limited knowledge of the actual vacuum chamber pressure. The data-to-simulation ratio \mathcal{R}_{ds} , measured by channel iCh , is the average on all valid data points of the ratio of the data observable over the re-weighted simulated observable.

$$\mathcal{R}_{ds}[\text{iCh}] = \frac{1}{nRuns} \sum_{\text{iRun}=0}^{nRuns} \frac{\mathcal{O}^d[\text{iCh}, \text{iRun}]}{\widetilde{\mathcal{O}}^s[\text{iCh}, \text{iRun}]} \quad (4.18)$$

In the above, the index iRun corresponds to a specific sub-run of Tables 4.1 and 4.2. The data-to-simulation calculation study was conducted on runs 200[7-9] and 300[7-9], and therefore

$$nRuns = 15.$$

4.5.5 Statistical uncertainty

The statistical uncertainty on \mathcal{R}_{ds} is assessed by summing the standard errors on the mean observable in a given sub-run in quadrature, then propagating the result onto the ratio in (4.18). Hence, a noisy channel, a brief sub-run or background readings that vary greatly in the same sub-run would all translate into a large statistical uncertainty for the measurement and affect the uncertainty on the data-to-simulation ratio accordingly. The statistical uncertainty is added in quadrature with the systematic uncertainty contributions detailed below to provide an estimate of the global uncertainty on the measurements.

4.5.6 Systematic uncertainties

The systematic contributions to the data/simulation ratio uncertainty are listed below. Comparisons of the hit rates, as recorded by the scaler on LYSO and CsI(pure) channels, are affected by three of these contributions, namely the uncertainty on the calculated α_P

factor, the uncertainty on the beam size measurements, and the uncertainty on the beam current measurements.

Comparisons of the dose rate, as recorded by the digitizers on CsI(Tl) and LYSO channels, are subject to the first three components named above, in addition to the uncertainty on the DAQ livetime and that on the energy calibration, and the uncertainty on the energy threshold.

α_P value

As mentioned in Section 4.5.3, the uncertainty on the pressure scale factor $\delta(\alpha_P)$ is provided by the SuperKEKB group. It is taken to be half the pressure correction. [81]

Beam size

The beam size uncertainty is also given to us by the SuperKEKB group. The values are

$$\delta(\sigma_{y,HER}) = 0.0371 \mu\text{m}$$

and

$$\delta(\sigma_{y,LER}) = 0.0137 \mu\text{m}.$$

Beam current

The beam current uncertainty is also given to us by the SuperKEKB group. The values are

$$\delta(I_{HER}) = \delta(I_{LER}) = 0.03 \text{ mA}$$

Energy calibration

The uncertainty on the energy calibration is given by propagating the uncertainty of all parameters entering into the calibration equation:

$$\delta(E)^2 = \left(\frac{\partial E}{\partial b} \delta b\right)^2 + \left(\frac{\partial E}{\partial c} \delta c\right)^2 + \left(\frac{\partial E}{\partial p_0} \delta p_0\right)^2 + \left(\frac{\partial E}{\partial p_1} \delta p_1\right)^2, \quad (4.19)$$

where E is obtained from the digitizer reading by applying (4.10). The uncertainty on the delivered beam dose (the time-integrated current) is neglected since it is very small compared to the calibration errors. Moreover, the covariance between the fit parameter values are neglected. They are in fact negative, so neglecting their contribution provides a conservative uncertainty estimate.

The relative energy uncertainty due to calibration and dose-dependence is evaluated at the beam dose corresponding to the beginning of the Beast II study days: 686 A · h. The results are reported in Figure 4.11 below.

It is striking from Figure 4.11b that the damage affecting the pure CsI crystals readout in the course of the experiment yield large calibration uncertainty. This complicates any attempt to conduct calorimetry and dose-dependent studies with these channels since the uncertainty on the uncertainty measurement is on the same scale as the measurement itself, and often even larger. For these reason, CsI was mostly used in injection background timing studies, where the relative rates matter much more than the absolute energy scales. Results of those more detailed studies are reported elsewhere [1].

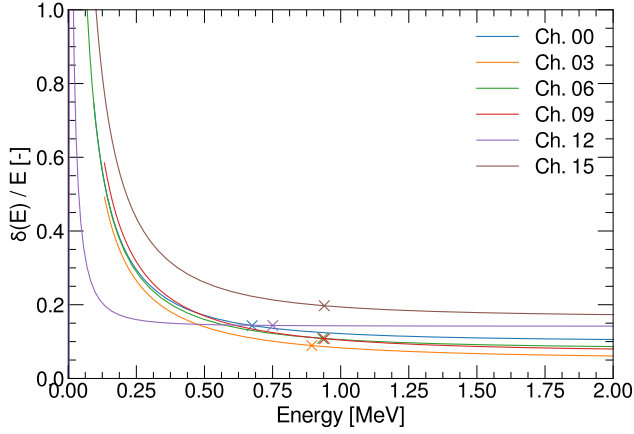
Energy threshold

The energy-equivalent thresholds incorporate the uncertainty of the energy calibration when calculating the energy corresponding to a specific pulse amplitude and using this value in the simulation. From Figure 4.11, the calibration uncertainty at the threshold energy is between 10% and 25% for the CsI(Tl) channels, between 35% and 225% for the CsI(pure) channels, and between 15% and 40% for the LYSO channels.

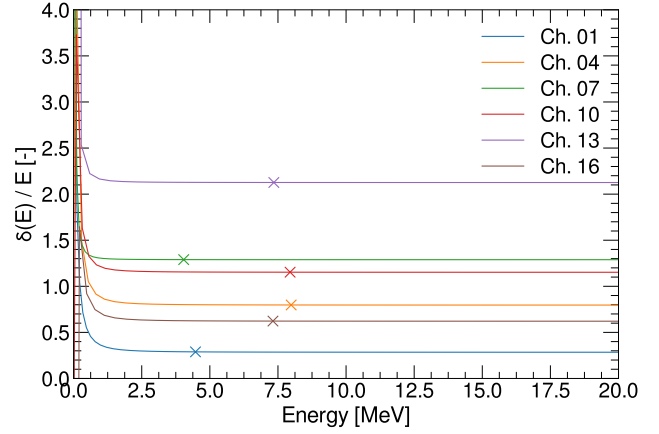
In order to propagate the threshold uncertainty onto the final results, we use modified data samples where artificial threshold are set to 1.3, 3.0 and 1.5 times the nominal value for CsI(Tl), CsI(pure), and LYSO, respectively. The analysis is then ran with these samples to check the impact on the calculated data-to-simulation ratios.

Livetime of the data acquisition system

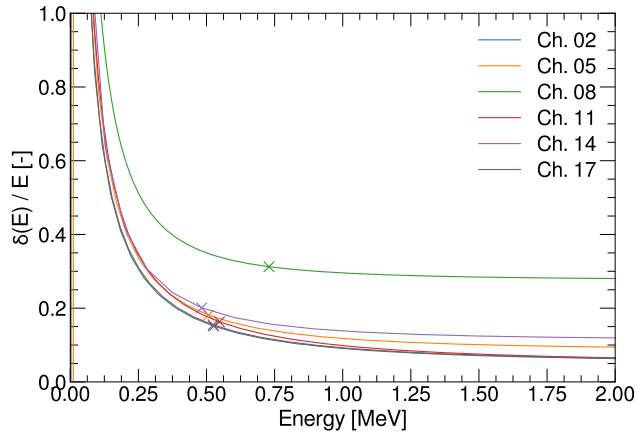
The data acquisition system (DAQ) did not always operate with the nominal 1:400 pre-scaling during the course of the experiment. This translates into a pre-scale factor for the



(a) CsI(Tl) crystal channels



(b) CsI(pure) crystal channels

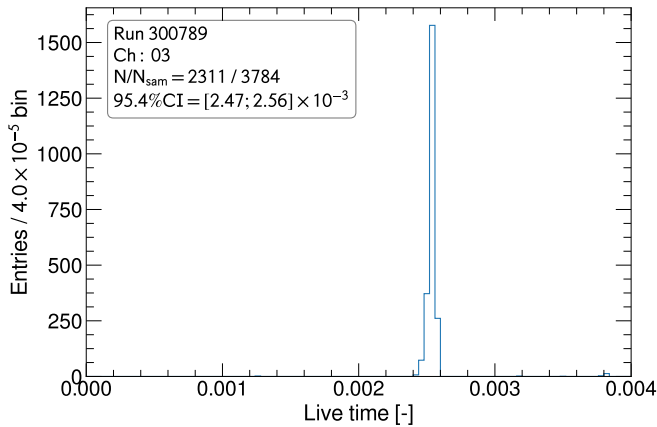


(c) LYSO crystal channels

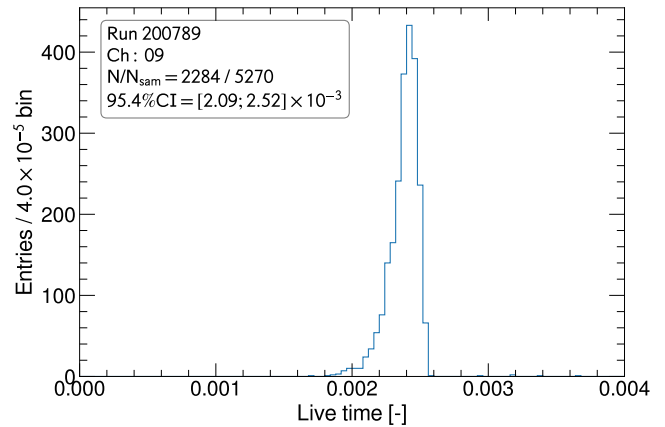
Figure 4.11: Relative calibration uncertainty of the crystal calorimeter units. The crosses indicate the nominal equivalent energy digitizer threshold setting during the Beast II study runs.

digitized data — see Section 4.3.4 — that varies in the course of the measurement, and channels that go off-line for seconds. The DAQ livetime is therefore measured in each data-taking run to determine the interval within which the livetime can be expected to vary. Example results are reported in Figure 4.12.

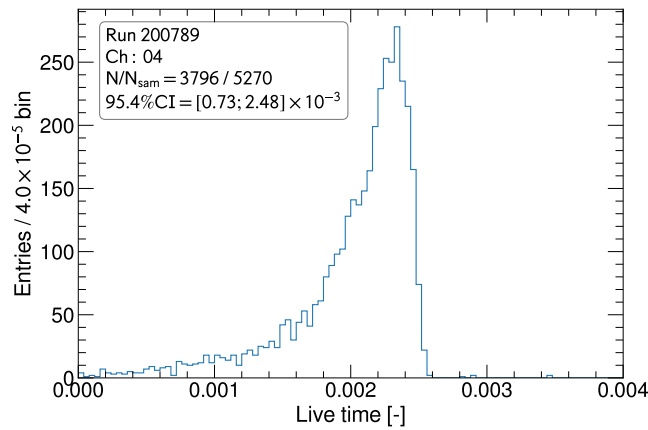
To account for this uncertainty contribution in the data-to-simulation comparisons, we use the limits of the interval that comprises 95.4% of the samples, around the nominal pre-scaling livetime value of 2.5×10^{-3} . If the data were Gaussian, this would provide a 2σ



(a) Narrow livetime distribution



(b) Average livetime distribution



(c) Wide livetime distribution

Figure 4.12: Three examples of DAQ livetime distributions. Most distributions are similar to panel 4.12b, however two extreme examples are shown for completeness in 4.12a and 4.12c. N/N_{sam} indicates the ratio of selected samples: those with a livetime value inconsistent with either a busy channel or with data recorded during an injection period. The interval that covers 95.4% of the selected samples is denoted 95.4% CI, and is used as an indicator of the livetime uncertainty.

interval around the nominal value. It is assumed that the measured dose rate is directly proportional to the DAQ livetime. As such, the limits of the 95.4% coverage interval, relative to the nominal value, are used as scaling factors for the dose rates in the systematic uncertainty studies.

4.6 Beam-gas interactions and beam conditions evolution in Phase 1

The Beast II experiment is also valuable to study long-term performance improvements of the accelerator as the commissioning program is undergoing. Two aspects are particularly useful for the experimentalist: the vacuum scrubbing process and the time structure of so-called “beam-dust” events, both contributing to background seen in Beast II and expected in Belle II. Vacuum scrubbing is the general term used to describe out gassing of the vacuum chamber impurities induced by beam circulating in the accelerator. Beam-dust events, on the other hand, correspond to rapid increases in few local pressure readings and may trigger beam aborts. Thought to be the result of beam particle vaporizing microscopic or macroscopic particles, they were previously observed and studied at many accelerator laboratories such as KEK [87, 53], CERN [52, 51] and DESY [88].

In both cases, we are interested in the long-term behaviour of these quantities, and see how they are related to operating conditions such as instantaneous and integrated currents. The latter is also known as the “beam dose” and is a measure of progress of the accelerator commissioning. The following section describes the approaches taken by the Beast II group to characterize these phenomena as well as their respective results.

4.6.1 Vacuum scrubbing

Phenomenology

In the particular context of particle accelerators, the typical thermal out gassing process is augmented by radiation-induced effects called electron-induced desorption (ESD) and photon-induced desorption (PSD). While the former is more typical of electron-positron colliders such as SuperKEKB, and can arise from machine-induced electron multipacting [89], the latter is the result of synchrotron photons from the accelerated charged beams — whose energy can be as high as few MeV — irradiating the vacuum chamber material [90].

With both phenomena, the desorption rate is a function of the integrated radiation dose on the vacuum chamber material and follow the same behaviour [91]. After an initial electron or photon dose D_0 , the out-gassing rate η follows a power-law dependence with respect to

the integrated beam dose D :

$$\eta = \eta_0 \left(\frac{D}{D_0} \right)^\beta \quad (4.20)$$

where η_0 is the desorption rate at the initial dose D_0 , and the coefficient β is a function of the irradiation energy spectrum, the material characteristics, and the physical process (ESD or PSD) behind the scrubbing.

Because such scrubbing releases gas molecules into the vacuum chamber, it should be directly observable in terms of a dynamic pressure dP/dI component. Moreover, the beam-gas interactions between the impurities and the charged beams produce increased particle losses around the accelerator. Such losses are observed with the Beast II systems as increased radiation levels. These two techniques are used to assess the rate of vacuum scrubbing, and provide a statement on the adequacy of the vacuum expected for Belle II operation.

Dynamic pressure measurement

The dynamic pressure is a measurement of the rate of gas released from the material per unit current circulated in the beam pipe. Therefore it is expected to track the desorption rate:

$$\frac{dP}{dI} \sim \eta \quad (4.21)$$

This dynamic pressure is the fundamental quantity used by the SuperKEKB group to quantify the rate of vacuum scrubbing [50]. However powerful, using a single dP/dI value for a given set of beam parameters remains an approximation. This fact is illustrated in Figure 4.13. This example shows that the residual gas pressure is not a function of the current alone. More importantly it also shows that dP/dI depends on other quantities such as the actual operating current — the relationship is not linear between 300 mA and 500 mA — and the time after the last injection. The data points at the far right, where currents are the highest, were taken immediately after an injection period and exhibit short-term pressure increase for decreasing currents (negative dP/dI).

With these warnings in mind, it is nonetheless useful to estimate this dynamical pressure term on a continuous basis. One approach is to neglect the base pressure inside the chamber — the equilibrium pressure when no beam is circulating — and assume linearity between pressures and currents. Examining only currents above 60% of the maximum

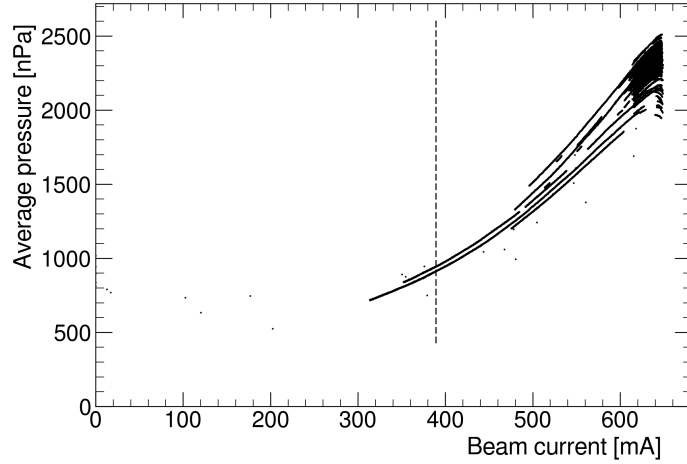


Figure 4.13: Example of P-I curves on a full day. Data shown are for the LER on 2016-05-08. The dashed line represents 60% of the maximum current value. Beam injection periods are removed. Reproduced from [1].

values to reduce the effects of base pressure, the dynamic pressure is estimated by

$$\frac{dP}{dI}(\text{est.}) = \frac{P}{I}. \quad (4.22)$$

A second approach to obtain the dynamic pressure is to consider the effect of the base pressure, which can be evaluated every time the beams are off for a sufficient period of time. Allowing a settling time of one hour was found to be adequate to measure the base pressure. Using this definition of the base pressure P_{base} ,

$$\frac{dP}{dI}(\text{daily}) = \frac{(P - P_{\text{base}})}{I}. \quad (4.23)$$

Dynamic pressure from machine-induced background measurement

The Beast II detectors also provide insight into the rate of vacuum scrubbing. An additional difficulty here lies in the fact that it is non-trivial to disentangle the background contribution due to beam-gas to those due to intra-bunch effects such as Touschek and electron cloud. According to the heuristic model of Equation 4.14, we can use the ratio O/I^2 as a proxy for Touschek-subtracted beam background contribution. As long as the

beam-gas contribution dominates the overall background radiation,

$$\frac{O}{I^2} \sim \eta, \quad (4.24)$$

can be used to study the vacuum process. In Equation 4.24 the observable O is a dose rate or hit rate, depending on the sub-detector of interest.

4.6.2 Analysis of transient “beam-dust” events

General description and motivation

During commissioning of the accelerator, one concern was the observation of localized pressure bursts and accompanying background spikes. The prevalent hypothesis for these observations are collisions between the beam electrons and positrons, and small particles such as dust coming off the vacuum chamber material [52, 51, 50]. These events will therefore be referred to as “beam-dust” events in this document.

Such beam-dust events are important during commissioning and running of an accelerator, since the corresponding increase in observed background often results in beam aborts and loss of operation time. The SuperKEKB group monitors these events by measuring pressure peaks around the beam pipe. The questions addressed in the present study are

- What is the time structure of these beam-dust events during Phase 1 of SuperKEKB, and does it change as vacuum scrubbing progresses?
- Do the pressure bursts measured by SuperKEKB correspond to background peaks seen in the Beast II detectors?
- Could the radiation resulting from these events be damaging to the detectors?

Analysis methodology

Qualitatively, beam-dusts events present sharp peaks in Beast II detectors observables, for example the deposited energy rate in the BGO, or the hit rate in the CsI crystals. These peaks are much higher than the typical signal, and last less than 2 seconds.

The analysis therefore consists of finding peaks that are at least six standard deviations above the mean signal, calculated using 60 seconds running time windows. To further exclude electronic noise peaks in the count, we require such peaks to be seen in at least four channels and in at least two different detector systems. The coincidence time window is set to 3 seconds since Beast II data coming from different sub-detectors is not perfectly aligned in time. These requirements were adjusted on a small sample of clearly identifiable peaks, then extended to the complete Phase 1 data set.

The results are compared to the list coming from the SuperKEKB accelerator group, who define beam-dust events as pressure bursts where any cold cathode pressure gauge value is 15% larger than the previous 1-second average. From this list, only burst events located in regions D01 and D02 — the straight subsections on either side of the Beast II detector, see Figure 1.3 — are considered. This amounts to 338 distinct burst events. The other regions were excluded since vacuum bump experiments outside this range showed no corresponding increase of the Beast II observables, and therefore these events would be impossible to correlate with Beast II data.

The time resolution of the events provided by SuperKEKB is one minute so we use one minute intervals also for the Beast II events. We calculate the cross correlation between the two lists to ensure there are no time misalignment between the two datasets. A peak at lag=0 indicates the correct time alignment, and the cross-correlation value outside the peak correspond to the number of accidental coincidences due to the finite time resolution.

Finally, we aim to provide a statement on the dose resulting from such events. To achieve this, we compare the peak level dose to the running average of the previous 60 seconds, and multiply by the probability of occurrence of such a peak for the given sub-detector that recorded it.

*
**

Chapter 5

Results and simulation

5.1 Specific results from the CsI(Tl), CsI(pure) and LYSO system

5.1.1 Calibration and time-dependence of the gain

The measured parameters from the initial calibration campaign are reported in Table 5.1 below. Refer to Appendix A.1 for the detailed results and calibration curves, as well as the plots for the CsI(pure) and LYSO channels, produced by collaborators.

These calibration constants were technically only valid before beams started circulating. The methodology used to characterize of the gain degradation as a function of beam dose is described in Section 4.4.2. Figure 5.1 shows typical relative gain results for each crystal type, and the complete results are reported in Appendix A.2. For some of the CsI(pure) channels, the PMT supply voltage settings were changed during the course of the experiment to reduce the gain by half, thus reducing the hit rates and and help preserving the PMTs. Nevertheless, the CsI(pure) channels showed a notable gain degradation, presumably from the sustained large currents in the tubes. We suspect that the gain degradation come from the tubes themselves since CsI crystals have been shown have a good radiation hardness, with only 20% gain degradation at doses as high as 143 Gy [92]. Moreover, the PMTs on the CsI(pure) channels shave a 48 mm diameter active window which means their active area is twice as large as the tubes on the CsI(Tl) channels. This makes them more susceptible to damage from a larger light intensity, thus larger currents. Because

Table 5.1: Crystals system calibration parameters versus crystal channel number (#) resulting from the initial calibration campaign. The relationship between energy and measured charge is described by Equation 4.9: parameter a is a hard-coded value in the digital signal processor settings. The values and uncertainties for b and c are obtained by the linear least squares algorithm. Reproduced from [1]

#	Material	a [pC/LSB]	b [pC/MeV]	c [pC]
0	CsI(Tl)	1.28	167.4 ± 0.7	-14.1 ± 11
1	CsI(pure)	0.32	5.45 ± 0.3	0.74 ± 0.3
2	LYSO	0.32	15.8 ± 0.6	1.2 ± 0.8
3	CsI(Tl)	1.28	102.6 ± 0.3	-9.1 ± 5
4	CsI(pure)	0.32	5.78 ± 0.3	1.13 ± 0.3
5	LYSO	0.32	19.2 ± 0.8	1.5 ± 1
6	CsI(Tl)	1.28	132.9 ± 0.4	-0.6 ± 6
7	CsI(pure)	0.32	5.81 ± 0.3	0.78 ± 0.3
8	LYSO	0.32	18.4 ± 0.7	-0.8 ± 1
9	CsI(Tl)	1.28	129.6 ± 0.4	-11.1 ± 7
10	CsI(pure)	0.32	5.76 ± 0.3	1.11 ± 0.3
11	LYSO	0.32	17.3 ± 0.7	0.2 ± 1
12	CsI(Tl)	1.28	114.1 ± 0.1	2.8 ± 2
13	CsI(pure)	0.32	5.39 ± 0.3	1.36 ± 0.3
14	LYSO	0.32	15.1 ± 0.6	4 ± 1
15	CsI(Tl)	1.28	128.6 ± 0.5	-7.6 ± 8
16	CsI(pure)	0.32	5.39 ± 0.3	1.29 ± 0.3
17	LYSO	0.32	17.3 ± 0.7	0.64 ± 0.9

they have been damaged to the point where the uncertainty on the energy calibration is comparable to the measurement itself, their usability for calorimetry purposes is limited.

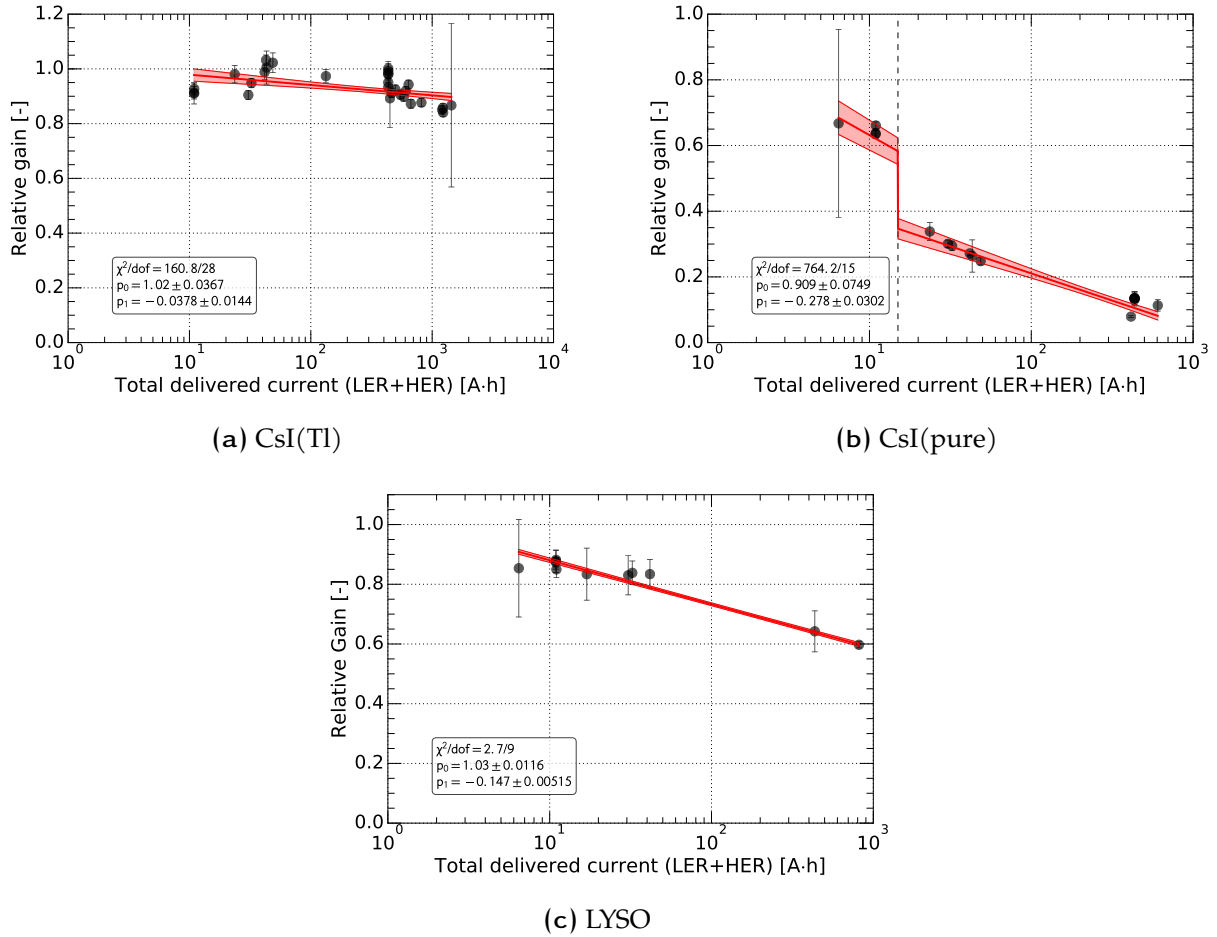


Figure 5.1: Relative gain with respect to the initial calibration for the three different crystal types. The red line corresponds to a $y = p_0 + p_1x$ linear fit of the relative gain vs. \log_{10} of the total delivered current, and the shaded area represents the projected uncertainty on the relative gain. On the CsI(pure) channel, the vertical dashed line indicates the integrated current value when the high-voltage settings were changed in order to manually reduce the gain by a factor 2. This also explains the broken line describing the relationship.

5.1.2 Energy spectra for different conditions

One of the ways to assess the quality of the simulation and the completeness of our background model is to measure the energy spectra of the machine-induced background in

different operating conditions. The next paragraphs present such spectra for nominal operation at the beginning and at the end of Phase 1, operation with deliberately larger beam size to study the Touschek effect, and operation with larger vacuum chamber pressure to study beam-gas interactions.

The injection periods are all removed from these studies since designing a model for the injection noise would be outside the scope of this project. An example spectrum taken during injection is nonetheless presented to provide a sense of the impact of injections on the overall backgrounds.

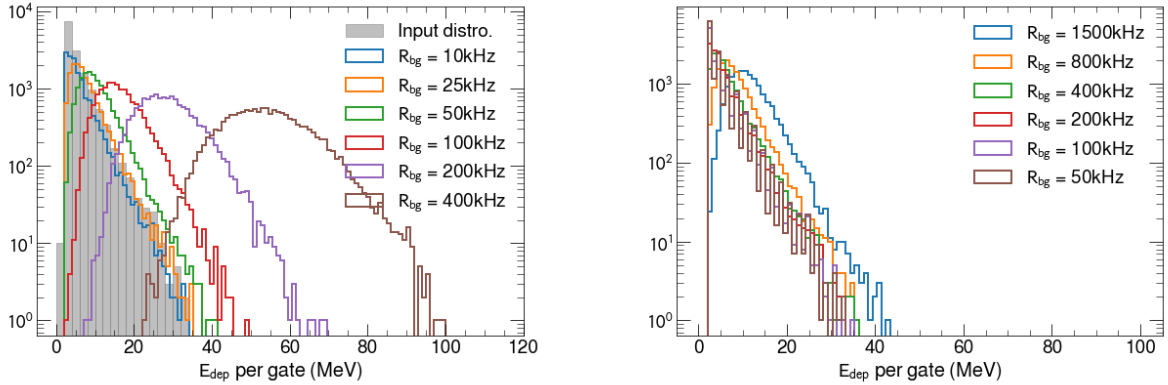
Before presenting the spectra for these all these different conditions, a short digression on the pile-up effects visible in the CsI(Tl) channels is warranted.

Pile-up effects in CsI(Tl) crystals

One recurrent feature in CsI(Tl) spectra is that the tails of the measured distributions are longer than those of the simulated ones. This is notable, for instance, in Figures 5.5a and 5.6c. A likely explanation for this is pile-up of low-energy hits within one charge integration gate. Since the time structure of the background is not known accurately for all beam conditions, such pile-up effects are not included in the simulated samples.

We set up a toy Monte Carlo experiment to determine, for different background rates, what the impacts on the spectra would be. To each simulated hit, we add a number of “parasitic” hits with the expected number of hits from each energy bin given by the input distribution shape and the assumed background rate. Then, for each simulated hit, the actual number of hits to be added from each energy bin is taken from a Poisson distribution centred at the expected value. The results for CsI(Tl) are shown in Figure 5.2a.

We see that pile-up of low-energy hits effectively smears the distributions, and enhances the tails while depleting the lower energy bins. Furthermore, the impact becomes noticeable for hit rates greater than 25 kHz. However, none of the shapes shown in Figure 5.2a matches what is measured *e.g.* in Figures 5.5a and 5.6c. It is likely that the time structure of the background is richer than the above models, and contains contributions from different frequencies. In the future, more elaborate description of pile-up effect could involve time structure information from measurement based on faster crystals. As of the Belle II software release current at the time of this study (release-01-00-02), there is no



(a) In a CsI(Tl) channel. The charge integration gate length on the CsI(Tl) channels is $6.2 \mu\text{s}$ (b) In a LYSO channel. The charge integration gate length is 260 ns to represent a LYSO channel.

Figure 5.2: Simulated pile-up effects in CsI(Tl) and LYSO crystals under different assumptions for the background rates R_{bg} . The input distribution “Input distro.” is identical in both panels.

framework in the ECL software to simulate such pile-up of machine background events within a charge integration gate. However, mixing recorded random trigger events with the simulated samples will account for these effects during data-taking.

A last interesting discussion point in relation to this topic is that the faster signal in LYSO crystals — and shorter associated charge integration gate — make their measurements more immune to pile-up effects. As seen in Figure 5.2b, the distortion of the energy spectrum for LYSO data does not occur below a 800 kHz background hit rate which supports the hypothesis that the tails in CsI(Tl) spectra are related to pile-up effects.

Explanatory notes related to the energy distribution plots

Figures 5.3 to 5.13 in the sections below present the spectra for at different conditions. These plots share a number of characteristics.

First there is only one simulated sample for all beam conditions, which includes the Tou-schek, Coulomb and bremsstrahlung (“Brems.”) contributions. These are represented as the coloured shaded areas. The relative amplitudes of the various contributions are weighted differently, using Equation 4.16, to represent the specific operating point where

the data were recorded. However since they all come from a single original sample, the statistical fluctuation between energy bins are identical in all plots.

Second, the sub-captions are labelled with the crystal locations with codes such as “F1” and “B2”. The first letter represent the longitudinal (forward or backward) direction of the detector, and the integer indicates the axial position (*e.g.* in ϕ). This naming scheme is illustrated in Figure 4.7.

Third, in agreement with the nomenclature used elsewhere in this document, an experiment in the electron beam is labelled “HER”, and one in the positron beam is labelled “LER”.

Finally, the recorded spectrum is added as a solid black line in all the plots. It is normalized with the sum of the simulated samples on the integral between 2 MeV and 8 MeV to enable comparisons based strictly on the distribution shapes.

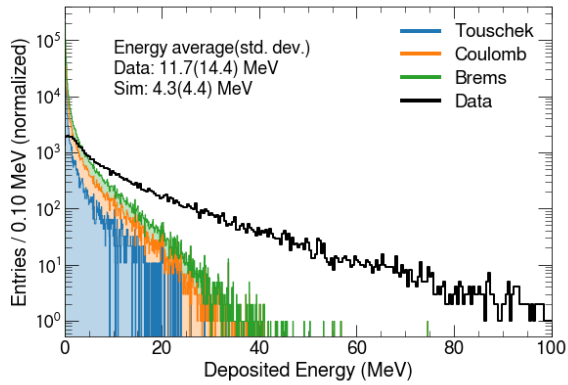
Single simulation sample; how they change from one page to the next. Position Colors, lines HER (electron), LER (positron) Missing data: the LYSO channel suffered from too much dead time due to data acquisition issues, so we had to discard it from the analysis.

Early operation (before electron-cloud effect countermeasures)

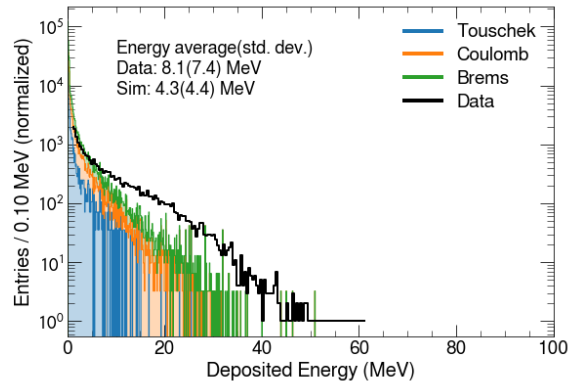
The electron-cloud effect (ECE, see Section 2.2.4) was observed early in commissioning and prevented operating the LER at currents beyond ~ 500 mA. Improvements to the vacuum chamber aimed at reducing this effect, discussed in Section 2.3.1 and visible in Figure 2.5, were implemented during the ‘Golden Week’ shut-down in May 2016. Figure 5.3 and Figure 5.4 show the spectra before these countermeasures were put in place.

As expected, the ECE affects the positron beam more than the electron beam. The larger tails of the spectra, not well described by simulation, are visible in the distributions of Figure 5.4 and not in those of Figure 5.3. We also see that the better energy resolution for LYSO crystals is more appropriate to capture the structure of the ECE background than the CsI(Tl) channels, which are more prone to pile-up of low energy deposits.

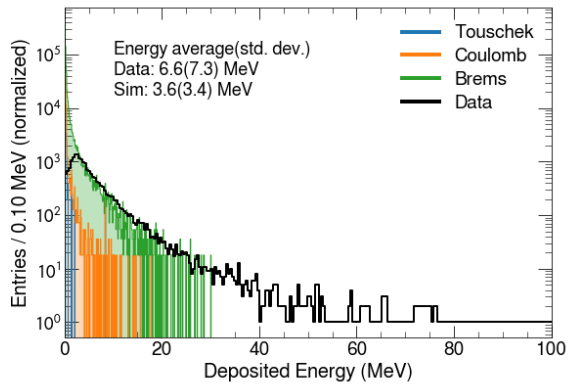
The spectra of Figure 5.4 should be compared to similar data recorded after the ECE countermeasures were installed, in order determine the efficacy of these measures.



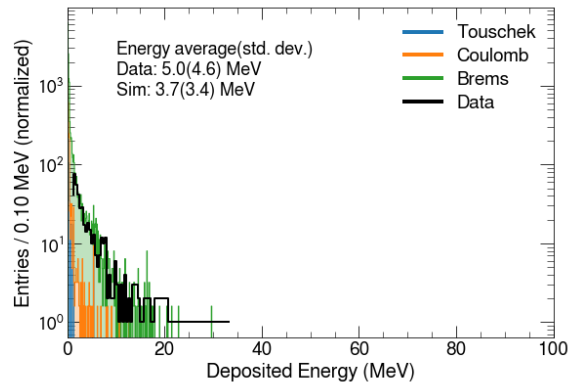
(a) CsI(Tl) F1



(b) LYSO F1

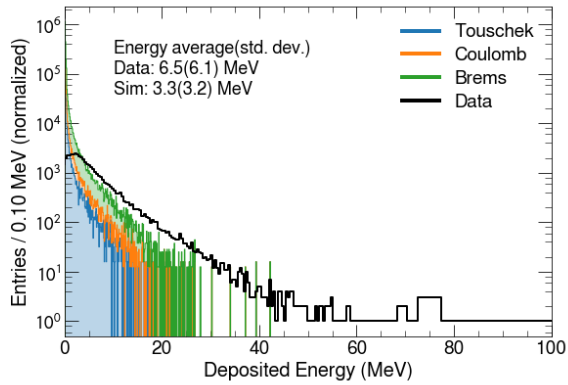


(c) CsI(Tl) B1

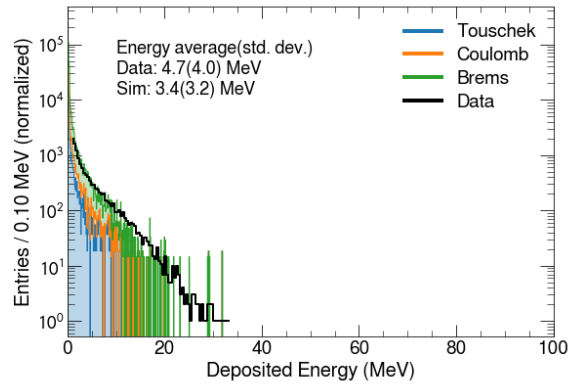


(d) LYSO B1

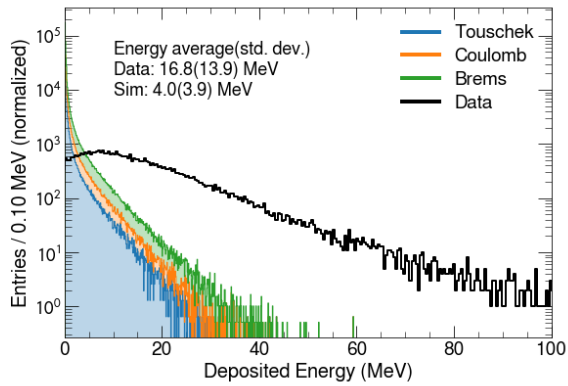
Figure 5.3: Representative spectra from an early HER run. These data were recorded on 2016-04-07, before the SuperKEKB improvements including measures to reduce the electron-cloud effect. The average energy above 1 MeV is given for both data (“Data”) and the sum of simulated samples (“Sim”), with the standard deviation in parentheses.



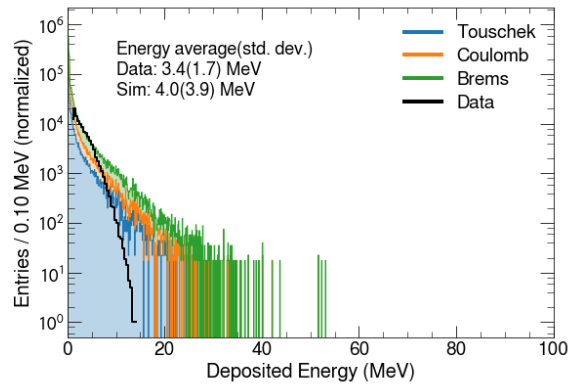
(a) CsI(Tl) F1



(b) LYSO F1



(c) CsI(Tl) B1

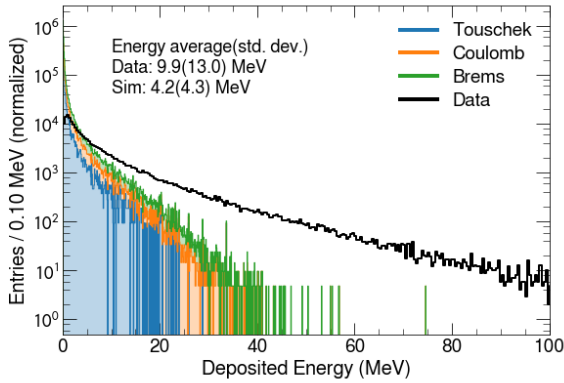


(d) LYSO B1

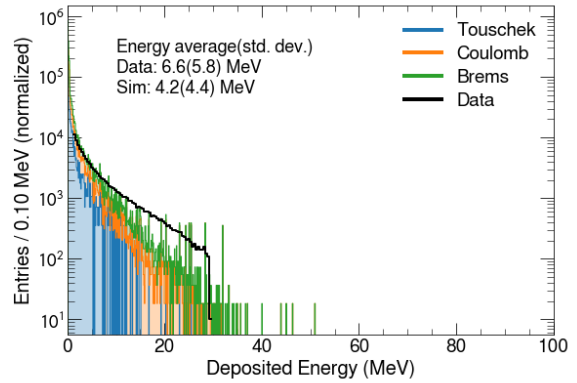
Figure 5.4: Representative spectra from an early LER run. These data were recorded on 2016-04-19, before the SuperKEKB improvements including the introduction of additional electron-cloud effect countermeasures. The average energy above 1 MeV is given for both data (“Data”) and the sum of simulated samples (“Sim”), with the standard deviation in parentheses.

Nominal operation

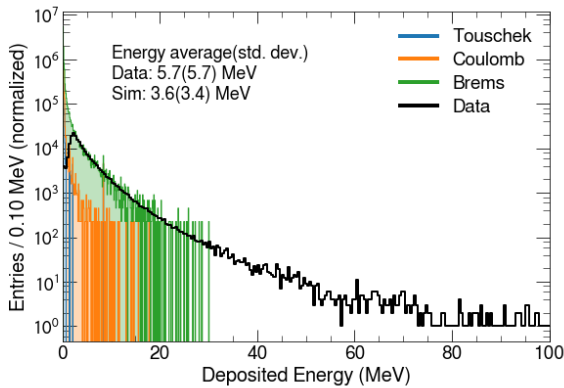
Before looking into the impact of different beam parameters on the energy spectra, it's worth presenting the results for the default conditions as a point of comparison. Figures 5.5 and 5.6 show spectra recorded during nominal operation in the Beast II dedicated study runs.



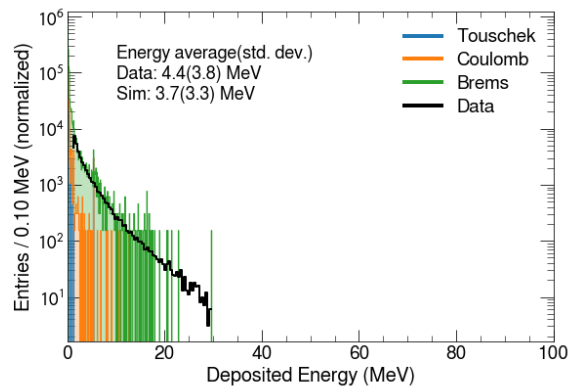
(a) CsI(Tl) F1



(b) LYSO F1



(c) CsI(Tl) B1

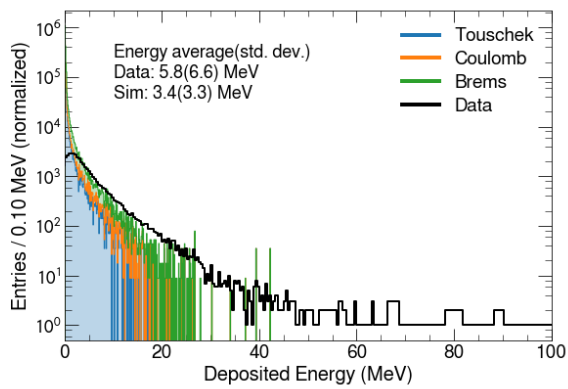


(d) LYSO B1

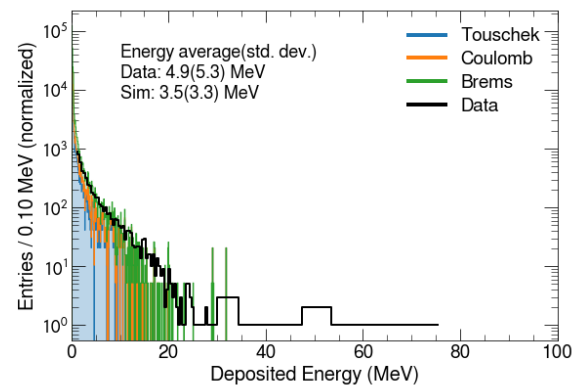
Figure 5.5: Representative spectra from a Beast II nominal HER run. These data were recorded on 2016-05-16, during the Beast II dedicated studies. The average energy above 1 MeV is given for both data ("Data") and the sum of simulated samples ("Sim"), with the standard deviation in parentheses.

One striking difference with the earlier spectra is that the high-energy tails indicative of the electron-cloud effect in the LER data are not present in nominal running. The data are well described by simulation, except for the CsI(Tl) in the forward F1 position during the

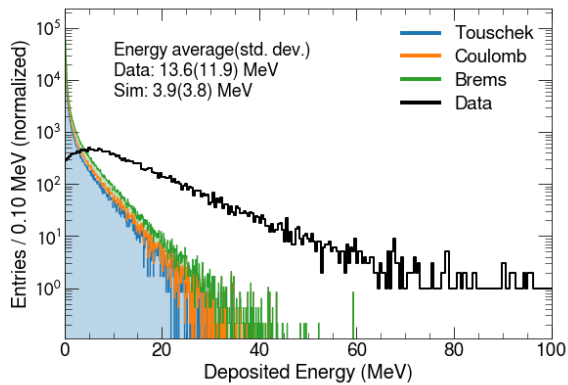
HER runs (Figure 5.5a), and the CsI(Tl) in the backward B1 position in the LER runs (Figure 5.6c). In both cases, the channel corresponds to the detector positioned immediately downstream from the interaction region, in the direction of the beam.



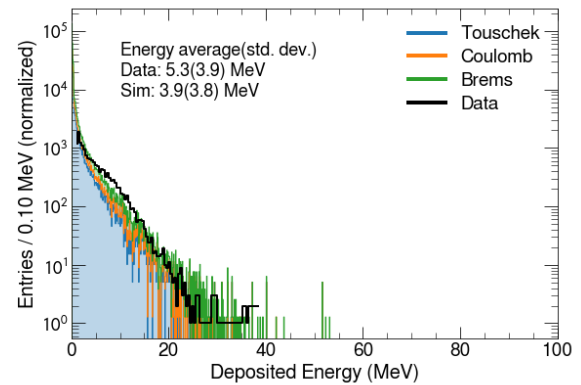
(a) CsI(Tl) F1



(b) LYSO F1



(c) CsI(Tl) B1



(d) LYSO B1

Figure 5.6: Representative spectra from a Beast II nominal LER run. These data were recorded on 2016-05-17, during the Beast II dedicated studies. The average energy above 1 MeV is given for both data (“Data”) and the sum of simulated samples (“Sim”), with the standard deviation in parentheses.

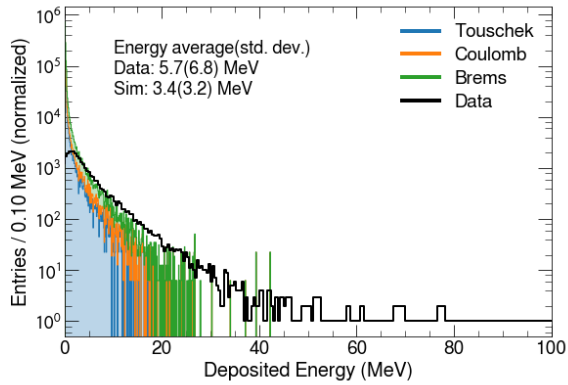
Touschek effect study

A qualitative study of the Touschek effect on the spectra is conducted by comparing Figure 5.7 with Figure 5.8 for the LER (37% more Touschek), and Figure 5.9 with Figure 5.10 for the HER (240% more Touschek).

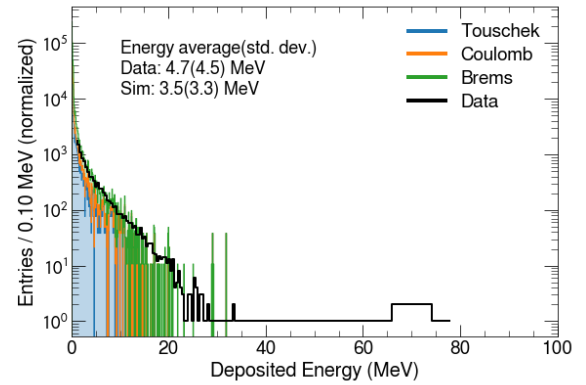
From the LER runs of Figures 5.7 and 5.8, we see that the backward CsI(Tl) channel (both panels (c)) exhibits a larger tail in the Touschek-enhanced than in the Touschek-diminished run. This tail represents part of the background that is not well modelled by our heuristic model of Eq. 4.14. On the forward channels of panels (a) and (b), however, there is no appreciable impact of beam size on the shape of spectra (beyond what is explained by our background model). Again, for the LER, the “backward” channels are downstream from the interaction region.

For the HER Touschek study, there is no clear impact of increasing the beam size by a factor of approximately 2.4. This can be seen by comparing Figures 5.9 and 5.10: even though the Touschek contributions are different, the shapes of the measured distributions are indistinguishable, so the part not explained by our background model (Eq. 4.14) is consistent in the two cases.

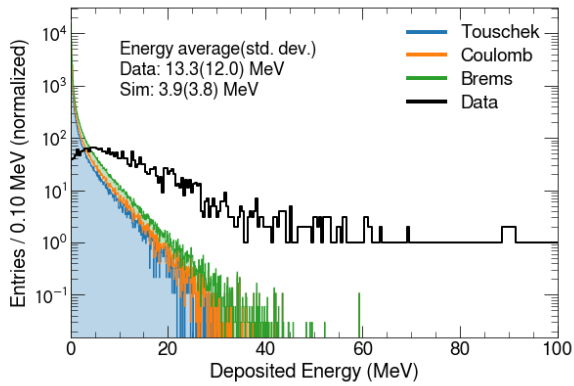
Note that for one of the sub-runs shown in panel 5.10b, the LYSO channel suffered from too much deadtime due to data acquisition issues, so we had to discard it from the analysis.



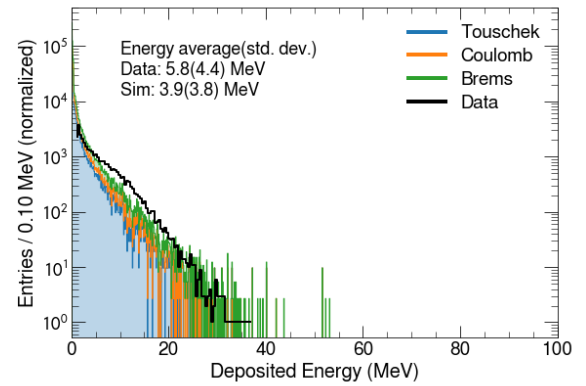
(a) CsI(Tl) F1



(b) LYSO F1

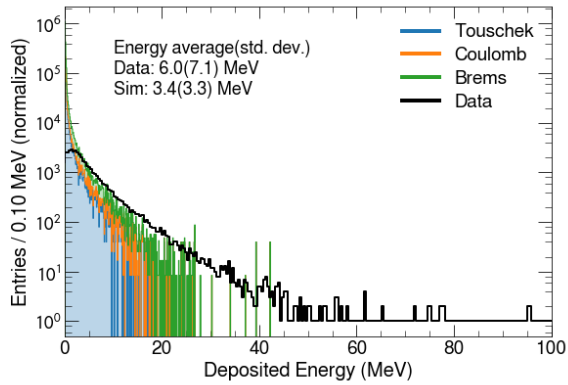


(c) CsI(Tl) B1

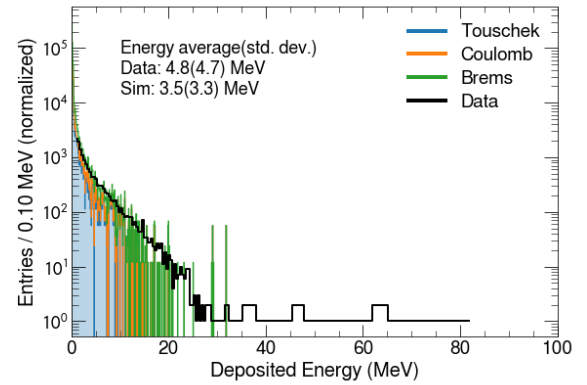


(d) LYSO B1

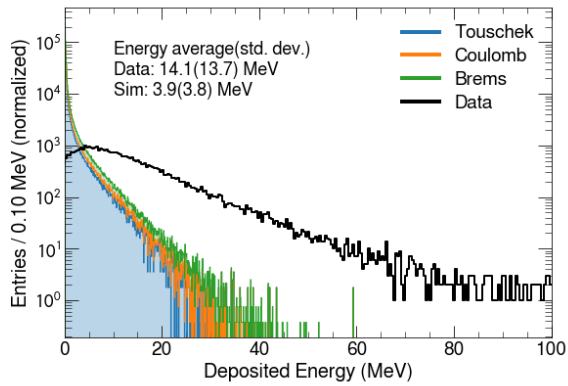
Figure 5.7: Representative spectra from a Touschek-diminished LER run. These data were recorded on 2016-05-17, during the Beast II dedicated studies. The setting for the emittance control knob is $ECK = 0.75$, and the vertical beam size is $\sigma_y = 74 \mu\text{m}$. The average energy above 1 MeV is given for both data (“Data”) and the sum of simulated samples (“Sim”), with the standard deviation in parentheses.



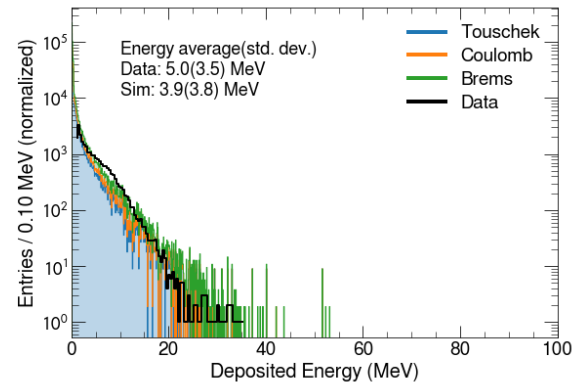
(a) CsI(Tl) F1



(b) LYSO F1

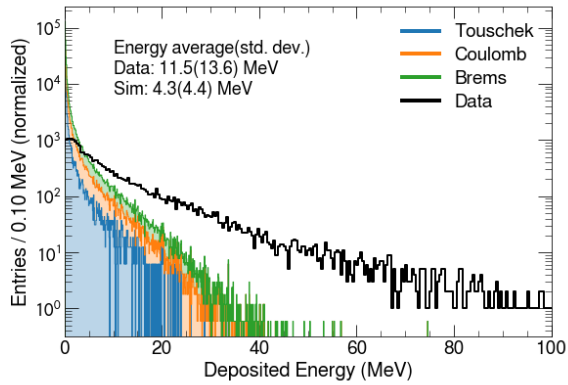


(c) CsI(Tl) B1

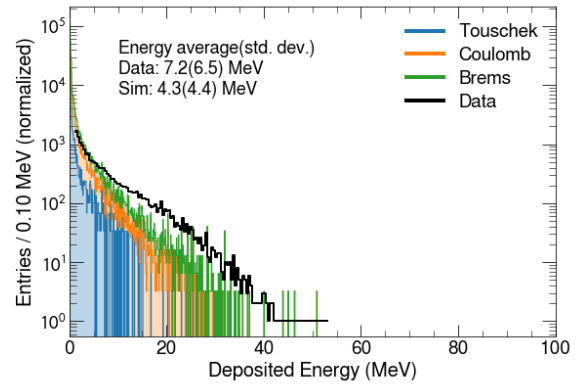


(d) LYSO B1

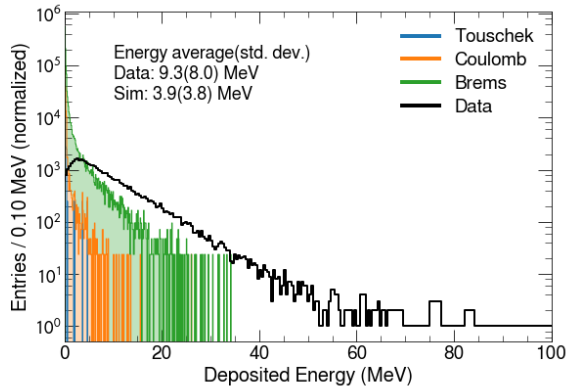
Figure 5.8: Representative spectra from a Touschek-enhanced LER run. These data were recorded on 2016-05-17, during the Beast II dedicated studies. The setting for the emittance control knob is $ECK = 0.00$, and the vertical beam size is $\sigma_y = 54 \mu\text{m}$. The average energy above 1 MeV is given for both data (“Data”) and the sum of simulated samples (“Sim”), with the standard deviation in parentheses.



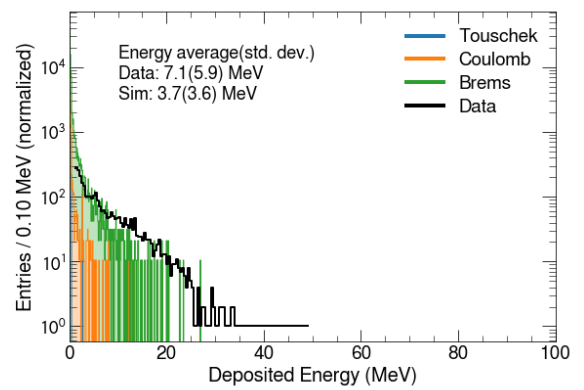
(a) CsI(Tl) F1



(b) LYSO F1

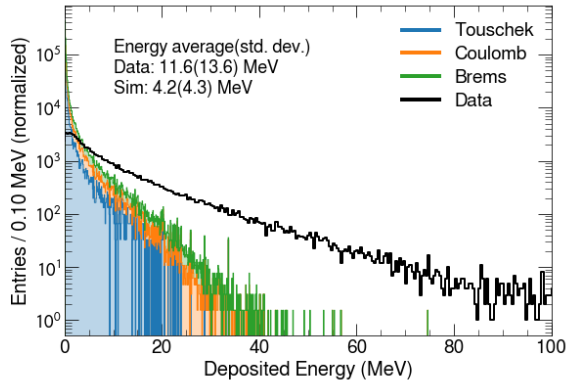


(c) CsI(Tl) B2



(d) LYSO B2

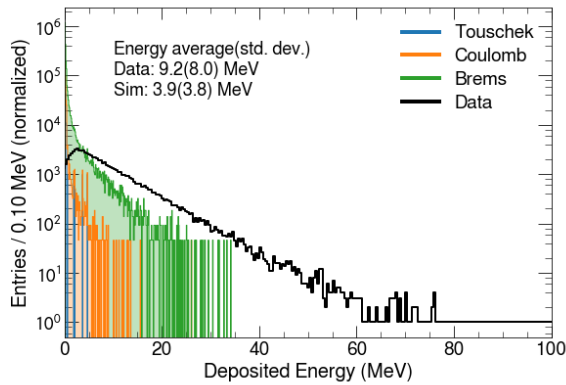
Figure 5.9: Representative spectra from a Touschek-diminished HER run. These data were recorded on 2016-05-17, during the Beast II dedicated studies. The bump height is $h_{\text{bump}} = 3.00$ mm, for σ_y (HER) = 120 μm . The average energy above 1 MeV is given for both data (“Data”) and the sum of simulated samples (“Sim”), with the standard deviation in parentheses.



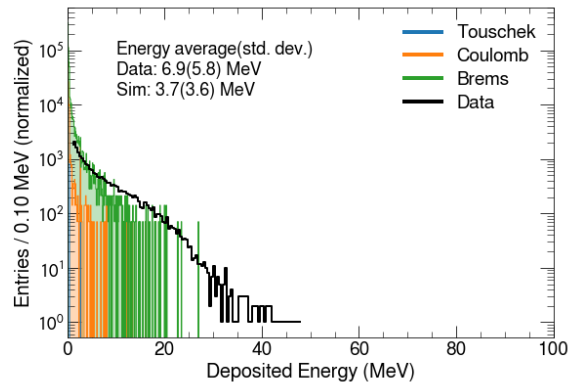
(a) CsI(Tl) F1

No data for
this channel

(b) LYSO F1



(c) CsI(Tl) B2

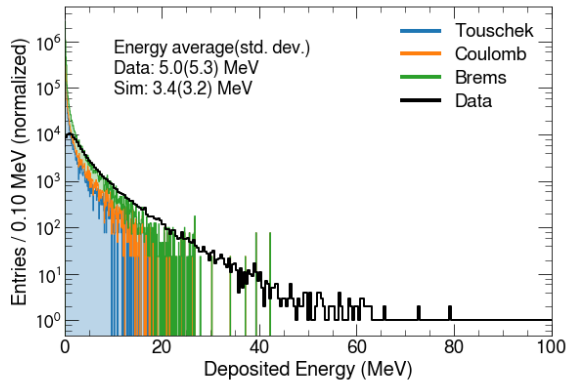


(d) LYSO B2

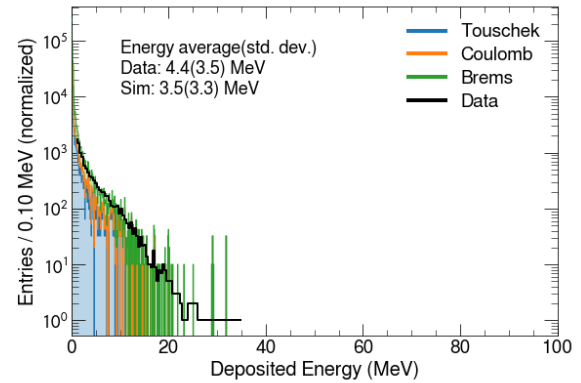
Figure 5.10: Representative spectra from a Touschek-study HER run. These data were recorded on 2016-05-17, during the Beast II dedicated studies. The bump height is $h_{\text{bump}} = 0.75$ mm, for σ_y (HER) = $50 \mu\text{m}$. LYSO had too much dead time due to data acquisition issues, so we had to discard it from the analysis. The average energy above 1 MeV is given for both data (“Data”) and the sum of simulated samples (“Sim”), with the standard deviation in parentheses.

Beam-gas enhanced runs

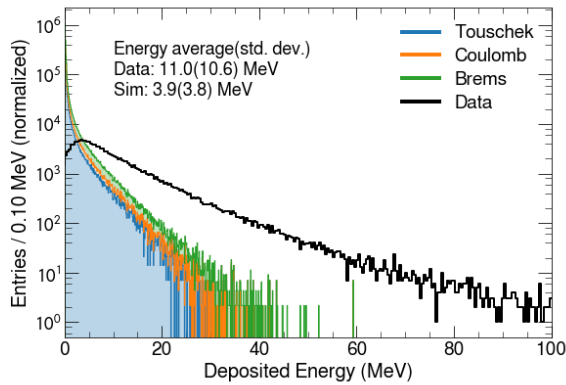
Figures 5.11 and 5.12 present spectra taken during pressure bump experiments in the LER and HER, respectively.



(a) CsI(Tl) F1



(b) LYSO F1



(c) CsI(Tl) B1

No data for
this channel

(d) LYSO B1

Figure 5.11: Representative spectra from a beam-gas enhanced LER run. These data were recorded on 2016-05-23 (run 5002), during the Beast II dedicated studies. The average pressure for the run is $P_{LER} = 2.0 \times 10^{-6}$ Pa (to be compared to the nominal value of 1.2×10^{-6} Pa). The average energy above 1 MeV is given for both data (“Data”) and the sum of simulated samples (“Sim”), with the standard deviation in parentheses.

Figure 5.11 shows that, with a pressure that is 67% larger than the nominal value, the Touschek contribution is still predicted to be a major contributor overall background levels. The measured spectra of the forward channels (panels 5.11a and 5.11b) are also qualita-

tively similar to those reported for the nominal conditions in Figure 5.6, and in good qualitative agreement with simulation. On the backward side, however, the larger rates during the peak of the pressure bump experiment are the likely cause for the larger pile-up observed in the CsI(Tl) channel of Panel 5.11c. Similar to what is seen in Figure 5.10, the data for one LYSO channel were discarded from the analysis because of dead time.

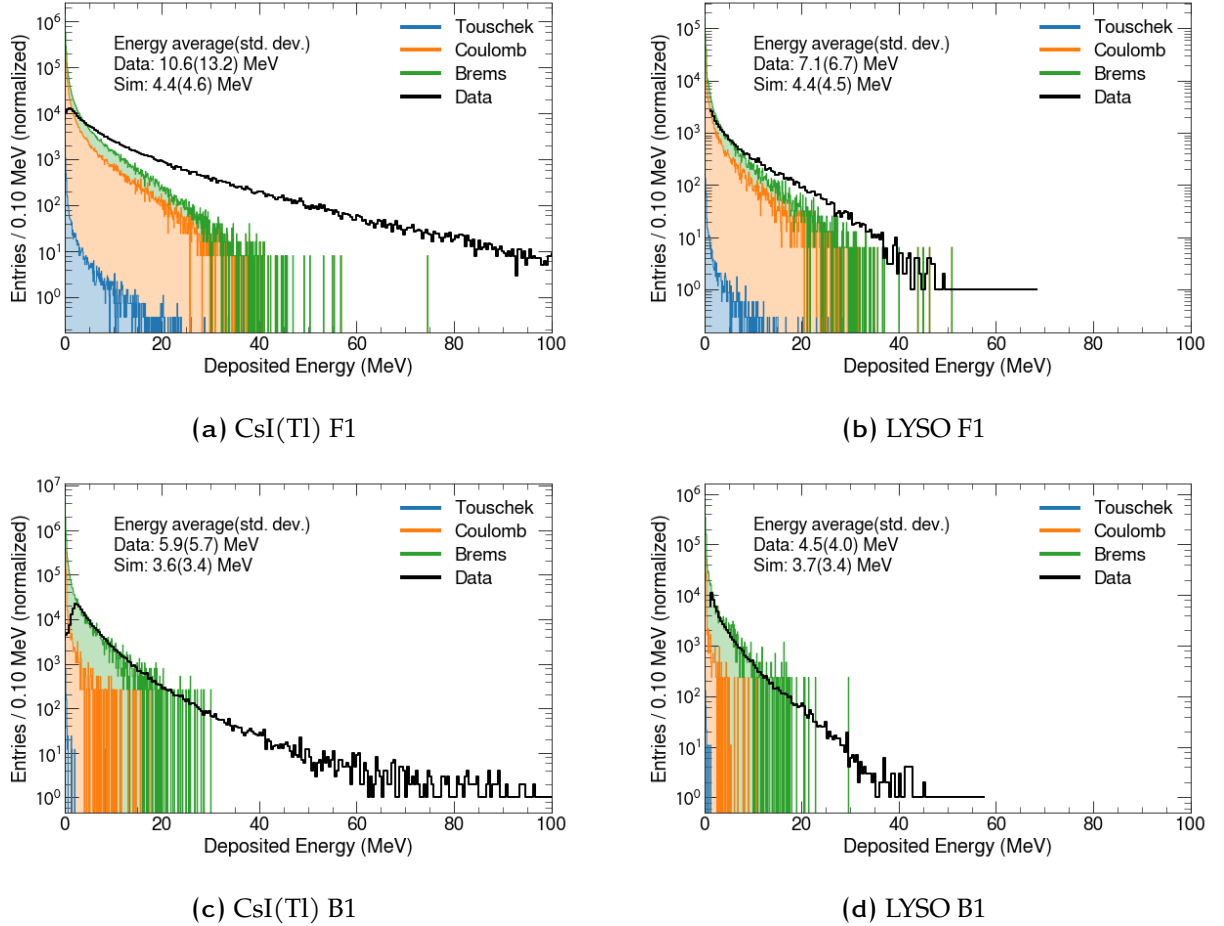


Figure 5.12: Representative spectra from a beam-gas enhanced HER run. These data were recorded on 2016-05-24 (run 6001), during the Beast II dedicated studies. The average pressure for the run is $P_{HER} = 1.5 \times 10^{-5}$ Pa (to be compared to the nominal value of 1.0×10^{-7} Pa). The average energy above 1 MeV is given for both data (“Data”) and the sum of simulated samples (“Sim”), with the standard deviation in parentheses.

The pressure bump experiment in the HER exhibits a much larger peak pressure, at around 150 times the nominal value. This run provides good parameters to test the beam-gas

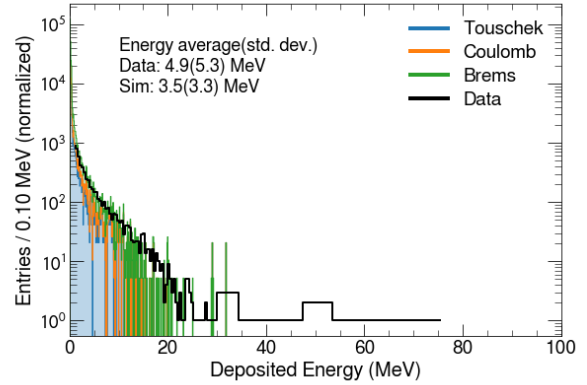
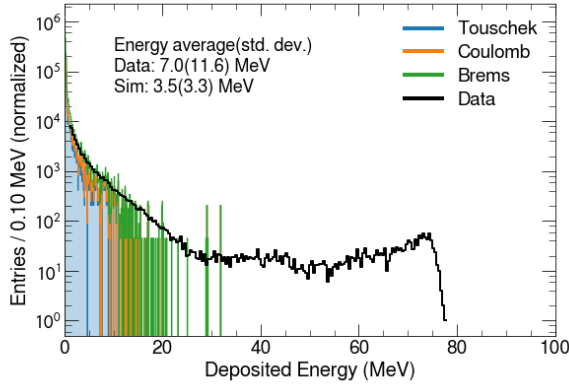
background model since the predicted Touschek contribution is insignificant. Except for panel 5.12a where the pile-up effects produce a notable discrepancy between measurements and simulation — again, this channel is downstream of the interaction region in HER runs — the measurements are in good agreement with simulation. This is a strong indication that the beam-gas background model provides the correct spectrum shape for these interactions during SuperKEKB commissioning.

Injection

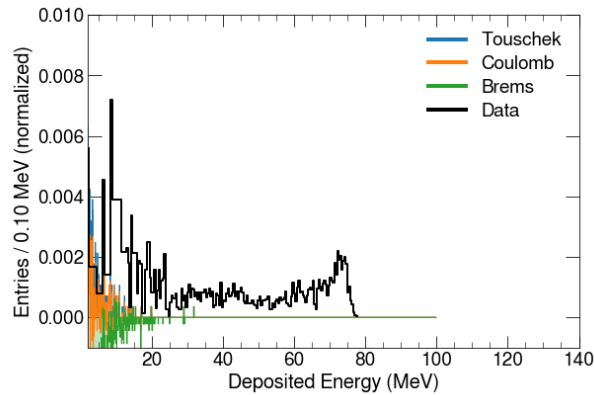
Injection periods are left out of all studies because the background associated with them was expected to depart strongly from the general model (Eq. 4.14). Figure 5.13 shows an example spectrum for typical injection conditions, as well as the difference with a spectrum recorded immediately after the injection period. The background model includes only the Touschek, Coulomb and Bremsstrahlung components, therefore the difference between the measurements and the coloured histograms corresponds to the contribution of the injection backgrounds, which are difficult to simulate.

Summary

Table 5.2 summarises the data presented in the previous subsections. The average energy above 1 MeV as well as standard deviations of each distributions are reported. The average energy is almost systematically greater in data than in simulation, and the effect is more pronounced in the CsI(Tl) channels because of the pile-up effects discussed above. There is no perceptible pattern in whether the excess in measured energy is greater in the forward or in the backward channels.



(a) Energy spectrum during an injection period (b) Nominal energy spectrum. Recorded 10 s after panel 5.13a.



(c) Difference between the injection and the nominal spectra.

Figure 5.13: Example spectra for typical injection conditions. These spectra were measured with the LYSO crystal at position F1 (see Figure 4.7). The coloured histogram indicate the background levels predicted by a Tauschek, Coulomb and Bremsstrahlung background model, neglecting any effect due to injection. The difference between the injection and the nominal spectra represents the measured contribution of the injection background to the overall beam-induced background. The average energy above 1 MeV is given for both data (“Data”) and the sum of simulated samples (“Sim”), with the standard deviation in parentheses.

Table 5.2: Summary of the crystals spectra: average energy and standard deviation above 1 MeV, where the standard deviation is the number in brackets. The number in square brackets in the first column cross-references the figure number where the data appear.

Run	Type	CsI(Tl)-F1	LYSO-F1	CsI(Tl)-B1	LYSO-B1	CsI(Tl)-B2	LYSO-B2
HER: Touschek scan at $\sigma_y = 120\mu\text{m}$ [5.9]	data	11.5(13.6)	7.2(6.5)	6.2(5.4)	-	9.3(8.0)	7.1(5.9)
	sim	4.3(4.4)	4.3(4.4)	3.6(3.4)	-	3.9(3.8)	3.7(3.6)
HER: Touschek scan at $\sigma_y = 50\mu\text{m}$ [5.10]	data	11.6(13.6)	-	6.2(6.0)	-	9.2(8.0)	6.9(5.8)
	sim	4.2(4.3)	-	3.6(3.4)	-	3.9(3.8)	3.7(3.6)
HER: Before ECE fixes [5.3]	data	11.7(14.4)	8.1(7.4)	6.6(7.3)	5.0(4.6)	9.5(8.6)	8.0(7.2)
	sim	4.3(4.4)	4.3(4.4)	3.6(3.4)	3.7(3.4)	3.9(3.8)	3.7(3.6)
HER: Nominal [5.5]	data	9.9(13.0)	6.6(5.8)	5.7(5.7)	4.4(3.8)	7.5(7.0)	-
	sim	4.2(4.3)	4.2(4.4)	3.6(3.4)	3.7(3.3)	3.9(3.8)	-
HER: Pressure bump [5.12]	data	10.6(13.2)	7.1(6.7)	5.9(5.7)	4.5(4.0)	7.9(7.1)	6.4(5.4)
	sim	4.4(4.6)	4.4(4.5)	3.6(3.4)	3.7(3.4)	3.9(3.8)	3.7(3.6)
LER: Before ECE fixes [5.4]	data	6.5(6.1)	4.7(4.0)	16.8(13.9)	3.4(1.7)	18.5(23.4)	4.3(2.9)
	sim	3.3(3.2)	3.4(3.2)	4.0(3.9)	4.0(3.9)	3.9(3.9)	4.0(4.1)
LER: Touschek scan at $\sigma_y = 54\mu\text{m}$ [5.8]	data	6.0(7.1)	4.8(4.7)	14.1(13.7)	5.0(3.5)	-	7.2(6.5)
	sim	3.4(3.3)	3.5(3.3)	3.9(3.8)	3.9(3.8)	-	4.0(4.0)
LER: Touschek scan at $\sigma_y = 74\mu\text{m}$ [5.7]	data	5.7(6.8)	4.7(4.5)	13.3(12.0)	5.8(4.4)	-	7.8(7.5)
	sim	3.4(3.2)	3.5(3.3)	3.9(3.8)	3.9(3.8)	-	4.0(4.0)
LER: Injection [5.13]	data	8.5(21.2)	7.0(11.6)	14.1(13.7)	6.3(6.0)	18.2(33.5)	11.4(12.8)
	sim	3.4(3.3)	3.5(3.3)	3.9(3.8)	3.9(3.8)	3.8(3.7)	4.0(4.0)
LER: Nominal [5.6]	data	5.8(6.6)	4.9(5.3)	13.6(11.9)	5.3(3.9)	15.3(21.3)	7.9(8.0)
	sim	3.4(3.3)	3.5(3.3)	3.9(3.8)	3.9(3.8)	3.8(3.8)	4.0(4.0)
LER: Pressure bump [5.11]	data	5.0(5.3)	4.4(3.5)	11.0(10.6)	2.8(1.4)	11.1(16.2)	4.6(5.1)
	sim	3.4(3.2)	3.5(3.3)	3.9(3.8)	3.9(3.8)	3.8(3.8)	4.0(4.0)

5.2 Beam-gas interactions and beam conditions evolution in Phase 1

We studied the beam-gas interactions in more detail using the residual gas model and measurements described in Section 4.2 in order to get an insight in how the gas mixture in the vacuum chamber affects the background measurements. The findings are reported in Section 5.2.1.

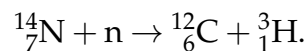
Section 5.2.4 presents and discusses the findings of multi-detector analyses aimed at describing the conditions evolution during Phase 1 based on beam-gas background. Finally, Section 5.2.5 presents the results of the beam-dust events studies aimed at determining if there's a well-defined time structure in those events.

Note: All results and conclusions presented in Section 5.2 have already been accepted for publication [1]. The material is original work produced by the author of this Dissertation, but has been reviewed by the Beast II working group as part of the collaborative publication process.

5.2.1 Effect of gas mixture on beam backgrounds

Sample results of residual gas analysis and effective atomic number

An off-line “dashboard-style” panel was assembled to present all aspects of the gas mixture measurements and the predicted impact on the beam-gas background. Figure 5.14 shows a screen capture of this panel. In the bottom plot, we see the relative abundances measured by the residual gas analyzer (RGA) compared with those obtained by using the gas model of Section 4.2. We see that the gases selected in this analysis can explain the observed abundances when they are combined in the optimal proportions. The only peak that is not accounted for is the one at $m/z = 3$. Such peak could be due to either ${}^3\text{He}^+$ or ${}^3\text{H}^+$ ions, both of which are quite exotic on the Earth's surface. However tritium is produced when a fast neutron interacts with nitrogen in the reaction



It also decays to ${}^3\text{He}$ so SuperKEKB, with its high level of neutron radiation, could provide an environment that is artificially rich in these species. On the other hand, after discussions

with SuperKEKB vacuum experts, we also believe that we cannot rule-out calibration issues of the RGA. This could mean that this peak would not correspond to any particular gas species. Since we have no way of testing either hypotheses, we decided to exclude the addition of tritium ions or other exotic molecules from the analysis.

The top-left plot in Figure 5.14 shows the best-fit gas concentrations to explain the measured RGA abundances. As expected, we see that the vacuum chamber gas is essentially di-hydrogen, water vapour and carbon monoxide, followed by light hydrocarbons. The relative proportion of these constituents is changing over the course of the pressure bump experiments, with the heavier fragments being liberated first in the chamber, then the di-hydrogen molecules. Such behaviour is seen in the two time series at the top-right of the figure. The effective atomic number is increasing even before the pressure starts increasing notably. This implies that the beam-gas background should also start rising before a pressure increase is measured.

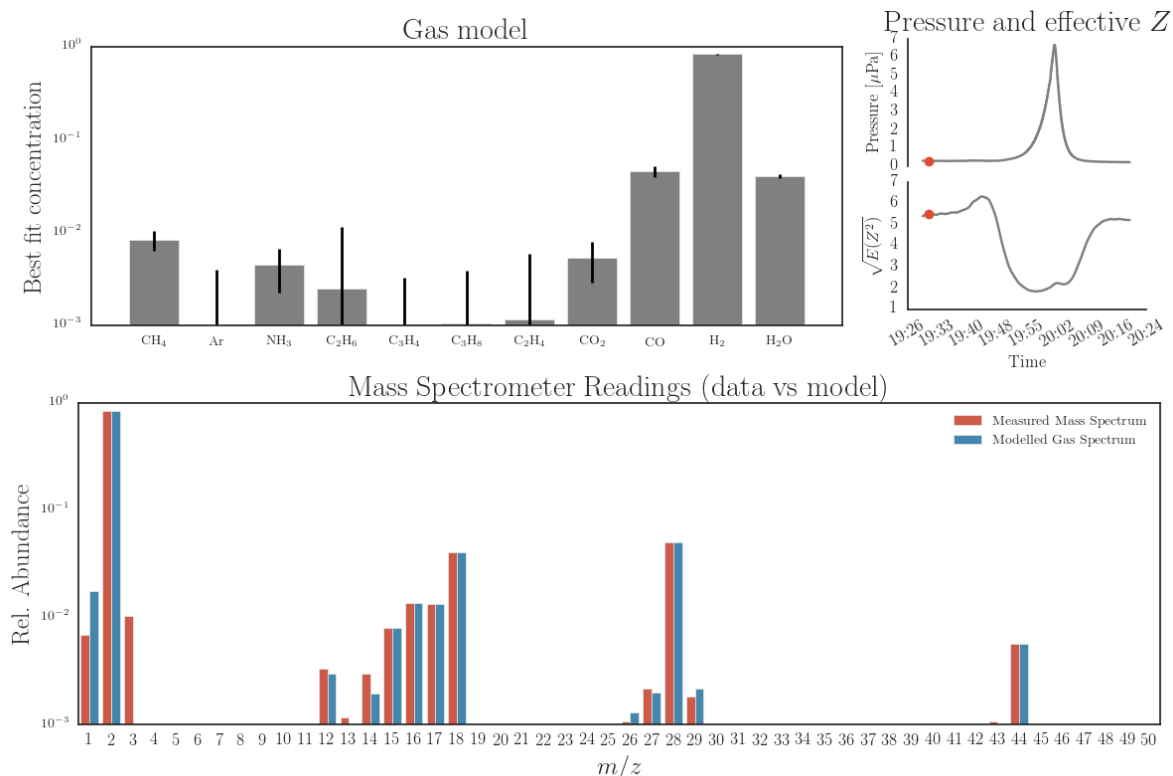


Figure 5.14: Gas contents off-line panel.

5.2.2 Time series of pressures, background and effective atomic number in pressure bump experiments

Figure 5.15 below shows example results obtained from the beam-gas constituents analysis and how it contributes to our understanding of the beam-gas interactions at SuperKEKB. The top panel shows the product of average pressure and beam current $P \cdot I$ with and

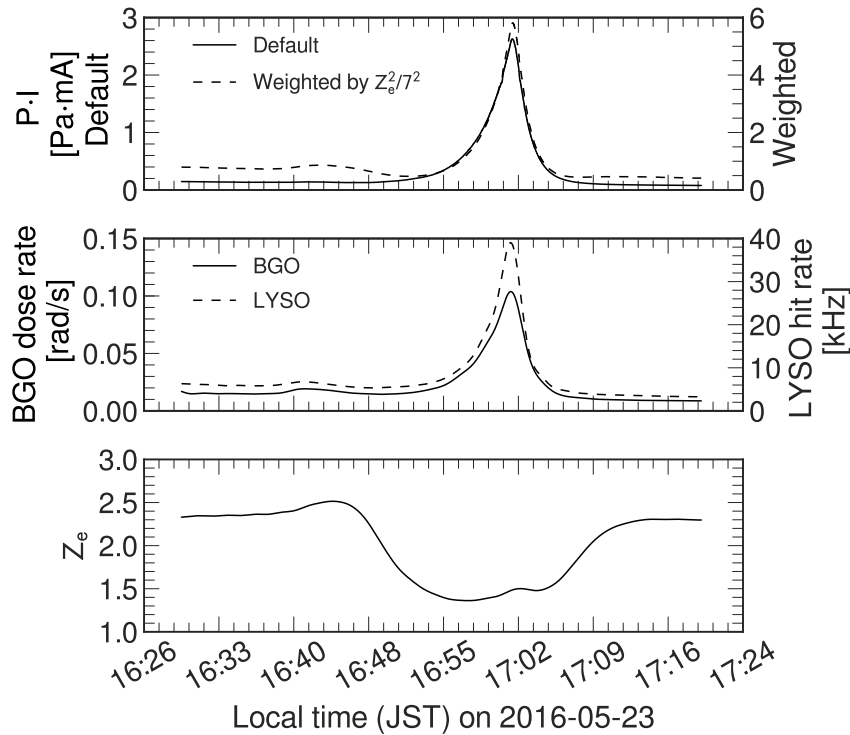


Figure 5.15: Time series of a pressure bump experiment and typical results.

without weighting with Z_e^2 as defined in Eq. 4.3. The central panel shows recorded background rates for one typical channel of two different subsystems, and the bottom panel shows the Z_e during the vacuum bump experiment.

Qualitatively, it is observed that the recorded background rates track the weighted $P \cdot I$ better than the default, un-weighted version. We see an increase of the hit rates around 16:42 which is not associated with any notable increase of the average pressure. The explanation is that heavier elements are released first. They don't contribute significantly to the pressure increase, yet the effective Z of the gas is larger then, and the Z^2 -dependence of beam-gas interactions produces a visible increase in the background rates.

5.2.3 Uncertainty on Z_e

The procedure used to calculate the uncertainty on Z_e is described in Section 4.2.4, and Figure 5.16 shows the results. In this section, the variable of interest is the square of Z_e since the beam-gas cross sections, hence the background rates, are proportional to Z_e^2 . On top of the relative magnitude of the confidence intervals, it is worth noting that the confidence intervals are not symmetrical around the nominal value.

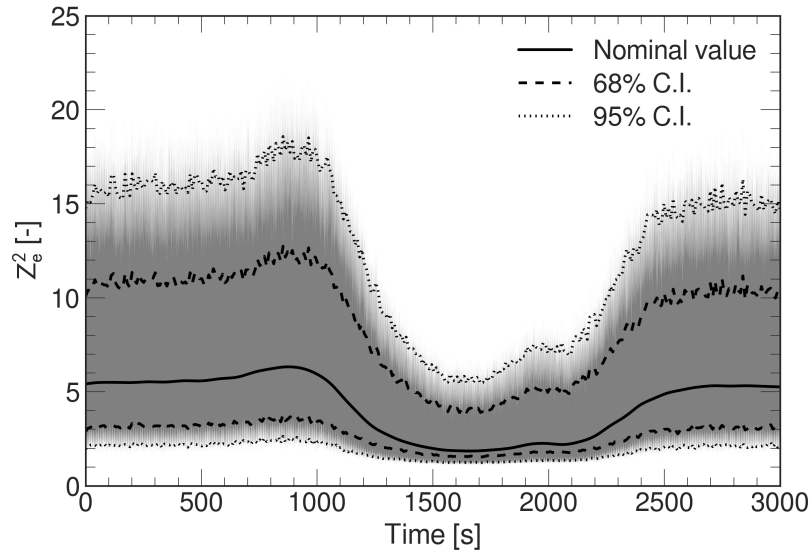


Figure 5.16: Confidence intervals around the Z_e^2 time series for the 2016-05-23 pressure bump experiment. The shaded area represents the 1000 different Monte Carlo pseudo-experiments overlaid with each other. Lines labeled 68% C.I. and 95% C.I. are the limits of confidence intervals around the nominal value.

This asymmetry arises from the non-linearities present in the Z_e calculations, and can be better observed by looking at a slice of the time series of Figure 5.16. Such a slice is presented in Figure 5.17, where we see the nominal Z_e^2 value at a specific time sample, as well as the PDF estimated by Monte Carlo methods. This PDF is asymmetric, therefore using it to produce confidence intervals for the nominal value will yield ranges that aren't symmetrically distributed around the nominal value. One way to summarize this study is to look at the confidence intervals as a function of Z_e^2 , as represented in Figure 5.18. This plot can be used to assess the uncertainty arising from Z_e^2 values when used to scale the simulation to experimental conditions.

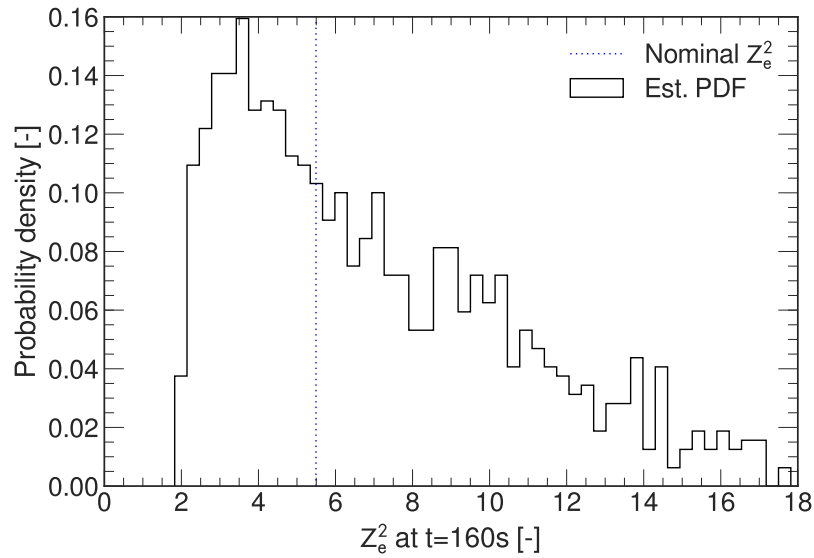


Figure 5.17: Example probability distribution of Z_e^2 . The distribution (Est. PDF) is estimated by Monte Carlo methods using 1000 independent pseudo-measurements with a 3 uncertainty on the RGA channels.

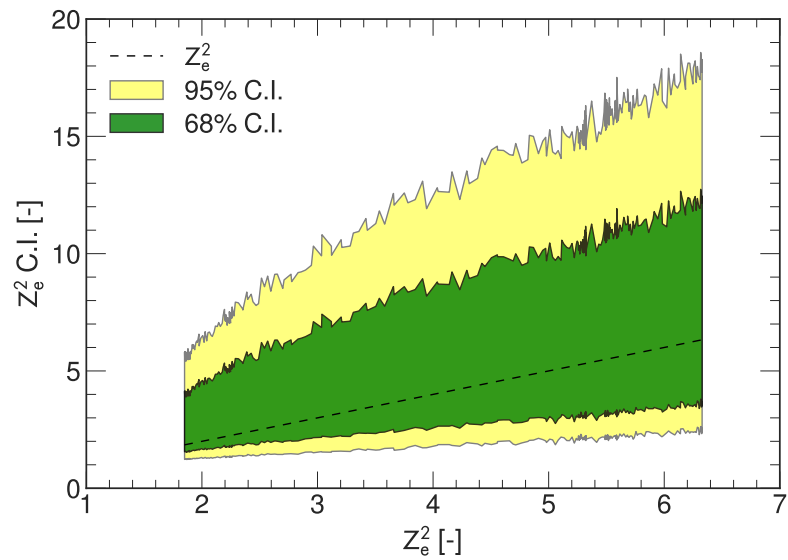


Figure 5.18: Confidence intervals around Z_e^2 as a function of Z_e^2 . The calculation was conducted using the 2016-05-23 pressure bump data.

5.2.4 Vacuum scrubbing and dynamic pressure

Measurement based on the dynamic pressure

Figure 5.19 shows the evolution of the base pressure, the equilibrium pressure with no beam currents, during Phase 1 operation. While the HER quickly reaches the equilibrium

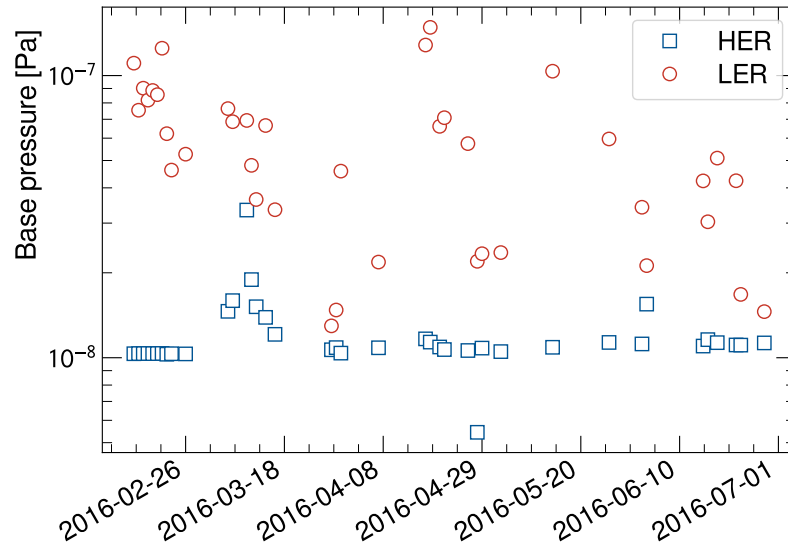


Figure 5.19: Base pressure measured as a function of date. Red circles represent LER measurements, while blue squares represent HER measurements. Reproduced from [1].

value of 10^{-8} Pa after it was turned on in March, the LER shows no appreciable asymptotic behaviour, with the minimum recorded pressure varying between 10^{-8} Pa and 10^{-7} Pa. Even if the daily variation is more dramatic than with the HER, the values remain well below the pressures observed during operation, which are on the order of 10^{-6} Pa or more during operation at full nominal current. Such variability in the base pressure should produce negligible effects on the dynamic pressure measurement.

Figure 5.20 shows a comparison of the two different estimates for dP/dI . Both the methods of Equations 4.22 and 4.23 are in good agreement, exhibiting a power-law behavior over more than 3 decades. This is the expected behavior when the base pressure is negligible compared to the dynamic component. The slopes between 100 A · h and 1000 A · h are $\eta_{\text{LER}} = -0.9$ for the LER and $\eta_{\text{HER}} = -0.6$ for the HER.

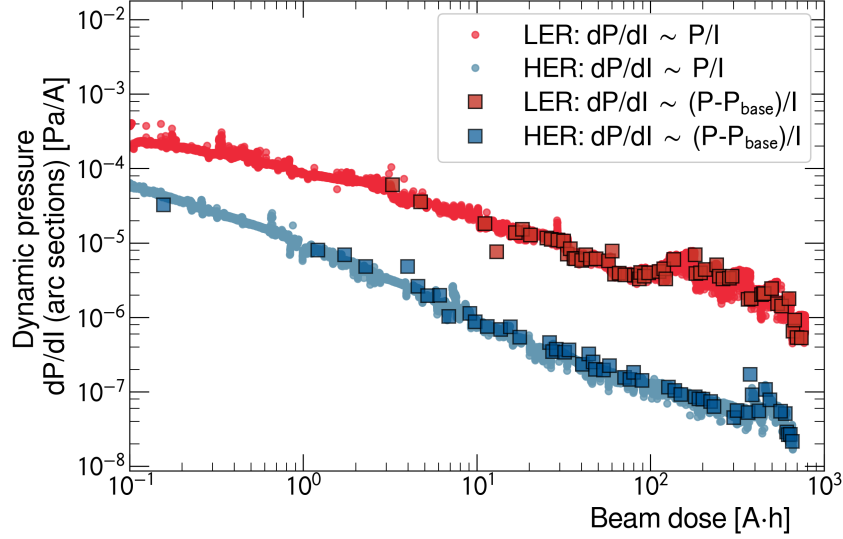


Figure 5.20: Comparison of two methods used to estimate the dynamic pressure. The circles are the SuperKEKB group results, obtained using equation (4.22) whereas the squares were obtained with Beast II data using equation (4.23). Blue points represent HER data and the red ones, LER data. Reproduced from [1].

Finally, the result in Figure 5.20 shows that, at the end of Phase 1, the HER dynamic pressure contribution is of comparable scale with the base pressure P_{base} for operating currents reaching $\mathcal{O}(1 \text{ A})$:

$$I \cdot \left. \frac{dP}{dI} \right|_{\text{HER}, 7 \times 10^2 \text{ A}\cdot\text{h}} \approx 2 \times 10^{-8} \text{ Pa} \sim P_{\text{base}}. \quad (5.1)$$

However, for the LER, the dynamic contribution at the end of Phase 1 dominates the base pressure by a factor of at least 10 at a 1 A beam current:

$$I \cdot \left. \frac{dP}{dI} \right|_{\text{LER}, 8 \times 10^2 \text{ A}\cdot\text{h}} \approx 6 \times 10^{-7} \text{ Pa} > 10 \cdot P_{\text{base}}. \quad (5.2)$$

Should dP/dI keep following the same power-law behaviour, the LER would have to be operated for more than $10^4 \text{ A}\cdot\text{h}$ in order for the dynamic pressure contribution at the design 3.6 A beam current to reach the same level as the base pressure.

Measurement based on Beast II detectors

Figures 5.21 and 5.22 show the scrubbing process as seen by the Beast II detectors for HER and LER scrubbing processes, respectively. As introduced in Equation 4.24, the ratio \mathcal{O}/I^2

is used as a proxy for Touschek-subtracted background, which is valid when the beam-gas contribution is dominating. This quantity is also analogous to the resorption rate η . The same general power-law dependence is observed across all detectors.

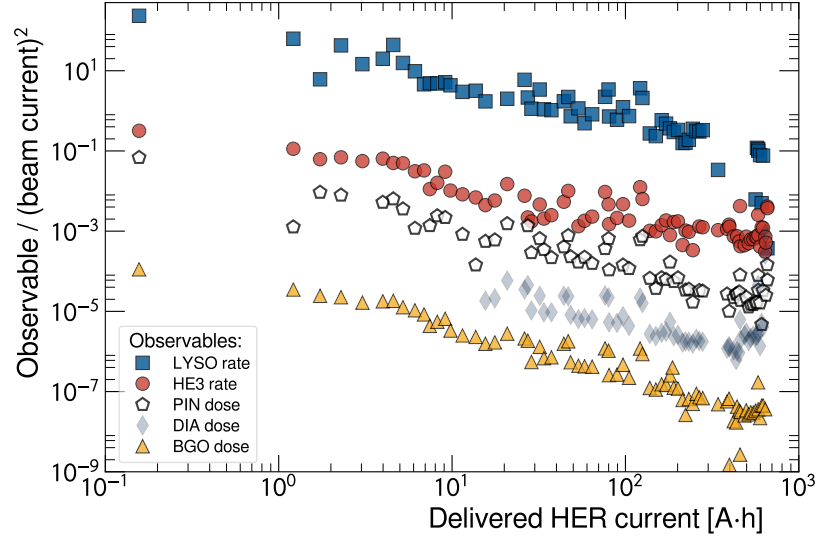


Figure 5.21: Measured Touschek-subtracted HER beam-induced background as a function of delivered current. Observable units are arbitrary: they have been adjusted to offset each data series for more clarity. Reproduced from [1].

For the HER scrubbing shown in Figure 5.21, LYSO, ^3He , PIN diodes and BGO are all in good agreement with the power-law model across four decades. However, the numerical values of the slopes are not compatible with the dP/dI value. They are also inconsistent with each other except for the LYSO and PIN diode sub-detectors, at -1.09 ± 0.08 and -0.98 ± 0.05 , respectively.

For the LER scrubbing shown in Figure 5.22, LYSO, ^3He , PIN diodes and BGO are all in agreement with the power-law model across one and a half decade. Quantitatively, the discrepancy between the slopes is however more pronounced than with the HER case.

In both figures 5.21 and 5.22, there is plateauing or increase of the rates beyond 400 A·h observed with all subdetectors. A possible explanation is related to conditioning of the non-evaporable getters (NEG) that happened during that period. Such conditioning is known to release heavier elements in the vacuum chamber, which produces considerably more background due to the Z^2 dependence.

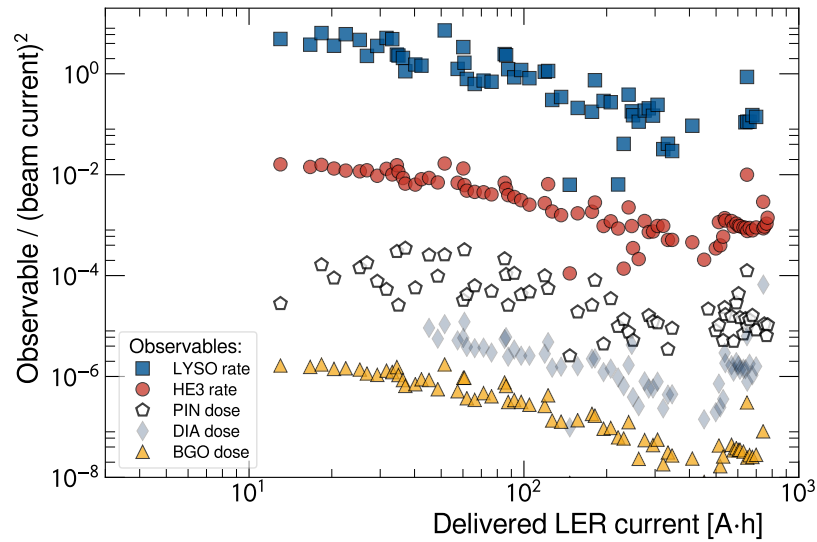


Figure 5.22: Measured Touschek-subtracted LER beam-induced background as a function of delivered current. Observable units are arbitrary: they have been adjusted to offset each data series for more clarity. Reproduced from [1].

Otherwise, the most significant improvement to the accelerator during this period is the addition of permanent magnets to the uncoated aluminium bellows meant to reduce electron multipacting at large currents. Measurements of the beam size by the SuperKEKB group showed that this effectively reduced the electron-cloud effect without changing beam orbit and optics [50].

5.2.5 Transient “beam-dust” events

This section presents the results of studies on transient events described in Section 4.6.2.

Observation in Beast II

Figure 5.23 shows examples of beam-dust events together with the results of the peak-finding algorithm described in Section 4.6.2. The algorithm functions as expected by selecting large-amplitude signal peaks while rejecting fluctuations that can be attributed to noise on some channels. A total of 598 beam-dust events were identified using this algorithm between 2016-04-05 and 2016-06-28.

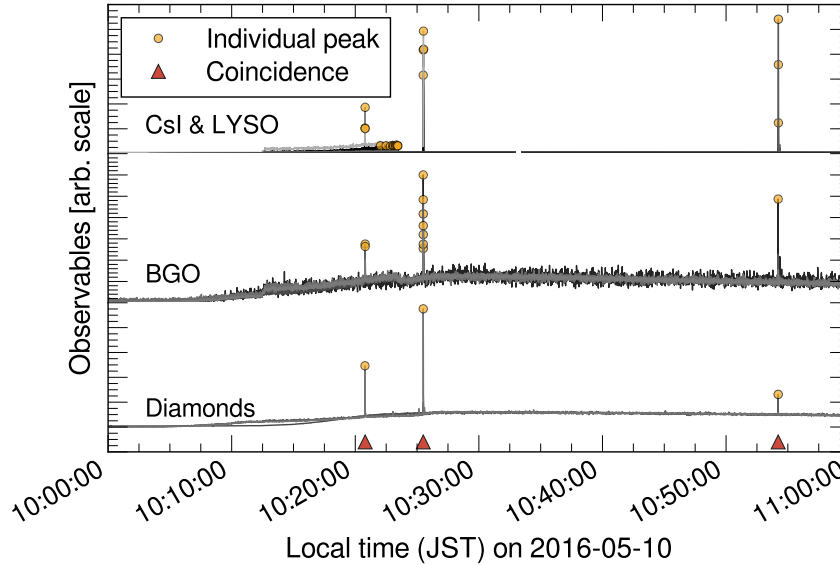


Figure 5.23: Example of beam-dust events and peak identification. All channels for the given sub-detectors are superimposed in different shades of gray. Circles indicate peaks found on individual channels, and triangles represent peaks selected based on the multi-channel, multi-detector coincidence requirement.

Comparison with the SuperKEKB list

Figure 5.24 shows a comparison of the time structure of vacuum burst events measured by SuperKEKB compared to the beam-dust events measured in Beast II. From this figure we see that there is no obvious steady reduction in the 48-hour rate of these events as scrubbing progresses, and more operation time would be needed to provide a statement on this aspect.

The second question to address is whether or not the pressure bursts correlate with the Beast II observations of the so-called beam-dust events. The answer is best expressed by displaying the data of Figure 5.25 as a cloud of points of the 48-hour rate seen by SuperKEKB pressure gauges against the rate observed by Beast II, and then calculating the Pearson product-moment correlation coefficient between the two sets. The result is shown in Figure 5.25. The coefficient of correlation is $r_{\text{beam-dust}} = 0.54$, which indicates a weak correlation. The relative weakness of this correlation is not fully understood.

Looking at the cross-correlation between the two lists, shown in Figure 5.26, gives us a different angle on the situation. The maximum correlation is obtained at lag = 0, and

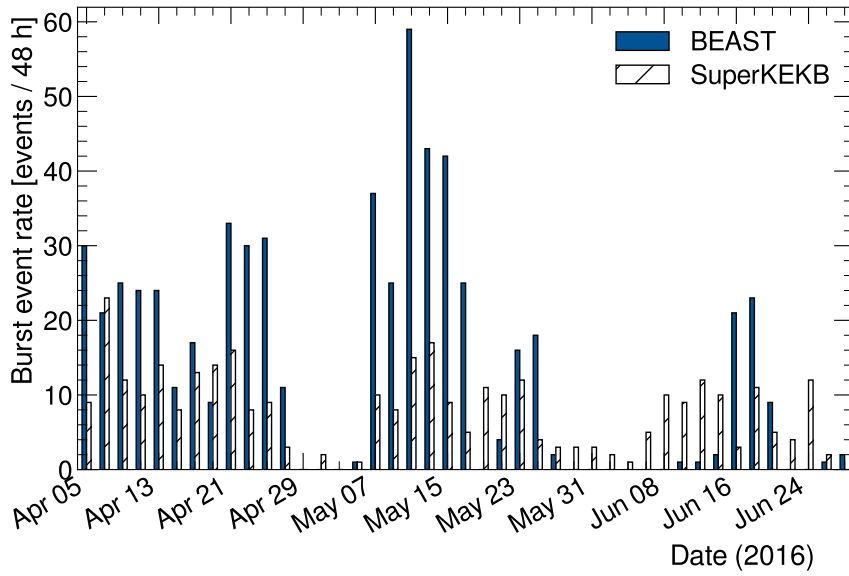


Figure 5.24: Comparison of the time structure of beam-dust events between SuperKEKB and Beast II for Phase 1 data. Reproduced from [1].

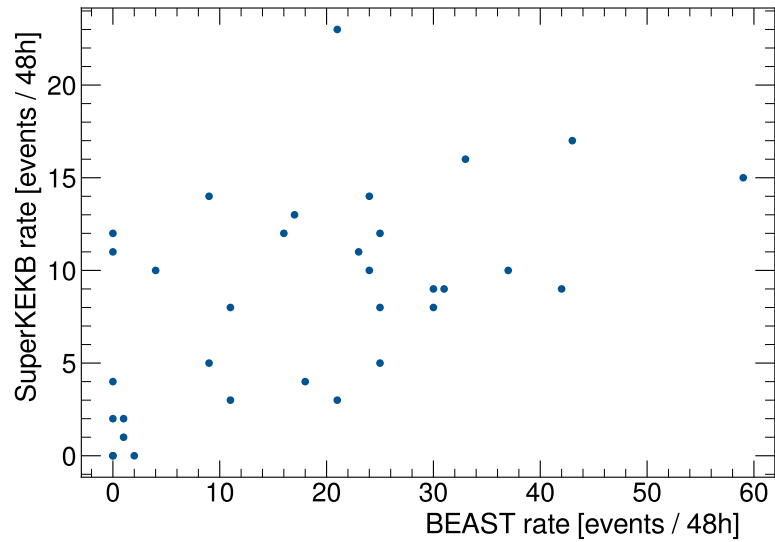


Figure 5.25: Scatter-plot of the beam-dust events 48-hour rate of from the SuperKEKB and Beast II lists. Reproduced from [1].

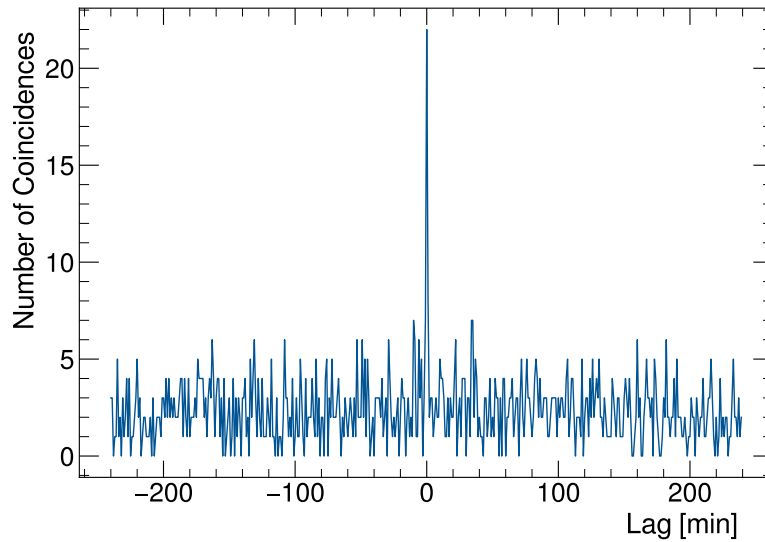


Figure 5.26: Cross-correlation between the beam-dust events from SuperKEKB and Beast II datasets. From [1].

therefore the relative weakness of the correlation of the scatter plot in Figure 5.25 cannot be attributed to some misalignment of the data coming from different sources.

Also of particular interest in Figure 5.26 is the relative height of the peak with respect to the side bands. There are 22 coincidence events in the joint data taking period, whereas the random coincidence level, given by the side bands, is 2.3 ± 1.5 . In other words, while 22 coincidences between Beast II and SuperKEKB is a very low fraction of the total burst events — 6.5% of the SuperKEKB list or 3.7% of the Beast II list — it is still significantly larger than what one would expect if they were uncorrelated.

Including pressure times series together with background rates from Beast II detectors suggests another hypothesis to explain this effect. An example of such plot is represented in Figure 5.27.

This result suggests that the effects of beam-dust events are very localized. The LER pressure burst seen around $t = 04:15$ is only observed in the BGO detectors, thus not recognized as a Beast II vacuum burst event. The converse is also true: the clear Beast II events found at $t = 06:15$ and $t = 08:45$ do not necessarily show a pressure increase in the nearby detectors. This locality would also explain why such events do not always result in beam aborts from beam loss monitors.

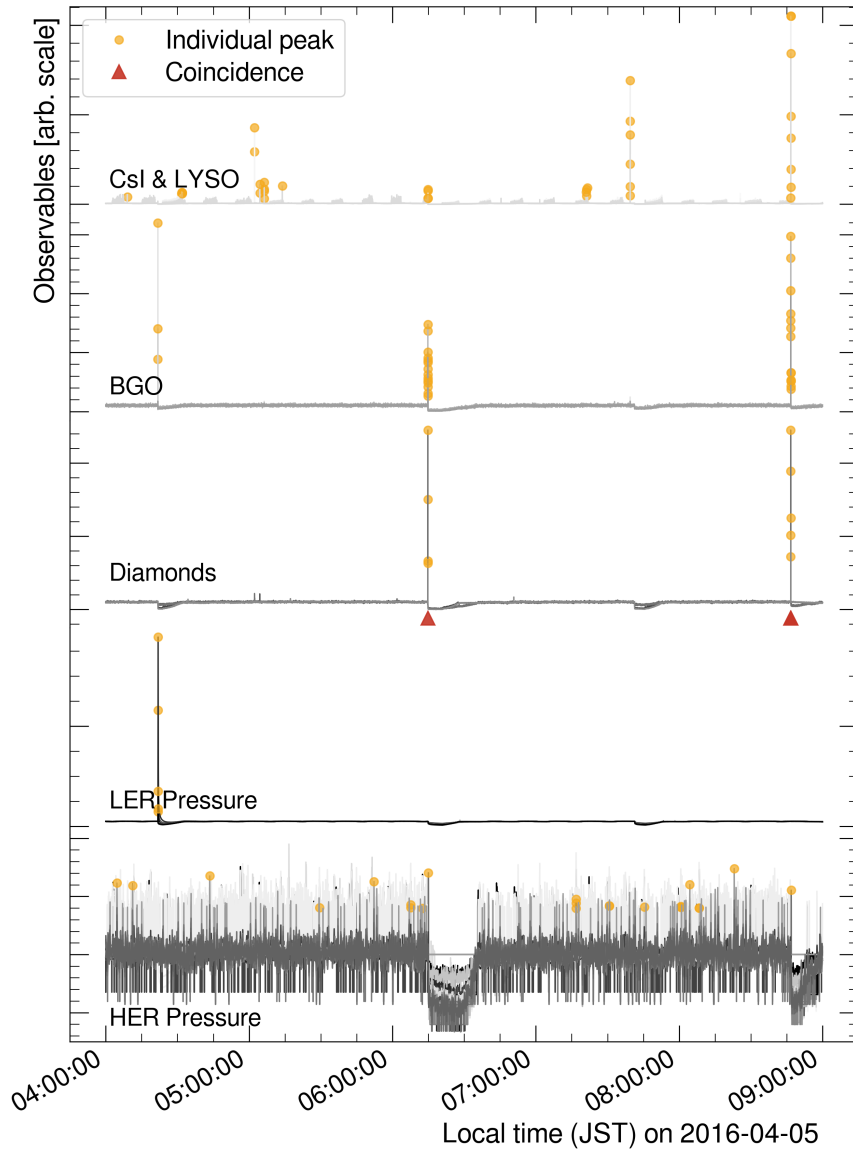


Figure 5.27: Example of beam dust events and corresponding pressure readings. All channels for the given sub-detectors are superimposed in different shades of gray. Circles indicate peaks found on individual channels, and triangles represent peaks selected based on the multi-channel, multi-detector coincidence requirement. A coincidence is defined as a peak seen at least four channels, which are in at least two different sub-detector systems. The vacuum chamber pressures are reported for reference only, and do not count in the coincidences.

Dependence of position on detection

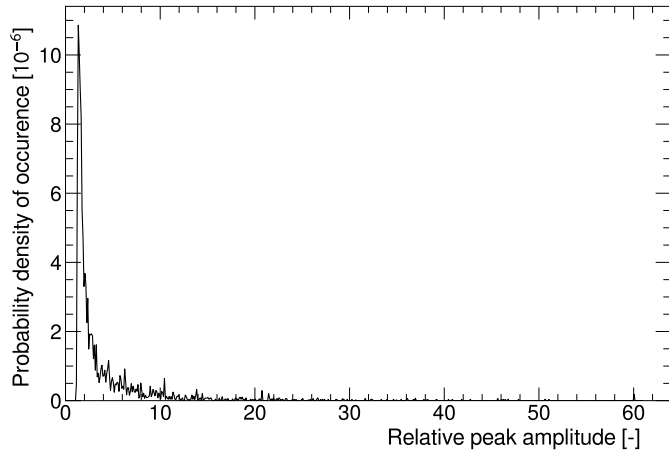
Our measurements also enable us to provide a statement on how the probability of detection a vacuum burst event with the Beast II detectors depends on the location of said burst event. The results are reported in Table 5.3. Only those transients occurring in the SuperKEKB sections close to Beast II, D01 and D02, were observed at a statistically significant rate.

Table 5.3: Number of vacuum bursts observed by Beast II detectors for each SuperKEKB section. N_{obs} is the number of events observed in coincidence by both Beast II and SuperKEKB detectors, N_{bkg} is the expected number of random coincidences, and p is the probability of the N_{bkg} fluctuating as high N_{obs} or more.

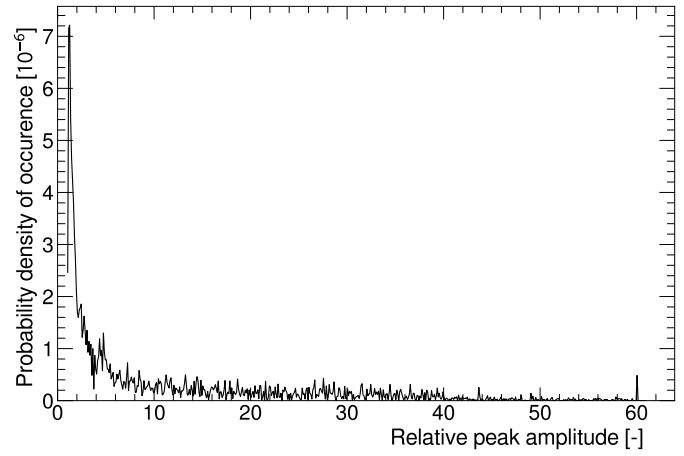
Section	LER			HER		
	N_{obs}	N_{bkg}	p	N_{obs}	N_{bkg}	p
D01	0	0.9	6.0×10^{-1}	13	1.2	5.3×10^{-11}
D02	9	1.1	3.3×10^{-7}	7	0.6	1.5×10^{-7}
D03	1	0.8	1.8×10^{-1}	1	0.2	1.4×10^{-2}
D04	2	1.6	2.0×10^{-1}	0	0.2	1.9×10^{-1}
D05	4	1.9	4.1×10^{-2}	7	2.1	1.6×10^{-3}
D06	3	1.2	3.5×10^{-2}	0	0.0	3.1×10^{-2}
D07	1	0.6	1.4×10^{-1}	0	0.2	1.9×10^{-1}
D08	2	0.2	1.7×10^{-3}	3	0.9	1.3×10^{-2}
D09	0	0.3	2.9×10^{-1}	0	0.1	7.6×10^{-2}
D10	0	2.1	8.8×10^{-1}	0	0.1	5.3×10^{-2}
D11	1	1.3	3.9×10^{-1}	0	0.0	1.5×10^{-2}
D12	0	0.3	2.7×10^{-1}	0	0.1	1.1×10^{-1}

Relative dose of the beam-dust events

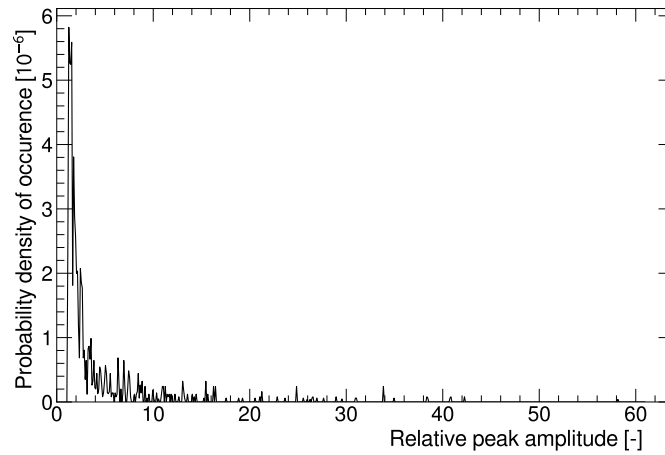
Figure 5.28 shows the probability distributions of the peak height amplitude of the beam dust events, relative to the average signal recorded in the previous 60 seconds, for three different sub-detectors. The relative dose delivered by these beam-dust events is obtained by multiplying this signal amplitude by the probability of occurrence of a deposit of such amplitude. For the crystals calorimeters (Figure 5.28b), these events represent 0.2% of the total dose. It corresponds to 0.05% and 0.03% of the total dose for the BGO (Figure 5.28a) and diamonds (Figure 5.28c) detectors, respectively.



(a) Detected by the BGO sub-detector. $P_{1s} = 0.012\%$.



(b) Detected by the crystals calorimeter sub-detector. $P_{1s} = 0.015\%$.



(c) Detected by the diamonds sub-detector. $P_{1s} = 0.007\%$.

Figure 5.28: Probability distributions of the beam-dust events amplitude. The peak amplitude on the x -axis is normalized by the background level, which is estimated by the average signal in the previous 60 seconds. P_{1s} indicates the total probability of observing one beam-dust event in a 1-second sample.

5.3 Quantitative comparison of data and simulation

Figure 5.29 presents examples of background measurements and corresponding simulation for LYSO hit rates, in the crystals that are located above the beam lines.

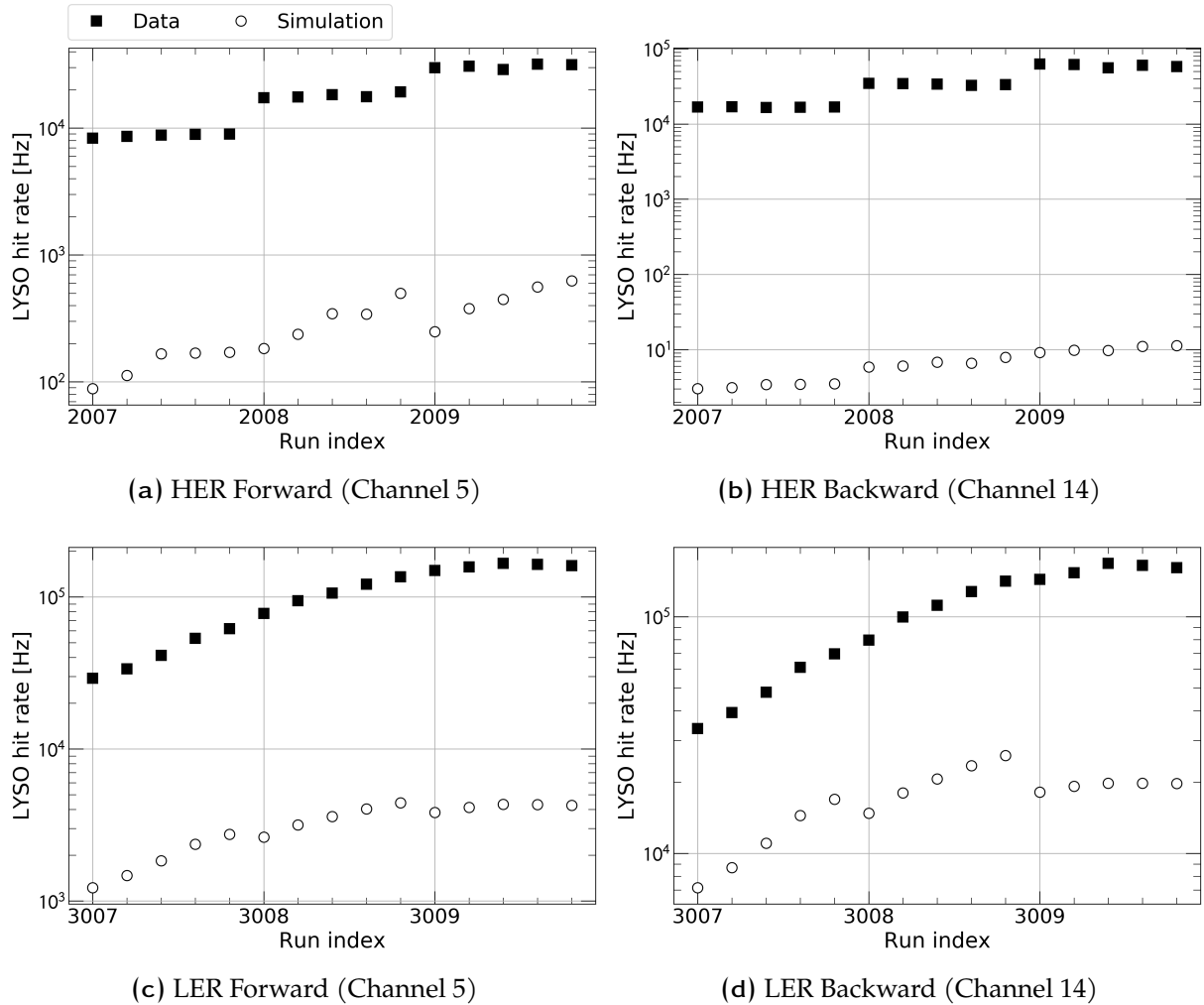


Figure 5.29: Examples of observed (“Data”) and simulated (“Simulation”) background rates in the Beast II dedicated runs. Refer to Tables 4.1 and 4.2 for the accelerator conditions corresponding to each run and sub-run. The simulated samples correspond to the sum of Touschek, Coulomb and Bremsstrahlung processes, scaled to the experimental conditions. The results are presented for the LYSO hit rate measurements for the channels located above the beam line.

It is noteworthy that the HER simulation, in panels 5.29a and 5.29b, is considerably smaller than the actual measurements. However, the measured HER backgrounds were three to

six times smaller than the corresponding levels measured in LER runs. A notable underestimation of the HER backgrounds is observed in all channels, as seen in Figure 5.30 which presents the results of the comparison between data simulation using the methodology described in Section 4.5.

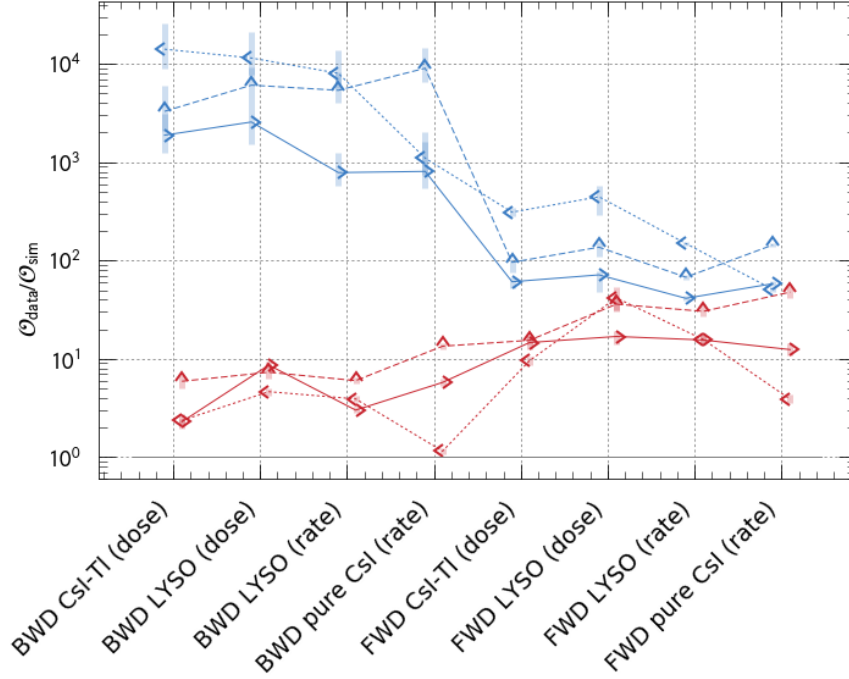


Figure 5.30: Data to simulation ratio for the crystals detectors using $\alpha_p = 3.0 \pm 1.5$ for both LER and HER data. The shaded bands correspond to the combined uncertainties. Red represents LER data, and blue represents HER data. Markers indicate the position of the detector channel with respect to the beam line: up, right (outside), left (inside). Lines connect channels at the same position to guide the reader.

The ratio measured for LER runs is systematically larger in the forward channels than it is in the backward channels. This difference is significant with $p = 0.000641$ ¹. Similarly, the ratio in the HER channels is larger in the backward channels ($p = 0.000511$). Although the precise reasons for this behaviour are unknown, the discrepancy between data and simulation is therefore systematically and significantly more important upstream of the beam crossing than it is downstream of it.

¹Based on a t -test for the means of two independent samples of scores implemented by the `scipy.stats.ttest_ind` function [93].

Table 5.4: Summary of the HER data/simulation results for the backward channels. All numbers are dimensionless since they either represent a ratio between data and simulation or the uncertainty on such ratio. The key for the location symbols is the following: \leftarrow means those channels on the inside of the ring, \uparrow means directly above the beam lines, and \rightarrow means on the outside of the beams.

Location	BWD CsI-Tl (dose)			BWD LYSO (dose)			BWD LYSO (rate)		
	\leftarrow	\uparrow	\rightarrow	\leftarrow	\uparrow	\rightarrow	\leftarrow	\uparrow	\rightarrow
Data/sim. ratio	14102	3290	1882	11473	6076	2562	8020	5384	783
Uncertainties									
Statistical	67.7	9.8	11.8	96.3	47.8	32.2	3.4	3.4	0.4
Beam current	+113 -114	14.3	+21.7 -22.2	+51.0 -51.1	19.2	+38.0 -38.9	31.0	17.2	5.5
Beam size	+48.8 -45.7	+11.8 -11.1	+14.3 -13.4	+42.3 -39.6	+78.0 -74.4	+17.4 -16.4	+50.4 -47.5	+64.5 -61.4	+7.4 -7.0
α_P factor	+4409 -11780	+1026 -2731	+538 -1264	+3571 -9481	+1507 -3043	+746 -1794	+2362 -5781	+1370 -2836	+214 -475
E threshold	30.3	8.9	11.7	438	385	347	N/A ^a	N/A ^a	N/A ^a
DAQ livetime	+1103 -362	+376 -70	+306 -14	+367 -298	+62 -177	+594 -2	$_b$	$_b$	$_b$
E calibration	2336	466	131	597	682	127	$_b$	$_b$	$_b$

^a The intermediate results required to evaluate this uncertainty contribution are not available.

^b This contribution does not affect results obtained with the scaler.

A break down of the results in Figure 5.30 and the uncertainty components specific to each channel into four different populations is displayed in Tables 5.4 to 5.7 below. All pure CsI channels are discarded from further analysis because of the calibration issues with these channels mentioned at the beginning of this chapter.

In Tables 5.4 to 5.7, the statistical uncertainties are calculated as the standard error on the mean from averaging all sub-runs together in a detector-specific channel. As noted in the tables, the systematic uncertainty related to the energy threshold for the LYSO scaler channels is not available. The effect of that threshold was not assessed experimentally in a systematic fashion, and the Beast II simulated sample do not contain individual hit information, preventing us from estimating systematic uncertainty due to the energy threshold using Monte Carlo. Given these limitations, we can only assume that the threshold effect will be small compared to other contributions such as the systematic uncertainty associated with the α_P factor.

Tables 5.4 to 5.7 show some geometric dependence in the data/simulation ratios: in the HER, the ratios are systematically larger inside the ring than outside of it, with the ratios

Table 5.5: Summary of the HER data/simulation results for the forward channels. See Table 5.4 for the symbol key.

	FWD CsI-Tl (dose)			FWD LYSO (dose)			FWD LYSO (rate)		
Location	←	↑	→	←	↑	→	←	↑	→
Data/sim. ratio	310.0	95.8	60.8	444.9	136.5	71.4	148.8	67.6	41.2
Uncertainties									
Statistical	2.0	0.6	0.3	6.0	1.0	0.5	0.2	0.1	0.1
Beam current	0.1	< 0.1	< 0.1	0.2	< 0.1	< 0.1	< 0.1	< 0.1	< 0.1
Beam size	10.7	3.4	2.0	15.3	4.7	2.4	5.1	2.4	1.4
α_P factor	+11.1 -12.1	+2.7 -2.8	+2.9 -3.2	+16.3 -17.7	+4.3 -4.6	+3.2 -3.5	+5.5 -6.1	+2.1 -2.3	+1.7 -1.8
E threshold	0.6	0.1	0.3	8.0	9.5	2.7	N/A ^a	N/A ^a	N/A ^a
DAQ livetime	+10.2 -6.7	+19.1 -1.8	+5.4 -1.5	+87.0 -4.5	+19.4 -2.5	+22.3 -1.3	_{-b}	_{-b}	_{-b}
E calibration	24.6	4.9	6.1	122	11.6	3.6	_{-b}	_{-b}	_{-b}

^a The intermediate results required to evaluate this uncertainty contribution are not available.

^b This contribution does not affect results obtained with the scaler.

Table 5.6: Summary of the LER data/simulation results for the backward channels. See Table 5.4 for the symbol key.

	BWD CsI-Tl (dose)			BWD LYSO (dose)			BWD LYSO (rate)		
Location	←	↑	→	←	↑	→	←	↑	→
Data/sim. ratio	2.4	5.9	2.3	4.6	7.3	8.6	3.9	6.0	3.0
Uncertainties									
Statistical	< 0.1	0.1	< 0.1	< 0.1	0.1	0.1	< 0.1	< 0.1	< 0.1
Beam current	< 0.1	< 0.1	< 0.1	< 0.1	< 0.1	< 0.1	< 0.1	< 0.1	< 0.1
Beam size	< 0.1	0.1	< 0.1	0.1	0.1	0.1	< 0.1	0.1	< 0.1
α_P factor	0.1	0.2	0.1	0.2	0.4	0.2	0.3	0.4	0.2
E threshold	< 0.1	< 0.1	< 0.1	0.2	0.4	0.3	N/A ^a	N/A ^a	N/A ^a
DAQ livetime	< 0.1	0.1	< 0.1	0.1	0.2	0.2	_{-b}	_{-b}	_{-b}
E calibration	0.4	0.8	0.2	0.2	0.8	0.4	_{-b}	_{-b}	_{-b}

^a The intermediate results required to evaluate this uncertainty contribution are not available.

^b This contribution does not affect results obtained with the scaler.

Table 5.7: Summary of the LER data/simulation results for the forward channels. See Table 5.4 for the symbol key.

Location	FWD CsI-Tl (dose)			FWD LYSO (dose)			FWD LYSO (rate)		
	←	↑	→	←	↑	→	←	↑	→
Data/sim. ratio	9.6	15.4	14.6	41.7	35.9	16.9	15.7	30.4	15.5
Uncertainties									
Statistical	0.1	0.1	0.1	0.4	0.3	0.1	< 0.1	< 0.1	< 0.1
Beam current	< 0.1	< 0.1	< 0.1	< 0.1	< 0.1	< 0.1	< 0.1	< 0.1	< 0.1
Beam size	0.1	0.2	0.2	0.5	0.4	0.2	0.2	0.3	0.2
α_p factor	0.4	+1.3 -1.8	+1.4 -1.9	+1.8 -1.9	+3.2 -4.3	+1.5 -2.0	+1.4 -1.8	+3.6 -5.2	+1.7 -2.4
E threshold	< 0.1	< 0.1	0.1	1.0	2.1	1.3	N/A ^a	N/A ^a	N/A ^a
DAQ livetime	+0.0 -0.2	+0.2 -0.4	+0.0 -0.4	+0.5 -1.2	+0.2 -1.0	+1.8 -0.4	- ^b	- ^b	- ^b
E calibration	0.8	0.8	1.5	11.5	3.1	0.9	- ^b	- ^b	- ^b

^a The intermediate results required to evaluate this uncertainty contribution are not available.

^b This contribution does not affect results obtained with the scaler.

from the detectors placed above the beam line in between. The connecting lines seen in Figure 5.30 highlight this behaviour. While we can only speculate on the cause of this observation, this dependence is less obvious for the LER runs so presumably it is linked to a difference in the driving background mechanism. There may be other, unaccounted, sources of background in the HER that exhibit large angular dependence.

Instrumental effects such as energy calibration and DAQ livetime are the most important uncertainty contributions in all but the HER backward measurements (Table 5.4) where the uncertainty on α_p dominates. This was apprehended by some members of our team before the experiment, and motivated the use of a scaler to measure hit rates as a proxy for dose rate that is faster and less dependent on the calibration of each channel.

The importance of the α_p contribution for the measurements in the HER backward channels indicates that the beam-gas mechanisms drive the overall machine-induced background. This is consistent with expectations that Touschek losses are less significant in HER runs because of the inverse dependence in energy (see Eq. 2.2). Furthermore, the α_p uncertainty contribution is greater in the HER backward channels than in those on the forward side. The opposite is true in the LER: the relative contribution of α_p to the total uncertainty is larger in the forward channels than in the backward ones. This suggests that the uncertainty on the beam-gas contribution has more impact on the total uncertainty at

locations before the beam crossing than it has after.

Example of graphical uncertainty budgets for the LYSO dose and rate measurements are reported in Figure 5.31 to provide a visual indication of the relative scales of the uncertainty contributions.

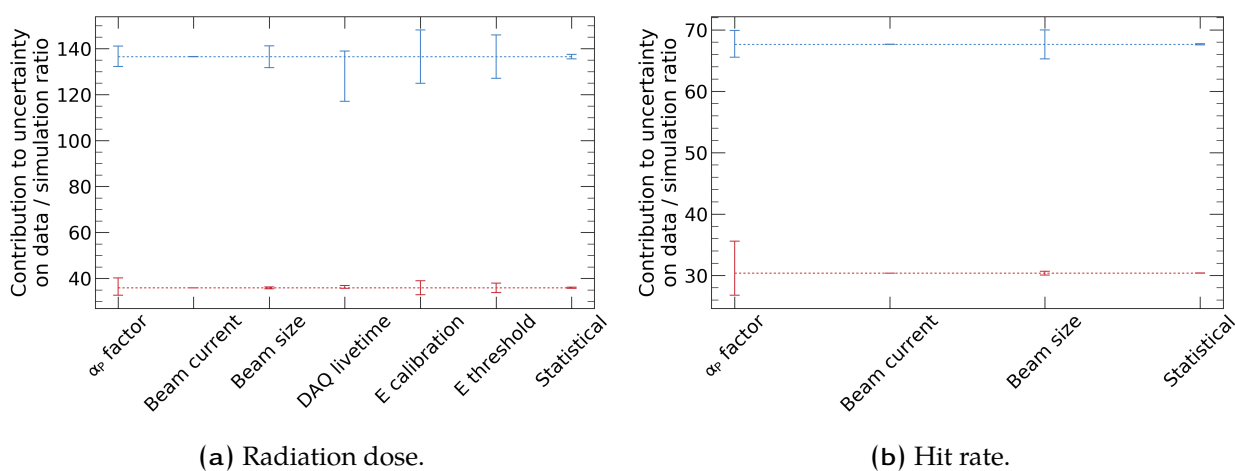


Figure 5.31: Uncertainty budget examples: LYSO crystal in position F2. The dashed lines correspond to the nominal central value and error bars represent the individual uncertainties propagated onto the final result. The blue markers represent the HER data while the red points represent the LER data.

Data from Tables 5.4 to 5.7 are combined into four different data/simulation factors — HER and LER, for either side of the beam crossing — in order to provide statements on expected background levels in future phases of Belle II. The median was chosen as the measure of central tendency and the quartile deviation as a measure of the dispersion. These quantities were preferred over the mean and standard deviation because ratios in the same sample are not necessarily compatible with each other. Yet, scaling simulation with meaningful values for each detector side and beam combination requires some representative values for the expected scales and the associated spread. Table 5.8 summarises the data/simulation study results with the crystals in Phase 1 that will be used to scale the simulation for future phases.

Table 5.8: Summary of the data/simulation results with the crystals in Phase 1. The values are given as median \pm quartile deviation.

	Data/Simulation ratio
HER Backward	5384 ± 3762
HER Forward	95.8 ± 66.8
LER Backward	4.6 ± 2.0
LER Forward	15.7 ± 9.1

5.4 Extrapolation to commissioning phases 2 and 3

We use the results in Table 5.8 in conjunction with the ECL background simulations to extrapolate the background levels to future phases of Belle II.

Such a study will allow a rapid verification once the instantaneous dose rate measurements are available from the detector. In particular, two different background scaling hypotheses are tested:

1. Scale the luminosity backgrounds by the actual luminosity; and scale the machine backgrounds by the data/simulation ratios observed in the LER in Phase 1, using separate scales for the forward and the backward end-caps. Underlining these rules are the following assumptions:
 - (a) the luminosity backgrounds are known perfectly, and the discrepancy between data and simulation observed in Phase 1 does not apply, and
 - (b) the large discrepancy between data and simulation observed in HER Phase 1 stems mostly from poor knowledge of the vacuum conditions. Therefore, only the LER results are valid since they were provided by a better controlled experiment.

2. Scale the luminosity backgrounds by the data/simulation ratios obtained for the LER in Phase 1; and scale the machine backgrounds by the respective LER and HER ratios found in Phase 1. Both the luminosity backgrounds would use separate scales for the forward and the backward end-caps. Underlining these rules are the following assumptions:

- (a) with no data on how the luminosity background simulation is performing, we can use the variance-weighted average of both the HER and LER data/simulation ratios observed in Phase 1, which is essentially equal to the LER ratio, and
- (b) the large discrepancy between data and simulation observed in HER Phase 1 is physically relevant and must be taken into account for the projections. Early Phase 2 data show that the data/simulation ratios for the HER are $\mathcal{O}(10^2 - 10^3)$, strengthening this hypothesis [94].

We will refer to the scaling rule 1 above as the *optimistic* background scaling, and to scaling rule 2 as the *pessimistic* scaling. Rule 1 is optimistic because it considers only the smallest data/discrepancy observed, which was measured in the LER, as the one that would affect the projections. Moreover, it considers that there are no errors in the geometry description in the Geant4 models, and that therefore the effects of luminosity backgrounds on the detector will be modelled perfectly. On the other hand, Rule 2 is said to be pessimistic since it considers that a large amount of the discrepancy observed in Phase 1 is related to the Geant4 geometry implementation, and as such it will also be reflected in the data/simulation ratios for the luminosity background. Moreover, it considers the large values obtained for the HER data/simulation ratios as real and need to be accounted for even if they translate into very high dose predictions.

Other scenarios obtained by combining the luminosity and machine backgrounds scaling rules differently, or by averaging the forward and backward ratios were also studied. However they provide intermediate results in terms of the total projected backgrounds, and presenting only the best-case and worst-case scenarios is more instructive.

In the next sections, the yearly predicted doses in the electromagnetic calorimeter (ECL) are presented as a function of the angular index θ_{ID} . For reference, Figure 5.32 shows the mapping between this index and position of the crystals within the detector. There are six simulated background contributions: Coulomb and Touschek, both for the HER and the LER, which consist of the four machine background contributions, as well as the two-photon and Bhabha process which are proportional to luminosity.



Figure 5.32: Mapping of the angular index θ_{ID} in the ECL. The forward side of the detector is on the right of the figure. Figure reproduced from [79].

5.4.1 Phase 2 of commissioning: $\mathcal{L} = 5.4 \times 10^{33} \text{ cm}^{-2}\text{s}^{-1}$

The highest luminosity achieved in Phase 2, $5.4 \times 10^{33} \text{ cm}^{-2}\text{s}^{-1}$, is approximately 10 times smaller than the planned value. It is expected that the machine backgrounds would be the dominating contribution.

Optimistic scenario

Figure 5.33 shows the total radiation dose projection for Phase 2 assuming the optimistic data/simulation scaling. The Touschek LER background is dominating in this picture, and all yearly equivalent doses are below the 10 Gy/yr tolerance value used in Belle 2. The luminosity backgrounds, negligible in the forward end-cap, are only a small fraction of the total backward end-cap background.

Pessimistic scenario

Figure 5.34 shows the total radiation dose projections for Phase 2 assuming the pessimistic data/simulation scaling. In this scenario, the luminosity backgrounds are 13.5 times larger, and the backwards HER backgrounds are scaled by a factor of approximately 5400. This gives a maximal dose of 96 Gy/yr delivered to the last row crystals on the backward side, although with considerable uncertainty. This dose is ten times larger than the accepted tolerance for Belle II operations.

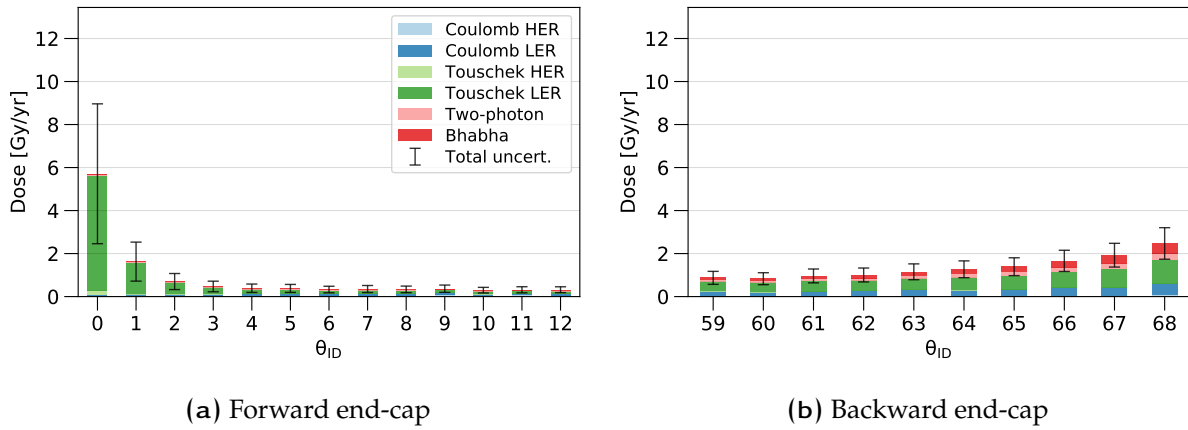


Figure 5.33: Total radiation dose projections for Phase 2 assuming the optimistic data/simulation scaling.

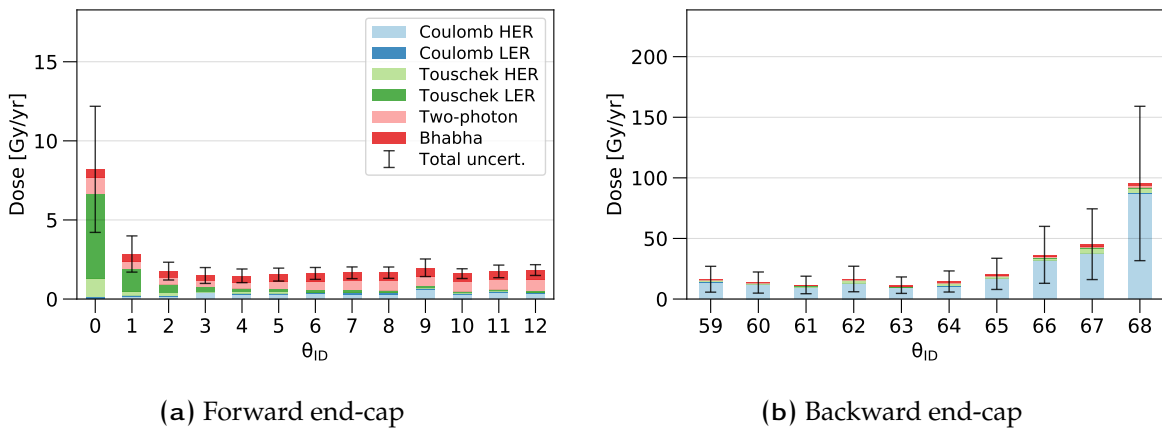


Figure 5.34: Total radiation dose projections for Phase 2 assuming the pessimistic data/simulation scaling.

5.4.2 Early physics operation: $\mathcal{L} = 5 \times 10^{34} \text{ cm}^{-2}\text{s}^{-1}$

In the first months of Phase 3 operations, the luminosity is expected to reach approximately ten times what was achieved in Phase 2, yet remaining ten times smaller than the full design luminosity. The machine backgrounds conditions are assumed to be the same as those during nominal operation.

Optimistic scenario

Figure 5.35 shows the total radiation dose projections for early Phase 3 conditions assuming the optimistic data/simulation scaling.

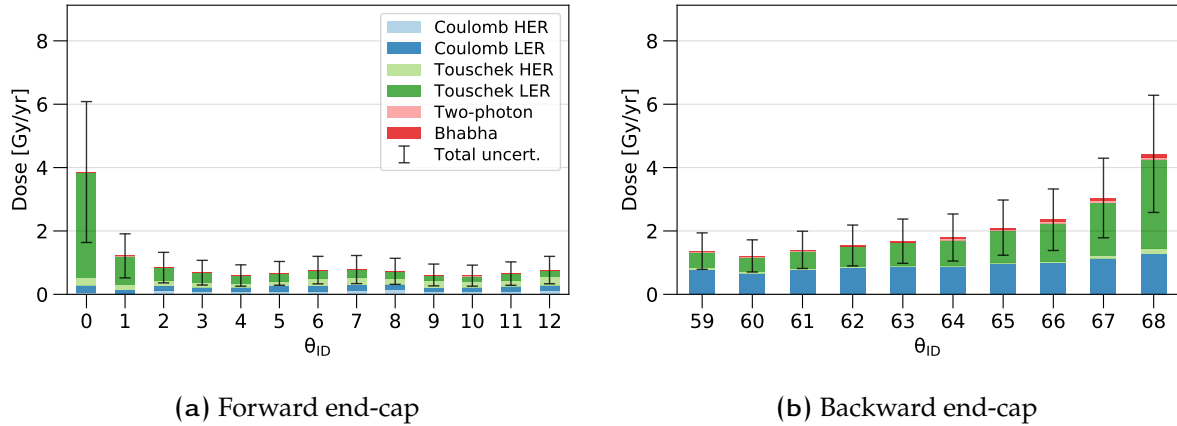


Figure 5.35: Total radiation dose projections for early Phase 3 conditions assuming the optimistic data/simulation scaling.

Similar to the Phase 2 predictions, the backgrounds in the forward end-cap are mostly coming from the Touschek losses in the LER. The backwards backgrounds are almost twice those predicted in Phase 2, with a Coulomb contribution comparable to the Touschek effect. In the optimistic scaling hypothesis, the HER backgrounds are only a small fraction of what they are in the LER and the luminosity-dependent backgrounds are negligible. The optimistic scaling hypotheses predicts yearly doses that are all smaller than the accepted tolerance.

Pessimistic scenario

Figure 5.36 shows the total radiation dose projections for early Phase 3 conditions assuming the pessimistic data/simulation scaling.

This scenario also predicts backgrounds dominated by the machine-induced contribution. Except for the first few rows of the forward end-cap, the prediction for the Touschek HER is, by far, larger than all the other contributions. This is counter-intuitive since both the

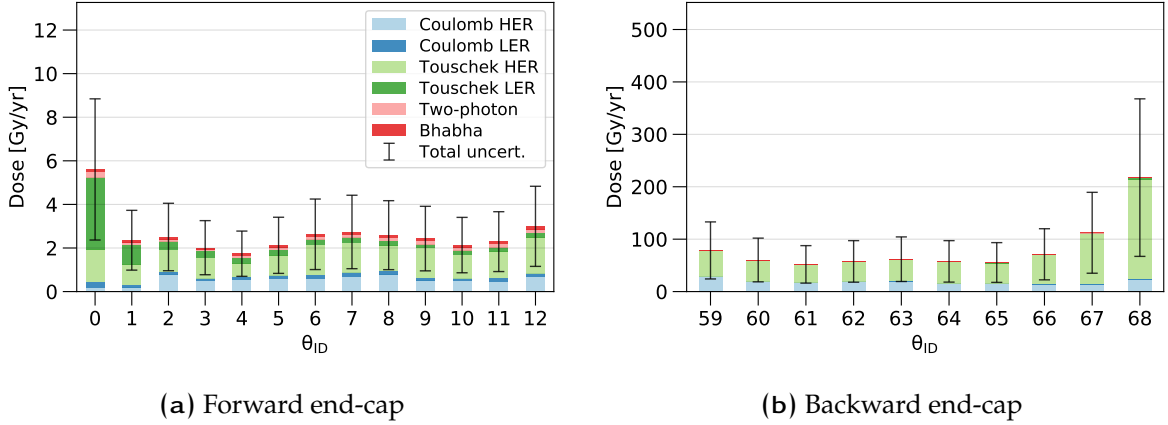


Figure 5.36: Total radiation dose projections for early Phase 3 conditions assuming the pessimistic data/simulation scaling.

Touschek model (see Eq. 2.2) and Phase 1 observations described in Section 5.3 indicate the Touschek contribution should be suppressed in the HER.

This last observation highlights one of the limits of the current approach: since the beam-gas and Touschek components cannot be easily separated in the Phase 1 crystals measurements, we have assumed that the discrepancy observed in the HER is due in equal amounts to an excess in beam-gas and Touschek. A competing hypothesis would be that simulation predicts the ratio of Touschek to beam-gas backgrounds contributions perfectly, and scale the vacuum pressure in the HER to meet the ratio predicted by simulation [1, 61]. Applying such scaling hypothesis to the LYSO rate measurements provides data/simulation ratios between 20 and 200 in the HER instead of the $\mathcal{O}(100 - 1000)$ presented in this document.

Nevertheless, the key take-away from this scenario is that, while the background level in the forward end-cap is compatible with the tolerance, the predictions in the backward end-cap are 10 to 20 times larger than the tolerance, also with a large uncertainty.

5.4.3 Full design luminosity: $\mathcal{L} = 8 \times 10^{35} \text{ cm}^{-2}\text{s}^{-1}$

The projections for the full design luminosity assume that only the luminosity-dependent contributions will be greater than the early operation. This implies that the beam currents,

the vacuum chamber pressures, and the vertical size of the stored beams all remain constant, while the final focussing system will shrink the beams at the interaction point by a factor ten compared to early Phase 3.

Optimistic scenario

Figure 5.37 shows the total radiation dose projections for nominal Phase 3 conditions assuming the optimistic data/simulation scaling. While the luminosity-dependent back-

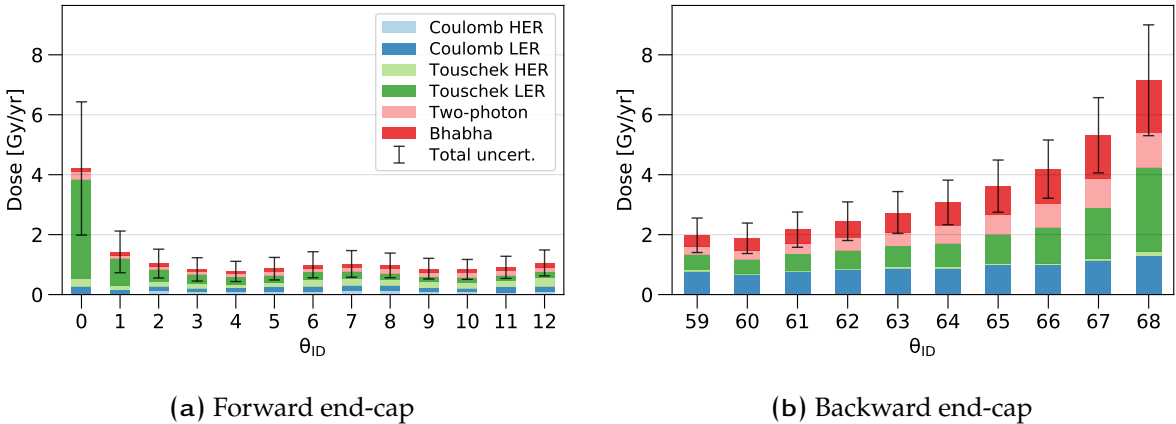


Figure 5.37: Total radiation dose projections for nominal Phase 3 conditions assuming the optimistic data/simulation scaling.

grounds are more important in these conditions, Touschek LER remains the most important contribution. Under an optimistic background simulation scaling hypothesis, the yearly dose remains below the Belle II tolerance even considering the full design luminosity.

Pessimistic scenario

Figure 5.38 shows the total radiation dose projections for nominal Phase 3 conditions assuming the pessimistic data/simulation scaling. This scenario predicts the largest backgrounds. In the forward end-cap, they are at, or below the 10 Gy/yr tolerance except in the very first row of crystals, in which they are 50 % larger. The luminosity-dependent sources form the largest contribution. In the backward end-cap, the total dose in most of

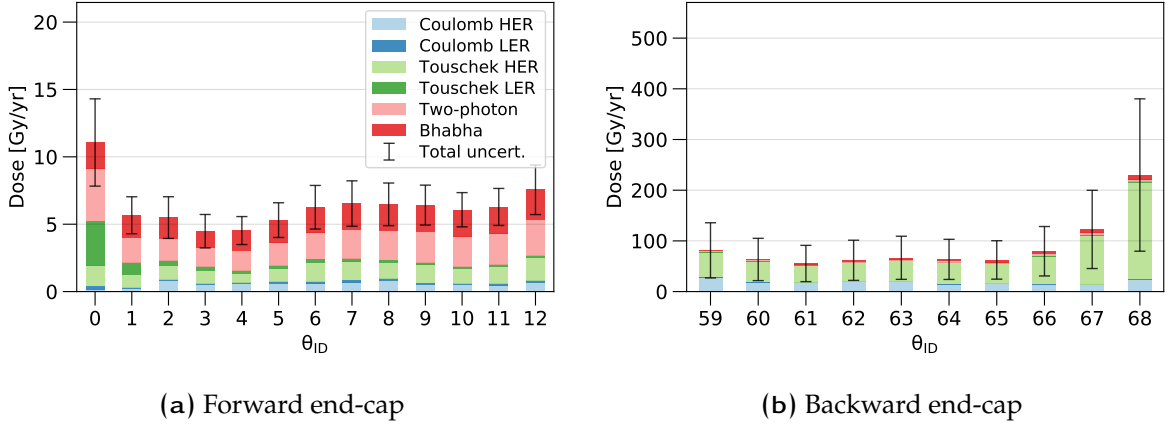


Figure 5.38: Total radiation dose projections for nominal Phase 3 conditions assuming the pessimistic data/simulation scaling.

the rows is between 60 Gy/yr and 80 Gy/yr, except in the last two rows where the doses are predicted to be significantly larger. This questions whether the ECL detector — or even Belle II as a whole — would survive such a high level of background, should this worst-case scenario materialize. Answering this question broadly and definitely would be beyond the scope of this dissertation, but it is possible to leverage earlier work conducted at the University of Victoria and assess the change in light yield resulting from the radiation damage.

Effect on the crystal light yield

We use an existing radiation hardness model in order to bring some perspective to the above yearly doses. It has been shown that the light yield LY of a CsI(Tl) crystal follows

$$LY(D) = \exp\left(-\left[O_a^{\min}F(D, \rho_a) + O_b^{\min}F(D, \rho_b)\right]\right) \quad (5.3)$$

where D is the dose in Grays, $F(D, \rho) = (1 - e^{-D/\rho})$, and $O_a^{\min}, O_b^{\min}, \rho_a, \rho_b$ are all empirical parameters characterizing the defects in the crystals and the radiation hardness associated to those defects. For Belle crystals, approximate average values are $O_a^{\min} = 0.13$, $O_b^{\min} = 0.35$, $\rho_a = 2.5$ Gy, and $\rho_b = 160$ Gy [95].

Figure 5.39 shows the relative light yield of the Belle II crystals after 6 years of operation at the nominal conditions under the optimistic data/simulation scaling rule. Figure 5.40

shows the same under the pessimistic scaling rule.

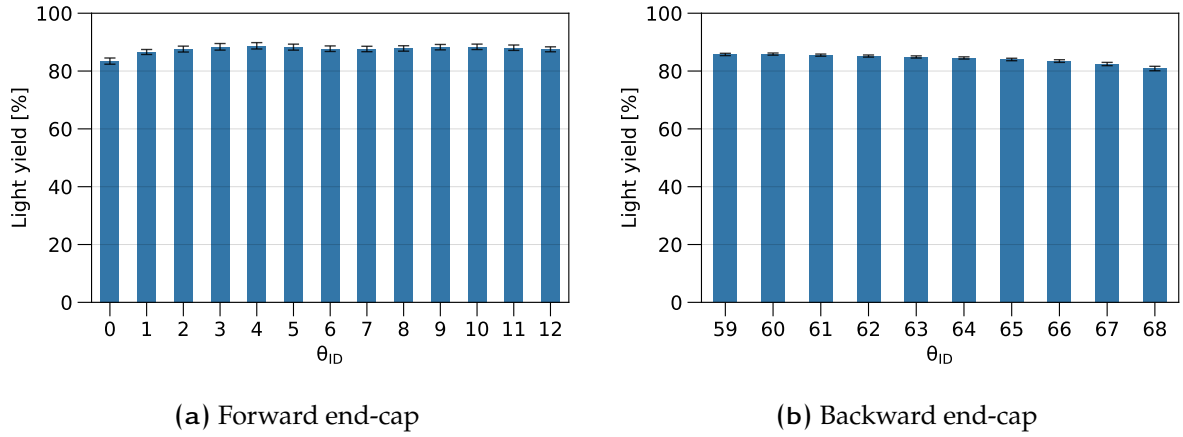


Figure 5.39: Relative light yield projection for nominal Phase 3 conditions assuming the optimistic data/simulation scaling.

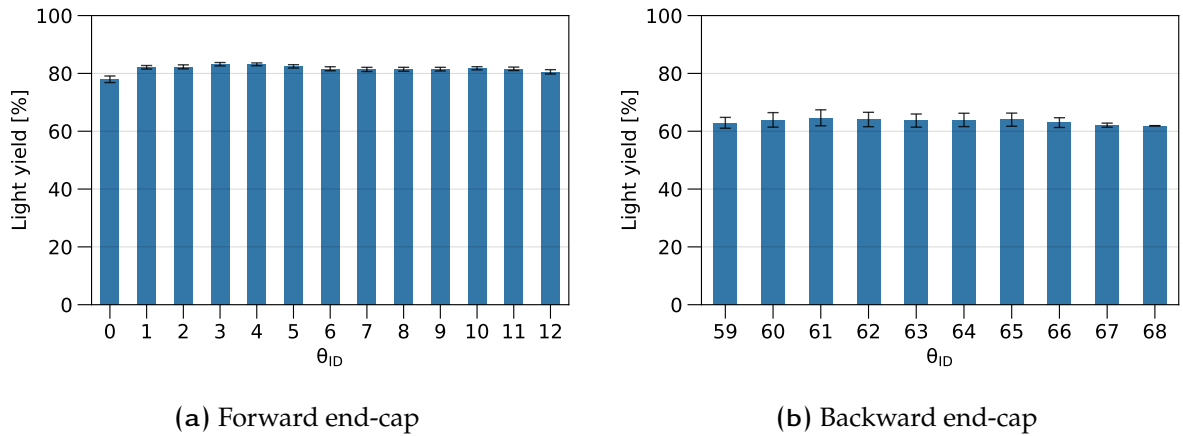


Figure 5.40: Relative light yield projection for nominal Phase 3 conditions assuming the pessimistic data/simulation scaling.

From these results, we conclude that, at the end Belle II operation, the light output produced by the Belle II crystals in the forward end-cap are expected to be between 80% and 90% of their initial light yield, depending on whether the optimistic or the pessimistic background scaling rule is considered.

For those crystals in the backward end-cap, the relative light yield is predicted to be between 60% and 85% depending on the row and the scaling hypothesis. Neglecting any

impact of radiation on the rest of the readout chain, this decrease in light yield would be directly proportional to an increase in the energy threshold to maintain minimal signal-to-noise ratio. A 40% decrease in light yield would also mean a 30% degradation of the photo-statistic contribution on the energy resolution, which depends on the root of the number of emitted photons. At 1 MeV or below, the photo-statistic contribution to the energy resolution is comparable in scale to the intrinsic scintillator resolution [96, 97]. However for photon energies expected in Belle II, the scintillator resolution become the dominant component so the total resolution is less affected.

Finally, despite a 40% reduction of their light yield, such radiation-damaged CsI(Tl) crystals would still provide more than ten times the amount of light than new pure CsI crystals. Therefore the radiation damage to the crystals alone could be tolerated if the situation does not improve, even if the pessimistic scenarios predict doses beyond the specifications.

*

**

Chapter 6

Concluding remarks

6.1 Aims

The question addressed in this dissertation is *“What are the quantitative characteristics of the beam-induced background radiation associated with single beams in Phase 1 of SuperKEKB operations under different beam configurations, and how precisely are these modelled in simulations of the accelerator?”*. In order to answer this question, we reached our general goals of measuring the beam backgrounds in the region of the where Belle II ECL endcaps are located, and exploiting the results to update the background predictions for the future phases of SuperKEKB commissioning.

Moreover, this document describes the work achieved to mitigate the background level in the ECL, through the implementation of a electromagnetic and neutron shields between the end-caps and the beam lines. It’s worth noting that, due to scheduling considerations, the design of the shields themselves could not leverage the knowledge gained from the first Beast II results. Nonetheless, the design optimization studies provided the best performances meeting the available volume and mass constraints, and therefore the ECL shields themselves wouldn’t be different if they had been designed using the Beast II results. The goal of *“mitigating the impact of the predicted machine-induced background through the provision of a radiation shield for the ECL”* was met with the successful installation of the shields in the detector within the overall construction schedule.

6.2 Findings

The findings are broken down into three main categories: those related to the shapes of energy distributions, observations showing the evolution of beam-gas conditions in Phase 1, and results pertaining to the level of agreement between simulation and measurements.

6.2.1 Energy distributions

We measured the machine backgrounds spectra under different operating conditions using data from the CsI(Tl) and LYSO crystals. After normalization, the general shapes of the LYSO spectra are consistent with the simulation in nominal conditions and outside of injection periods. Background sources that are not modelled, namely the electron-cloud effect and the injection noise, manifested themselves as higher-energy structures in the spectra extending up to 80-100 MeV. Studies of beam-gas and Touschek runs showed that, with LYSO, the measurements match the predicted shapes.

The CsI(Tl) spectra do not exhibit as much fine-grained structure as those obtained from LYSO, due to a lower energy resolution of the former. The analysis power of the spectra obtained with CsI(Tl) is also much lower due to pile-up effects: the distributions are broadened by having multiple low-energy hits during the acquisition windows.

Therefore we found that LYSO, with its good light output and fast signal time structure, has a distinctive advantage over CsI(Tl) for measuring the structure of the relatively low-energy spectra of machine backgrounds, which, in nominal conditions are mostly below 40 MeV.

6.2.2 Evolution of beam conditions in Phase 1

We found that the nature of the residual gas constituents in the vacuum chamber has a notable impact on the level of beam-gas backgrounds, and that the effective atomic number is a good descriptor for this effect. The explanatory power of this metric appeared to be limited by the measurement uncertainty of the residual gas analyser, which was used uncalibrated in Phase 1. Moreover, the study was constrained to the LER since there was no such device in the HER.

Measurements of the vacuum scrubbing showed a reduction of dynamic pressure with respect to the delivered beam dose (the time-integrated current). The reduction followed a power-law as expected, and a corresponding reduction of beam-gas background was measured by all Beast II detectors. From a power-law model, we predict that the low-energy ring should be operated for more than 10^4 A·h after the end of Phase 1 to reach the desired vacuum level at the design current.

Moreover, the Beast II group was able to observe an improvement in the background conditions after the implementation of countermeasures against the electron-cloud effect by the SuperKEKB group.

Finally, a study of transient background phenomena, referred to as “beam-dust events” after their most probable cause, showed that the data does not indicate a reduction in the rate of those events as commissioning progresses. Moreover, there was only a weak correlation between the Beast II detections and those seen with other monitors scattered around SuperKEKB, implying that the impacts of these events are highly localized. Only those transients occurring in the SuperKEKB sections close to Beast II were observed at a statistically significant rate.

6.2.3 Agreement between data and simulation

We found that the absolute value of measured dose rates — for CsI(Tl) and LYSO channels — and hit rates — for CsI(pure) and LYSO channels — is significantly greater than what was simulated. The average discrepancy was approximately a factor 10 in the LER. It was significantly larger in the forward (upstream) detectors: four times what was observed in the backward channels.

A similar result was more difficult to assess for the HER, where the lower pressure, unknown residual gas, and lower relative contribution from Touschek meant a larger relative uncertainty on the measurement. Nonetheless, our results were larger than predictions by a factor ranging from a few hundred to a few thousand, which was corroborated by early results in Phase 2. However, the measured HER backgrounds were three to six times smaller than the corresponding levels measured in LER runs. In the HER, the data/simulation ratio was also significantly larger in the upstream channels, which are on

the backward side of the detector: the backward ratio was 40 times larger than the forward ratio.

6.3 Implications

This work has implications for the future phases of Belle II commissioning, as well as, more generally for future generations of e^+e^- collider experiments.

6.3.1 For Belle II

The main implication for Belle II is that, since the measured backgrounds are at least an order of magnitude larger than simulation, extra care must be taken when interpreting that simulation to predict the life expectancy of the detector. Machine-induced backgrounds are notoriously difficult to predict accurately, and a large safety margin should be considered.

For the ECL end-caps specifically, our projections show that the light yield of the forward end-cap crystals is expected to drop by 10% to 20% over the duration of the experiment, depending on whether we use optimistic or pessimistic projections for the background dose rate. For the backward end-cap, the decrease in light yield could reach 40% in the worst-case scenario. The resulting reduction in energy resolution would be compounded with the radiation damage on the rest of the readout chain, so this should be considered when evaluating the performance of the detector towards the end of the experiment.

6.3.2 For future e^+e^- colliders

For the broader e^+e^- community and future experiments such as the International Linear Collider (ILC) or Future Circular Collider (FCC), this work sets the scale of the different background-generating phenomena, and provides a benchmark to evaluate machine background models. It showed that available numerical tools were applicable to show how the backgrounds change with the operating conditions of the accelerator, although the uncertainty on the absolute scale of those predictions can be quite large. This implies

that measuring the background level as early as possible in the accelerator commissioning process is a well-motivated approach.

6.4 Recommendations

The perspective gained through the accomplishment of this work enables us to formulate the following recommendations regarding beam backgrounds at SuperKEKB/Belle II. These recommendations fall into three main categories: measurements, models, and background management.

6.4.1 Background measurement methodologies

Monitor the residual gas constituents more precisely. Using calibrated residual gas analyzers more precisely in both vacuum chambers of SuperKEKB would reduce the uncertainty on the effective atomic number. This work showed the importance of the nature of the residual gas to quantify the level of beam-gas background expected. Yet, the current readings offer mostly qualitative information about the constituents of that gas, and for only one of the beams. Having more precision on the residual gas would enable a more definitive determination of the dependence on the atomic number. This information should then be fed into the next evolution of the accelerator simulation software (see the other recommendation below to that effect).

Provide more precise pressure calibrations. As of writing this Dissertation, there is very limited knowledge of the vacuum chamber pressures when these are at the bottom of their range, around the 10^{-8} Pa. In general, the large uncertainty associated with the pressure correction factor also means that the pressure readings do not provide the quantitative information necessary to make precise statements about the expected level of beam-gas backgrounds. Having more rigorous pressure sensor calibrations would reduce one of the major contributions to the total uncertainty of the results presented.

Use fast detectors for the electromagnetic background with good low-energy resolution. The spectra presented in Section 5.1.2 show the limits of using large CsI(Tl) crystals to

assess the energy distributions of beam-induced backgrounds. Since the background hit rates can be large and are mostly at energies below 40 MeV, faster and smaller crystals such as LYSO were observed to perform better in all observed conditions.

Monitor the calibration of the background detectors more frequently. A significant difficulty in this work was to recover from the severe degradation of the detectors and to compensate their calibration for any sensitivity drift. In a future background measurement experiment, there should be systematic means to monitor the “health” of the systems on a continuous basis. This feature should be designed early in the experiments since physical access to the detectors is often limited. In line with the previous recommendation, the natural radioactivity occurring in LYSO crystals could be exploited to provide such continuous monitoring.

Analyse the Phase 2 and Phase 3 parametric scans early. The data recorded in Phase 2 and Phase 3 should be analysed promptly to test whether the data/simulation discrepancy observed in the HER is due to Touschek losses, beam-gas scattering, or other un-modelled contributions. One of the shortcomings of the current study is the inability to disentangle the background contributions with quantitative certainty. Phases 2 and 3 operation, at beam parameters distinct from those in Phase 1, should produce a different proportion of each background contributor. There should be early checks of the level of agreement between our models and the measurements to test the different background scaling hypotheses discussed in this Dissertation.

6.4.2 Background models

Improve the fluid mechanics model in accelerator simulations. The beam-gas background has been shown by this work to be a significant contribution to the data/simulation discrepancy. This finding is also corroborated by other work studying the beam lifetime as a proxy for the background level [1]. An incremental improvement of the background simulations should involve modelling how the average pressure is projected onto all local pressure measurements, also how this position-dependent pressure affects beam-gas background generation.

Incorporate a multi-constituent residual gas model in the accelerator simulations. In line with the first recommendations of both Sections 6.4.1 and 6.4.2, the beam-gas interaction model should incorporate a mixture of different residual gas constituents. This work demonstrated that the residual gas is indeed composed of a plurality of species, each having specific beam-gas interaction cross sections. The effective atomic number model used in this Dissertation enabled the use of simulation tools that require a single value for the atomic number of the gas. However, there could be benefits to incorporate multiple gases in the accelerator models and have a more complete description of how the different mixtures affect the level of beam-gas background produced. For example, there are extra terms in Equation 2.6 that do not solely depend on the square of the atomic number.

Undertake a verification and validation study of the SAD software. The complexity of the simulation software involved, together with a heavy reliance of the detector design work on the outputs of the simulations, justify a dedicated effort to understand these tools better. There should be a thorough review of each of the functionalities of the software and of each step in the analysis pipeline, and the implementation of unit testing for the critical elements to ensure their usability. Verification and Validation (V&V) frameworks are common place in a production-grade software life-cycles (see [98], for example).

Validate the implementation of the accelerator and detector geometry. The detectors, vacuum chambers and surrounding environment are implemented in Geant4. The accuracy of this implementation should be assessed by conducting a systematic cross-check with engineering drawings, when available. Because beam background is generated when lost particles collide with the walls of the vacuum chamber and interact with the surrounding material, any inconsistency in the material description will translate into differences between the simulated and the measured results.

6.4.3 Background management

Re-assess the shielding strategy for the whole Belle II detector. Given the expected excess in machine background compared to the levels used in the Belle II design phase, it would be useful to reconsider the shielding strategy for the whole Belle II detector and see possible areas where extra shielding would be added. Such passive elements could

be inserted, for example, during the detector replacements or upgrades that are already planned to recover from the expected radiation damage. As mentioned in Section 6.1, the ECL shield is already an optimal design considering the mass and volume constraints, but there should be a detector-wide effort to determine the best shield placements and potential improvements given the expected background situation.

Consider planning for detector replacements or upgrades. The results presented in this Dissertation paint a pessimistic picture of the background situation in the operation phase of Belle II, specifically on the backward side. Given the limitations of this study, it is of course a possibility that the situation will not be as dire as the one presented. Yet, already preparing recovery plans would mitigate the risk of machine downtime associated with having to redesign and build new detector systems within a few months notice.

Study the impact of radiation damage on the physics performance of the detector. According to the results presented in this Dissertation, the damage to the detectors, specifically on the backward side, are expected to be significant. There should be a dedicated effort to determine how the damage to the different systems affect the overall physics measurements, in order to prioritize any maintenance or shielding work.

Exploit the ECL shields background monitor real time data. When available, compare the readings of the background monitors installed within the ECL shields to provide an independent check of the data/simulation discrepancy. The simulation should fully implement these detectors and a model of the readout chain. A live display of the background rates measured by these sensors together with their simulated output for the current beam conditions would provide valuable information about an unexpected background situation. This would also provide advanced data about the degradation rate of the Belle II systems due to machine background, and about the rate at which they approach their design usage limits.

6.5 Final remarks

Phase 1 of SuperKEKB commissioning was a necessary experiment for the group to gain expertise about the main contributions to machine background, their modelling and the useful ways to characterize them experimentally. The conditions were notably different than those expected for the Physics runs, yet the work enabled us to provide advanced warning about the quantitative accuracy of the background models used to determine the life expectancy and the performance of the Belle II detector.

Backgrounds can be affected by differing SuperKEKB operations, including collimator settings, and these studies indicate that there is a need to ensure that the backgrounds are reduced as much as possible, as these studies suggest that, without further mitigation, backgrounds may be at a level that shortens the lifetime of parts of the Belle II detector.

Going forward, monitoring the background levels closely, improving the predictive power of our models, and elaborating plans in case pessimistic projections materialize will each be critical to ensure the integrity of the detector and adequate performance throughout its operation. The success of the Belle II programme depends on it.

*

**

Bibliography

- [1] P. M. Lewis, *et al.*, “First Measurements of Beam Backgrounds at SuperKEKB”, *Nuclear Instruments and Methods in Physics Research Section A: Accelerators, Spectrometers, Detectors and Associated Equipment* **A914** (2019) 69–144, [arXiv:1802.01366](https://arxiv.org/abs/1802.01366) [physics.ins-det].
- [2] J. Brodzicka, *et al.*, “Physics achievements from the Belle experiment”, *Progress of Theoretical and Experimental Physics* **2012** no. 1, (2012) 110.
- [3] J. P. Lees, V. Poireau, V. Tisserand, E. Grauges, and Others, “Time-Integrated Luminosity Recorded by the BABAR Detector at the PEP-II e^+e^- Collider”, *Nuclear Instruments and Methods in Physics Research Section A: Accelerators, Spectrometers, Detectors and Associated Equipment* **A726** (2013) 203–213, [arXiv:1301.2703](https://arxiv.org/abs/1301.2703) [hep-ex].
- [4] K. Abe, *et al.*, “Observation of Large CP Violation in the Neutral B Meson System”, *Physical Review Letters* **87** no. 9, (2001) 091802, [arXiv:0107061](https://arxiv.org/abs/0107061) [hep-ex].
- [5] B. Aubert, *et al.*, (The BABAR Collaboration), “Observation of CP violation in the B^0 meson system”, *Physical Review Letters* **87** (Aug, 2001) 091801.
- [6] The Royal Swedish Academy of Sciences, “Broken Symmetries - Scientific Background on the Nobel Prize in Physics”, 2008. http://www.nobelprize.org/nobel_prizes/physics/laureates/2008/advanced.html.
- [7] B. Aubert, *et al.*, (The The BABAR Collaboration), “Measurement of the CP asymmetry amplitude $\sin 2\beta$ with B^0 mesons”, *Physical Review Letters* **89** (Oct, 2002) 201802.

- [8] K. Abe, *et al.*, (The Belle Collaboration), “Improved measurement of mixing-induced CP violation in the neutral B meson system”, *Physical Review D* **66** (Oct, 2002) 071102.
- [9] J. Beringer, *et al.*, (The Particle Data Group), “Review of particle physics”, *Physical Review D* **86** (Jul, 2012) 010001.
- [10] K. Park, *et al.*, “Observation of a Narrow Charmoniumlike State in Exclusive $B^\pm \rightarrow K^\pm \pi^+ \pi^- J/\psi$ Decays”, *Physical Review C* **91** no. 4, (2015) 045203.
- [11] (The Belle II Collaboration), E. Kou and P. Urquijo, eds., *The Belle II Physics Book*. 2018. [arXiv:1808.10567](https://arxiv.org/abs/1808.10567) [hep-ex].
- [12] The Belle II Collaboration and the SuperKEKB Accelerator Group, “Public general slides”, 2016. <https://confluence.desy.de/display/BI/Public+GeneralSlides>. [Online; accessed 2018-10-20].
- [13] (The Belle II Collaboration), E. Kou and P. Urquijo, “Introduction”, in *The Belle II Physics Book* [11]. [arXiv:1808.10567](https://arxiv.org/abs/1808.10567) [hep-ex].
- [14] J. Bennett, “Belle II physics prospects, status and schedule”, *Journal of Physics: Conference Series* **770** no. 1, (2016) 012044.
- [15] J. M. Roney and D. MacFarlane, “BABAR celebrates its 25th anniversary”, *CERN Courier* (March-April, 2019), p. 19.
- [16] A. D. Sakharov, “Violation of CP invariance, C asymmetry, and baryon asymmetry of the universe”, *Soviet Physics Uspekhi* **34** no. 5, (May, 1991) 392–393.
- [17] M. Endo, S. Mishima, and M. Yamaguchi, “Recent measurements of cp asymmetries of $b \rightarrow \phi k^0$ and $b \rightarrow \eta' k_s$ at b -factories suggest new cp violation in left-handed squark mixing”, *Physics Letters B* **609** no. 1, (2005) 95 – 101.
- [18] B. Aubert, *et al.*, (The BABAR Collaboration), “Observation of cp violation in $b \rightarrow \eta' K^0$ decays”, *Phys. Rev. Lett.* **98** (Jan, 2007) 031801.
- [19] K.-F. Chen, *et al.*, (The Belle Collaboration), “Observation of time-dependent cp violation in $B^0 \rightarrow \eta' K^0$ decays and improved measurements of cp asymmetries in $B^0 \rightarrow \phi K^0$, $K_S^0 K_S^0 K_S^0$ and $B^0 \rightarrow j/\psi K^0$ decays”, *Phys. Rev. Lett.* **98** (Jan, 2007) 031802.

- [20] R. Itoh, “Status of Belle II and physics prospects”, *Nuclear and Particle Physics Proceedings* **285-286** (2017) 155 – 159. Sixth Workshop on Theory, Phenomenology and Experiments in Flavour Physics Interplay of Flavour Physics with Electroweak symmetry breaking.
- [21] J. P. Lees, *et al.*, (The BABAR Collaboration), “Evidence for an excess of $\bar{B} \rightarrow D^{(*)} \tau^- \bar{\nu}_\tau$ decays”, *Physical Review Letters* **109** (Sep, 2012) 101802.
- [22] J. P. Lees, *et al.*, (The BABAR Collaboration), “Evidence of $B^+ \rightarrow \tau^+ \nu$ decays with hadronic b tags”, *Physical Review* **D88** (Aug, 2013) 031102.
- [23] G. Ciezarek, M. Franco Sevilla, B. Hamilton, R. Kowalewski, T. Kuhr, V. Lüth, and Y. Sato, “A Challenge to Lepton Universality in B Meson Decays”, *Nature* **546** (2017) 227–233, [arXiv:1703.01766](https://arxiv.org/abs/1703.01766) [hep-ex].
- [24] S. Lavignac, I. Masina, and C. A. Savoy, “ $\tau \rightarrow \mu \gamma$ and $\tau \rightarrow e \gamma$ as probes of neutrino mass models”, *Physics Letters B* **520** no. 3, (2001) 269 – 278.
- [25] B. W. Lee and R. E. Shrock, “Natural suppression of symmetry violation in gauge theories: Muon- and electron-lepton-number nonconservation”, *Phys. Rev. D* **16** (Sep, 1977) 1444–1473.
- [26] B. Aubert, *et al.*, (The BABAR Collaboration), “Searches for lepton flavor violation in the decays $\tau^\pm \rightarrow e^\pm \gamma$ and $\tau^\pm \rightarrow \mu^\pm \gamma$ ”, *Phys. Rev. Lett.* **104** (Jan, 2010) 021802.
- [27] K. Hayasaka, *et al.*, (The Belle Collaboration), “New search for $\tau \rightarrow \mu \gamma$ and $\tau \rightarrow e \gamma$ decays at Belle”, *Physics Letters B* **666** no. 1, (2008) 16 – 22.
- [28] M. Khlopov, *Fundamentals of Cosmic Particle Physics*, **ch. 2. Hidden sector of particle physics**, pp. 15–68. SpringerLink : Bücher. Cambridge International Science Publishing Limited, 2012.
- [29] R. Essig, P. Schuster, and N. Toro, “Probing Dark Forces and Light Hidden Sectors at Low-Energy e+e- Colliders”, *Physical Review* **D80** (2009) 015003, [arXiv:0903.3941](https://arxiv.org/abs/0903.3941) [hep-ph].
- [30] B. Batell, M. Pospelov, and A. Ritz, “Probing a Secluded U(1) at B-factories”, *Physical Review* **D79** (2009) 115008, [arXiv:0903.0363](https://arxiv.org/abs/0903.0363) [hep-ph].

- [31] The Belle II Collaboration, “Super KEKB and Belle II”, 2017.
https://www.belle2.org/project/super_kekb_and_belle_ii. [Online; accessed 2018-07-23].
- [32] K. Akai, K. Furukawa, and H. Koiso, “Superkekb collider”, *Nuclear Instruments and Methods in Physics Research Section A: Accelerators, Spectrometers, Detectors and Associated Equipment* **907** (2018) 188 – 199. Advances in Instrumentation and Experimental Methods (Special Issue in Honour of Kai Siegbahn).
- [33] The SuperKEKB Accelerator Group.
- [34] T. Abe, *et al.*, “Belle II Technical Design Report”, Tech. Rep. KEK-REPORT-2010-1, KEK — High Energy Accelerator Research Organization, Nov., 2010.
[arXiv:1011.0352](https://arxiv.org/abs/1011.0352) [physics.ins-det].
- [35] S. D. Henderson and M. Sullivan, “Beam Induced Detector Backgrounds and Irradiation in e^+e^- colliders”, in *Handbook of Accelerator Physics and Engineering*, A. W. Chao, K. H. Mess, M. Tigner, and F. Zimmermann, eds., ch. 3.3.9, pp. 286–293. World Scientific publishing, Singapore, 2nd ed., 2013.
- [36] T. Natsui, Y. Ogawa, M. Yoshida, and X. Zhou, “High charge low emittance RF gun for SuperKEKB”, in *Proc. of International Particle Accelerator Conference (IPAC’12)*, New Orleans, Louisiana, USA, May 20-25, 2012, International Particle Accelerator Conference, pp. 1533 – 1535. JACoW, Geneva, Switzerland, May, 2012.
- [37] T. Miura *et al.*, “[Upgrade Status of Injector LINAC for SuperKEKB](#)”, in *Proc. of International Particle Accelerator Conference (IPAC’14)*, Dresden, Germany, June 15-20, 2014, no. 5 in International Particle Accelerator Conference, pp. 59–61. JACoW, Geneva, Switzerland, July, 2014.
- [38] T. Kamitani *et al.*, “[SuperKEKB Positron Source Construction Status](#)”, in *Proc. of International Particle Accelerator Conference (IPAC’14)*, Dresden, Germany, June 15-20, 2014, no. 5 in International Particle Accelerator Conference, pp. 579–581. JACoW, Geneva, Switzerland, July, 2014.
- [39] K. Sasahara, *et al.*, “Positron production from a tungsten single crystal at the KEK 8-GeV electron linac”, in *Proc. of ICFA2001 Beam Dynamics Workshop on Laser Beam Interactions*, Stony Brook, U.S.A. 2001.

- [40] C. Bernardini, G. F. Corazza, G. Di Giugno, G. Ghigo, J. Haissinski, P. Marin, R. Querzoli, and B. Touschek, “Lifetime and Beam Size in a Storage Ring”, *Physical Review Letters* **10** no. 9, (May, 1963) 407–409.
- [41] A. Piwinski, “The Touschek effect in strong focusing storage rings”, tech. rep., DESY-98-179, 1998. [arXiv:9903034 \[physics\]](#).
- [42] H. Bruck, *Accélérateurs circulaires de particules*. Presses Universitaires de France, Paris, 1966.
- [43] J. L. Duff, “Single and multiple Touschek effects”, in *CERN Accelerator School: Accelerator Physics*, pp. 114–130. Berlin, Germany, 1988. CERN Report LAL-RT-88-08.
- [44] K. Hirata, “An introduction to SAD”, in *Proceedings of the 2nd Advanced ICFA Beam Dynamics Workshop*, J. Hagel and E. Keil, eds. Lugano, Switzerland, Apr, 1988.
- [45] S. Agostinelli, *et al.*, “Geant4—a simulation toolkit”, *Nuclear Instruments and Methods in Physics Research Section A: Accelerators, Spectrometers, Detectors and Associated Equipment* **506** no. 3, (2003) 250–303.
- [46] O. B. Malyshev, “Gas dynamics modelling for particle accelerators”, *Vacuum* **86** no. 11, (2012) 1669–1681.
- [47] F. C. Porter, “Luminosity lifetime at an asymmetric e^+e^- collider”, *Nuclear Instruments and Methods in Physics Research Section A: Accelerators, Spectrometers, Detectors and Associated Equipment* **302** no. 2, (1991) 209–216.
- [48] P. C. Marin, “Designing accelerator vacuum systems”, in *CERN Accelerator School : Vacuum Technology*, pp. 271–280. Snekersten, Denmark, May, 1999. CERN Report OPEN-2000-286.
- [49] M. A. Furman, “Electron-cloud effect”, in *Handbook of Accelerator Physics and Engineering*, A. W. Chao, K. H. Mess, M. Tigner, and F. Zimmermann, eds., ch. 2.4.14, pp. 137–163. World Scientific Publishing, Singapore, 2nd ed., 2013.
- [50] Y. Suetsugu, K. Shibata, T. Ishibashi, K. Kanazawa, M. Shirai, S. Terui, and H. Hisamatsu, “First commissioning of the SuperKEKB vacuum system”, *Physical Review Accel. Beams* **19** (Dec, 2016) 121001.

- [51] T. Baer, *et al.*, “UFOs in the LHC”, Tech. Rep. CERN-ATS-2011-276, CERN, Sep, 2011. <https://cds.cern.ch/record/1379150>.
- [52] G. Papotti, M. Albert, B. Auchmann, E. Holzer, M. Kalliokoski, and A. Lechner, “Macroparticle-Induced Losses During 6.5 TeV LHC Operation”, in *Proceedings of International Particle Accelerator Conference (IPAC'16), Busan, Korea, May 8-13, 2016*, no. 7 in International Particle Accelerator Conference, pp. 1481–1484. JACoW, Geneva, Switzerland, June, 2016. doi:10.18429/JACoW-IPAC2016-TUPMW023.
- [53] Y. Tanimoto, T. Honda, and S. Sakanaka, “Experimental demonstration and visual observation of dust trapping in an electron storage ring”, *Physical Review Special Topics - Accelerators and Beams* **12** (Nov, 2009) 110702.
- [54] A. W. Chao, K. H. Mess, M. Tigner, and F. Zimmermann, eds., *Handbook of Accelerator Physics and Engineering*. World Scientific publishing, Singapore, 2nd ed., 2013.
- [55] K. Shibata, “SuperKEKB Vacuum System”, in *Joint INFN-CERN-EuCARD-AccNet Workshop on Electron-Cloud Effects: E-CLOUD'12*, p. 5 p. La Biodola, Isola d’Elba, Italy, June, 2012.
- [56] W. Kaabi, H. Jenhani, A. Variola, G. Keppel, and V. Palmieri, “Titanium Nitride Coating as a Multipactor Suppressor”, in *23rd Particle accelerator Conference, PAC'09*, p. WE5PFP004. Vancouver, Canada,, May, 2009.
- [57] T. Ishibashi, Y. Suetsugu, and S. Terui, “Collimators for SuperKEKB Main Ring”, in *Proc. of International Particle Accelerator Conference (IPAC'17), Copenhagen, Denmark, 14–19 May, 2017*, no. 8 in International Particle Accelerator Conference, pp. 2929–2932. JACoW, Geneva, Switzerland, May, 2017.
- [58] K. Kanazawa, “Status of SuperKEKB construction”, *Nuclear and Particle Physics Proceedings* **273-275** (2016) 204 – 209. 37th International Conference on High Energy Physics (ICHEP). Distributed under a Creative Commons Attribution 4.0 International License (CC BY 4.0).
- [59] T. Kohriki, “Belle-II(Nano beam) IR= ± 41.5 mrad.(Top view A)”, 2014.
- [60] I. Nakamura, Sept., 2003.

- [61] S. R. de Jong, “8th Background Campaign: ECL”, in *17th Open Meeting of the Belle II Collaboration*. KEK, Tsukuba, Japan, Feb, 2014.
- [62] A. Beaulieu, “Electromagnetic Calorimeter – End-cap shields project definition report”, tech. rep., BELLE2-NOTE-TE-2015-032, 2015.
- [63] A. Beaulieu, “Electromagnetic Calorimeter – End-cap shields conceptual design report”, tech. rep., BELLE2-NOTE-TE-2015-023, 2015.
- [64] A. Beaulieu, “Electromagnetic Calorimeter – End-cap shields technical design report”, tech. rep., BELLE2-NOTE-TE-2016-002, 2016.
- [65] The Belle II Collaboration, “Public structure”, 2017.
<https://confluence.desy.de/display/BI/Public+Structure>. [Online; accessed 2017-07-13].
- [66] Dassault Systèmes, “SolidWorks 2016 Professionnal”. Academic licence provided by CMC Microsystems, 2016.
- [67] A. C. Fernandes, M. Felizardo, A. Kling, J. G. Marques, and T. Morlat, “Studies on the efficiency of the neutron shielding for the SIMPLE dark matter search”, *Nuclear Instruments and Methods in Physics Research Section A: Accelerators, Spectrometers, Detectors and Associated Equipment* **623** no. 3, (2010) 960–967.
- [68] T. Ebisawa, *et al.*, “Shield evaluation of cold neutron curved guide tubes for J-PARC neutron resonance spin echo spectrometers”, *Nuclear Instruments and Methods in Physics Research Section A: Accelerators, Spectrometers, Detectors and Associated Equipment* **600** no. 1, (2009) 126–128.
- [69] M. Igashira, H. Kitazawa, and N. Yamamuro, “A heavy shield for the gamma-ray detector used in fast neutron experiments”, *Nuclear Instruments and Methods in Physics Research Section A: Accelerators, Spectrometers, Detectors and Associated Equipment* **245** no. 2–3, (1986) 432–437.
- [70] I. Stekl, S. Pospíšil, V. E. Kovalenko, V. Vorobel, C. Leroy, F. Piquemal, R. Eschbach, and C. Marquet, “Monte-Carlo simulations of neutron shielding for the ATLAS forward region”, *Nuclear Instruments and Methods in Physics Research Section A: Accelerators, Spectrometers, Detectors and Associated Equipment* **452** no. 3, (2000) 458–469.

- [71] J. Aad and Others, “The ATLAS Experiment at the CERN Large Hadron Collider”, *Journal of Instrumentation* **3** no. 08, (2008) S08003.
- [72] J. Sodomka, C. Leroy, J. Palla, S. Pospisvil, and I. Vstekl, “The Shielding of the ATLAS Forward Region from the point of view of Materials Technology and some Construction Aspects”, Tech. Rep. ATL-TECH-98-033, CERN-ATL-TECH-98-033, CERN, 1998.
- [73] J. Han-Tao, T. Jing-Yu, and Y. Zheng, “Study on collimation and shielding of the back-streaming neutrons at the CSNS target”, *Chinese Phys. C* **37** no. 11, (2013) 117002.
- [74] S. Blondel, *Optimisation du blindage contre les neutrons pour le démonstrateur de SuperNEMO et analyse de la double désintégration β du néodyme-150 vers les états excités du samarium-150 avec le détecteur NEMO 3*. PhD thesis, Université Paris Sud, Orsay, 2013.
- [75] G. Lindström and V. Angela, “Notes on the fluence normalisation based on the NIEL scaling hypothesis”, tech. rep., ROSE/TN/2000-02, 2000.
<https://rd48.web.cern.ch/rd48/technical-notes/rosetn00-02.ps>.
- [76] G. Lindström and V. Angela, “Displacement damage in silicon, on-line compilation”, 2000. <http://rd50.web.cern.ch/RD50/NIEL/default.html>.
- [77] ANSYS inc., “ANSYS Mechanical, Release 15”. Academic licence provided by CMC Microsystems, 2013.
- [78] R. E. von Mises, “Mechanik der festen Körper im plastisch deformablen Zustand.”, *Nachrichten von der Gesellschaft der Wissenschaften zu Göttingen, Mathematisch-Physikalische Klasse* **1** (1913) 582–592.
- [79] S. R. de Jong, *Study of thermal neutron flux from SuperKEKB in the Belle II commissioning detector*. PhD thesis, University of Victoria, 2017.
- [80] J. H. Gross, *Mass spectrometry: A textbook*. Springer Berlin Heidelberg, Berlin, Heidelberg, 2 ed., 2011.
- [81] Y. Suetsugu. Private communication, 2016.

- [82] D. J. Mitchell, "Measurement and calibration techniques used in computer partial pressure analysis", *Journal of Vacuum Science & Technology A: Vacuum, Surfaces, and Films* **3** no. 3, (May, 1985) 527–532.
- [83] M. Derrick, D. Gacek, N. Hill, B. Musgrave, R. Noland, E. Petereit, J. Repond, R. Stanek, and K. Sugano, "Design and construction of the ZEUS barrel calorimeter", *Nuclear Instruments and Methods in Physics Research Section A: Accelerators, Spectrometers, Detectors and Associated Equipment* **309** no. 1-2, (Nov, 1991) 77–100.
- [84] Hamamatsu Photonics K.K., "R580 Photomultiplier Tube", TPMH1100E0, June, 2014. https://www.hamamatsu.com/resources/pdf/etd/R580_TPMH1100E.pdf. [Online; accessed 2010-04-30].
- [85] Hamamatsu Photonics K.K., "Photomultiplier Tubes and Assemblies for Scintillation Counting & High Energy Physics", TPMZ0003E0, April, 2017. https://www.hamamatsu.com/resources/pdf/etd/High_energy_PMT_TPMZ0003E.pdf. [Online; accessed 2010-04-30].
- [86] M.-M. Bé, *et al.*, *Table de Radionucléides*, vol. 3 of *Monographie BIPM-5*. Bureau International des Poids et Mesures, Pavillon de Breteuil, F-92310 Sèvres, France, 2006.
- [87] H. Saeki, T. Momose, and H. Ishimaru, "Observations of dust trapping phenomena in the tristan accumulation ring and a study of dust removal in a beam chamber", *Review of Scientific Instruments* **62** no. 4, (1991) 874–885, <http://dx.doi.org/10.1063/1.1142024>.
- [88] F. Zimmermann, "Trapped dust in HERA and DORIS", Tech. Rep. DESY-HERA-93-08, DESY, Hamburg, Jul, 1993. <http://cds.cern.ch/record/252789>.
- [89] J. W. Flanagan, K. Ohmi, H. Fukuma, S. Hiramatsu, M. Tobiyama, and E. Perevedentsev, "Observation of Vertical Betatron Sideband due to Electron Clouds in the KEKB Low Energy Ring", *Physical Review Letters* **94** (Feb, 2005) 054801.

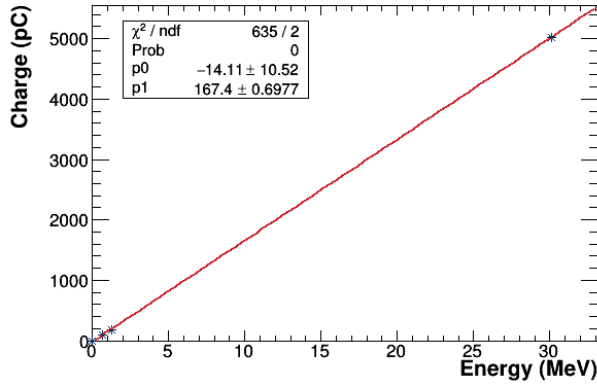
- [90] O. Gröbner, A. Mathewson, H. Störi, P. Strubin, and R. Souchet, “Studies of photon induced gas desorption using synchrotron radiation”, *Vacuum* **33** no. 7, (1983) 397–406.
- [91] O. B. Malyshev, “Gas dynamics modelling for particle accelerators”, *Vacuum* **86** no. 11, (2012) 1669 – 1681. Vacuum Gas Dynamics: Theory, experiments and practical applications.
- [92] A. Boyarintsev, *et al.*, “Study of radiation hardness of pure CsI crystals for belle-II calorimeter”, *Journal of Instrumentation* **11** no. 03, (Mar, 2016) P03013–P03013.
- [93] E. Jones, T. Oliphant, P. Peterson, *et al.*, “SciPy: Open source scientific tools for Python”, 2001–. <http://www.scipy.org/>. [Online; accessed 2018-10-20].
- [94] L. Santelj, “Phase 2 background simulation”. Internal communication presented during the 2018-10-10 BEAST/Backgrounds group meeting., 2018.
- [95] S. Longo and J. Roney, “Radiation hardness of 30 cm long CsI(Tl) crystals”, *Journal of Instrumentation* **11** no. 08, (2016) P08017.
- [96] P. Dorenbos, J. T. M. de Haas, and C. W. E. van Eijk, “Non-proportionality in the scintillation response and the energy resolution obtainable with scintillation crystals”, *IEEE Transactions on Nuclear Science* **42** no. 6, (Dec, 1995) 2190–2202.
- [97] M. Moszynski, M. Kapusta, D. Wolski, M. Szawlowski, and W. Klamra, “Energy resolution of scintillation detectors with large area avalanche photodiodes and photomultipliers light readout”, in *1997 IEEE Nuclear Science Symposium Conference Record*, vol. 1, pp. 206–211 vol.1. Nov, 1997.
- [98] “IEEE Standard for System, Software, and Hardware Verification and Validation”, *IEEE Std 1012-2016 (Revision of IEEE Std 1012-2012/ Incorporates IEEE Std 1012-2016/Cor1-2017)* (Sep., 2017) 1–260.
- [99] E. Oberg, F. D. Jones, H. H. Ryffel, and C. J. McCauley, *Machinery’s Handbook*. Industrial Press, Inc. Industrial Press, Incorporated, 2012.
- [100] MatWeb LLC, “The MatWeb™ Materials Database”, 2017. <http://www.matweb.com>.

Appendices

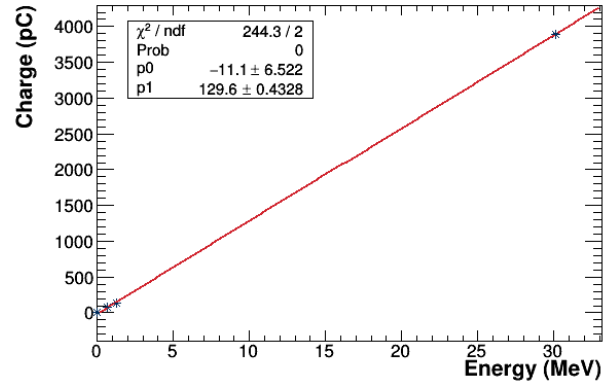
Appendix A

Detailed calibration results

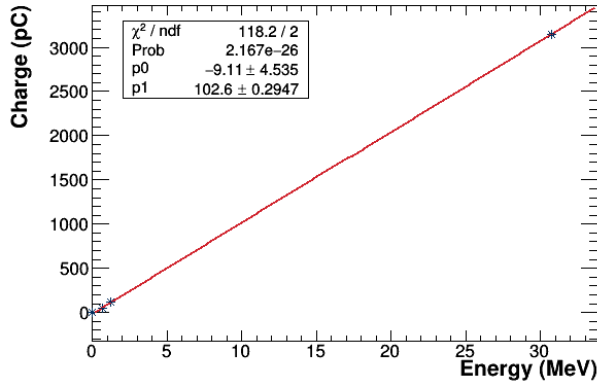
A.1 Initial calibration campaign



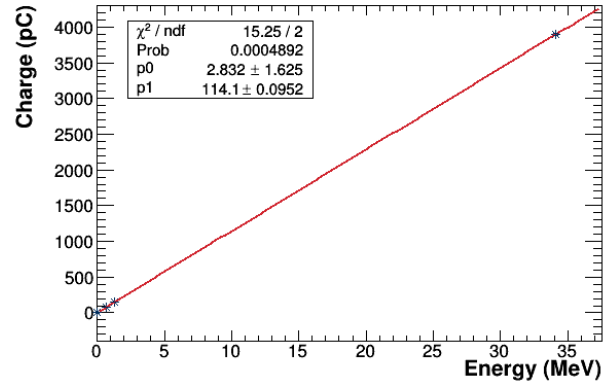
(a) F1



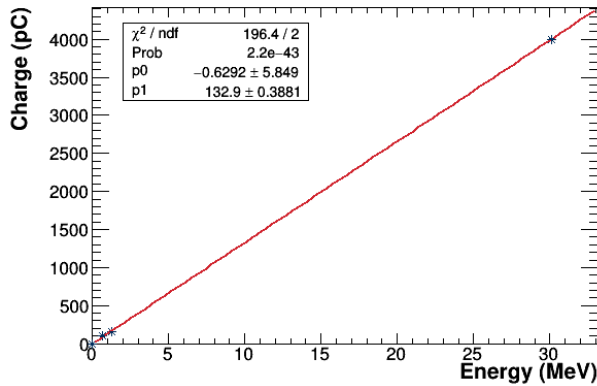
(b) B1



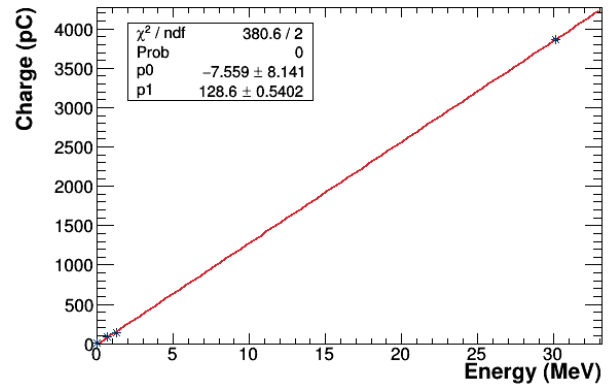
(c) F2



(d) B2

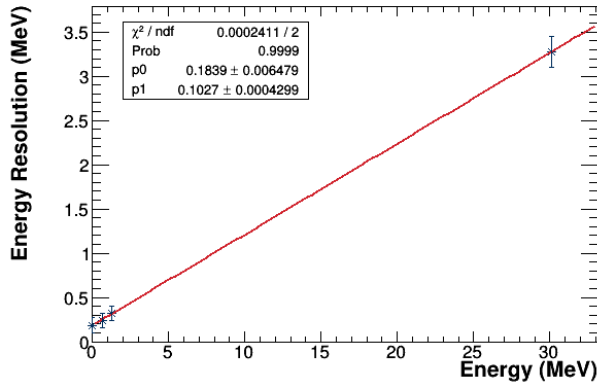


(e) F3

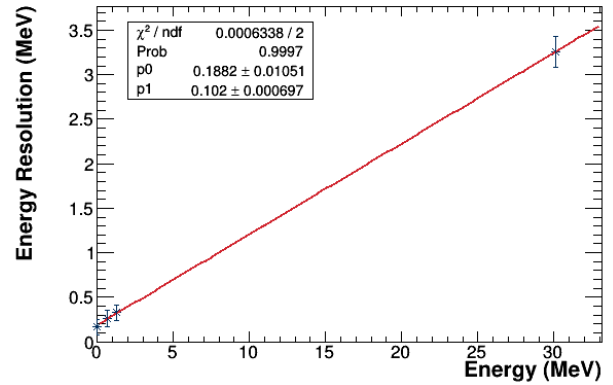


(f) B3

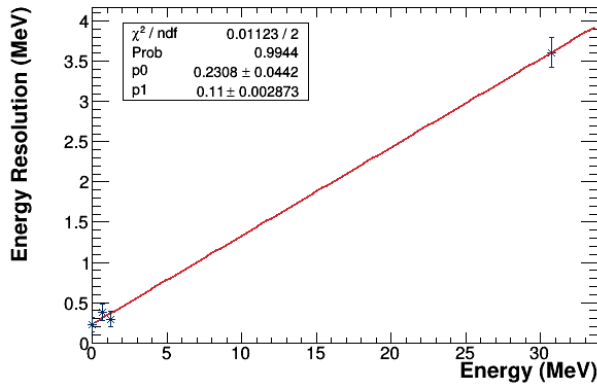
Figure A.1: Calibration curves for the six CsI(Tl) channels. The red line corresponds to a $y = p_0 + p_1x$ linear fit of the measured charge vs. energy. In the notation of Equation 4.8, $c = p_0$ and $b = p_1$.



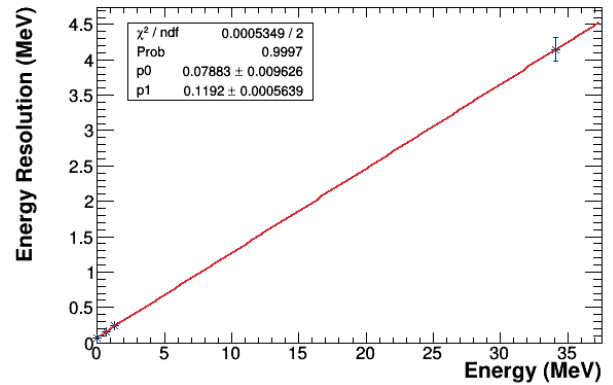
(a) F1



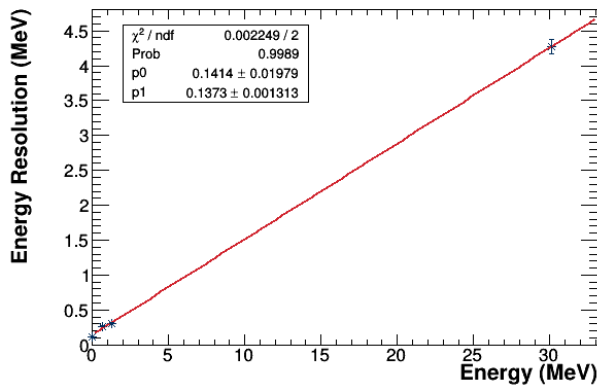
(b) B1



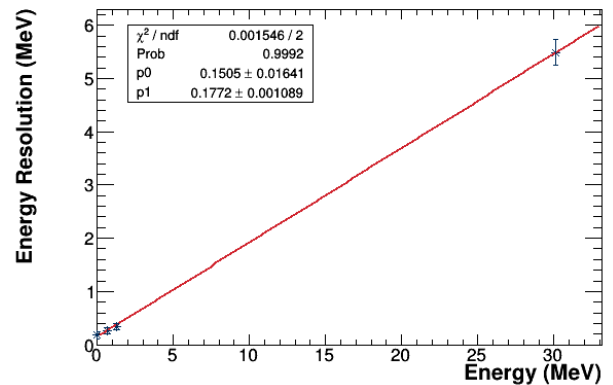
(c) F2



(d) B2

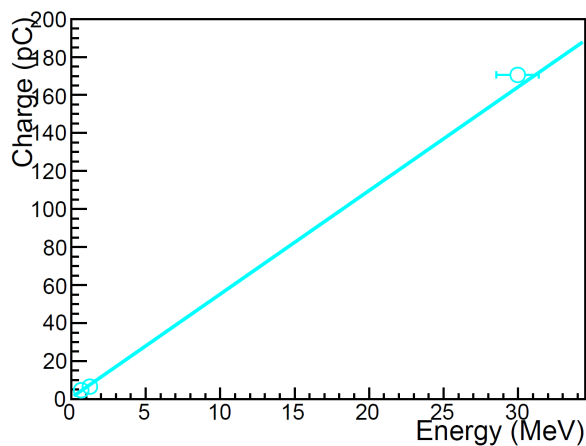


(e) F3

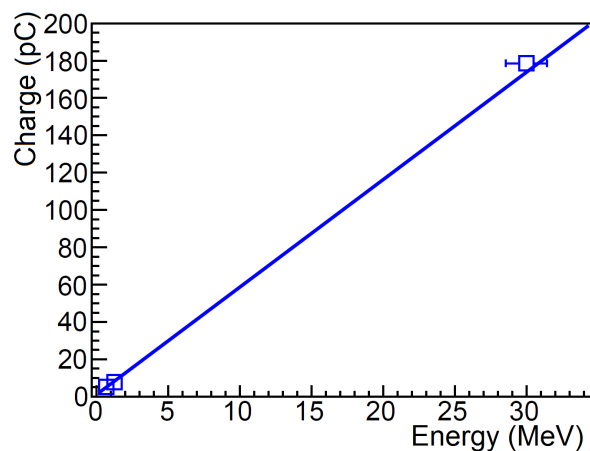


(f) B3

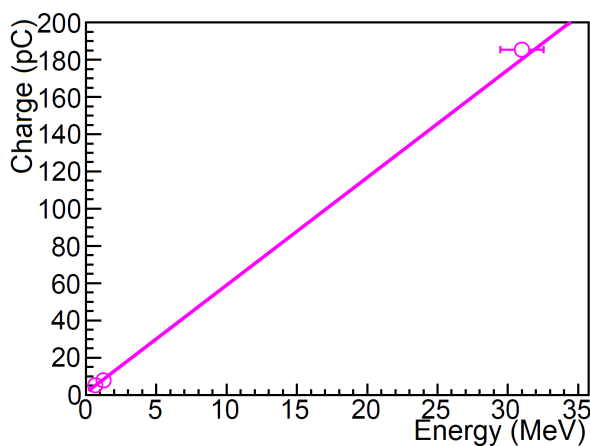
Figure A.2: Measured energy resolution for the six CsI(Tl) channels. The red line corresponds to a $y = p_0 + p_1x$ linear fit of the energy resolution vs. energy. Error bars are present on all data points and correspond to the error on the *RMS* parameter calculated by the fit algorithm.



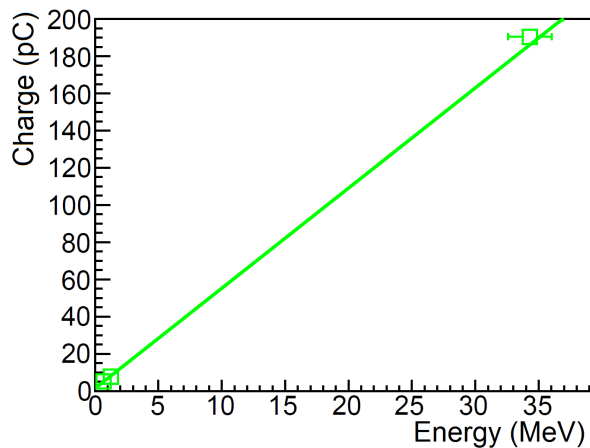
(a) F1



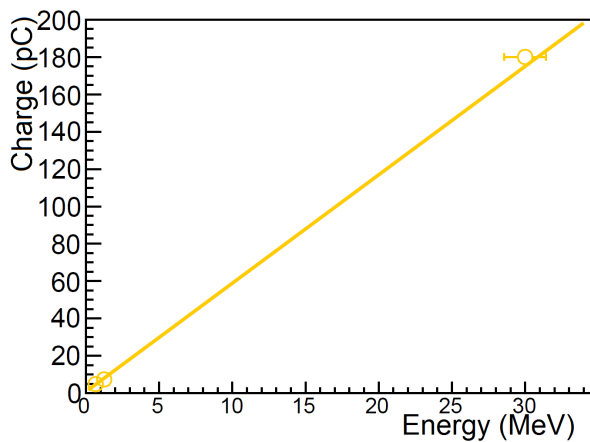
(b) B1



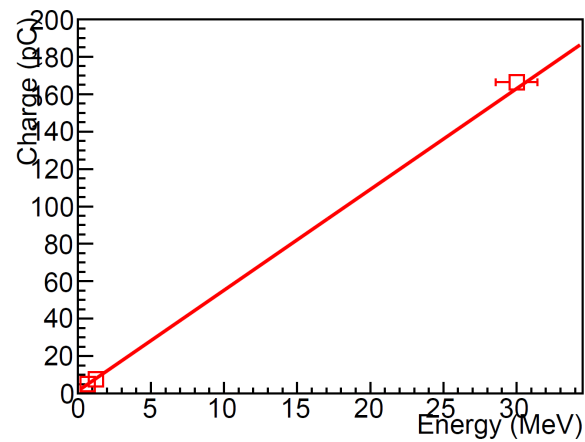
(c) F2



(d) B2

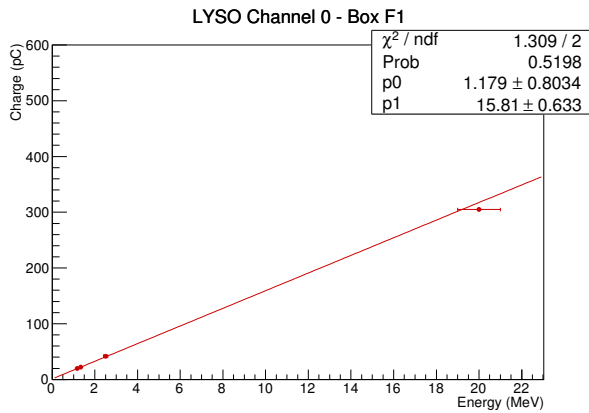


(e) F3

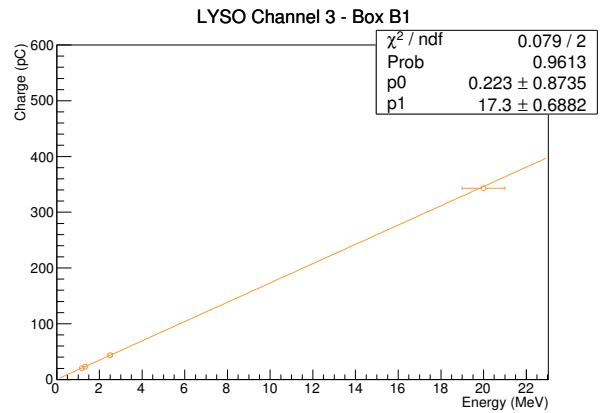


(f) B3

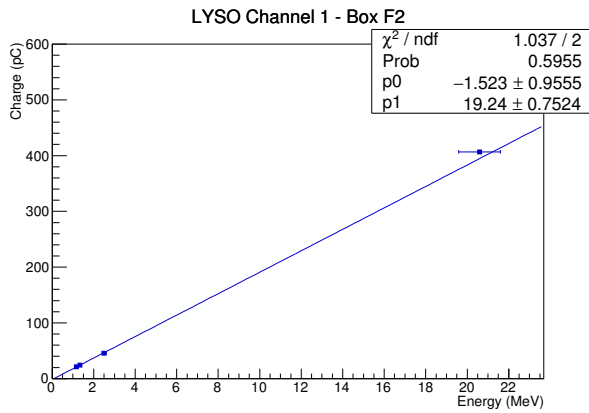
Figure A.3: Calibration curves for the six CsI(pure) channels. The line corresponds to a linear fit of the measured charge vs. energy. Credits: Riccardo de Sangro (2016).



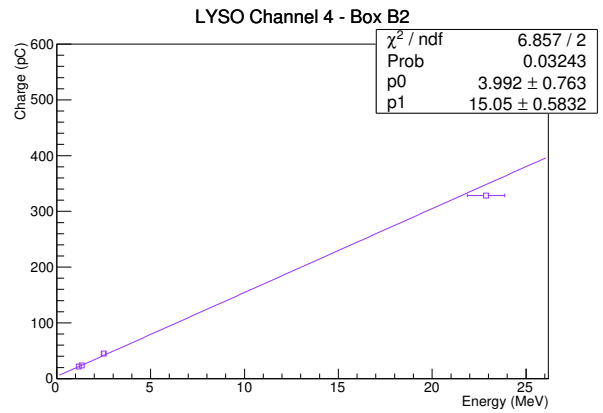
(a) F1



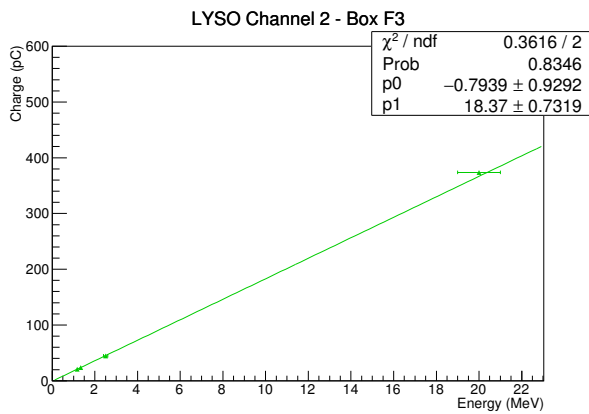
(b) B1



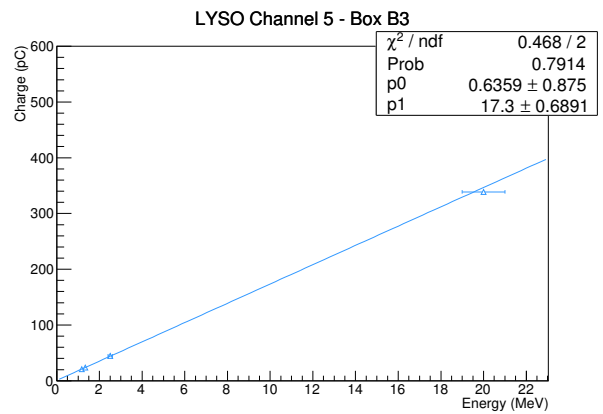
(c) F2



(d) B2



(e) F3



(f) B3

Figure A.4: Calibration curves for the six LYSO channels. The line corresponds to a $y = p_0 + p_1x$ linear fit of the measured charge vs. energy. In the notation of Equation 4.8, $c = p_0$ and $b = p_1$. Credits: Alessandro Rossi (2016).

A.2 Gain degradation as a function of beam dose

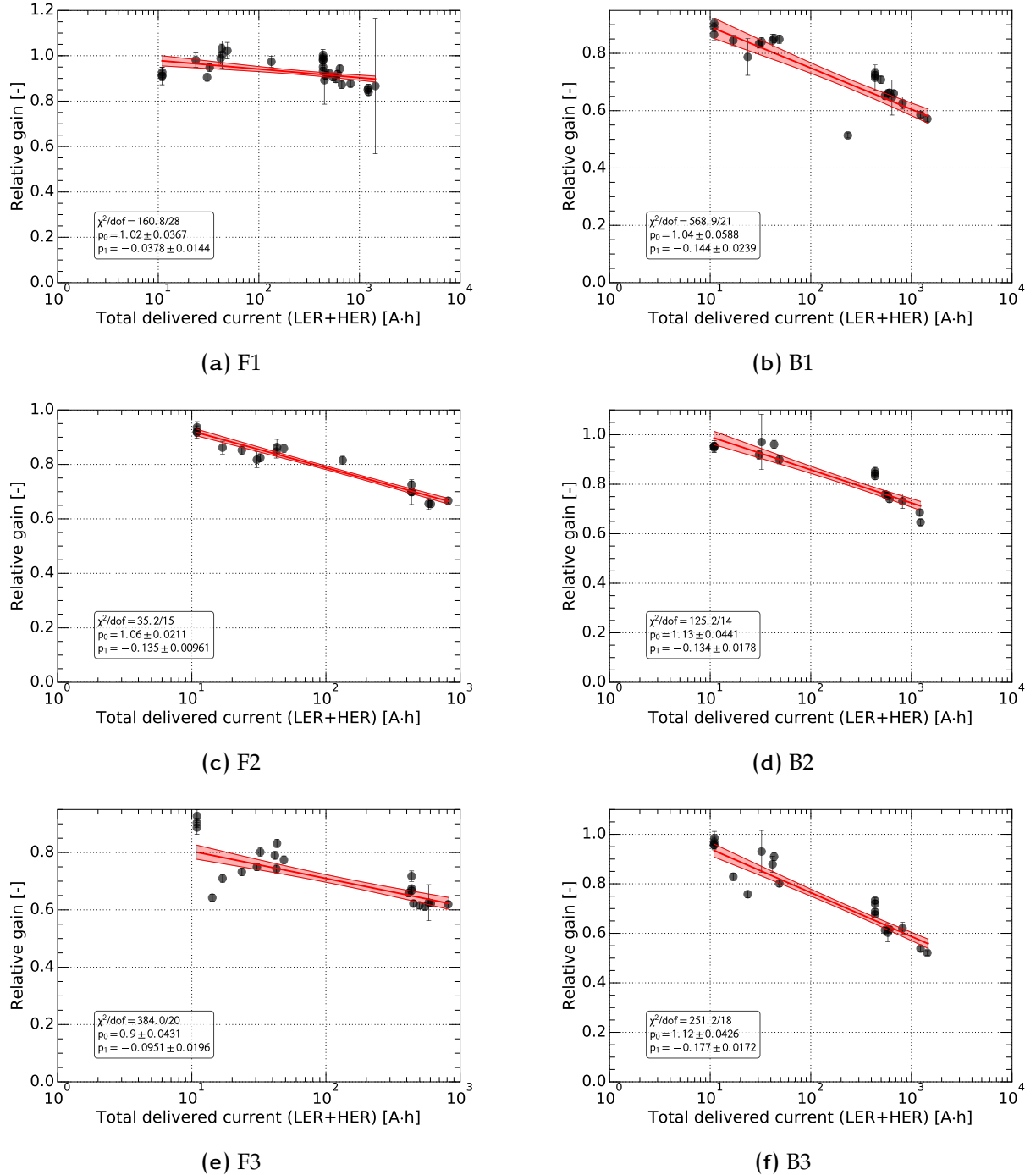


Figure A.5: Relative gain curves for the six CsI(Tl) channels. The red line corresponds to a $y = p_0 + p_1 x$ linear fit of the relative gain vs. \log_{10} of the total delivered current, and the shaded area represents the projected uncertainty on the relative gain.

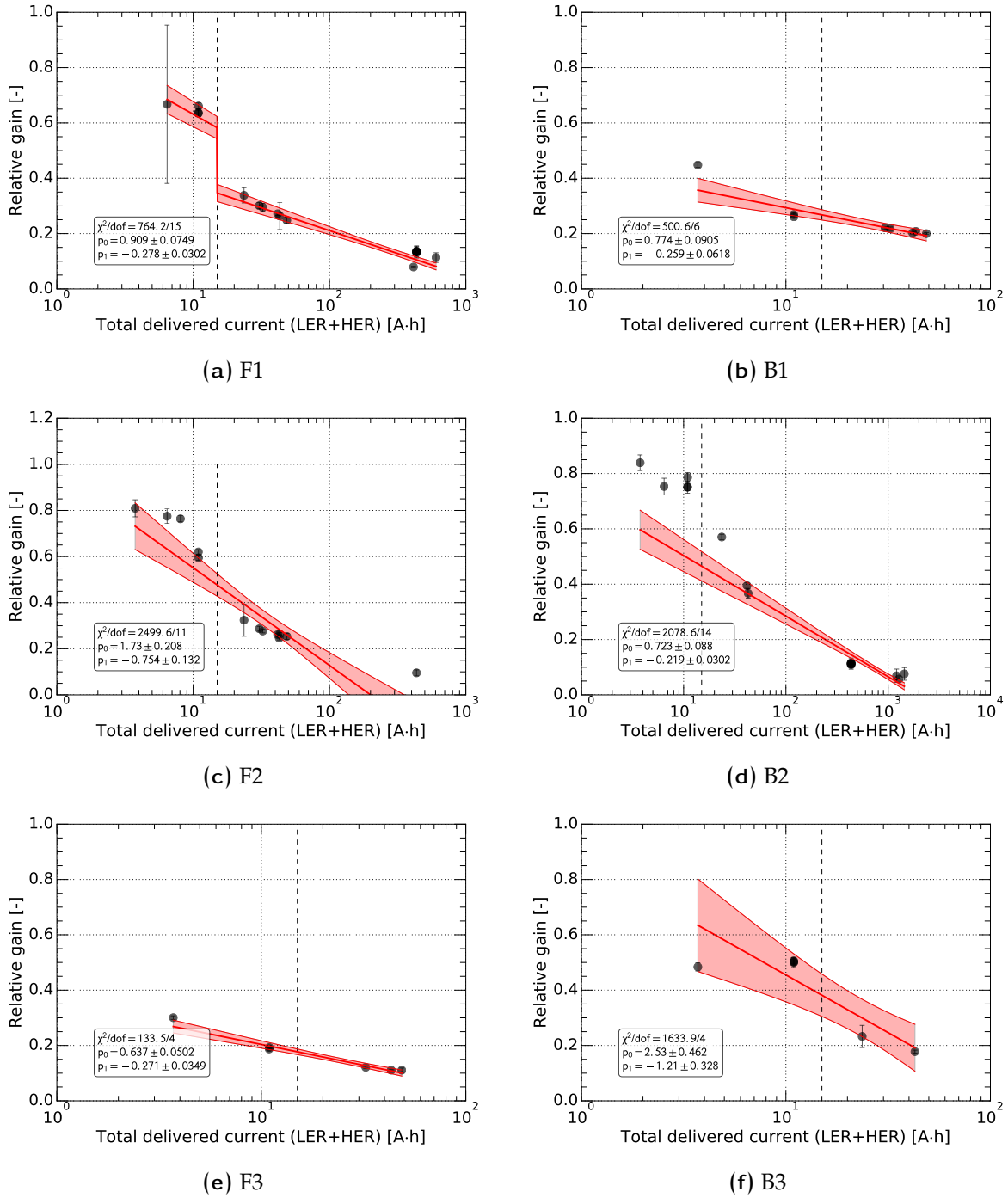
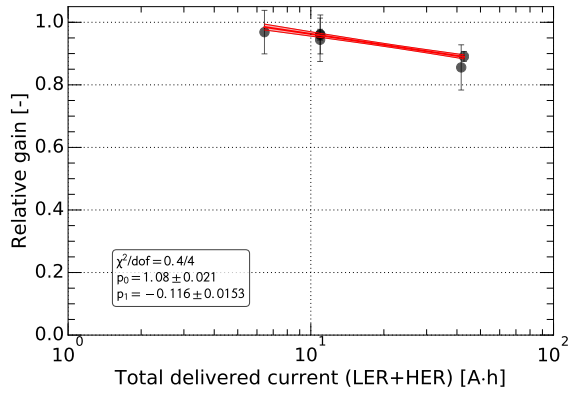
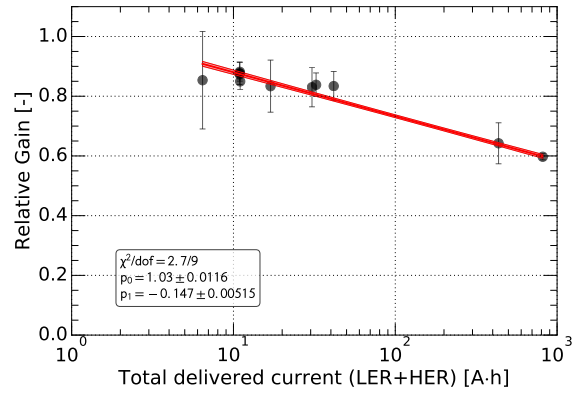


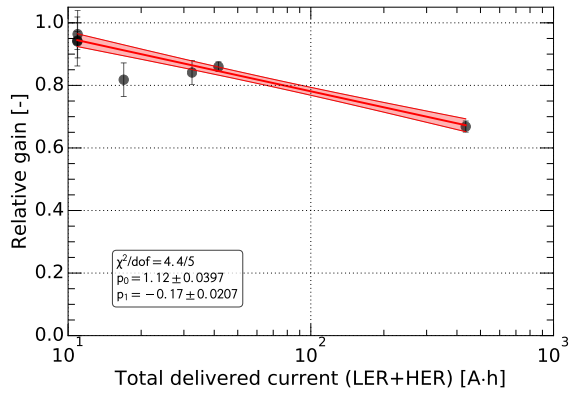
Figure A.6: Relative gain curves for the six CsI(pure) channels. The red line corresponds to a $y = p_0 + p_1x$ linear fit of the relative gain vs. \log_{10} of the total delivered current, and the shaded area represents the projected uncertainty on the relative gain. indicates the integrated current value when the high-voltage settings were changed in order to manually reduce the gain by a factor 2. This also explains the broken line describing the relationship. Not all channels were affected by this change.



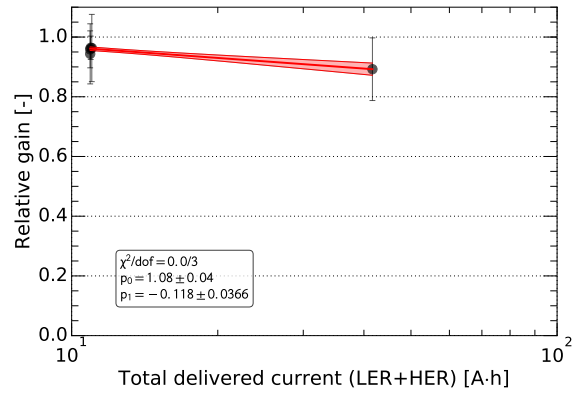
(a) F1



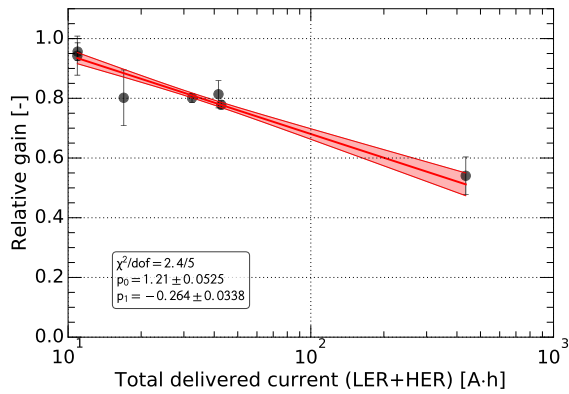
(b) B1



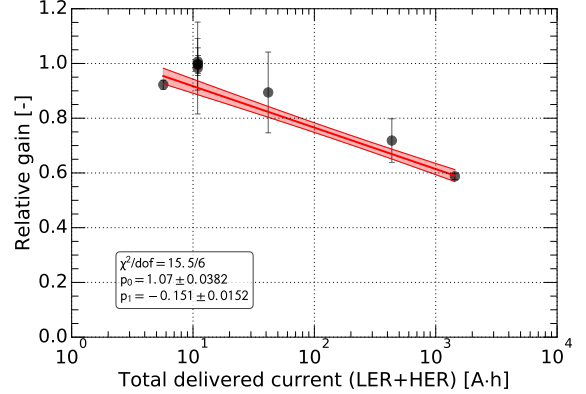
(c) F2



(d) B2



(e) F3



(f) B3

Figure A.7: Relative gain curves for the six LYSO channels. The red line corresponds to a $y = p_0 + p_1 x$ linear fit of the relative gain vs. \log_{10} of the total delivered current, and the shaded area represents the projected uncertainty on the relative gain.

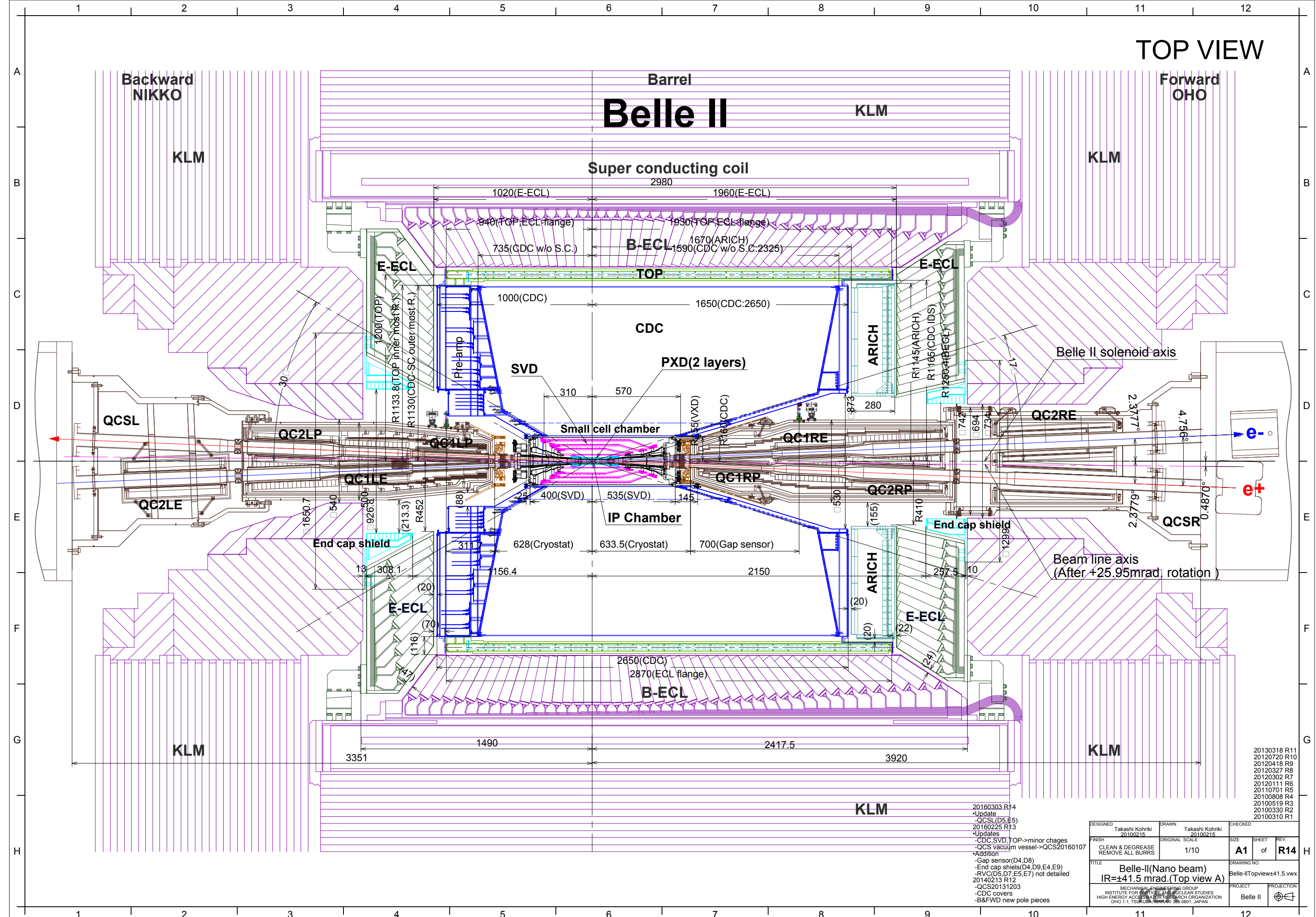
Appendix B

Mechanical Drawings

Contents

B.1 Belle-II Top View 41.5-R14	B-2
B.2 ECL Endcap Shields Envelopes ECL-SHLDS-000	B-3

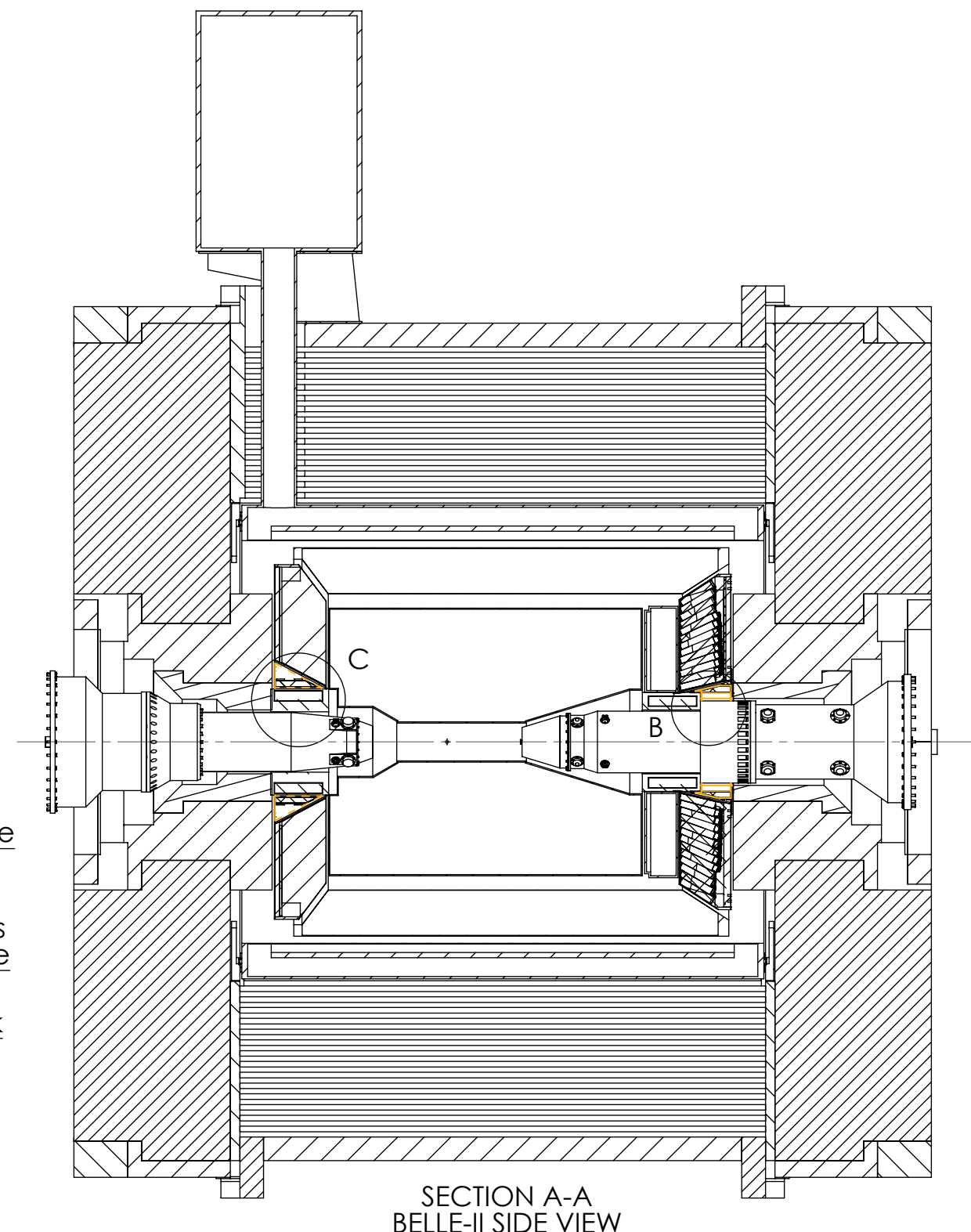
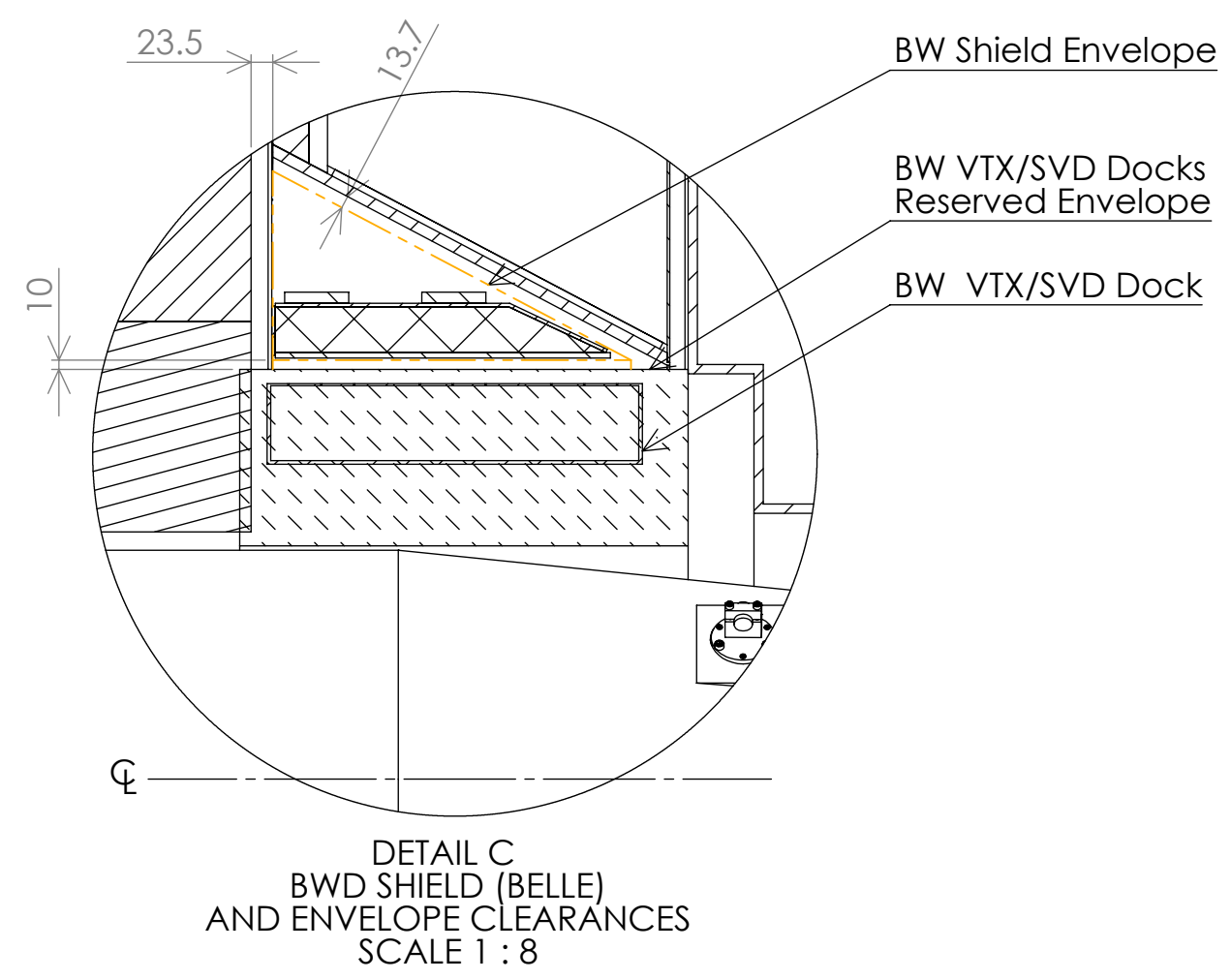
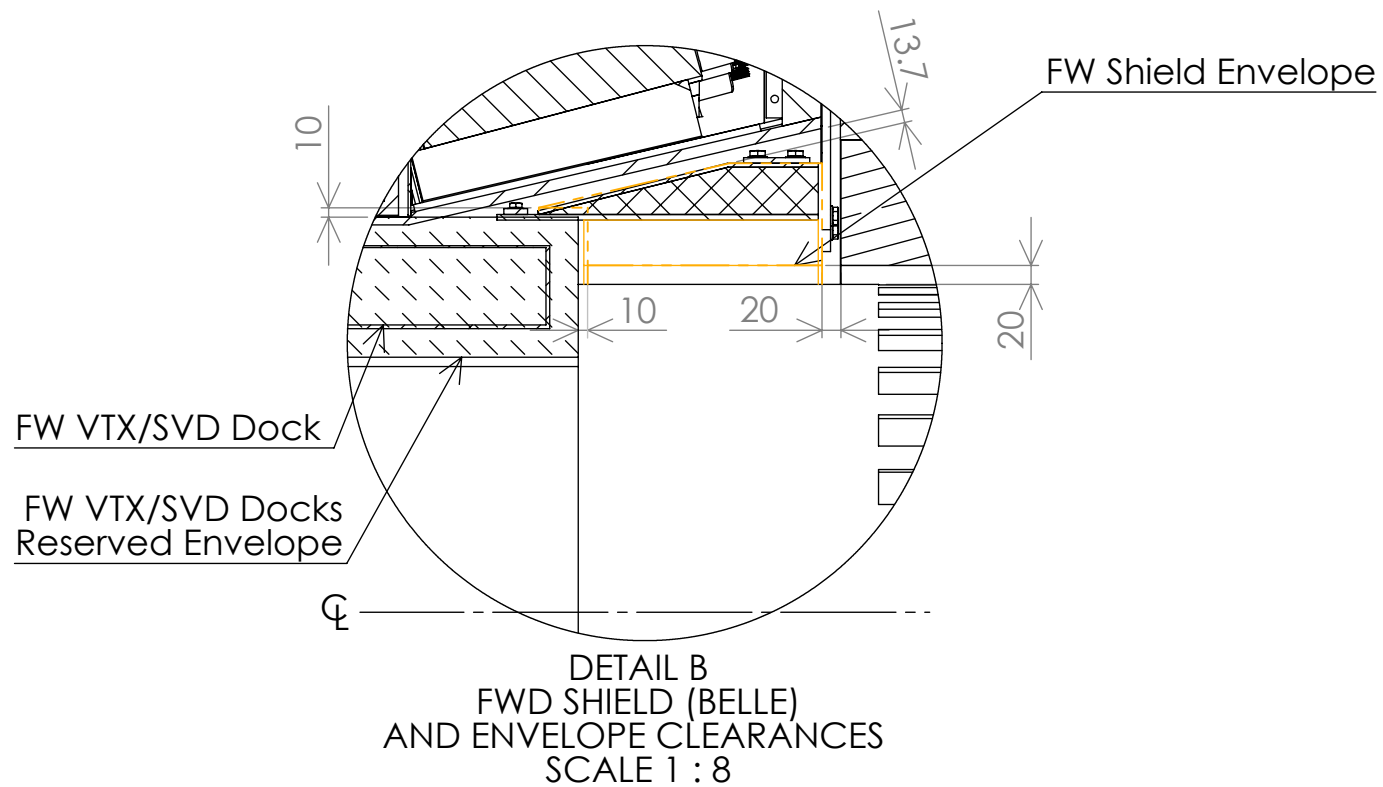
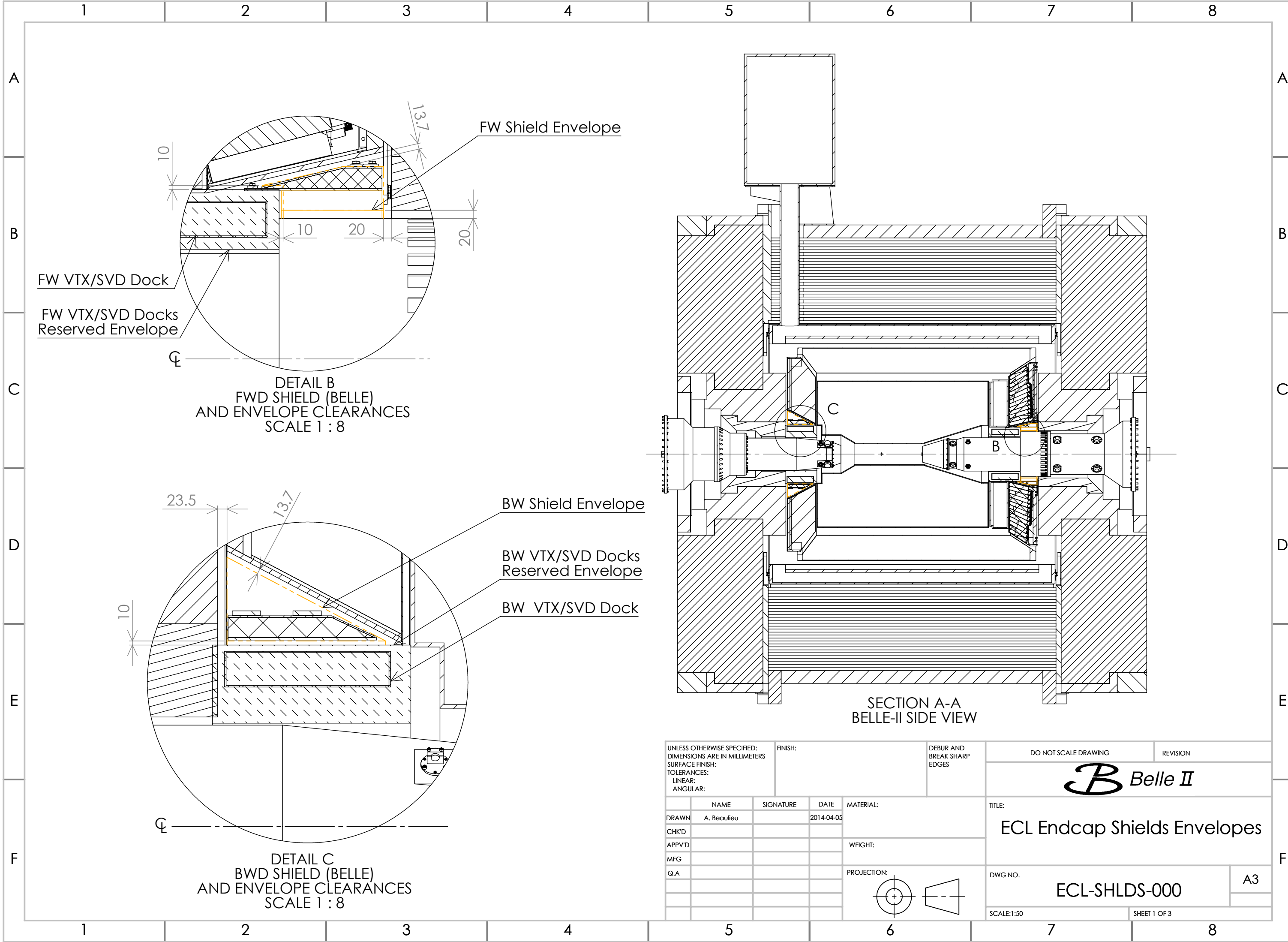
Drawing reproduced from T. Kohriki, "Belle-II(Nano beam) IR= ± 41.5 mrad.(Top view A)" KEK, (2014)

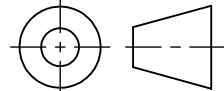


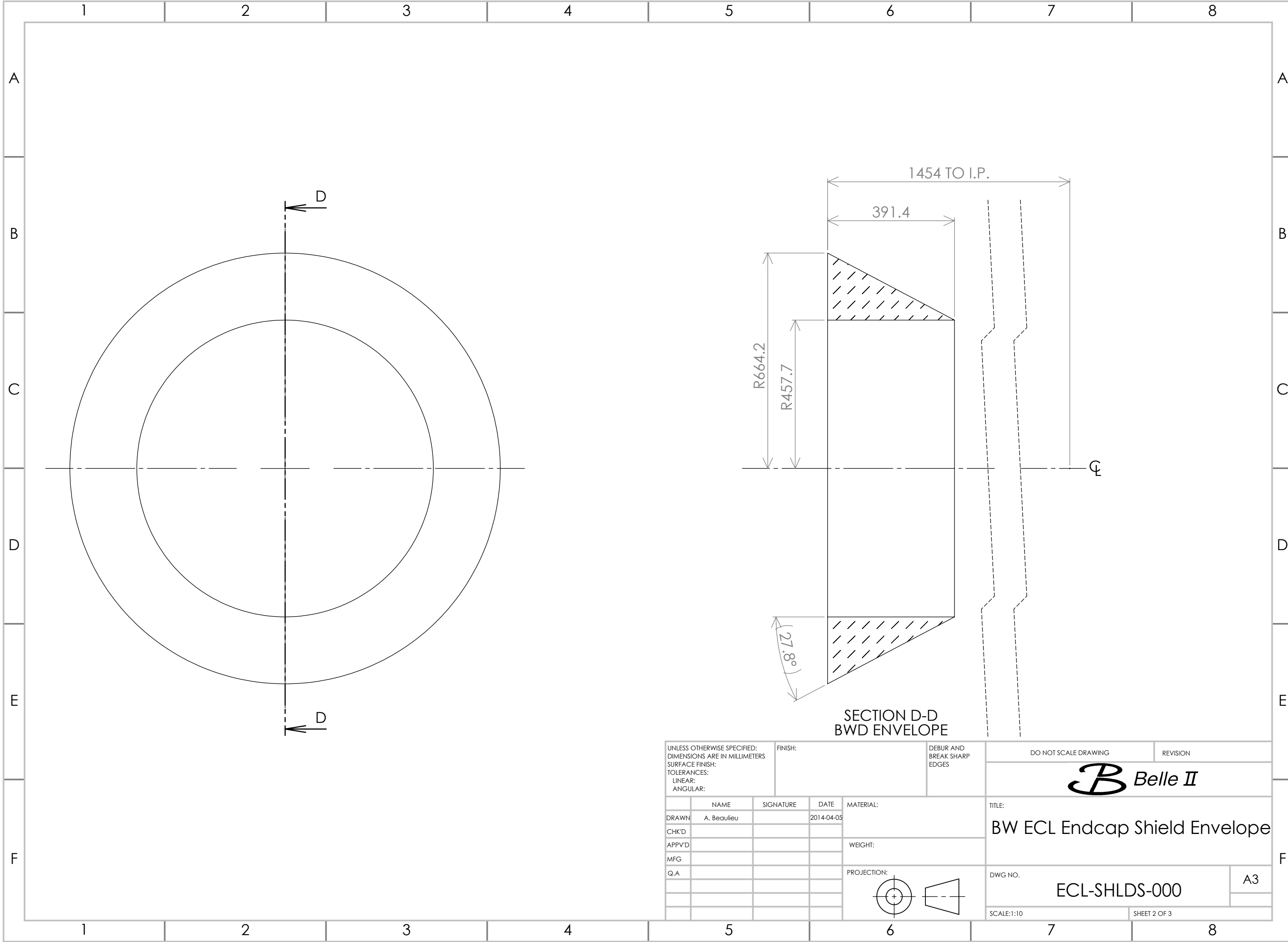
- 20160303 R14
- Update
- QCS1(D5,E5)
- 20160225 R13
- Updates
- CDC,SVD,TOP->minor changes
- QCS vacuum vessel->QCS20160107
- Addition
- Gap sensor(D4,D8)
- End cap shields(D4,D9,E4,E9)
- RVC(D5,D7,E5,E7) not detailed
- 20140213 R12
- QCS20131203
- CDC covers
- B&FWD new pole pieces

DESIGNED Takashi Kohriki 20100215	DRAWN Takashi Kohriki 20100215	CHECKED
FINISH CLEAN & DEGREASE REMOVE ALL BURRS	ORIGINAL SCALE 1/10	SIZE SHEET REV. A1 of R14
TITLE Belle-II(Nano beam) IR= ± 41.5 mrad.(Top view A)		
DRAWING NO. Belle-IITopviewz41.5.vwx		
PROJECT Belle II		

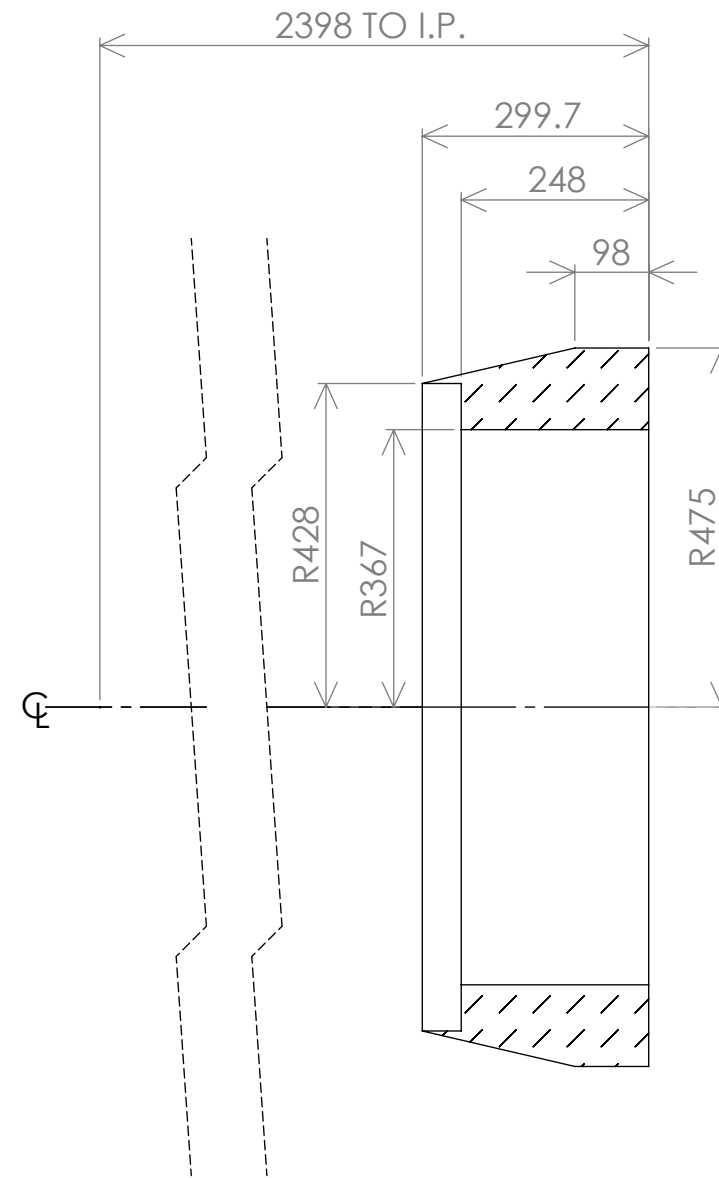
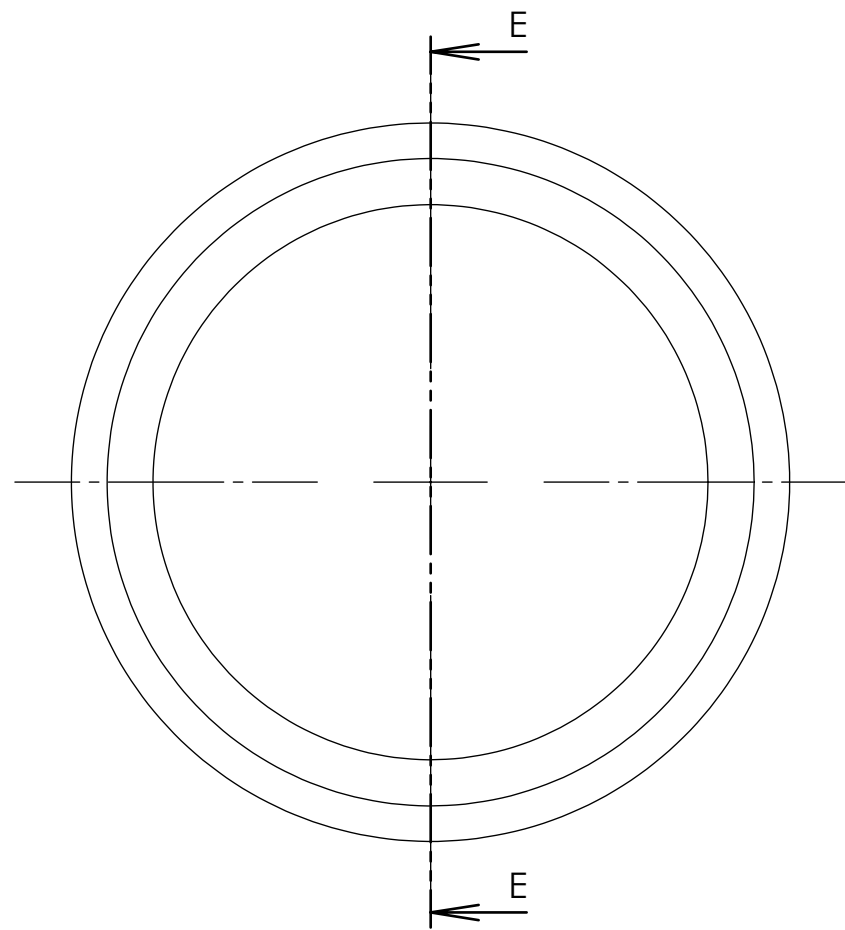
- 20130318 R11
- 20120720 R10
- 20120418 R9
- 20120327 R8
- 20120302 R7
- 20120111 R6
- 20110701 R5
- 20100808 R4
- 20100519 R3
- 20100330 R2
- 20100310 R1



UNLESS OTHERWISE SPECIFIED: DIMENSIONS ARE IN MILLIMETERS SURFACE FINISH: TOLERANCES: LINEAR: ANGULAR:		FINISH:	DEBUR AND BREAK SHARP EDGES	DO NOT SCALE DRAWING	REVISION
DRAWN A. Beaulieu		SIGNATURE	DATE 2014-04-05	 <p>Belle II</p> <p>ECL Endcap Shields Envelopes</p>	
CHK'D			MATERIAL:		
APPV'D			WEIGHT:		
MFG			PROJECTION:		
Q.A					
				DWG NO. ECL-SHLDS-000	A3
				SCALE:1:50	SHEET 1 OF 3



UNLESS OTHERWISE SPECIFIED: DIMENSIONS ARE IN MILLIMETERS SURFACE FINISH: TOLERANCES: LINEAR: ANGULAR:				FINISH:		DEBUR AND BREAK SHARP EDGES		DO NOT SCALE DRAWING		REVISION	
								B Belle II			
DRAWN A. Beaulieu				SIGNATURE		DATE 2014-04-05		TITLE: BW ECL Endcap Shield Envelope			
CHK'D								WEIGHT:			
APPV'D								PROJECTION:			
MFG										DWG NO. ECL-SHLDS-000	
Q.A								SCALE:1:10		SHEET 2 OF 3	
										A3	



SECTION E-E
FWD ENVELOPE

UNLESS OTHERWISE SPECIFIED: DIMENSIONS ARE IN MILLIMETERS SURFACE FINISH: TOLERANCES: LINEAR: ANGULAR:				FINISH:		DEBUR AND BREAK SHARP EDGES		DO NOT SCALE DRAWING		REVISION	
								B Belle II			
DRAWN A. Beaulieu				SIGNATURE		DATE 2014-04-05		MATERIAL:		TITLE: FW ECL Endcap Shield Envelope	
CHK'D								WEIGHT:			
APPV'D								PROJECTION:		DWG NO. ECL-SHLDS-000	
MFG										A3	
Q.A										SCALE:1:10	

Appendix C

Results of the ECL shields conceptual design studies

The next sections contain the performance plots for the five set of concepts. They are all organized as follows. First the result of a material scan is presented; these show the material density in units of inverse radiation length $1/x_0$. Second, the map of the yearly dose in the entire ECL is presented. Third, the total yearly dose averaged over the crystal θ_{ID} is presented. The last plot is the yearly neutron flux in the diodes, again as a function of crystal row index.

For the θ_{ID} averages, the small gray dots correspond to the result averaged over a single row, while the large black dots with error bars represent an average over nominally 4 rows (sometimes less to exclude the innermost rows and avoid averaging together end-cap rows with barrel rows). The error bars correspond to the statistical uncertainty associated with the size of the simulation samples.

Again, row 0 refers to the innermost row of crystal of the forward end-cap, whereas row 69 is the innermost row of the backward end-cap.

C.1 Without shields

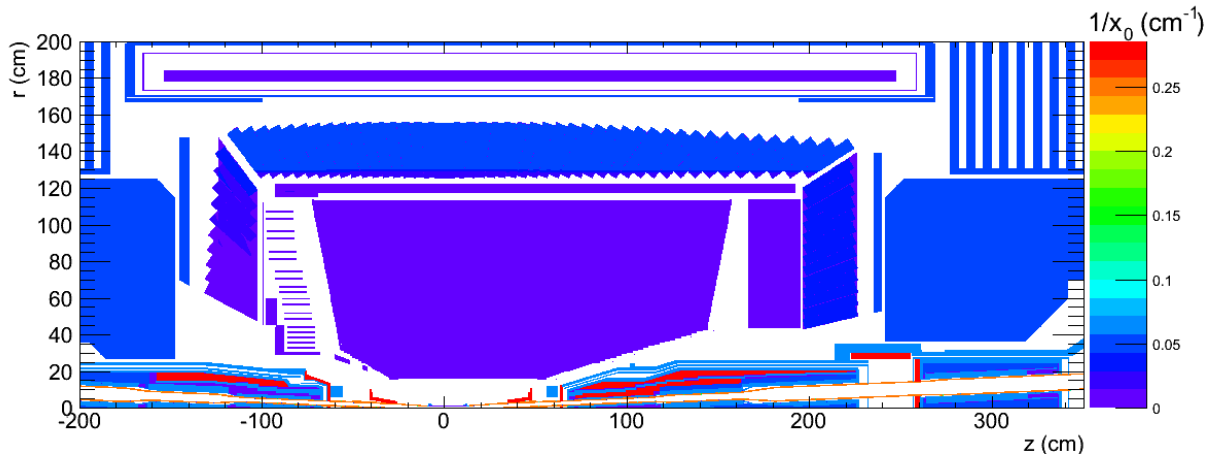


Figure C.1: Material scan without shields

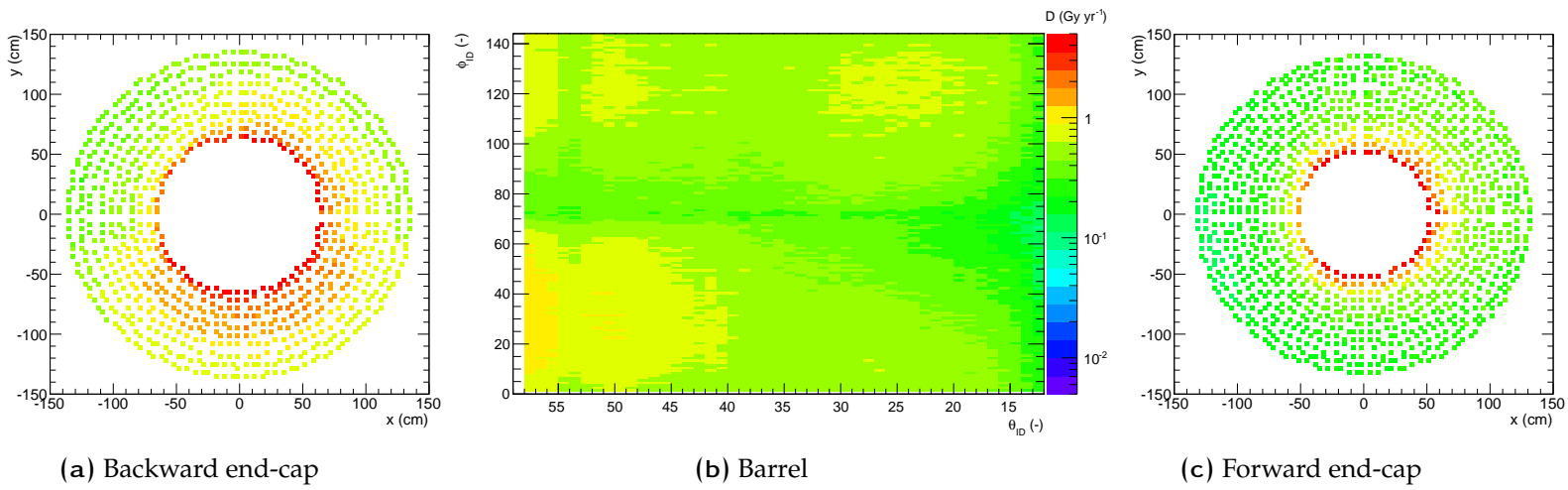


Figure C.2: Map of the does (in log scale) deposited in the ECL without shields

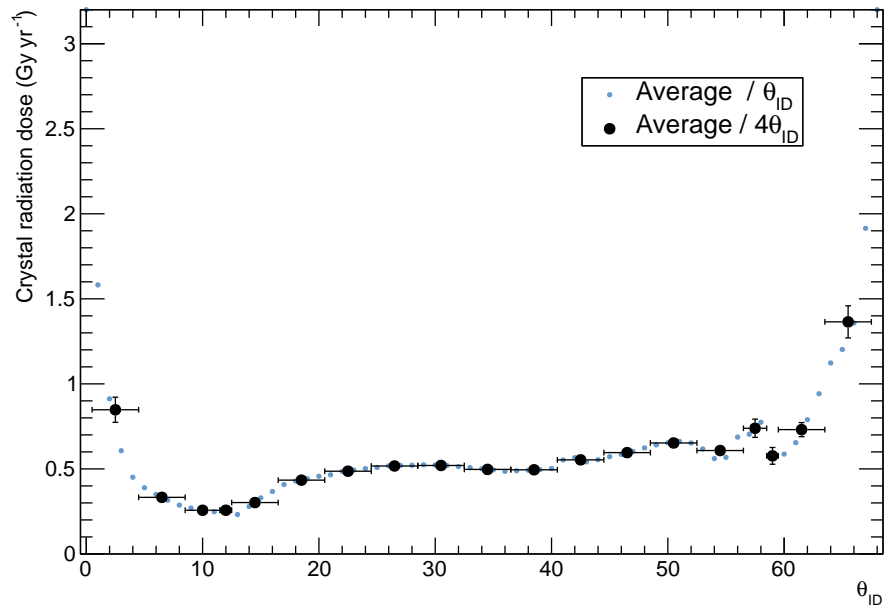


Figure C.3: Radiation dose as a function for crystal row index without shields

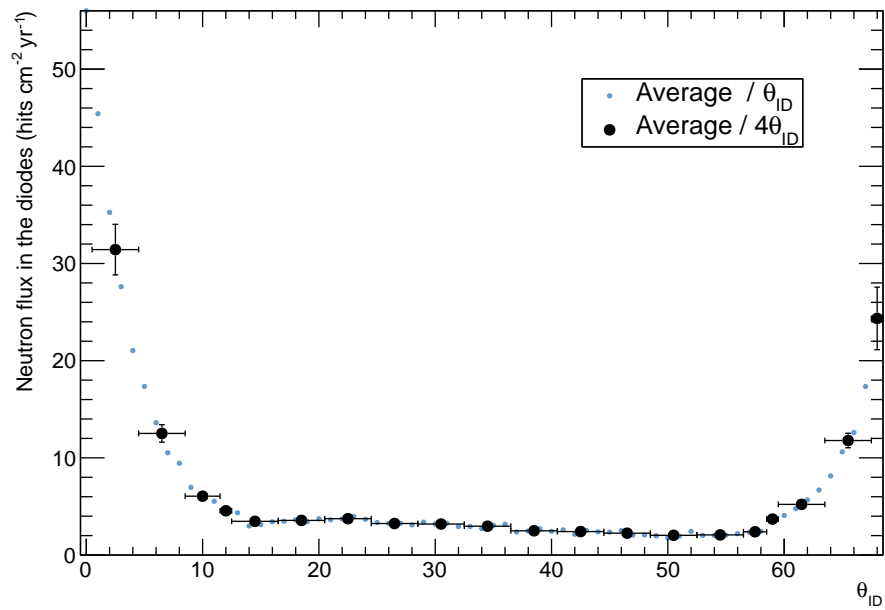


Figure C.4: Neutron flux as a function for crystal row index without shields

C.2 Concepts 0

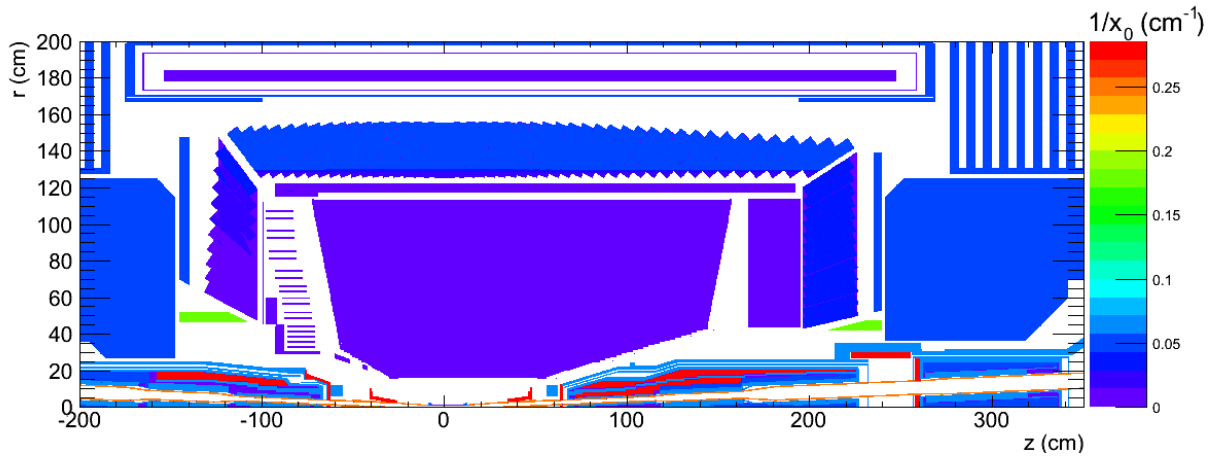


Figure C.5: Material scan of concepts 0

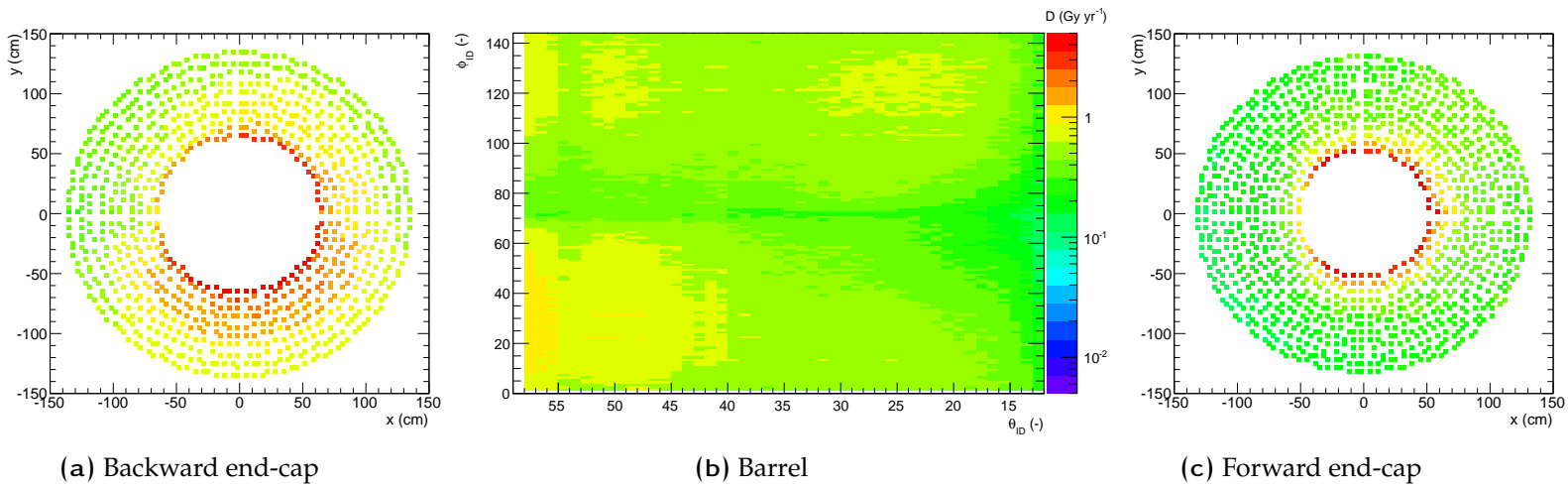


Figure C.6: Map of the dose (in log scale) deposited in the ECL with concepts 0

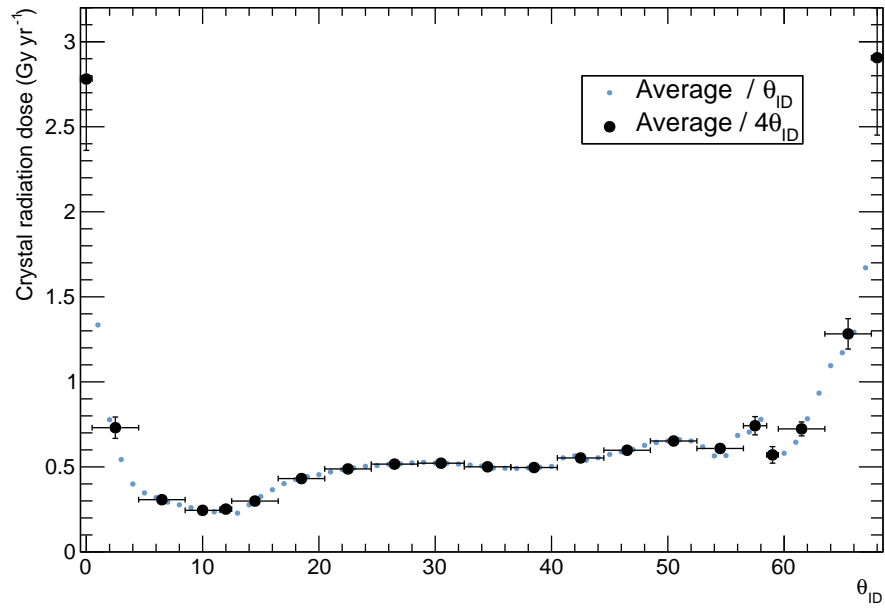


Figure C.7: Radiation dose as a function for crystal row index for concepts 0

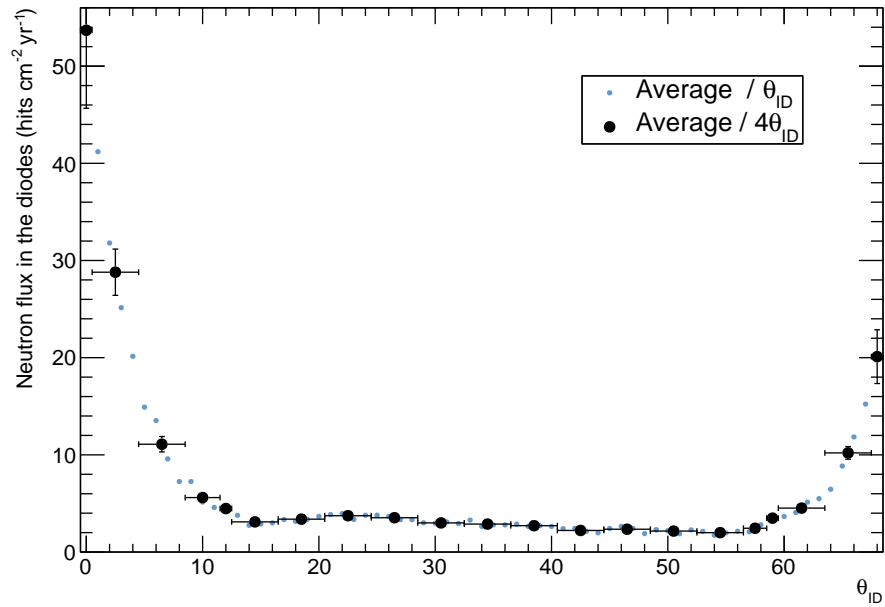


Figure C.8: Neutron flux as a function for crystal row index for concepts 0

C.3 Concepts A₁

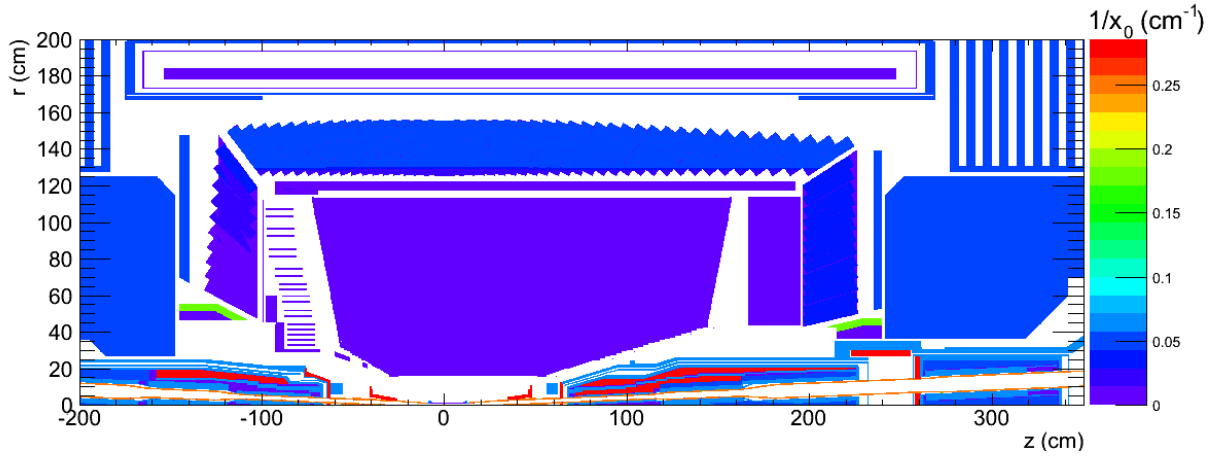


Figure C.9: Material scan of concepts A₁

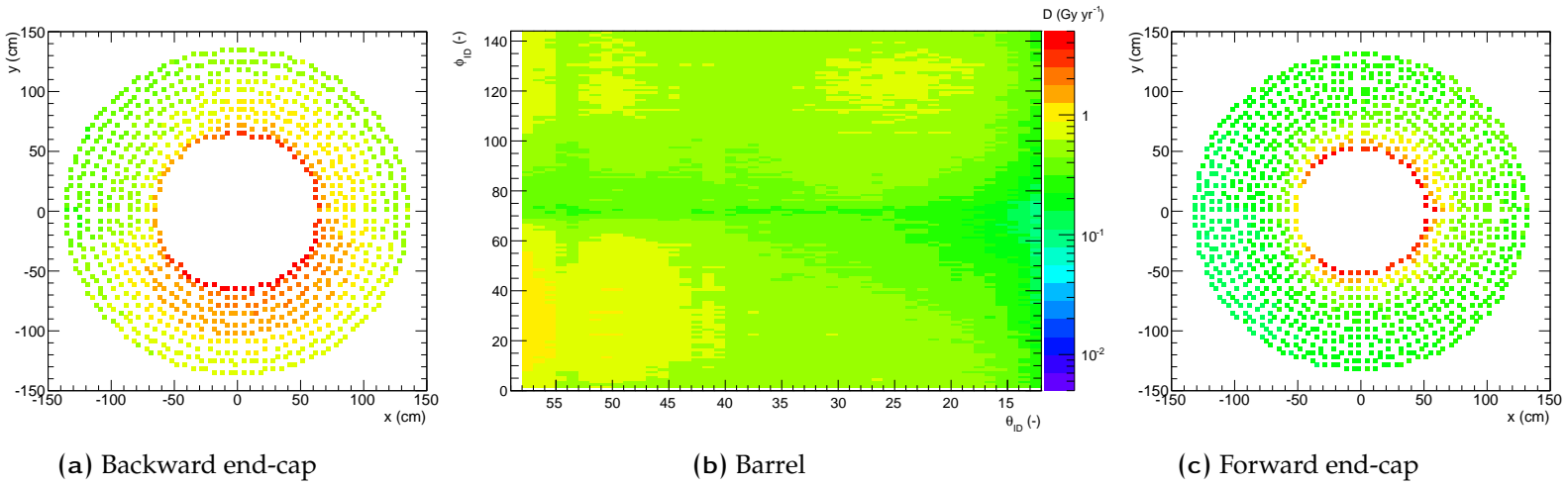


Figure C.10: Map of the dose (in log scale) deposited in the ECL with concepts A₁

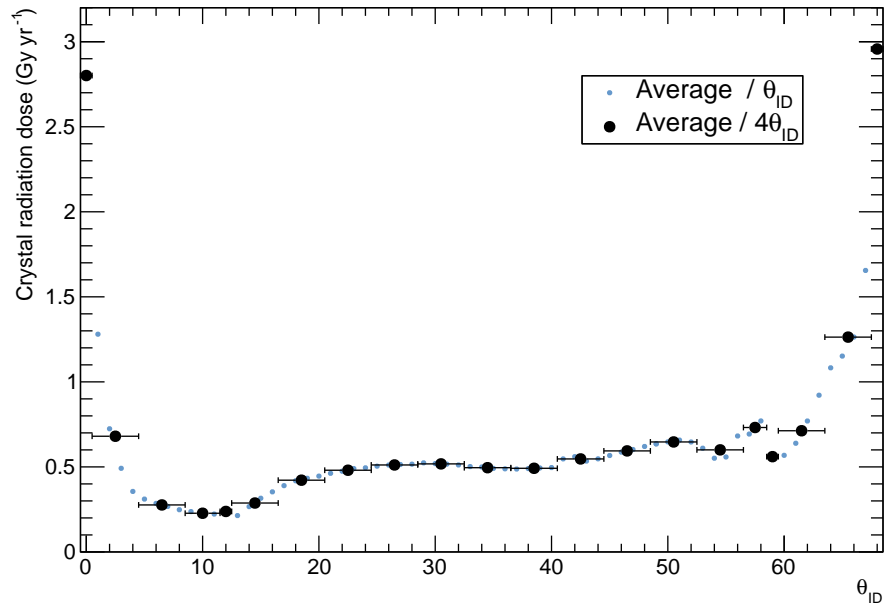


Figure C.11: Radiation dose as a function for crystal row index for concepts A₁

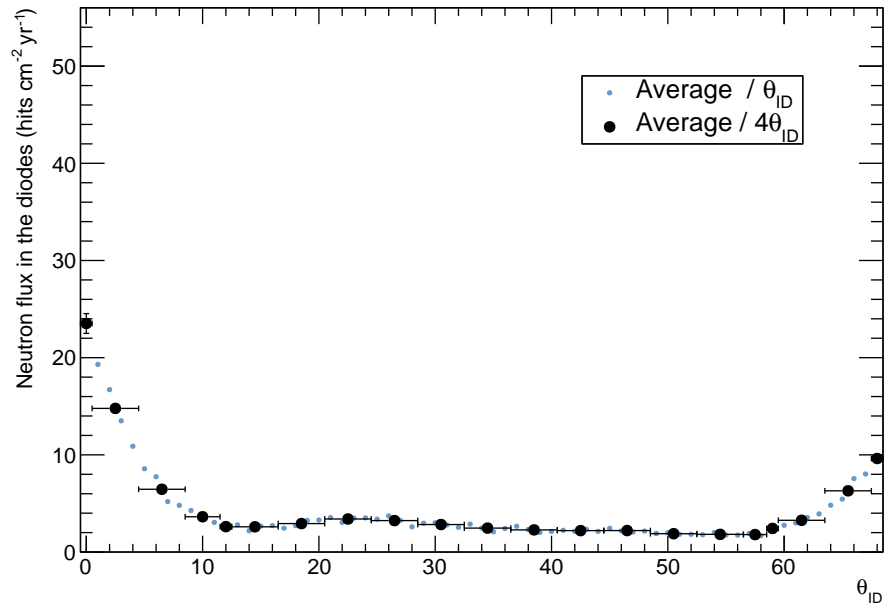


Figure C.12: Neutron flux as a function for crystal row index for concepts A₁

C.4 Concepts A₂

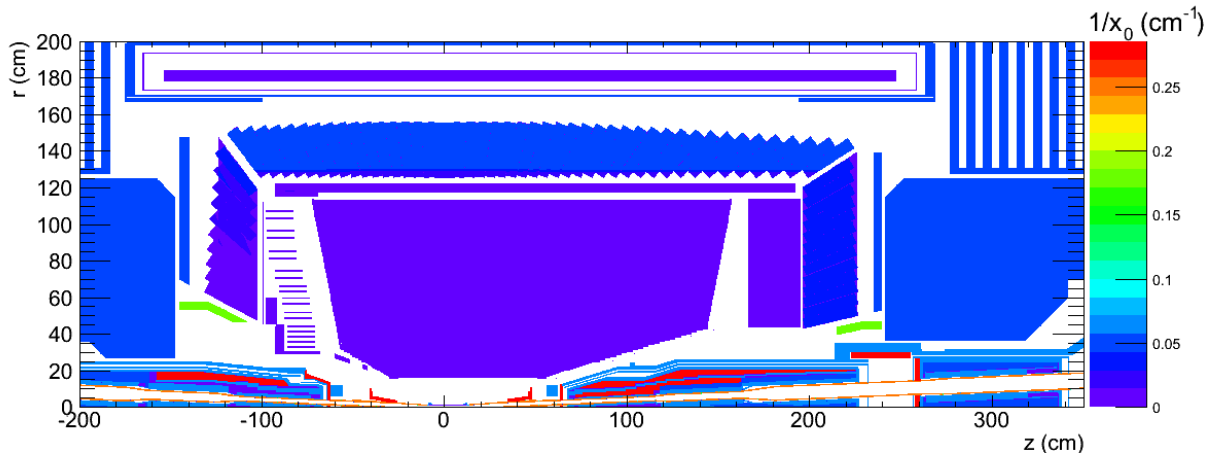


Figure C.13: Material scan of concepts A₂

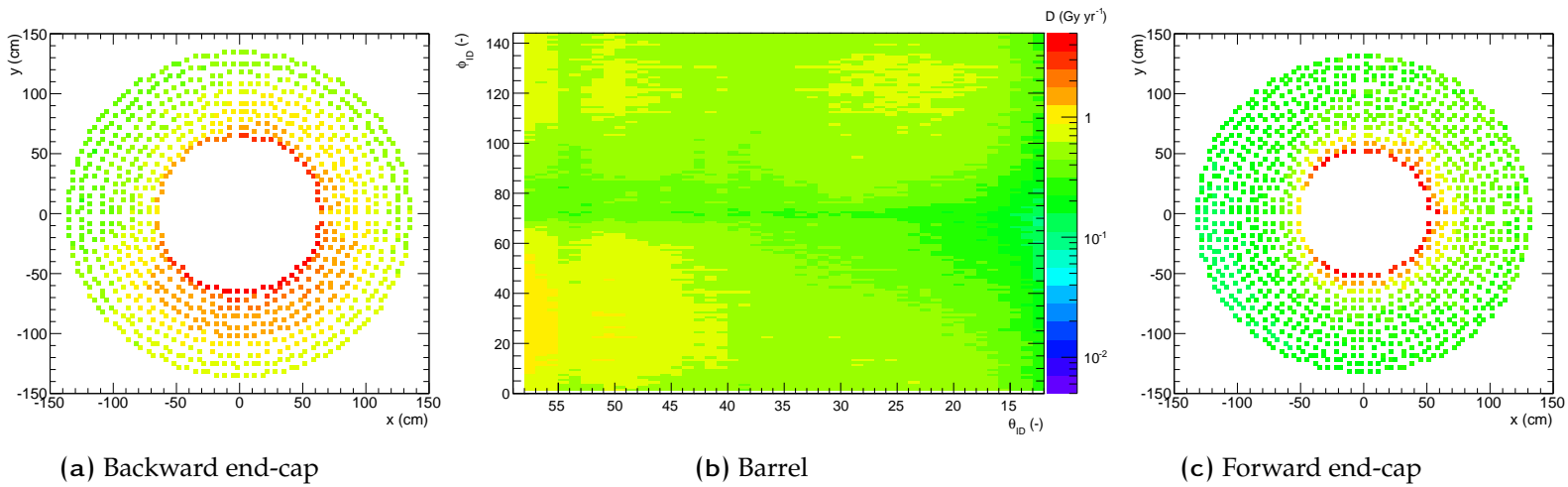


Figure C.14: Map of the dose (in log scale) deposited in the ECL with concepts A₂

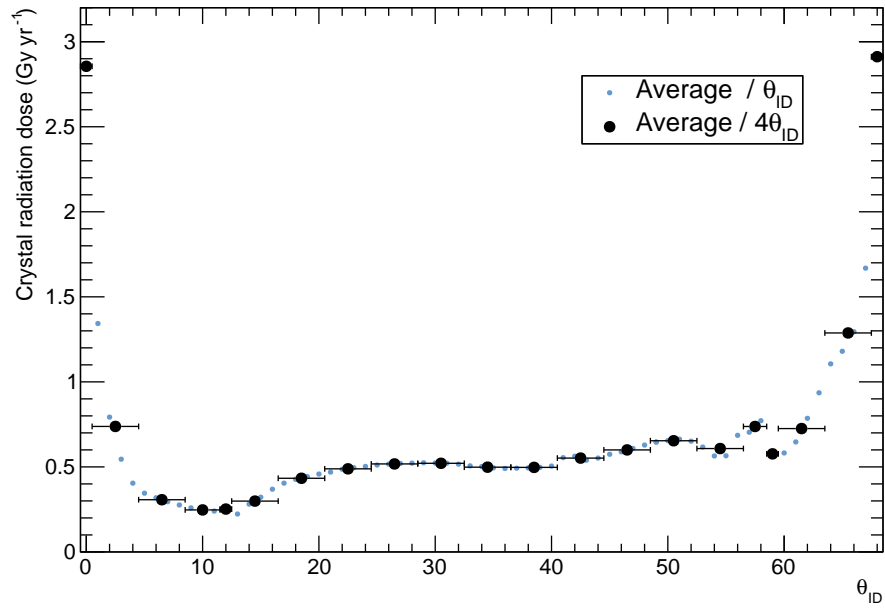


Figure C.15: Radiation dose as a function for crystal row index for concepts A₂

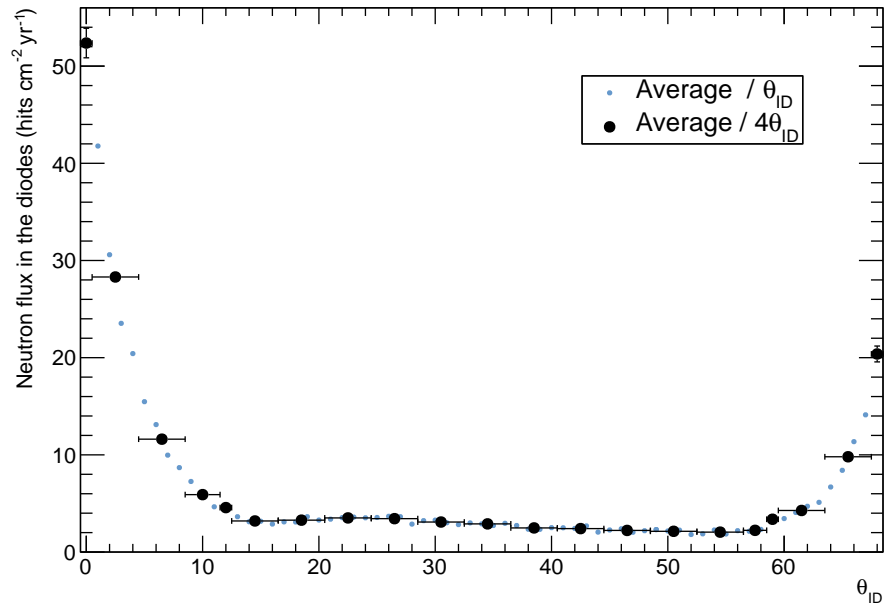


Figure C.16: Neutron flux as a function for crystal row index for concepts A₂

C.5 Concepts B₁

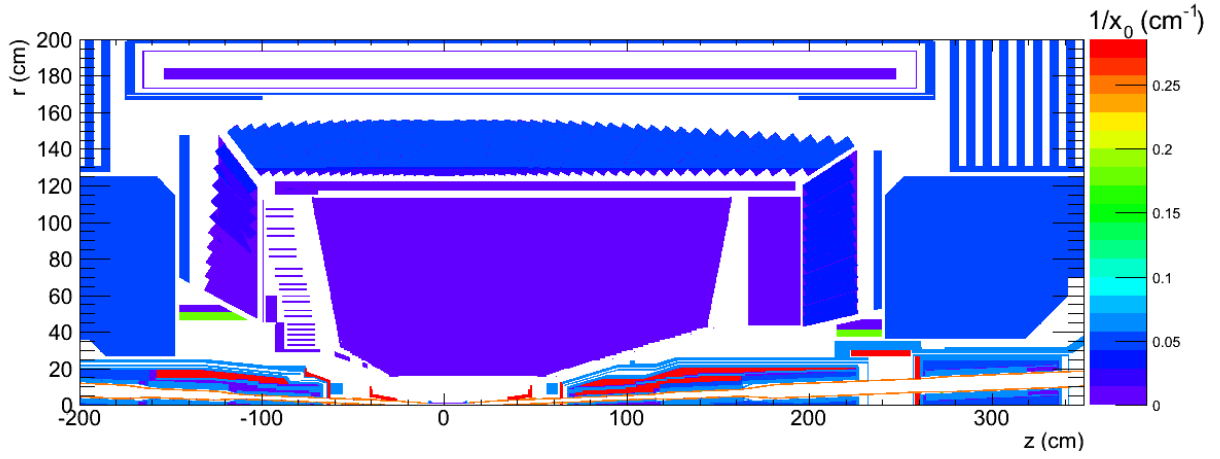


Figure C.17: Material scan of concepts B₁

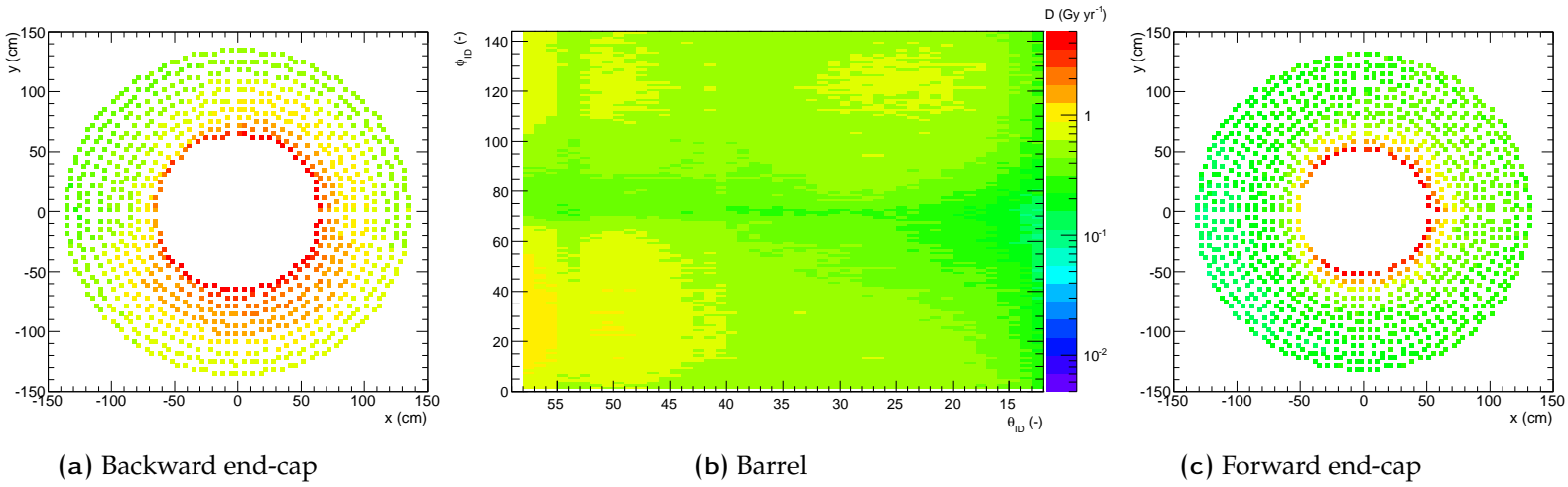


Figure C.18: Map of the dose (in log scale) deposited in the ECL with concepts B₁

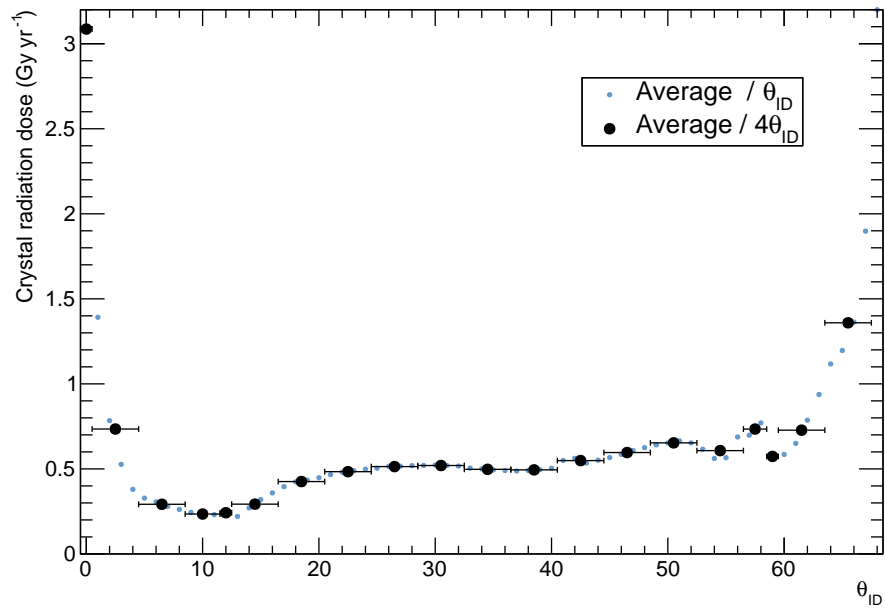


Figure C.19: Radiation dose as a function for crystal row index for concepts B₁

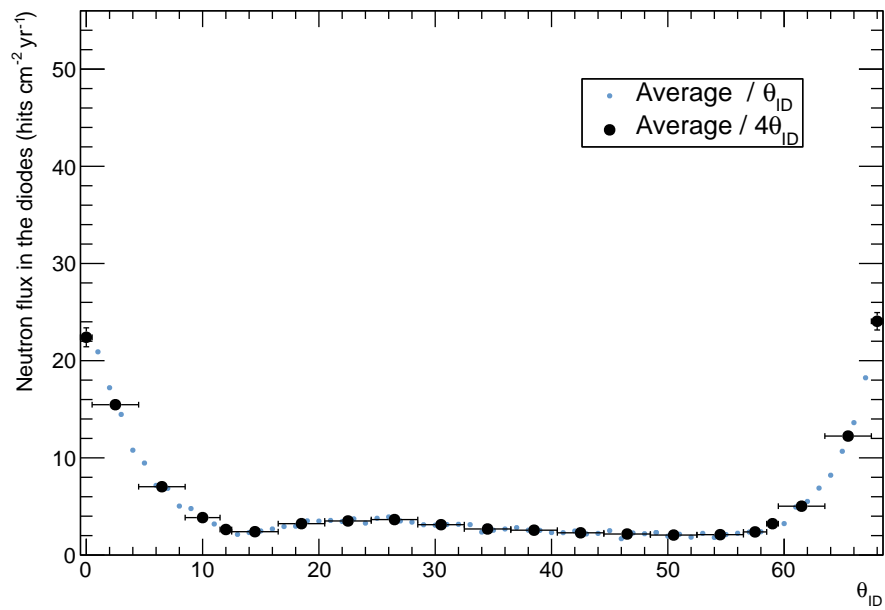


Figure C.20: Neutron flux as a function for crystal row index for concepts B₁

C.6 Concepts B₂

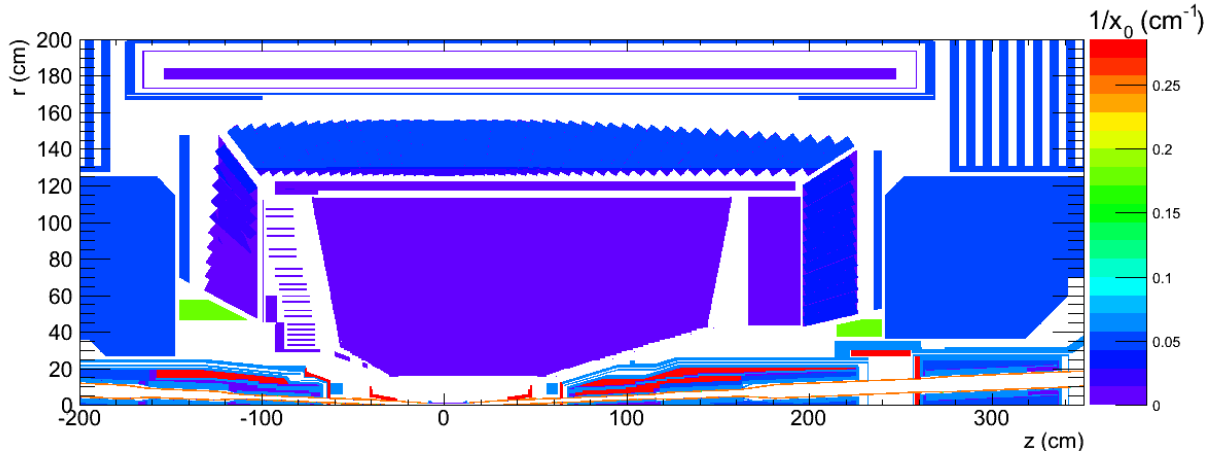


Figure C.21: Material scan of concepts B₂

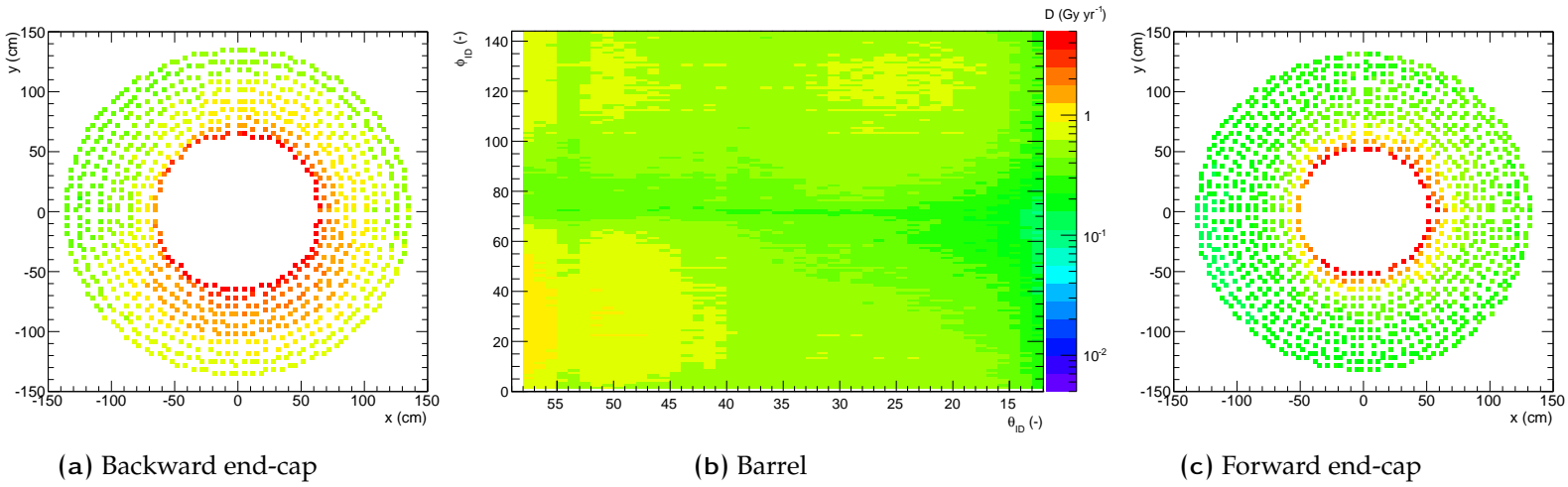


Figure C.22: Map of the dose (in log scale) deposited in the ECL with concepts B₂

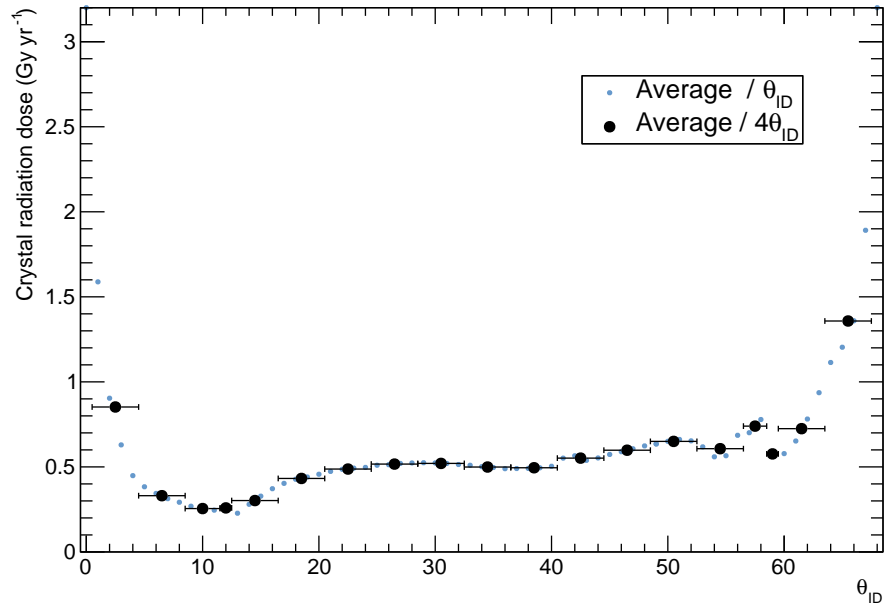


Figure C.23: Radiation dose as a function for crystal row index for concepts B₂

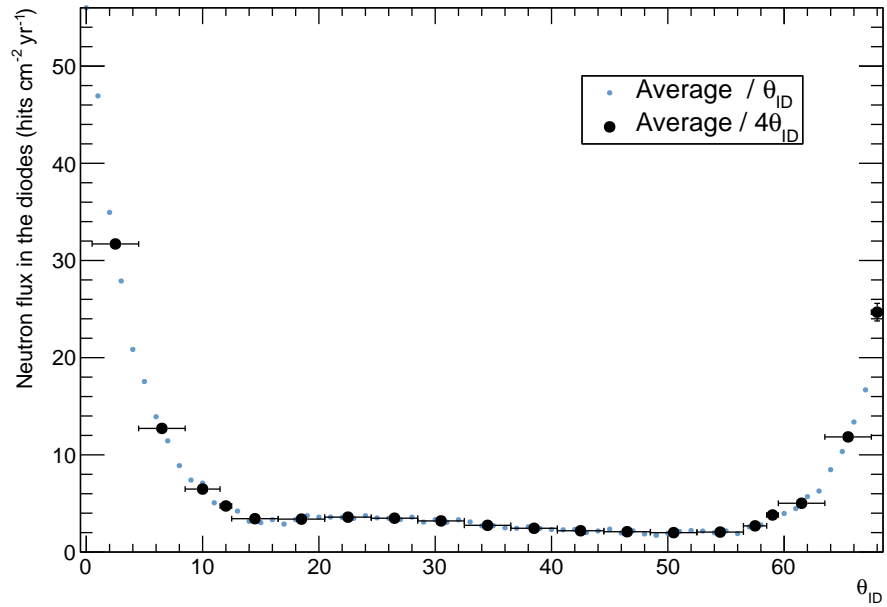


Figure C.24: Neutron flux as a function for crystal row index for concepts B₂

C.7 Concepts C_1

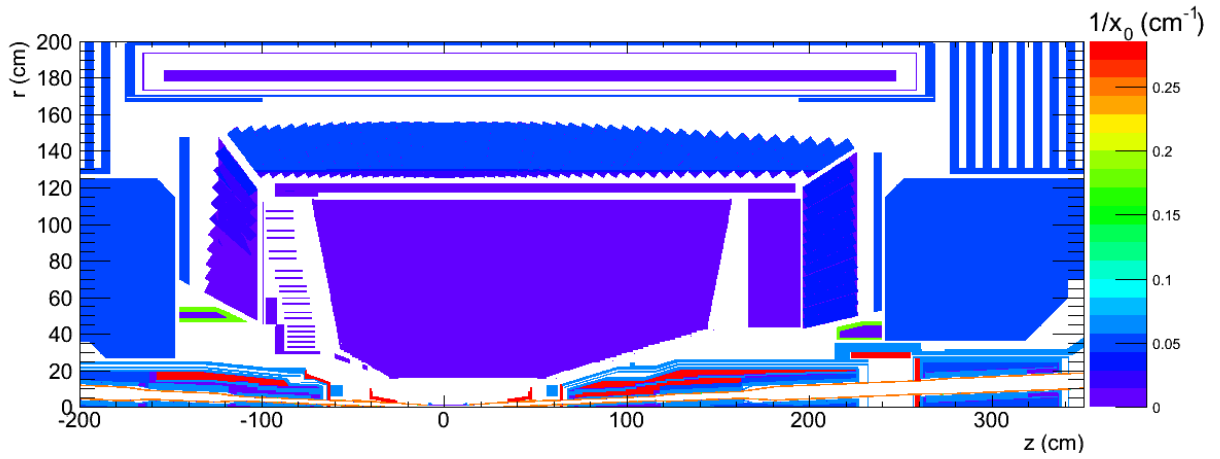


Figure C.25: Material scan of concepts C_1

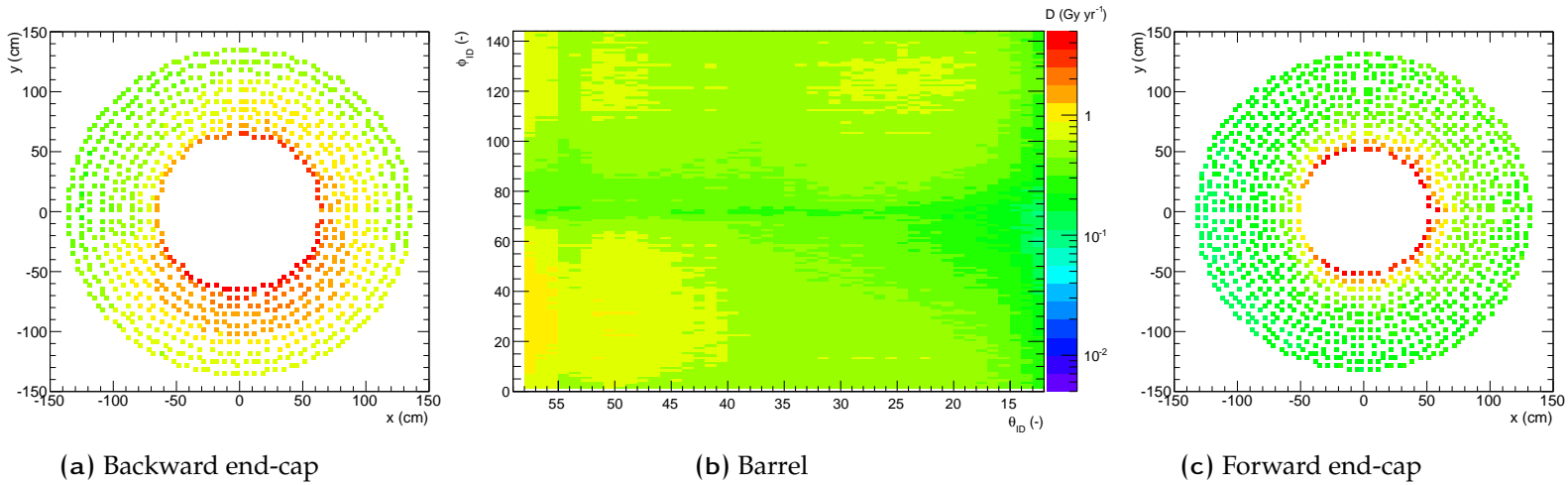


Figure C.26: Map of the dose (in log scale) deposited in the ECL with concepts C_1

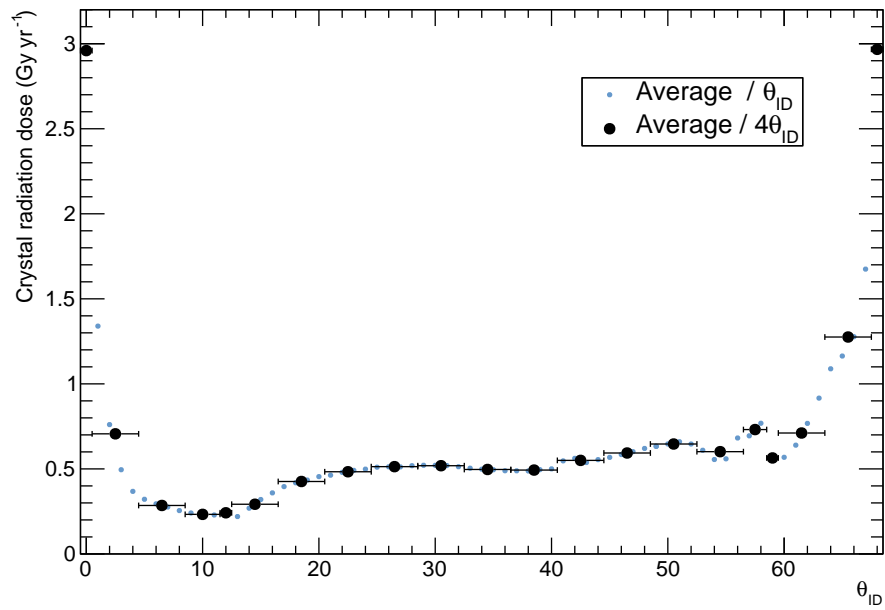


Figure C.27: Radiation dose as a function for crystal row index for concepts C_1

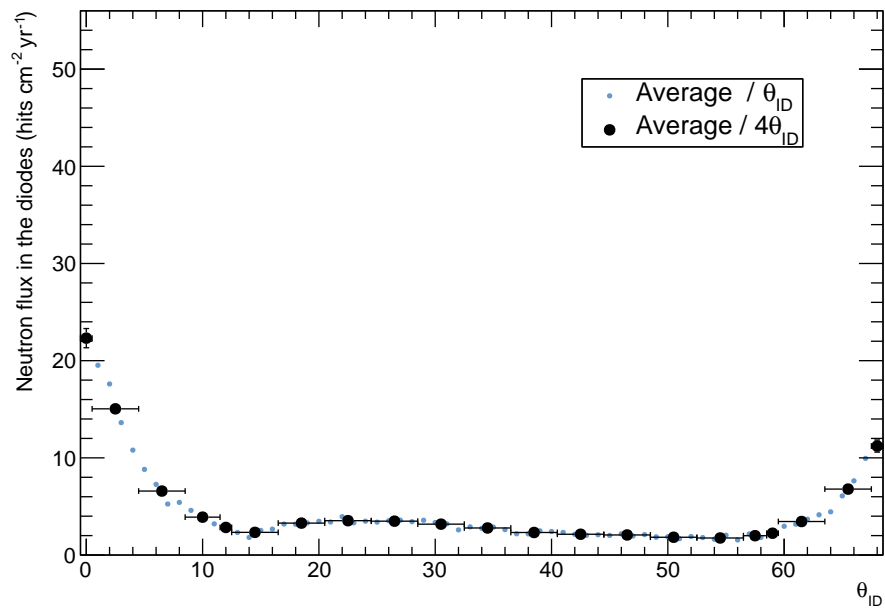


Figure C.28: Neutron flux as a function for crystal row index for concepts C_1

C.8 Concepts C₂

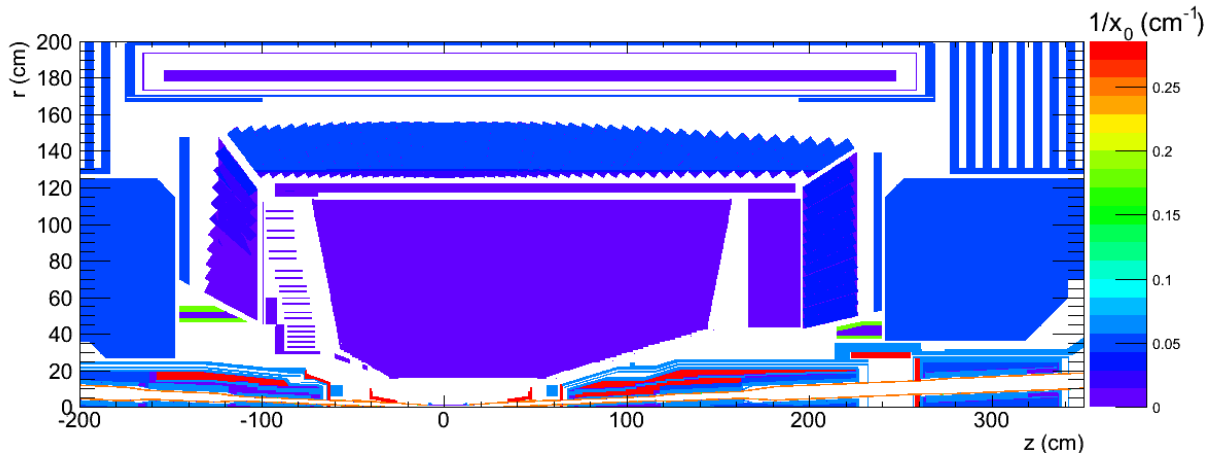


Figure C.29: Material scan of concepts C₂

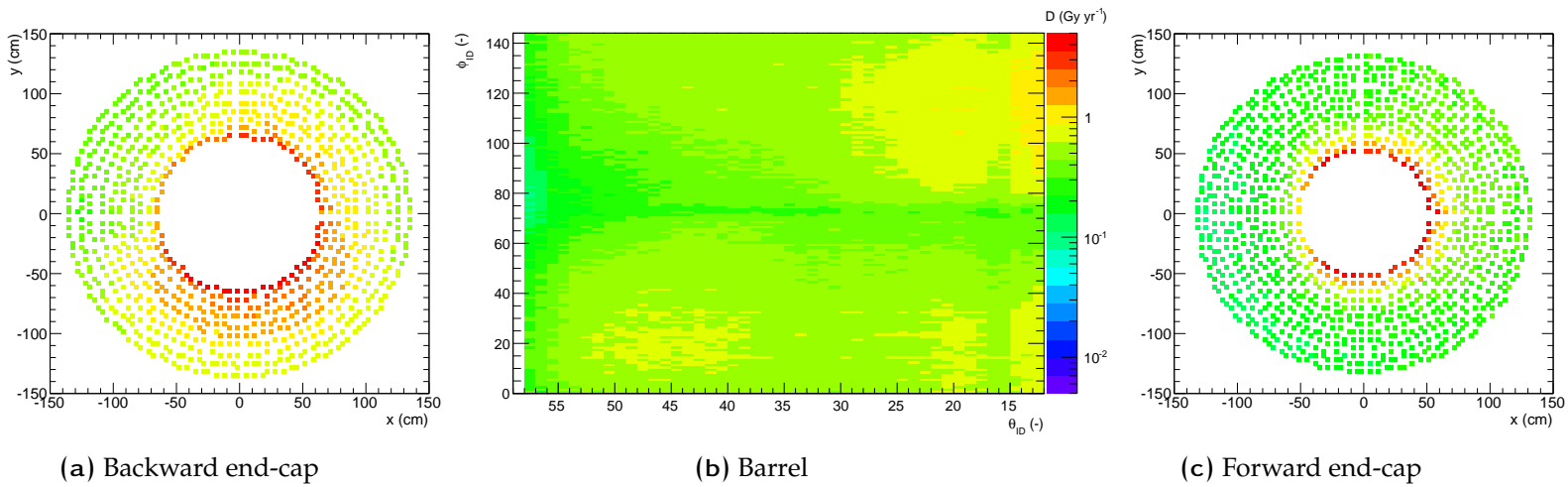


Figure C.30: Map of the dose (in log scale) deposited in the ECL with concepts C₂

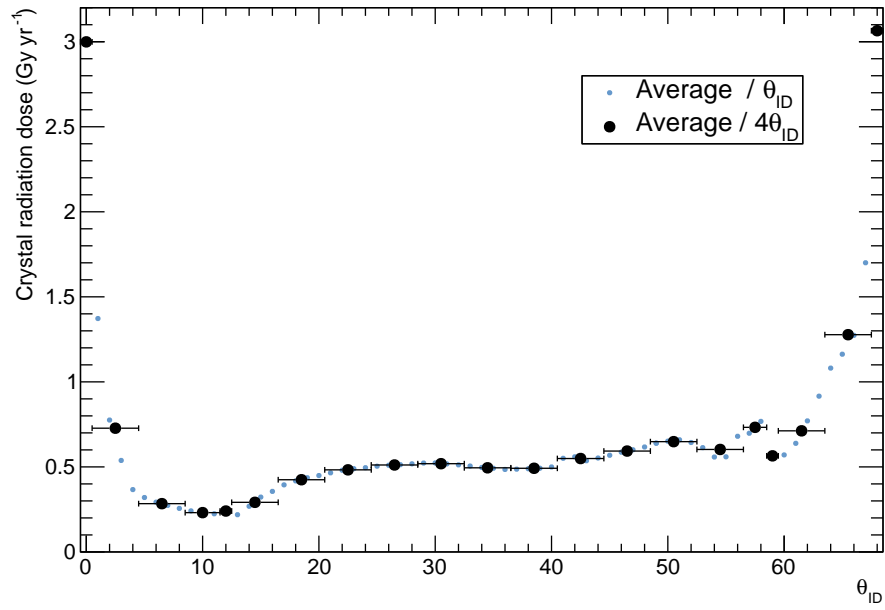


Figure C.31: Radiation dose as a function for crystal row index for concepts C_2

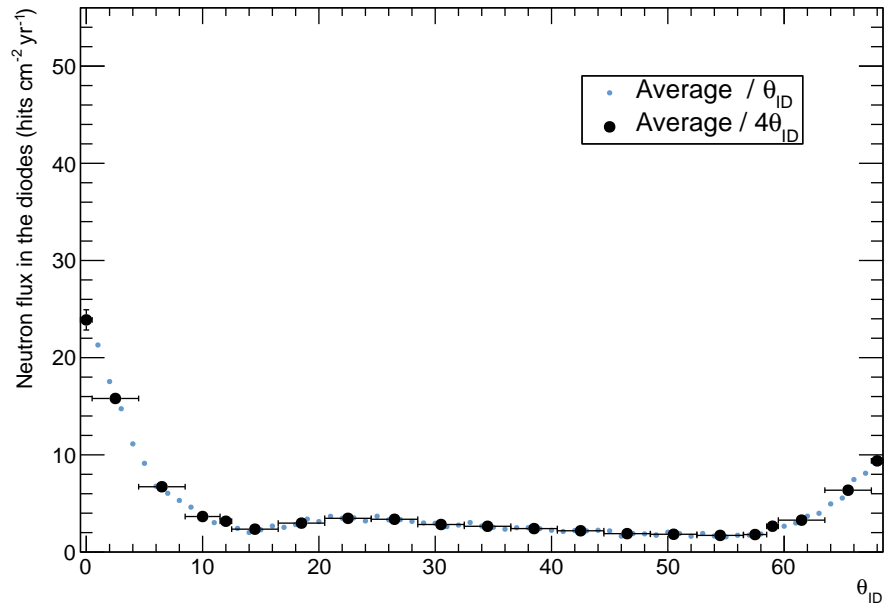


Figure C.32: Neutron flux as a function for crystal row index for concepts C_2

Appendix D

Detail of the ECL shields technical design

The next sections contain the detail of technical design studies and the design choices that led to the final shield geometries. It complements the general information about the shield design reported in section 3, in the body of this Dissertation.

In section D.1, the modelled supports and load conditions are described with respect to a general frame of reference, and the general approach to the structural analyses is explained in greater detail than in section 3.

Section D.2 presents the geometries, components, materials and manufacturing for each of the sub-systems of the backward shield, together with the relevant calculations and justifications. Section D.3 presents the same information for the forward shield. The results of the structural analyses are summarized in section D.4.

Finally, section D.5 describes the fabrication process and documents the design changes that were required to help either fabrication or installation.

D.1 General design of the shields

D.1.1 System of reference

The system of reference used in all further discussions is defined in Figure D.1. The origin is located at the intersection of the shells revolution axis and the plane where the shields

attachments join the ECL end-cap. The Z axis is along the shells revolution axis and points away from the Belle II interaction point, the Y axis is directed vertically upwards, and the X axis completes a right-handed coordinate system.

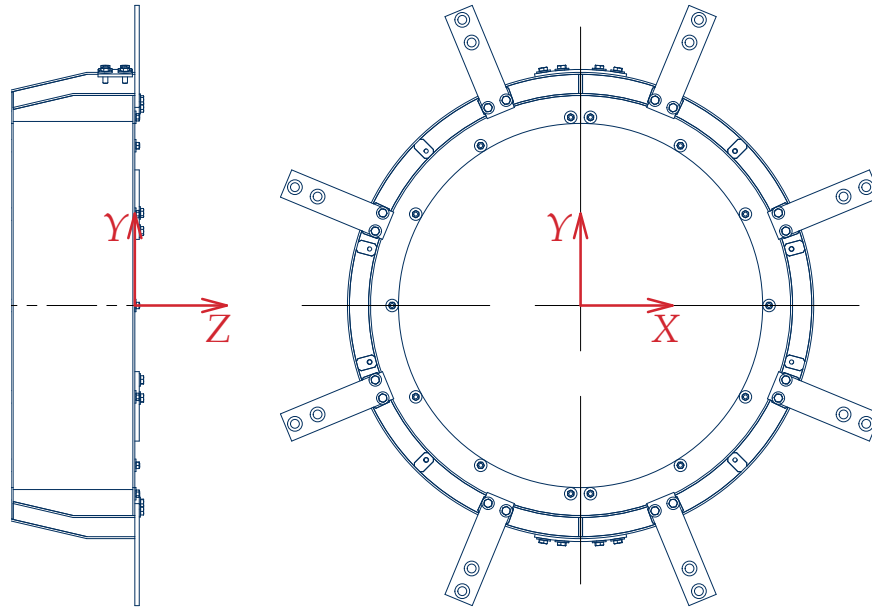


Figure D.1: System of reference for the load cases

D.1.2 Applied loads and design safety factor

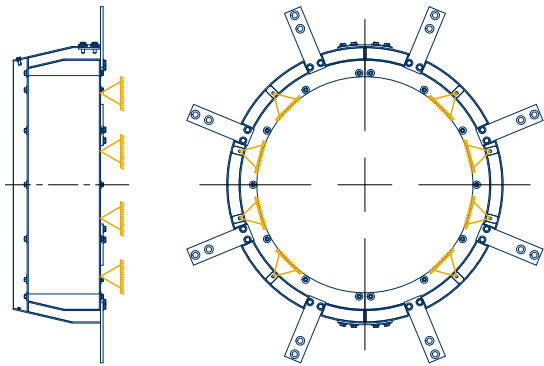
Definition of the loads

The loads applied to the ECL shields are derived from the ECL design report. We defined 10 different load and support scenarios for each shield, listed in Table D.1. In this table, the "Figure" line indicates which sub-figure of Figure D.2 represents the supports and the direction of the force.

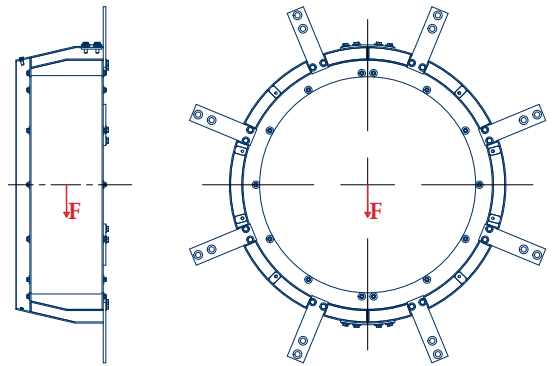
It is important to note that all loads on the shields were assumed to be static: the shields have no mobile parts, and the repetition rate of transportation and potential earthquake loads is low enough that fatigue effects can be neglected.

Table D.1: Load and support scenarios for both shields. The “Figure” lines indicate which schematic representation of the load or support is relevant. Numbering starts at 4 to maintain compatibility between this report and preliminary communications that included loads during transportation.

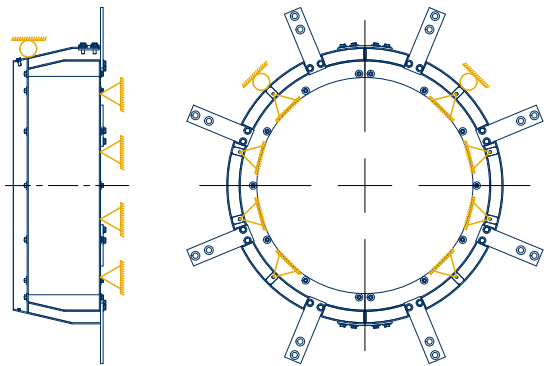
Description		Rotating H→V		On crane, towards installation jig				Attached to Belle II			
Case Number		4	5	6	7	8	9	10	11	12	13
Shield orientation		H	V	V	V	V	V	V	V	V	V
Supports Figure		D.2c	D.2c	D.2a	D.2a	D.2a	D.2a	D.2e	D.2e	D.2e	D.2e
Loads	Gravity	1G	1G	1G	1G	1G	1G	1G	1G	1G	1G
	Figure	D.2f	D.2b	D.2b	D.2b	D.2b	D.2b	D.2b	D.2b	D.2b	D.2b
	Earthquake x	-	-	-	-	-	-	-	0.3G	-	-
	Figure								D.2d		
	Earthquake y	-	-	-	-	-	-	-	-	0.3G	-
	Figure									D.2b	
	Earthquake z	-	-	-	-	-	-	-	-	-	0.3G
	Figure										D.2f
Crane work x	-	-	-	0.3G	-	-	-	-	-	-	-
Figure				D.2d							
Crane work y	0.3G	0.3G	-	-	0.3G	-	-	-	-	-	-
Figure	D.2b	D.2b			D.2b						
Crane work z	0.3G	0.3G	-	-	-	0.3G	-	-	-	-	-
Figure	D.2f	D.2f				D.2f					



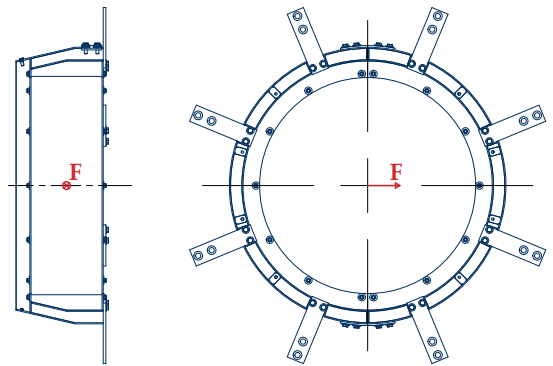
(a) Supports during transport and assembly



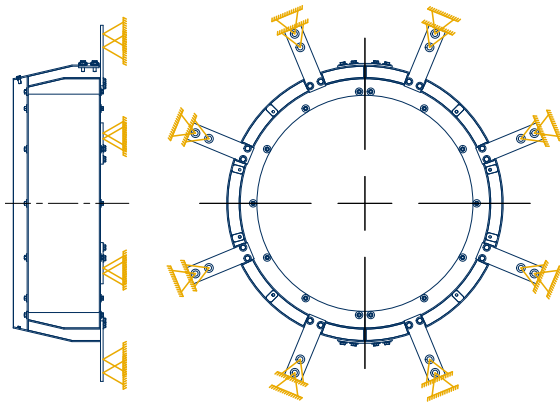
(b) Force along $-y$



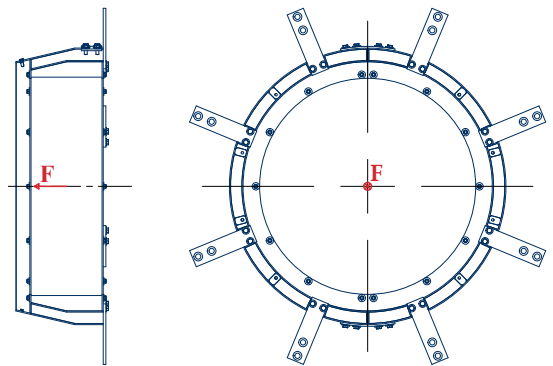
(c) Supports during crane operation



(d) Force along $+x$



(e) Supports after installation to the end-caps



(f) Force along $-z$

Figure D.2: Load and support scenarios. Blue: shield; Red: forces; : spherical support (crane hooks); : beam fixed at one end (bolted support).

Description of the supports

The shields are supported by bolted connections with either the jig adapters or the ECL end-caps, except for cases 4 and 5 where a special attachment can also be used for lifting operations. The bolted connections are modelled as rigid beam elements fixed at one end and connected to the shield at the other. Moreover, the mating surfaces are assumed to be frictionless. This is a conservative assumption since, in this view, the bolts themselves need to support all the load. Because the surface of the ECL end-cap where the shields are attached consists of irregular thin sheet metal, a good "friction joint" cannot be assumed between these two.

For cases 4 and 5, there are also a crane attachment on each side of the $Y - Z$ plane that are modelled as spherical joints: allowing all rotations but no translation.

Mechanical properties of selected materials

The properties below were assumed for the mechanical resistance studies [77].

Lead

- Density: $\rho = 11.3 \text{ g/cm}^3$
- Young's Modulus: $E = 14 \text{ GPa}$
- Poisson's Ratio: $\nu = 0.42$
- Tensile Yield Strength: $\sigma_y = 18 \text{ MPa}$
- Tensile Ultimate Strength: $\sigma_u = 18 \text{ MPa}$

304 Stainless steel

- Density: $\rho = 7.75 \text{ g/cm}^3$
- Young's Modulus: $E = 193 \text{ GPa}$

- Poisson's Ratio: $\nu = 0.31$
- Tensile Yield Strength: $\sigma_y = 207$ MPa
- Tensile Ultimate Strength: $\sigma_u = 586$ MPa

Polyethylene

- Density: $\rho = 0.95$ g/cm³
- Young's Modulus: $E = 1.1$ GPa
- Poisson's Ratio: $\nu = 0.42$
- Tensile Yield Strength: $\sigma_y = 25$ MPa
- Tensile Ultimate Strength: $\sigma_u = 33$ MPa

Finite element analysis methodology

The methodology used to conduct the mechanical resistance studies using ANSYS is outlined below.

1. Simplify the model to make the analysis more manageable
 - Use symmetries in the geometry, loads, and supports (when applicable) to reduce the problem size
 - Remove details such as countersinks, threads, and chamfers in low-stress areas
 - Remove other components irrelevant for the study. Here, the polyethylene layer was completely suppressed. This is equivalent to assuming it does not contribute to the stiffness of the product, nor to the inertial loads.
2. Define loads and supports
 - Loads and support are specific to each load scenario. See paragraphs "[Definition of the loads](#)" and "[Description of the supports](#)" above for the support type and location of each case.

3. Define material properties

- Material properties are common to all load and support scenarios. See paragraph “[Mechanical properties of selected materials](#)” above for values entered in the FEA software.

4. Define model mesh

- Use default “medium” mesh with size controls in the critical areas, leaving the element order to be program-controlled. The resulting element types are SOLID186 and SOLID187 elements, which are quadratic 3D 20-node homogeneous and 3D 10-node tetrahedral structural solid elements, respectively. The bolts are represented by BEAM188: 3D linear finite strain beam elements. An example of such meshed model is reported in Figure [D.3a](#).

5. Converge maximum stresses

- Conduct ANSYS’s automatic convergence study. After first calculation, the mesh is refined in the areas with the largest stresses. The study stops when the change between steps is less than 5%. We call the final value the “converged stress”, meaning the stress is then considered independent of the mesh size. An example of refined mesh, for the forward load case #13, is reported in Figure [D.3b](#).

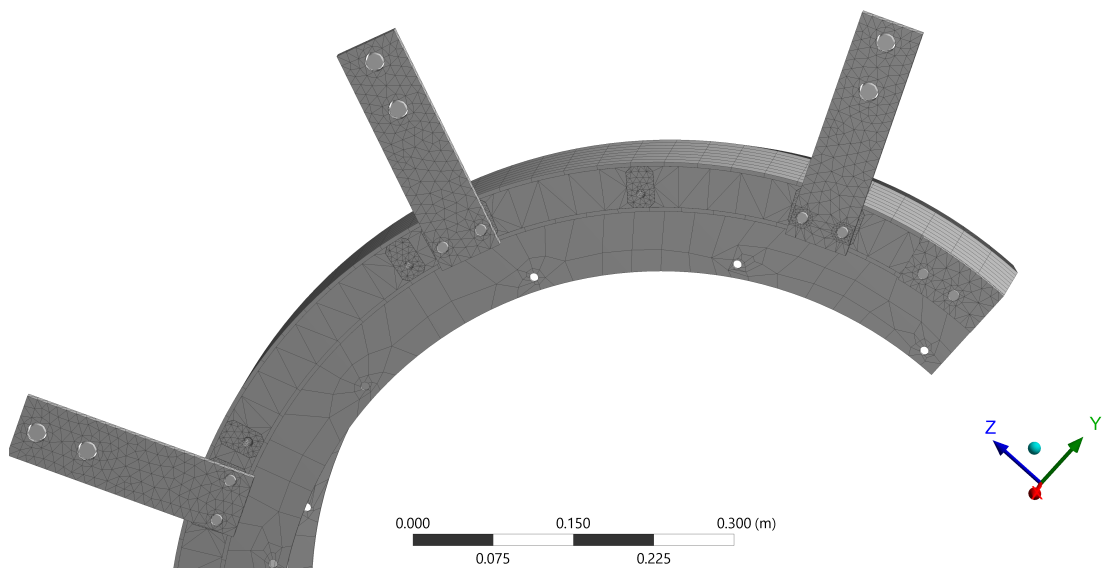
Design safety factor

The static mechanical resistance studies use the von Mises yield criterion for mechanical resistance [78]. This criterion predicts failure when the equivalent tensile stress σ_v reaches the elastic limit σ_y — also known as yield strength — of the material. This σ_v is equal to σ_{11} in the specific case of pure uni-axial tension, and more generally corresponds to

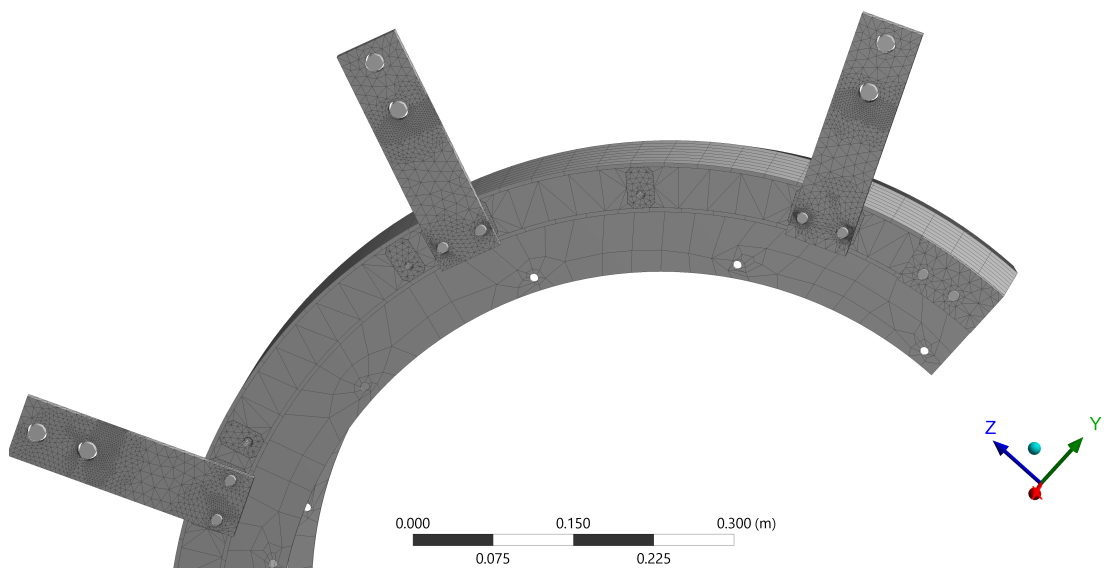
$$\sigma_v = \sqrt{\frac{(\sigma_{11} - \sigma_{22})^2 + (\sigma_{22} - \sigma_{33})^2 + (\sigma_{33} - \sigma_{11})^2 + 6(\sigma_{12}^2 + \sigma_{23}^2 + \sigma_{13}^2)}{2}}, \quad (\text{D.1})$$

where σ_{ij} are the components of the stress tensor. We use the stress safety factor SF_σ of 4 to determine whether or not the product has the required mechanical resistance for the application. This safety factor is defined as

$$SF_\sigma = \frac{\sigma_y}{\sigma_v} \geq 4. \quad (\text{D.2})$$



(a) Original



(b) After two refinement steps in case FWD #13

Figure D.3: Example of meshed model

The maximal displacements d_{\max} were also checked to ensure the shields would not contact surrounding structures during operation or installation. They are expected to be much smaller than the clearances around the product, which are at least 10 mm. The criterion for acceptance was set to be smaller than the 1.5 mm default manufacturing tolerance:

$$d_{\max} \leq 1 \text{ mm.} \quad (\text{D.3})$$

D.2 Design of the backward shield

D.2.1 Shell

The main purposes of the shell are to contain the electromagnetic radiation shield, and provide attachment points to fix the two halves together as well as fixing the shield assembly to the jigs and the ECL end-caps. The shield comprises two symmetrical shells.

Geometry

The geometry of one of the shells is represented in Figure D.4. The mounting points for transport, described later in this section, are drawn transparent.

Components, materials and manufacturing

The shells are welded assemblies of nominally 4mm and 6mm thick AISI304 stainless steel sheets. Because they will be manufactured in Canada, we use the use of the closest imperial equivalent dimension: gauge #9 (3.97 mm) and gauge #4 (5.95 mm) respectively [99].

The sheet metal components will be laser-cut to dimensions using provided CAD geometry, and cold-rolled where needed. They will be welded with continuous beads to ensure the assemblies are tight and allow casting the lead for the electromagnetic radiation shield .

The two shells are attached together by two identical pairs of plates above and below the shield, shown in Figure D.5. The rear connections are identical to those of the Belle design.



Figure D.4: Geometry of the shells of the backward shield

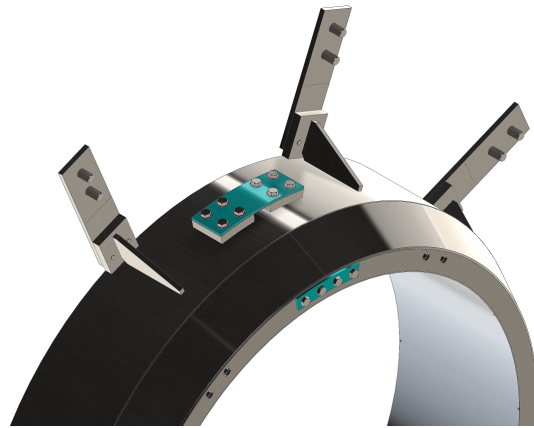


Figure D.5: Method of connecting the two backward shield halves together. The parts in **turquoise** are what is being referred to as the "Connection Plates"

Calculations and justification

The materials and manufacturing process is strongly inspired by the original Belle shields. Moreover, discussions with potential Canadian manufacturer MarShield confirmed that sheet thicknesses greater than 1/8" would provide minimal deformation of the shells during the lead casting process.

The finite elements analysis (FEA) studies, reported at the end of this section, showed that the shells, including the connection plates of Figure D.5, are not the critical element under any of the load and support scenarios so their design is governed by the above manufacturing guideline about warping during lead casting.

D.2.2 Electromagnetic radiation shield

The electromagnetic radiation shield (EMR shield) is composed of a thickness of dense material to absorb photons and high-energy electrons. The chosen concept is a layer of lead that is cast in the shells, such commonly used in the nuclear power industry.

Geometry

The geometry of one of the EMR shields is represented in Figure D.6.



Figure D.6: Geometry of the backward electromagnetic radiation shield

Components, materials and manufacturing

The EMR shield system is composed on only one part per shield half. It is made of a 36 mm thick layer of pure lead, that is cast in the shells. This casting process is commonly

used in the nuclear industry. During the design phase, we found two potential Canadian manufacturers having capability and experience in this kind of projects. The process can involve multiple re-heating of the parts to fill potential voids left in the initial casting, as well as testing the final product with radiation sources to ensure no residual cavities are found before delivery of the product. These companies are :

- MarShield Custom Radiation Shielding Products, 4140 Morris Dr, Burlington ON
- Ultraray Radiation Protection, 760 Pacific Rd #3, Oakville ON

Calculations and justification

Calculation of the required lead thickness is detailed in Section 3.2 of this document. These studies showed that the selected concept, with a nominal 40 mm thick layer of lead would reduce the radiation dose by 13% in the innermost row of the backward ECL end-cap.

Most significantly, it was observed that the actual lead thickness could deviate within -0.5 cm to +1.0 cm without appreciable change in the shielding efficiency. This result was previously reported in Figure 3.6, where the radiation level safety factor — how many times the expected dose is smaller than the acceptable limit — is displayed as a function of the variation of lead thickness for both shields.

The final thickness value of 36 mm is within that range, and was obtained as a compromise to allow sufficient room for the shell and the neutron radiation shield within the available volume.

D.2.3 Neutron shield

Geometry

The neutron radiation shield system is composed of four sub-assemblies each covering 90° and arranged as depicted in Figure D.7. The geometry of one of these sub-assemblies is represented in Figure D.8. They are held to the shield shell by means of an aluminium cover.

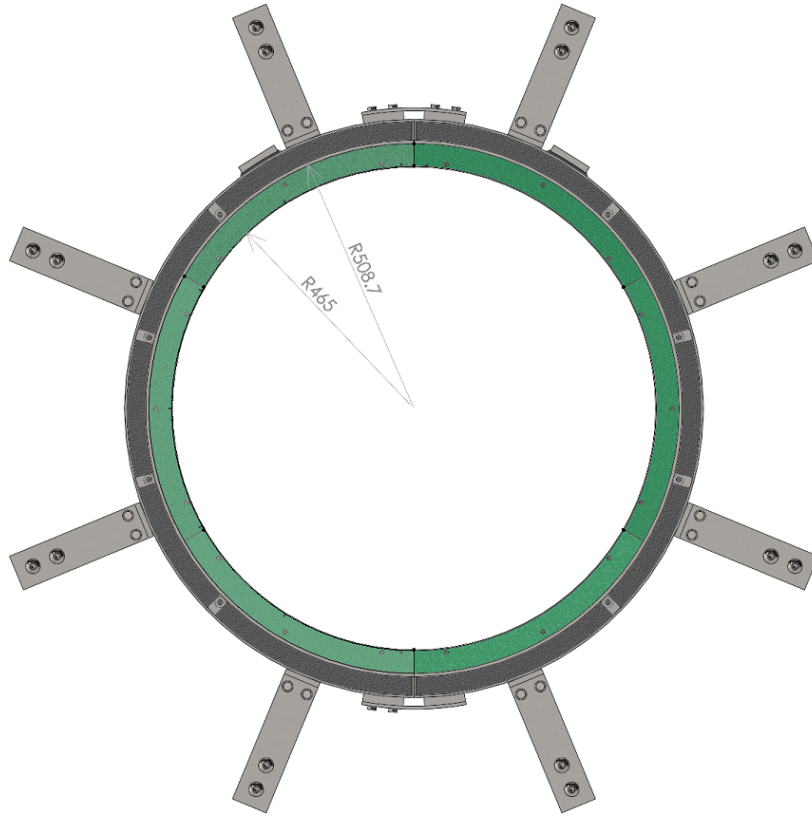


Figure D.7: Layout of the backward neutron radiation shield system (textured green ) inside the shield.



Figure D.8: Geometry of a backward neutron absorber sub-assembly. The parts were made transparent to show details of the assembly method.

Components, materials and manufacturing

Each sub-assembly as shown in Figure D.8 is made of 11 layers of 1"-thick 5% borated polyethylene. These profiles will be cut to shape using water-jet and those needing extra features such as threads, counter-bores will be machined to the final geometry.

Each sub-assembly is held together with three (3) stainless steel rods, threaded on both ends. These rods also ensure alignment of each profile of the stack, since they thread on the last (smallest) part and are secured with a nut and washer to the first part. The details are visible in Figure D.9

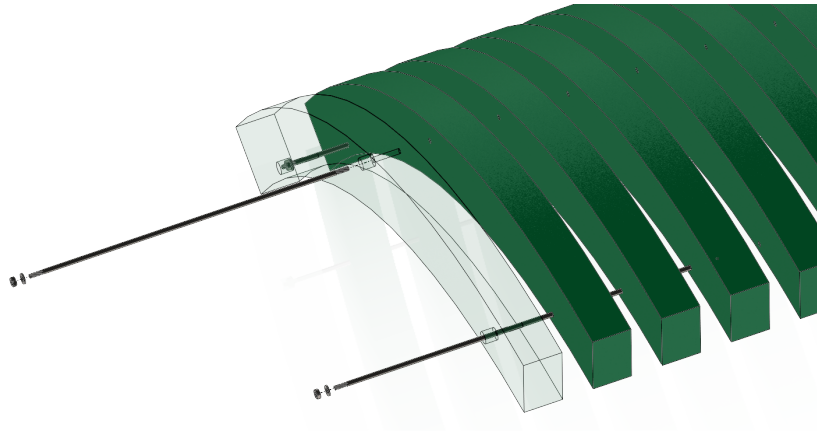


Figure D.9: Exploded view showing the assembly method of the backward neutron absorber

Lastly, the neutron absorbers are held in place by an aluminium alloy cover fastened to the shell such that the neutron absorber can be replaced if needed. Details of this cover is seen in Figure D.10.

Calculations and justification

The design thickness of the neutron absorber was determined to be 50 mm during the conceptual design studies in section 3.2. The technical design of the shield with the thicknesses needed for the shells gave a final thickness of 43.7 mm. As it can be observed in Figure 3.7, with a neutron absorber that is 6.3 mm thinner than the conceptual value, the predicted neutron flux is still more than 10 times smaller than the design limit.

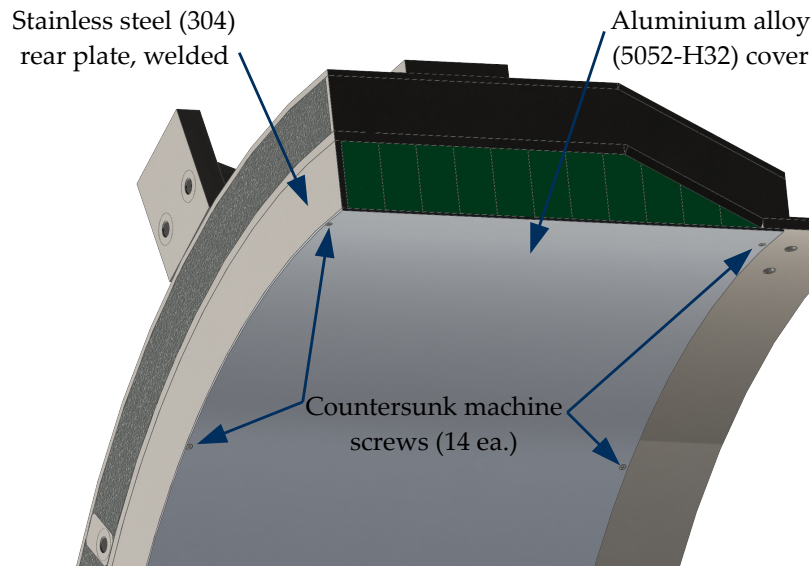


Figure D.10: Details of the backward neutron absorber cover

D.2.4 Mounting points for transport and installation

Two different sets of mounting points exist on the shield:

1. those to fix the jig adapter — the item that connects the shield to the ECL extraction device —, and
2. those used to attach plates on the shield for lifting and transport.

During crane operation, the shield is also attached to the jig adapter, as represented in Figure D.11.

Geometry

The eight (8) mounting points for the backward jig adapter are included in the lead part and connect the inner shell to the outer shell. Their layout is represented in Figure D.12, whereas Figure D.13 shows detail of their geometry.

The mounting points for craning operation are represented in Figure D.14. These M16 nuts welded to the shells provide anchors to fasten the lifting supports with a 30-mm hole for lifting shackles.

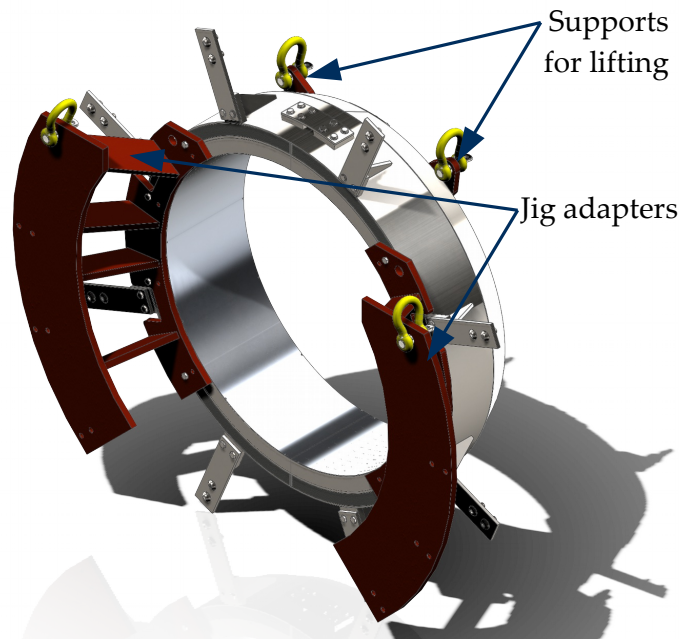


Figure D.11: Components of the backward shield during crane operation.

Components, materials and manufacturing

The threaded bushings of Figure D.13 are machined out of 304 stainless steel, and they are welded to the shell.

The mounting points for the lifting are attached to 316 stainless steel M16 nuts as shown in Figure D.14. This allows fastening the support plate, made of 19-mm thick ASTM A36 steel, which provides a 30-mm hole to connect a shackle to the front of the shield.

Calculations and justification

The calculation of the structural resistance of the mounting points for the jig adapter was conducted using Finite Element Analysis with the ANSYS Mechanical software [77]. The bolts are modelled by 19-mm long, 10-mm diameter beam elements that connect the mounting holes with the "ground". No other support is assumed for cases 7,8 and 9 of Table D.1, which represent movements while the shield is on the assembly jig. In other words, we neglect the contribution from friction to the bolted joint, which is a conservative assumption. Such assumption would be close to reality should the joint be not properly pre-loaded.

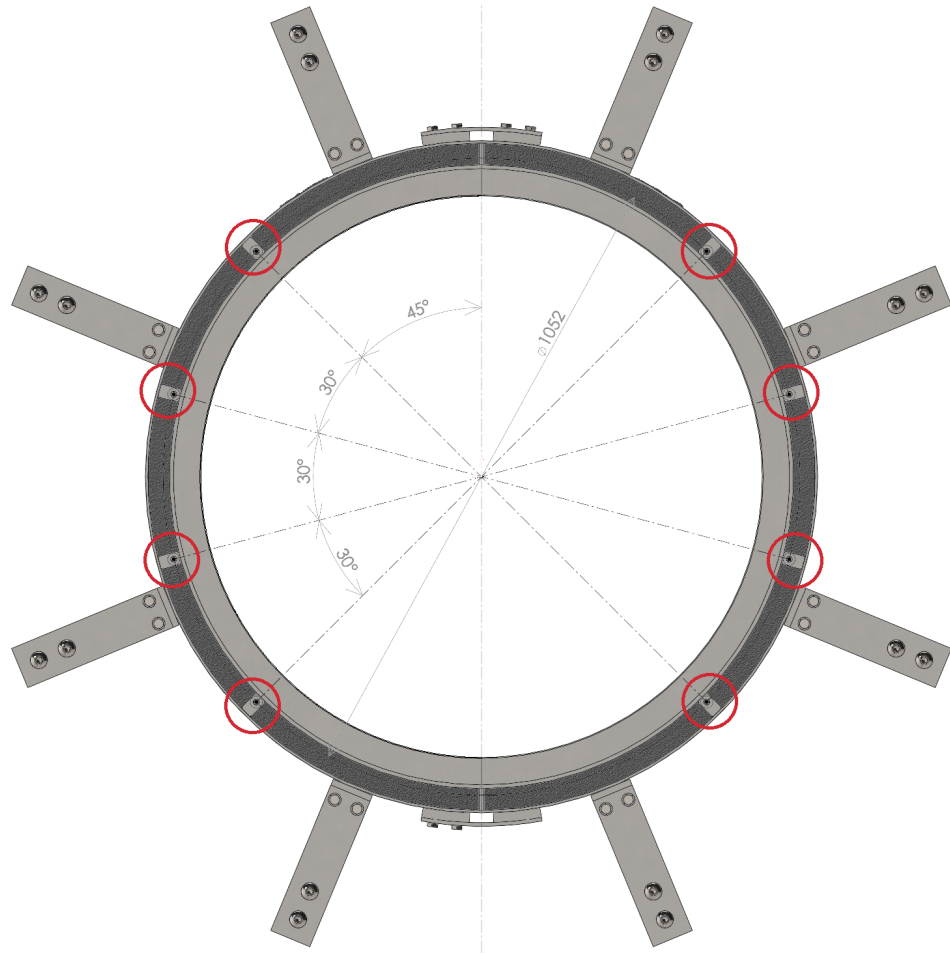


Figure D.12: Layout of the mounting points to fix the backward jig adapter. The items are circled in red.

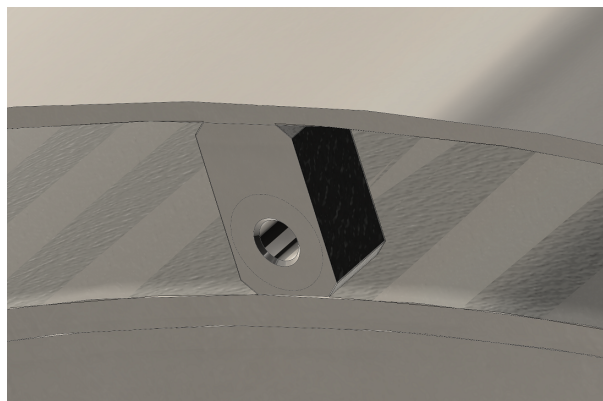


Figure D.13: Geometry of a mounting point for the backward jig adapter

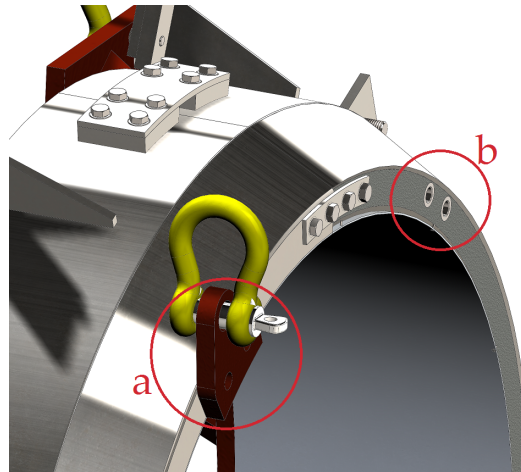


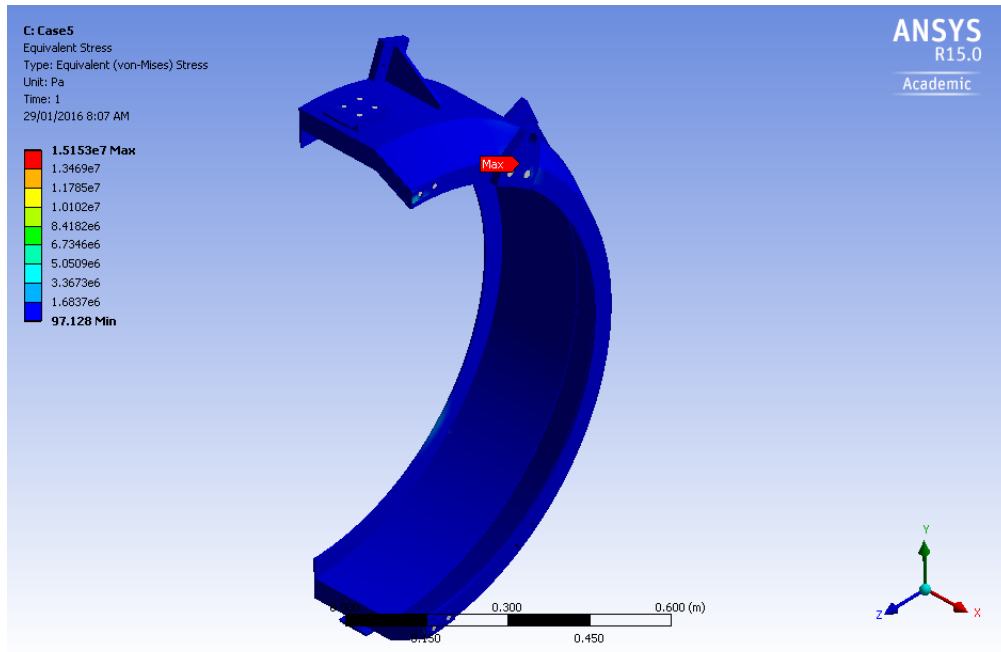
Figure D.14: Mounting points for backward lifting support (label 'a'). Parts have been removed on the right assembly to show the two M16 nuts (label 'b') welded to the shells

Case 5 provided the highest level of equivalent stresses during lifting and transportation, with $\sigma_v = 15.2$ MPa. The distribution of the stresses is shown in Figure D.16. The plate on which is welded the M16 nuts (referred to as the "mounting points") is the most loaded component for this scenario. The results of Figure D.15b present the converged stresses after only two steps of mesh refinement in the highest-stress regions. This refinement produced only slight change in the values, as reported in Table D.2.

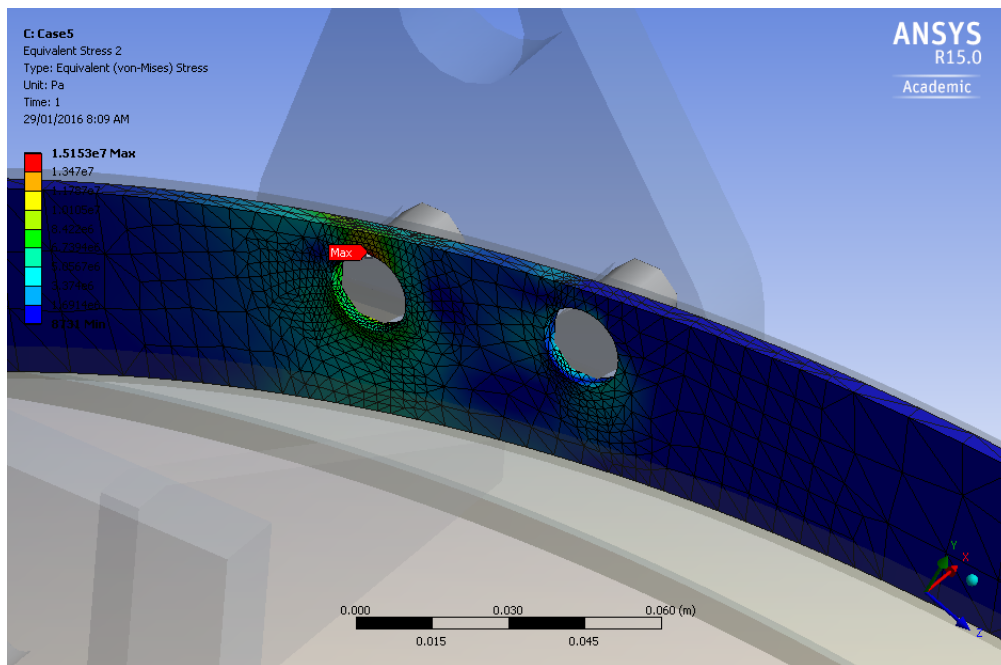
Case 8 provided the highest level of equivalent stresses after fixing on the jig, and during installation to the ECL end-cap, at $\sigma_v = 11.7$ MPa. The distribution of the stresses is shown in Figure D.16. This stress is significantly lower than that of the attachments to end-caps after installation to the shields. These mounting points are not the critical components. The results of Figure D.16b present the converged stresses after only one step of mesh refinement in the highest-stress regions. This refinement produced only slight change in the values, as reported in Table D.3.

D.2.5 Attachments to end-cap

The attachments to the end-cap are the components that hold the shield in place during normal operation. They are designed to be as close as possible to those in Belle to ensure compatibility.

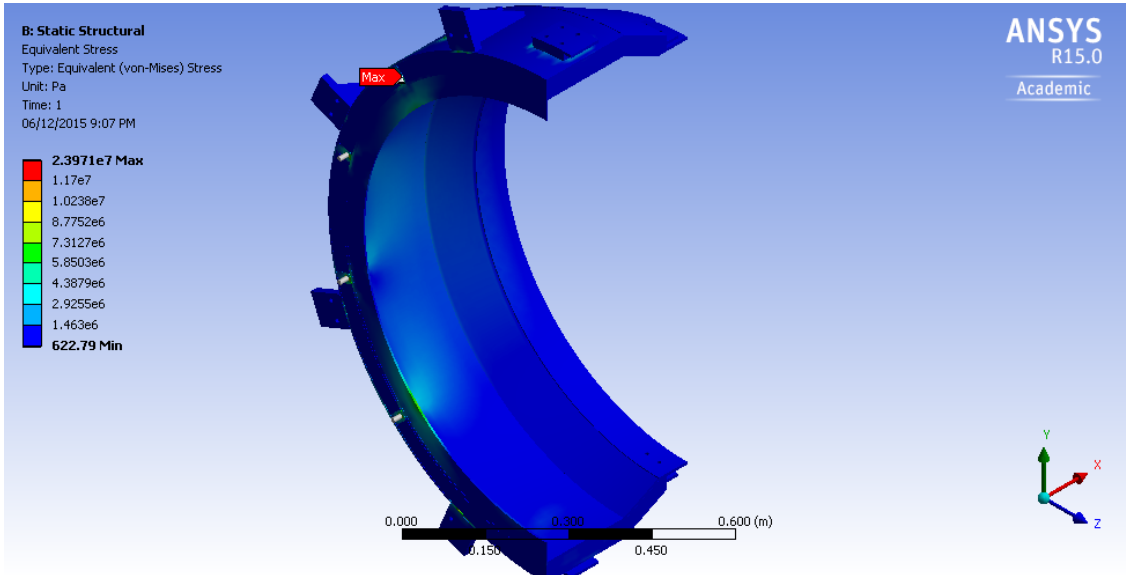


(a) Overall distribution

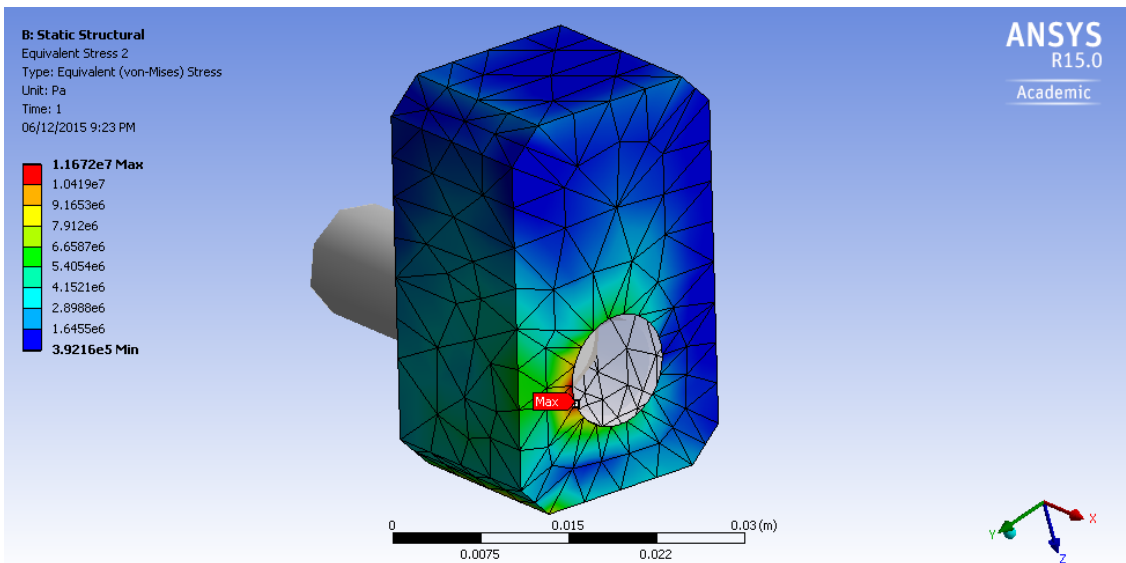


(b) Details of the critical element: the front cover plate on which is welded the M16 nuts

Figure D.15: Equivalent stress distribution of the backward shield during loading case 5



(a) Overall distribution



(b) Details of the critical element: the assembly mounting point

Figure D.16: Equivalent stress distribution of the backward shield during loading case 8

Table D.2: Convergence study results for the equivalent stresses on the backward ECL front cover during loading case 5

Solution Nb.	Equivalent stress (MPa)	Change (%)	Nb. of Nodes	Nb. of Elements
1	13.8	-	122080	36464
2	14.5	5.0	132611	45085
3	15.1	4.4	149747	56292

Table D.3: Convergence study results for the equivalent stresses on the backward ECL assembly jig bushing during loading case 8

Solution Nb.	Equivalent stress (MPa)	Change (%)	Nb. of Nodes	Nb. of Elements
1	11.6	-	111200	34780
2	11.7	0.76	129372	46288

Geometry

The geometry of the attachments to the end-cap is shown in Figure D.17.

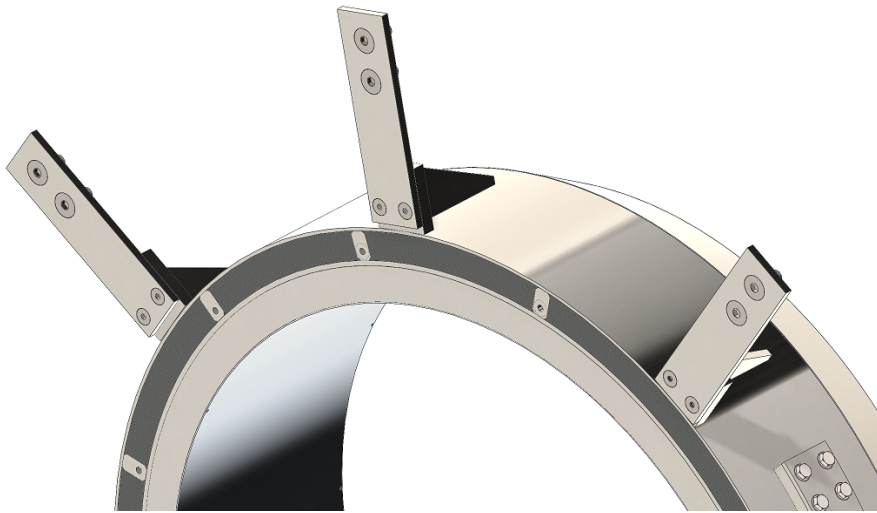


Figure D.17: Geometry of the attachments to backward ECL end-cap

Components, materials and manufacturing

This sub-system consists of eight (8) copies of a two-part assembly: one gusset welded to the shell, and one attachment plate which provides two M10 countersunk clearance holes allow fastening each plate to the shield with flat-head socket cap screws. The gusset itself is a welded assembly of 304 stainless steel plates which will be cut to shape using laser cutting. The attachment plate is also made of 304 stainless steel, and is made to be as close as possible to the Belle part. The only differences are the two M10 holes that are countersunk to improve clearance and shifted to a larger radius to account for the larger diameter of the shield.

The plates attach to the end-cap by means of two (2) M16 × 2.0 × 40 mm flat-head socket cap screws. The choice of flat head screws instead of regular hex head bolts is driven by the required clearance between these fasteners and the pole piece of the magnetic flux return steel.

Calculations and justification

The structural resistance of these parts were also assessed using FEA. This time, the loading case #13 — after final installation, with a 0.3G acceleration along the z axis — is the one which is predicted to produce the largest stress according to the results. The stress distribution in the shield is shown in Figure D.18, with details on the loaded part shown in Figure D.19. The maximum equivalent stress is predicted to be 35.1 MPa near the clearance hole used to fasten the end-cap attachment plate to the shield. Again, it is important to note that the bolted connections are modelled in the frictionless contact limit. If proper assembly methods are used (the bolts are tightened to the correct torque), the mating surface will bear the majority of the load resulting in a lower stress at the clearance hole.

The results of Figures D.18 and D.19 represent the “converged stresses” after four (4) steps of mesh refinement in the critical areas. The results of the convergence study are shown in Figure D.20.

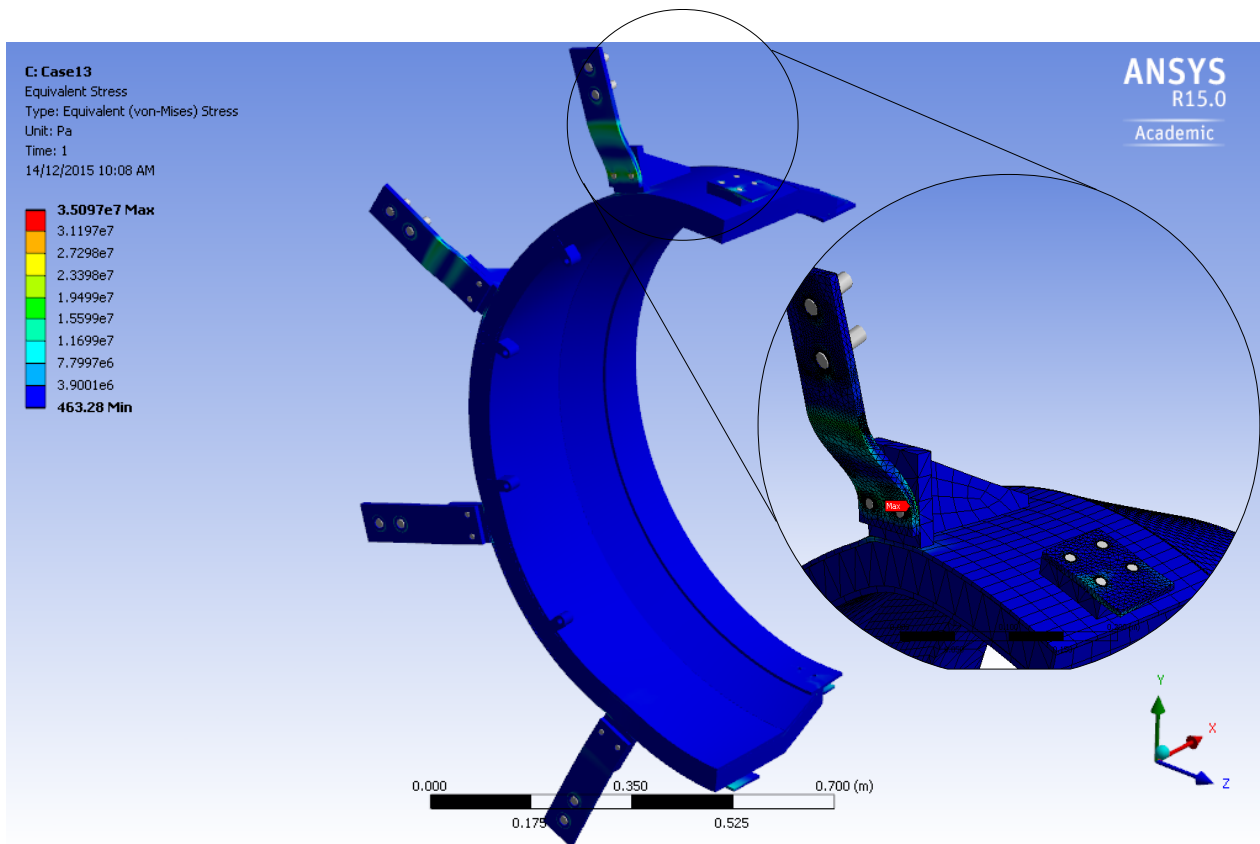


Figure D.18: Equivalent stress distribution in the backward shield during loading case #13.

D.3 Design of the forward shield

The general design of the forward shield is similar to that of the backward one. As such, many descriptions encountered in Section D.2 are also valid for the forward shield and are reproduced here for completeness.

D.3.1 Shell

The main purposes of the shell are to contain the electromagnetic radiation shield, and provide attachment points to fix the two halves together as well as fixing the shield assembly to the jigs and the ECL end-caps. The shield comprises two symmetrical shells.

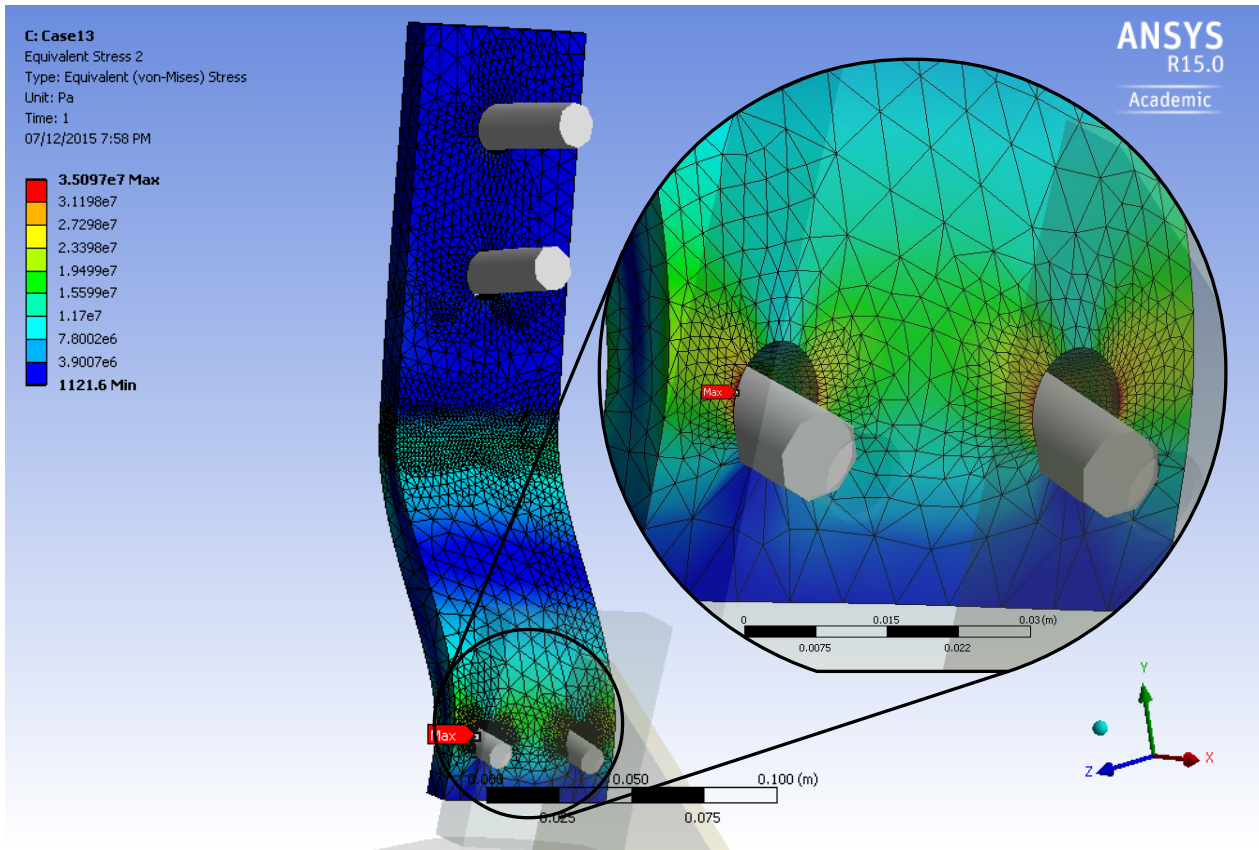


Figure D.19: Details of the equivalent stress distribution in the backward shield end-cap attachment during loading case #13.

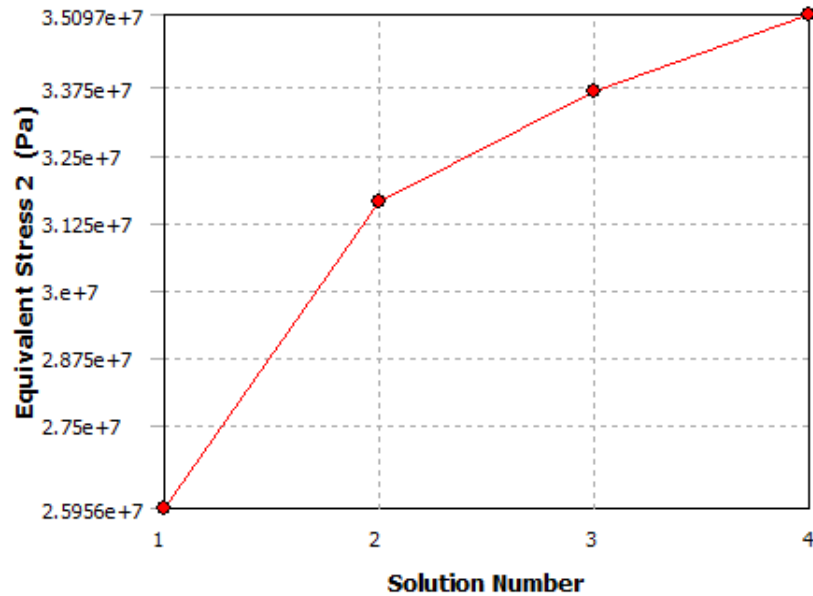
Geometry

The geometry of one of the shells is represented in Figure D.21. The mounting points for transport, described below are drawn transparent.

Components, materials and manufacturing

The shells are welded assemblies of nominally 4 mm and 6 mm thick AISI304 stainless steel sheets. Because they will be manufactured in Canada, we use the use of the closest imperial equivalent dimension: gauge #9 (3.97 mm) and gauge #4 (5.95 mm) respectively [99].

The sheet metal components will be laser-cut to dimensions using provided CAD geometry, and cold-rolled where needed. They will be welded with continuous beads to ensure



Solution Nb.	Equivalent stress (MPa)	Change (%)	Nb. of Nodes	Nb. of Elements
1	26.0	-	156863	60683
2	31.6	19.7	178407	73426
3	33.7	6.3	274649	136598
4	35.1	4.1	555713	334205

Figure D.20: Convergence study for the equivalent stress on the backward ECL attachment plate in loading case #13

the assemblies are tight and allow casting the lead for the electromagnetic radiation shield.

The two shells are attached together by two identical pairs of plates above and below the shield, shown in Figure D.22 below.

Calculations and justification

The materials and manufacturing process is strongly inspired by the original Belle shields. Moreover, discussions with potential Canadian manufacturer MarShield confirmed that sheet thicknesses greater than 1/8" would provide minimal deformation of the shells during the lead casting process.

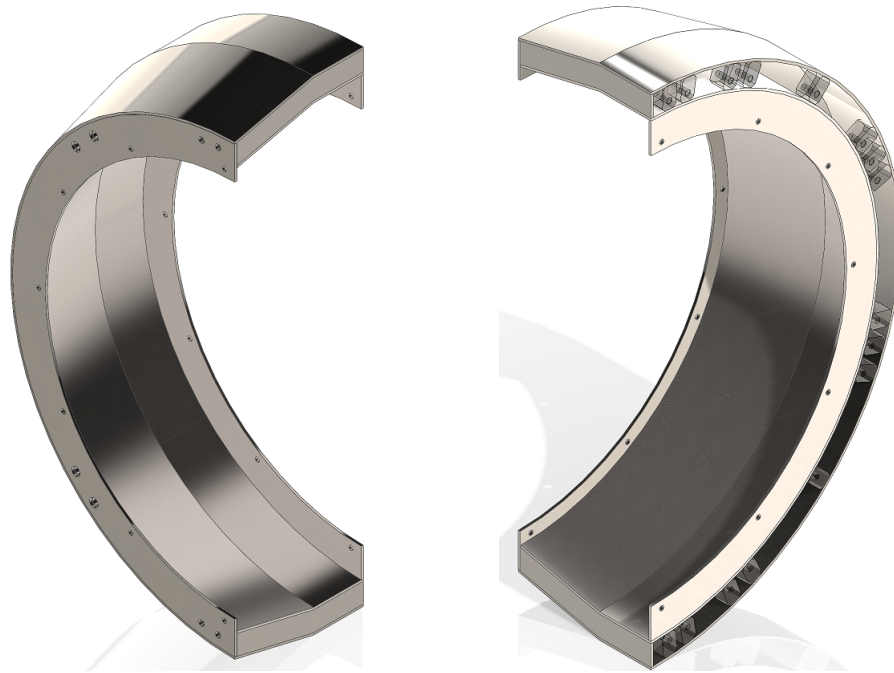


Figure D.21: Geometry of the shell of the forward shield

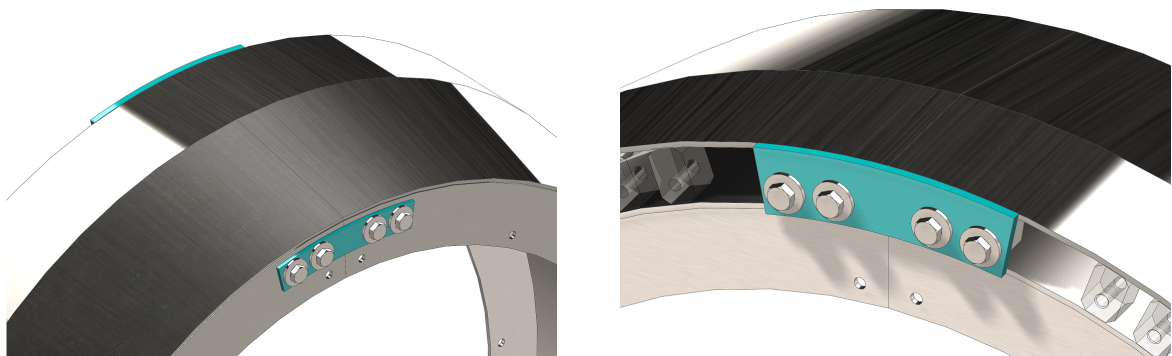


Figure D.22: Method of connecting the two forward shield halves together. The parts in **turquoise** are what is being referred to as the "Connection Plates"

The finite elements analysis (FEA) studies showed that the shells, including the connection plates of Figure D.22, are not the critical element under any of the load and support scenarios so their design is governed by the above manufacturing guideline about warping during lead casting.

D.3.2 Electromagnetic Radiation Shield

The electromagnetic radiation shield (EMR shield) is composed of a thickness of dense material to absorb photons and high-energy electrons. The chosen concept is a layer of lead that is cast in the shells, such commonly used in the nuclear power industry.

Geometry

The geometry of one of the forward EMR shields is represented in Figure D.23.



Figure D.23: Geometry of the forward electromagnetic radiation shield

Components, materials and manufacturing

The EMR shield system is composed on only one part per shield half. It is made of a 39 mm thick layer of pure lead, that is cast in the shells. This casting process is commonly used in the nuclear industry. At least two (2) Canadian manufacturers have capability and experience in this kind of process, and their contact details are listed in Section D.2.2.

Calculations and justification

Calculation of the required lead thickness is detailed in Section 3.2 of this document. These studies showed that the selected concept, with a nominal 40mm thick layer of lead would reduce the radiation dose by 19% in the innermost row of the forward ECL end-cap.

Most significantly, it was observed that the actual lead thickness could deviate within -0.5 cm to +1.0 cm without appreciable change in the shielding efficiency. This result was reported in Figure 3.6.

The final thickness value of 39 mm is within that range, and was obtained as a compromise to allow sufficient room for the shell and the neutron radiation shield within the available volume.

D.3.3 Neutron Shield

Geometry

The neutron radiation shield system is composed of six (6) sub-assemblies each covering 60° and arranged as in the backward shield, depicted in Figure D.7. The geometry of one of these sub-assemblies for the forward shield is represented in Figure D.24. They are held to the shield shell by means two 4-mm stainless steel rods each.

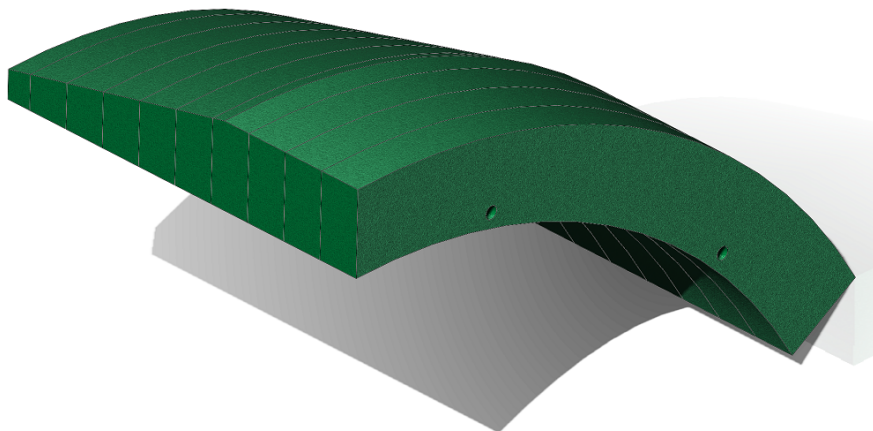


Figure D.24: Geometry of a backward neutron absorber sub-assembly

Components, materials and manufacturing

Each sub-assembly as shown in Figure D.24 is made of 11 layers of 1"-thick polyethylene. These profiles will be cut to shape using water-jet and those needing extra features such as threads, counter bores or angles will be machined to the final geometry. Similarly to the backward shield, borated polyethylene was preferred over regular HDPE for the neutron absorber to increase the safety margin at a negligible cost.

Each sub-assembly is held together with two (2) stainless steel rods, threaded on both ends. These rods also ensure alignment of each profile of the stack. The holes are visible in Figure D.24, and details are seen in Figure D.25. The neutron absorbers are also held in place by these rods, which are inserted into clearance holes produced in the shell.

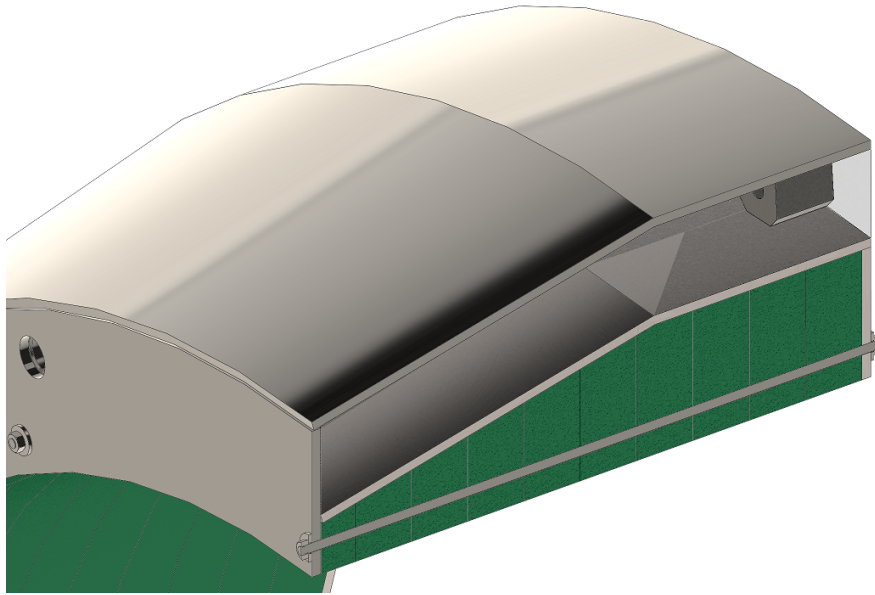


Figure D.25: Section view showing the assembly method of the forward neutron absorber

Calculations and justification

The design thickness of the neutron absorber was determined to be 60.5 mm during the conceptual design studies (see Section 3.2). The technical design of the shield with the thicknesses needed for the shells gave a final thickness of 57 mm. As it can be observed in

Figure 3.7, with a neutron absorber that is 3.5 mm thinner than the conceptual value, the predicted neutron flux is still approximately than 5 times smaller than the design limit.

D.3.4 Mounting points for transport and installation

Similarly to the backward shield, two different sets of mounting points exist on the shield:

1. those to fix the jig adapter — the part that connects the shield to the assembly device —, and
2. those used to attach plates on the shield for lifting and transport.

During crane operation, the shield is also attached to the jig adapter, as represented in Figure D.26.

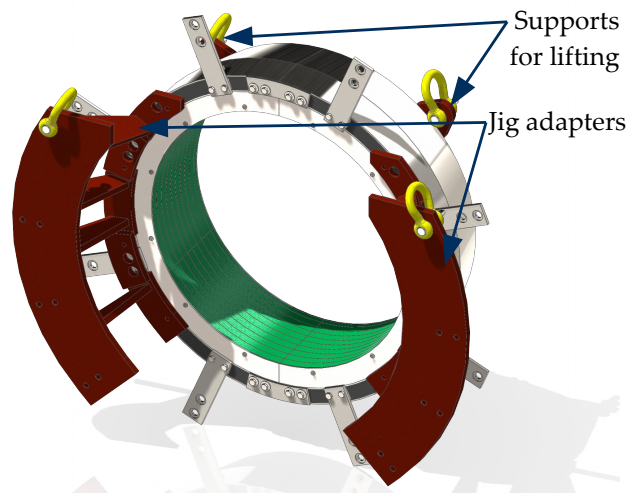


Figure D.26: Components of the forward shield during crane operation. The supports for lifting are optional.

Geometry

The eight (8) mounting points for the forward jig adapter are included in the lead part and connect the inner shell to the outer shell. Their layout is represented in Figure D.27.

Figure D.28 shows the detail of their geometry. While very similar to those of the backward shield in their design (see Figure D.13), their dimensions are different.

The mounting points for craning operations are represented in Figure D.29. They are installed as provisions to enable the use of lifting shackles on the shield instead of wrapping a sling around it in order to make it vertical during the installation process (loading cases #4 and #5).

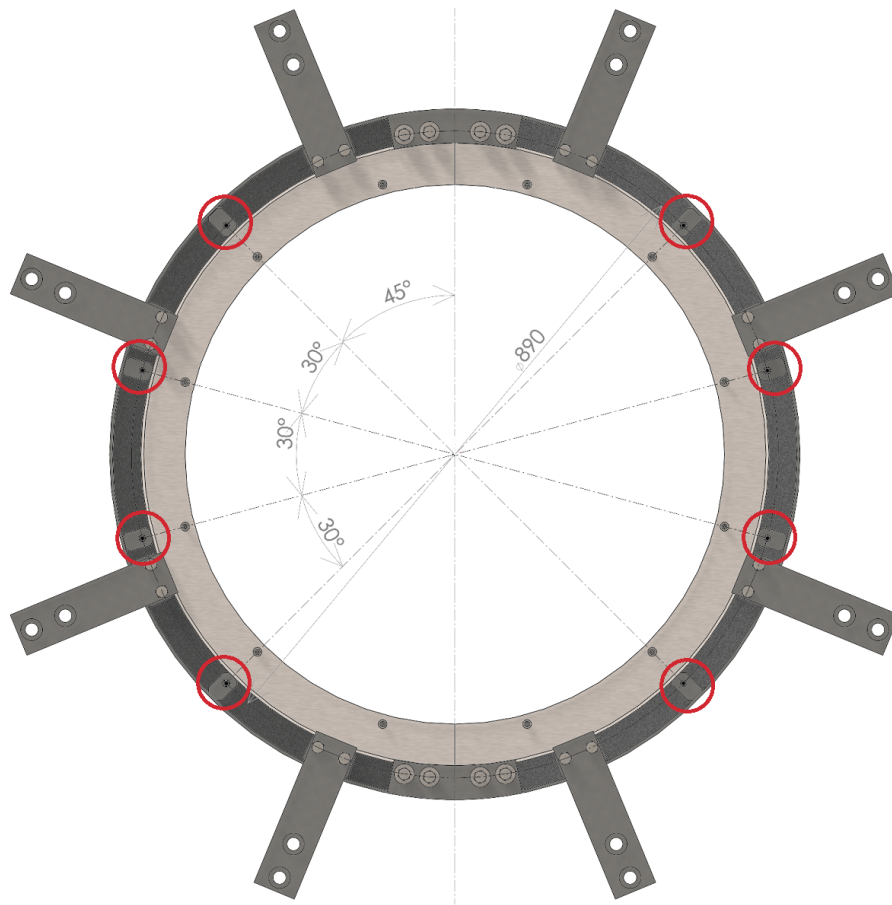


Figure D.27: Layout of the mounting points to fix the forward jig adapter. These items are circled in red.

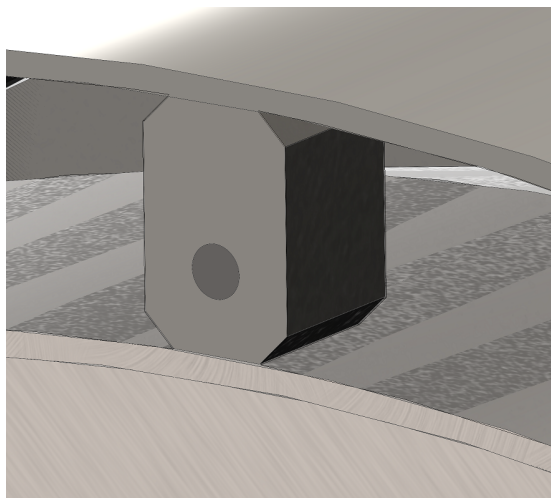
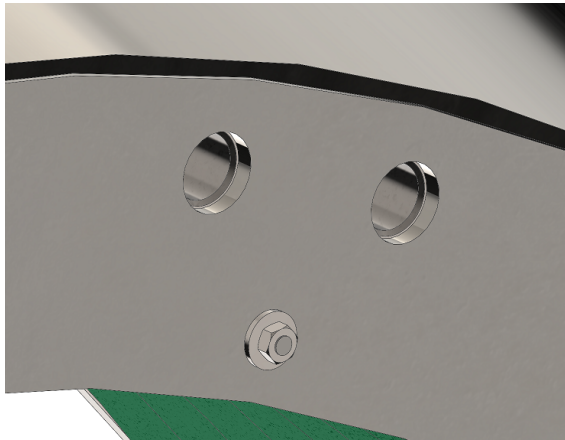
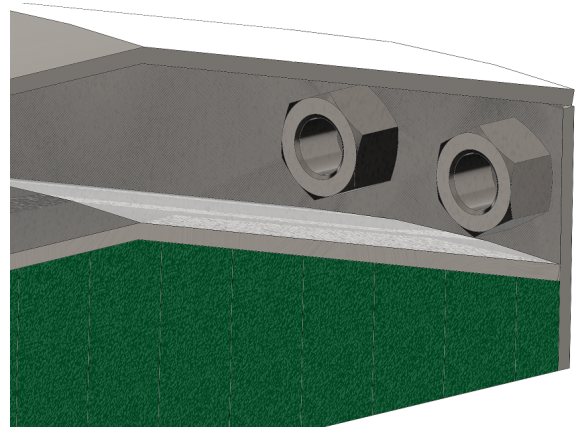


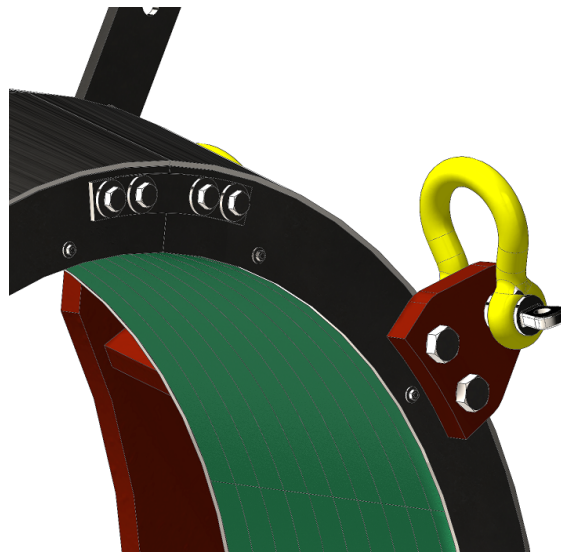
Figure D.28: Geometry of a mounting point for the forward jig adapter



(a) View from outside



(b) Section view showing the M16 nuts welded inside the shell



(c) View from outside with lifting support and 7/8" shackle

Figure D.29: Mounting points for lifting supports

Components, materials and manufacturing

The threaded bushings of Figure D.28 are machined out of 304 stainless steel, and they are welded to the shell. The other mounting points for the lifting are stainless steel nuts welded inside the shell, as it is visible in Figure D.29b.

Calculations and justification

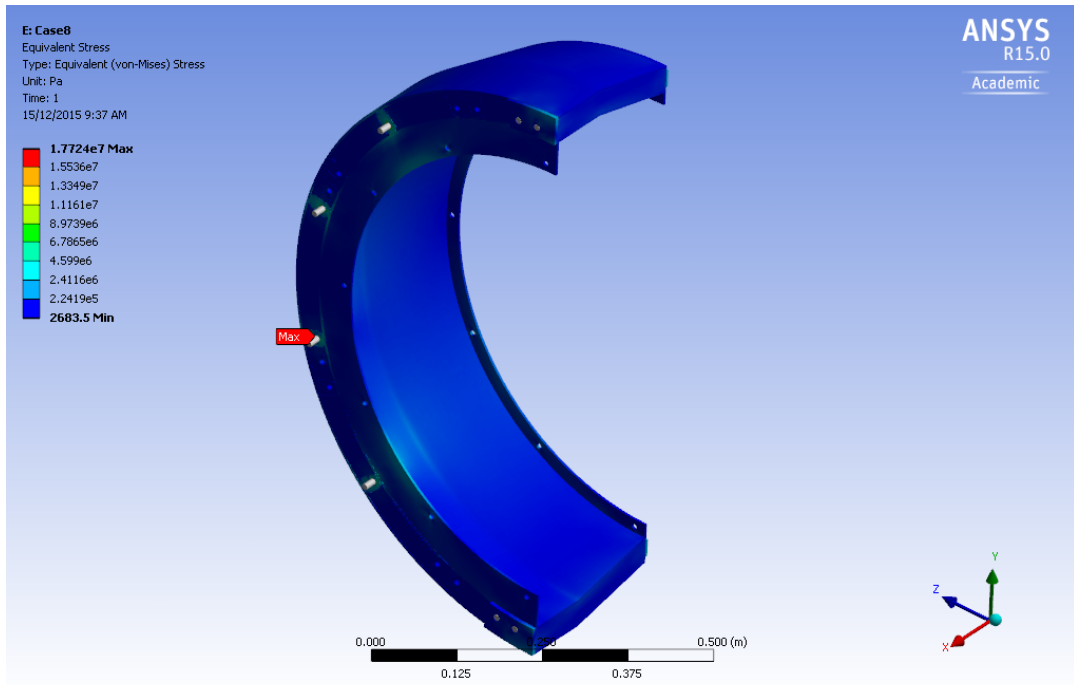
The calculation of the structural resistance of the mounting points for the jig adapter was conducted using Finite Element Analysis with the ANSYS Mechanical software [77]. The bolts are modelled by 19-mm long, 10-mm diameter beam elements that connect the mounting holes with the "ground". No other support is assumed for cases 7,8 and 9 of Table D.1, which represent movements while the shield is on the assembly jig. In other words, we neglect the contribution from friction to the bolted joint, which is a conservative assumption. Such assumption would be close to reality should the joint be not properly pre-loaded, a situation observed in the Belle years.

Case 8 provided the highest level of equivalent stresses, at $\sigma_v = 17.7$ MPa. The distribution of the stresses is shown in Figure D.30b. This stress is significantly lower than that of the attachments to end-caps after installation to the shields. These mounting points are not the critical components. The results of Figure D.30b present the converged stresses after two steps of mesh refinement in the highest-stress regions.

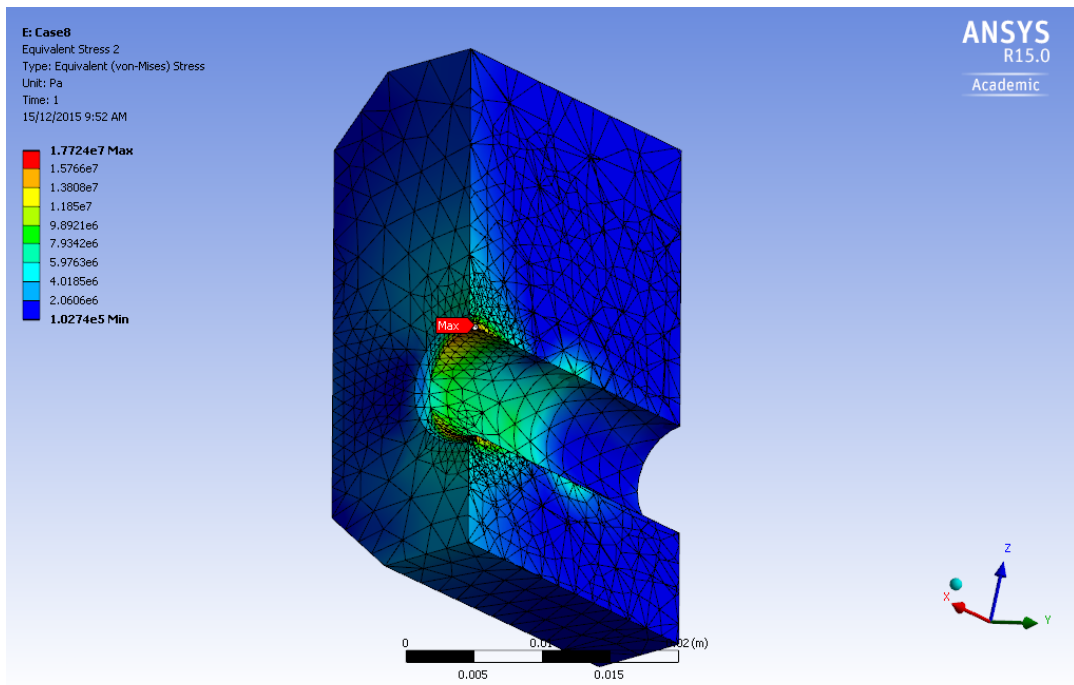
The mesh refinement is visible in Figure D.30b, where the mesh — uniform at the beginning of the study — is finer at areas where the stress gradient is larger. The results are reported in Table D.4.

Table D.4: Convergence study results for the equivalent stresses on the backward ECL assembly jig bushing during loading case 8

Solution Nb.	Equivalent stress (MPa)	Change (%)	Nb. of Nodes	Nb. of Elements
1	14.6	-	97108	34004
2	16.4	11.8	152989	72432
3	17.7	7.6	314073	187896



(a) Overall distribution



(b) Details of the critical element: the assembly mounting point.

Figure D.30: Equivalent stress distribution of the forward shield during loading case 8

D.3.5 Attachments to end-cap

The attachment to the end-cap are the components that hold the shield in place during normal operation.

Geometry

The geometry of the attachments to the end-cap is shown in Figure D.31.

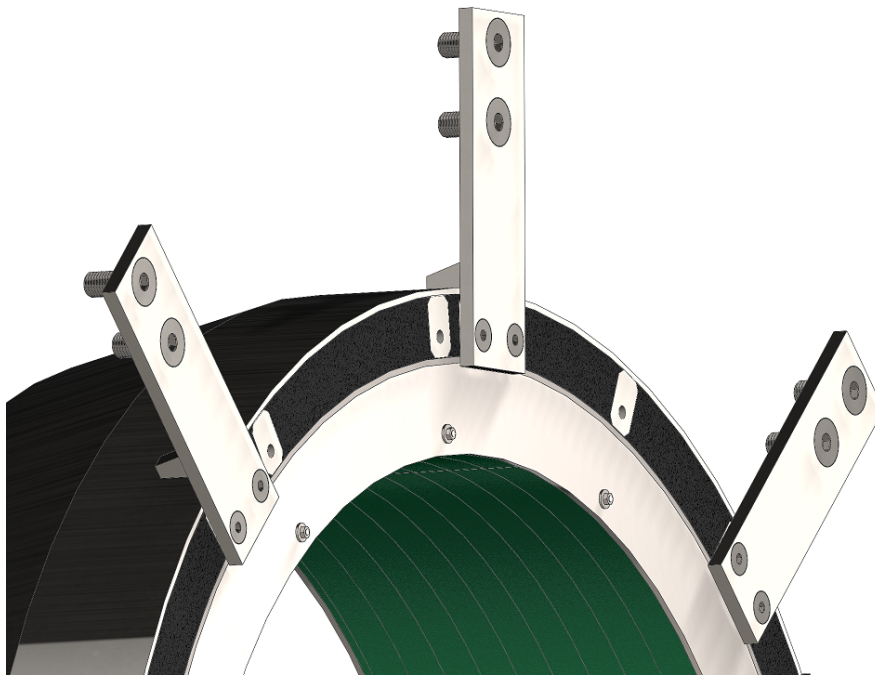


Figure D.31: Geometry of the attachments to forward ECL end-cap

Components, materials and manufacturing

This sub-system consists of eight copies of a welded assembly of 304 stainless steel plates which will be cut to shape by laser. The attachment plates are almost identical to the Belle part, to ensure compatibility. The only difference are the two M10 clearance holes allow fastening each plate to the shield with flat-head socket cap screws. They are countersunk in Belle II to increase clearance since the button-head bolt heads in Belle were just 5 mm

away from the magnetic flux return pieces (hence violating the usual “10-mm rule” design constraint).

The plates attach to the end-cap by means of two M16 × 2.0 × 40 mm flat-head socket cap screws. The choice of flat head screws instead of regular hex head bolts is driven by the required clearance between these fasteners and the pole piece of the magnetic flux return steel.

Calculations and justification

The structural resistance of these parts were also assessed using FEA. This time, the loading case #13 — after final installation, with a 0.3G acceleration along the z axis — is the one which is predicted to produce the largest stress according to the results. The stress distribution in the shield is shown in Figure D.32, with details on the loaded part shown in Figure D.33. The maximum equivalent stress is predicted to be 35.1 MPa near the clearance hole used to fasten the end-cap attachment plate to the shield. Again, it is important to note that the bolted connections are modelled in the frictionless contact limit. If proper assembly methods are used (the bolts are tightened to the correct torque), the mating surface will bear the majority of the load resulting in a lower stress at the clearance hole.

Moreover, frictionless contacts imply that the stresses are calculated assuming that the fastener bear the full load of the joint, which is also conservative from the point of view of the resistance of the fasteners themselves. The maximal load on the M10 fasteners is 0.54 kN axial and 0.46 kN shear, which translates into an equivalent stress well below the 689 MPa (100,000 psi) rating from the vendor.

The results of Figures D.32 and D.33 represent the “converged stresses” after three steps of mesh refinement in the critical areas. The results of the convergence study are shown in Figure D.34.

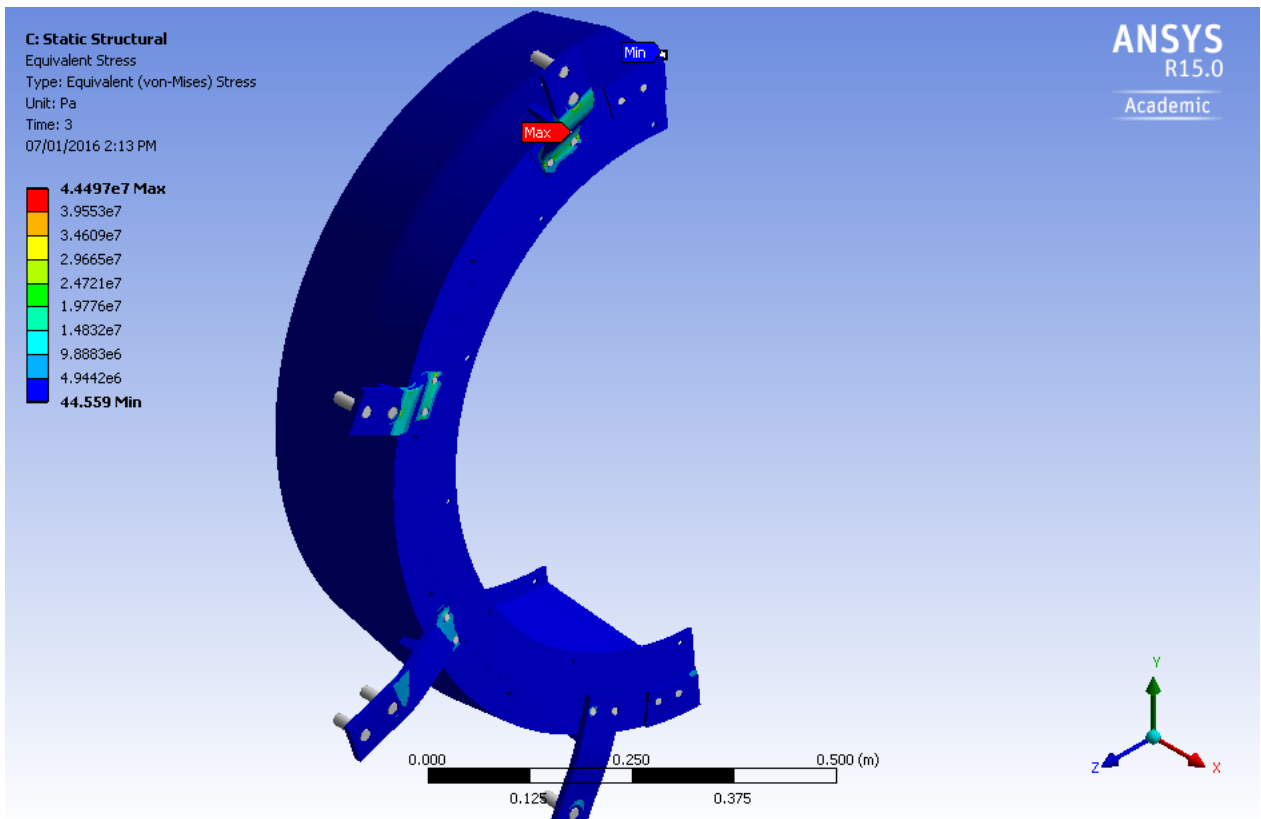


Figure D.32: Equivalent stress distribution in the forward shield during loading case #13.

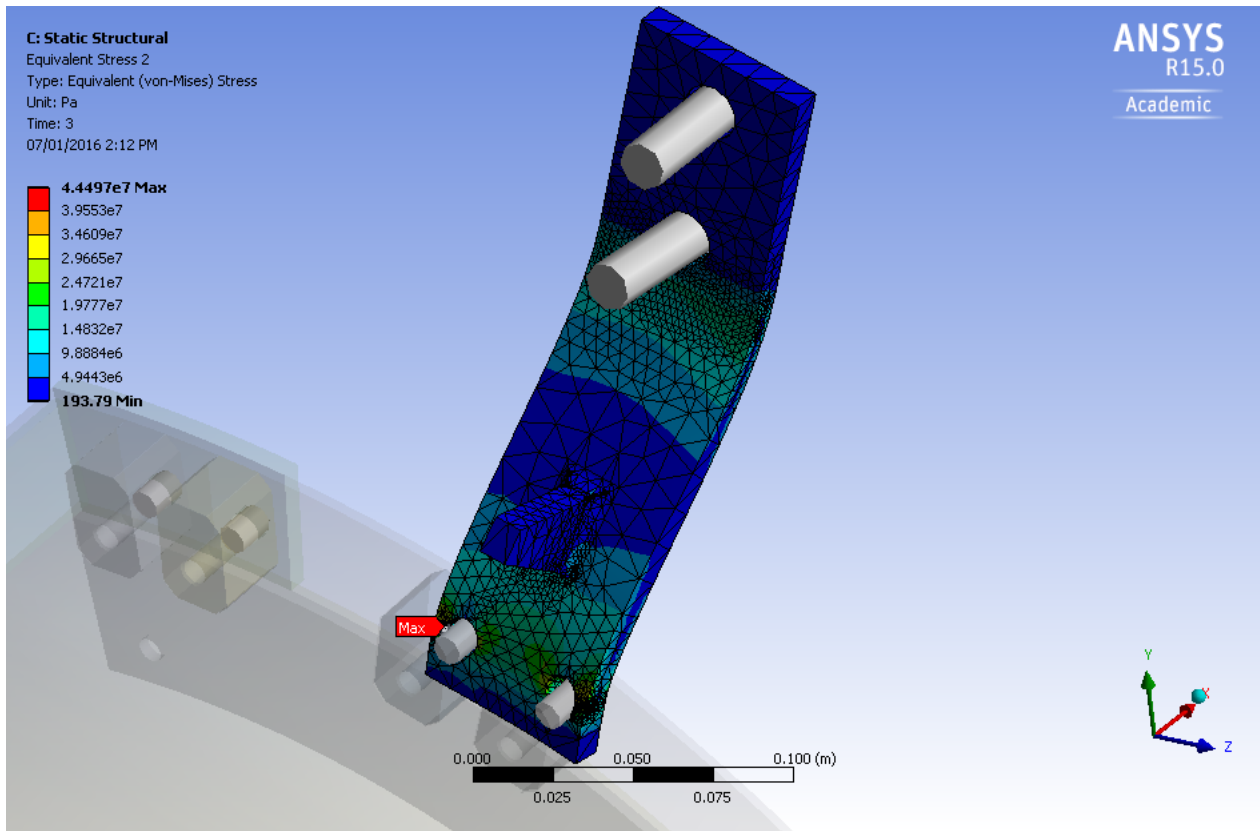


Figure D.33: Details of the equivalent stress distribution in the forward shield end-cap attachment during loading case #13.

Solution Nb.	Equivalent stress (MPa)	Change (%)	Nb. of Nodes	Nb. of Elements
1	40.1	-	90918	40563
2	45.3	10.2	125634	62126
3	44.5	-1.8	224383	128477

Figure D.34: Convergence study for the equivalent stress on the forward ECL attachment plate in loading case #13

D.4 Summary of structural analyses

Table D.5 contains all results for the studied load cases. Both the forward and backward load cases #13 provide the largest converged stresses. The minimal safety factor is 5.9 for the backward shield, and 4.7 for the forward shield. These values are above 4, so we consider that the current design is safe.

The equivalent stresses on the bolts can be calculated using the von Mises criterion given by Eq. (D.1). One can check that the safety factor for a standard 316 stainless steel fastener, rated up to 689 MPa (100,000 psi), is always over 30. No fastener resistance issue is expected.

For cases 7 and 11, the absence of symmetry plane between the loads and the geometry requires simulation of the full geometry. For that reason, we were not able to obtain mesh size-converged stresses while respecting the problem size limit for our ANSYS license. Even if the stresses cannot be compared to the converged values of Table D.5, the values were much below the yield stress so we expect no mechanical resistance issues in these cases.

Table D.5: Summary of the results of the Finite Element Analysis for structural resistance

Case Number		Max equiv. stress (MPa)	Max. displacement (μm)	Max. bolt load [†] axial/shear (kN)	Safety Factor ($\sigma_y = 207 \text{ MPa}$) (-)
Backward	4	12.4	15	0.85 / 0.22	>10
	5	15.2	17	0.08 / 0.56	>10
	7	-	-	-	-
	8	11.7	84	-0.43 / 1.00	>10
	9	11.2	34	-0.71 / 0.80	>10
	11	23.2	54	0.19 / 0.65	8.9
	12	27.8	84	0.45 / 0.70	7.4
	13	35.1	82	0.64 / 0.57	5.9
Forward	4	10.7	11	0.24 / 0.12	>10
	5	13.4	18	0.25 / 0.44	>10
	7	-	-	-	-
	8	18.5	16	-0.17 / 0.62	>10
	9	14.2	14	-0.08 / 0.47	>10
	11	-	-	-	-
	12	39.7	69	0.37 / 0.54	5.2
	13	44.5	85	0.54 / 0.46	4.7

†: According to von Mises stresses. The most loaded bolts are all M10.

D.5 Fabrication and commissioning

D.5.1 Vendor

A public bidding process was managed by the University of Victoria Purchasing Services. The winner of the process was not part of the early manufacturer network exploration during the project definition phases. However we were convinced of their ability to deliver quality components because of their good documentation practices, extensive supplier network, and rich previous experiences with sheet metal stainless steel. Their proximity to the University of Victoria also made possible frequent visits to follow the fabrication process more closely. The project was awarded to

- Turbulent Diffusion Technology Inc., 2601 Murray St Port Moody, BC V3H 1X1, Canada

who managed and sub-contracted the work in agreement with our contract terms.

D.5.2 Modifications from design drawings

Apart from the expected heat-induced geometric deviation during welding, three items were manufactured differently than the original specification drawings. There are no impact on the shields performance or usability, but these changes should nonetheless be documented.

Forward bushings

The forward bushings are installed in sets of three: two of them for the attachment plates to the end-caps — visible in Figure [D.31](#) — and the remaining one for the end-cap assembly jig, seen in Figure [D.26](#). These bushings are separated by a 12-mm gap.

During a visit to the manufacturer on January 27th, 2017, we were informed this gap was not sufficient for the welding nozzle, and the bushings were instead welded at the outside edges only after producing a supplementary 5-mm fillet on that edge for better penetration. See Figure [D.35](#) for a picture showing two of such completed welds.

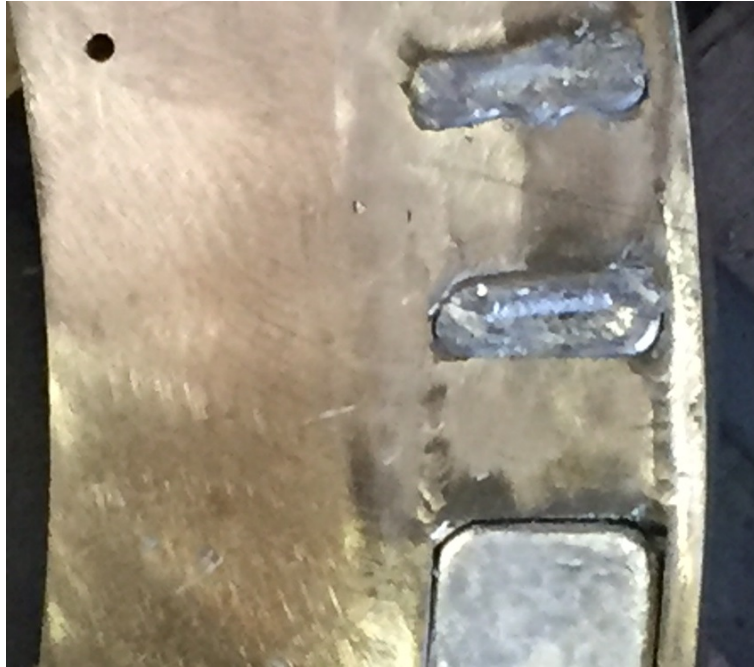


Figure D.35: Example picture of the forward shield bushing welds (as built). The picture was taken after casting the lead in the shells, and before drilling of the M10 threaded holes.

Since the designed weld were designed to run on both sides of the bushing, we need to re-asses the strength of the joint.

Geometry The dimensions of the loaded weld beads are reported in Figure D.36. As with all fillet welds, it always fails in shear regardless of the loading direction. The failure will occurs along the throat of the weld, in plane perpendicular to the hypotenuse in a section view of the fillet. This is represented in Figure D.37. Therefore the area under stress is

$$\begin{aligned} A_s &= \frac{1}{\sqrt{2}} \cdot 5 \text{ mm} \cdot 15.4 \text{ mm} \\ &= 89.8 \text{ mm}^2. \end{aligned} \tag{D.4}$$

Material properties The bead is made of the same wire filler material as the rest of the ECL shields welds. Supplier data for 310 Stainless Steel (AMS 5694) Filler Metal^a reported in the Matweb Engineering Materials Database [100] mentions an ultimate tensile strength

^aPrivate communication with the manufacturer confirmed the use of this filler material

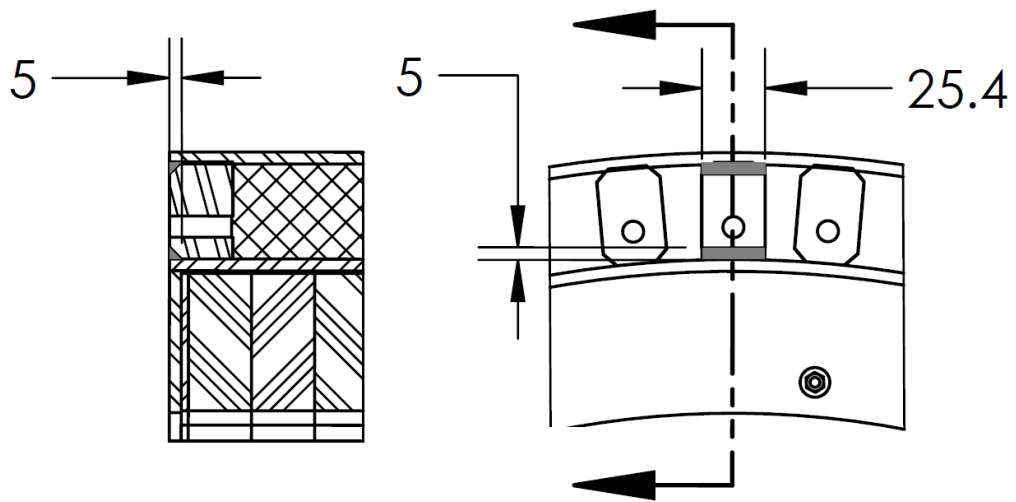


Figure D.36: As-built geometry of the loaded weld beads on the forward shield bushings. The grey areas represent the weld beads.

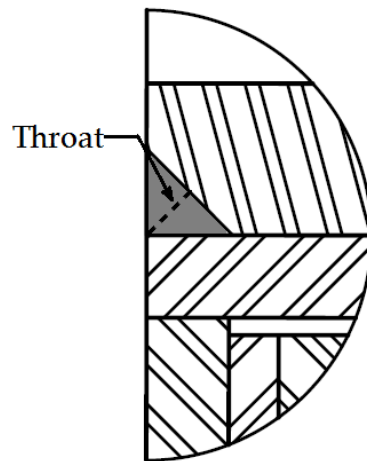


Figure D.37: Failure plane in a fillet weld. The grey area represents a weld beads.

of

$$\sigma_u = 586 \text{ MPa [85 ksi]}$$

and a yield strength of

$$\sigma_y = 379 \text{ MPa [55 ksi]}$$

where the value in brackets is the original specification in imperial units. By using the von Mises criterion [78], we approximate the shear strength of the material to

$$\begin{aligned}\sigma_s &= \frac{1}{\sqrt{3}}\sigma_y \\ &\approx 219 \text{ MPa.}\end{aligned}\tag{D.5}$$

The surrounding material, 304 stainless steel, has a nominal $\sigma_y = 207$ MPa.

Loads To check the resistance of the structure without re-doing all numerical studies, we consider conservative assumptions simplifying the problem. We calculate the safety factor of joints if the whole mass of a forward half-shield is held by only one of these bushings. Furthermore, we applied the load in a direction as to “pull” it out of the shells such that only the welds are providing mechanical resistance (as opposed to having contributions from the surrounding structure). The half-shield assemblies have a mass $m = 186$ kg (estimated from the SolidWorks model), so this corresponds of a load

$$\begin{aligned}P &= mg \\ &= 1825 \text{ N}\end{aligned}\tag{D.6}$$

taken by both weld beads. This conservative load can be compared to the maximum load taken by the bolt that attaches to these bushings. From loading case FWD # 13 results reported in Table D.5, the maximum calculated load is 540 N axially and 460 N in shear, or an “equivalent von Mises load” of 884 N on the bolt. This justifies our statement that $P = 1825$ N is a conservative load on the bushing, yet in the right order of magnitude so that the calculation is meaningful.

Stress calculation Still conservatively assuming this load is taken under pure shear both the top and bottom welds, the area under stress is twice that of a single bead. The shear stress is therefore

$$\begin{aligned}\sigma &= \frac{P}{2A_s} \\ &= 10.2 \text{ MPa}\end{aligned}\tag{D.7}$$

Result and implications The 10.2 MPa pure shear provides a safety factor of almost $SF_\sigma = 21.5$ for the weld bead itself. This factor sufficient to ensure mechanical resistance of the weld. If one considers the same stresses in the surrounding material — 304 stainless steel,

which has a lower elastic limit — the safety factor is down to just under $SF_{\sigma} = 11.8$. This is also well beyond our design guideline of $SF_{\sigma} \geq 4$.

In conclusion, the departure from the design weld beads during fabrication shouldn't pose any significant risk to the mechanical soundness of the structure.

Backward attachment plates

The gussets to attach the backward shield to the end-cap (ref. Figure [D.17](#)) were welded at the wrong angular position (23° instead of 22.5°) because of an ambiguity in the drawings we provided. This was noticed just before shipping, so instead of moving these welded parts, we decided to manufacture wider attachment plates that would be attached to a laser-cut jig replicating the mounting holes on the end-cap. The actual plates were 12.6 mm wider than the original design.

The bolt clearance holes were then drilled to match the actual positions on the shield, which were off by approximately 5 mm. Wider plates shouldn't have any impact other than increased structural resistance since there are no surrounding components that can interfere with them in the final application. However, extra care must be taken during installation: since they were produced to match as-built positions, each one is uniquely numbered (1 through 8) and must be installed at the corresponding position. The as-built plates are represented in Figure [D.38](#).

Backward neutron absorber cover

For the backward shield, the neutron absorber cover is an aluminium alloy sheet fastened with small countersunk screws to the shells (see Figure [D.10](#)). The design screw size was $M2 \times 0.6$. However the tension required to hold the cover in place was greater than expected due to geometric distortions from welding. Many of these screws broke during assembly, so the manufacturer upgraded to $M2.5 \times 0.45$ screws and this solves the problem. No impact other than strengthening the cover is expected from this change.

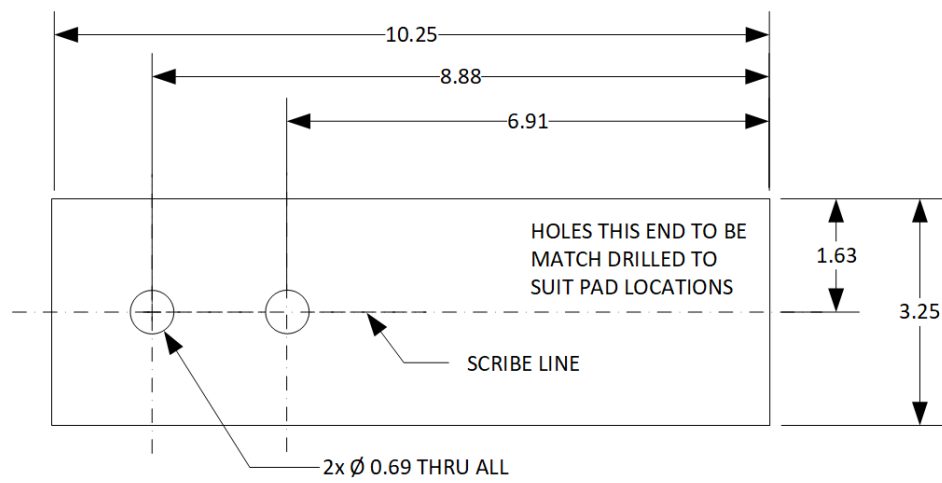


Figure D.38: As-built backward end-cap attachment plate. Drawing based on the material provided by Brenco Industries for Turbulent Diffusion Technology.

*
**